

Quantitative Mechanics of Biological Cells

by

Saurabh Kaushik

A thesis submitted for the degree of

Doctor of Philosophy

to the

Jawaharlal Nehru University



Soft Condensed Matter Group

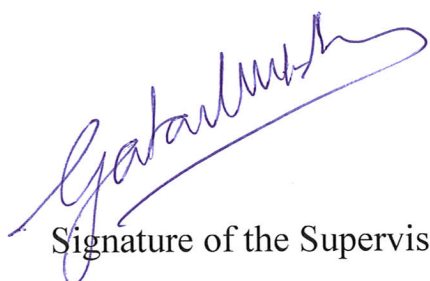
Raman Research Institute

Bangalore, INDIA

August 2024

Declaration

I hereby declare that the work presented in this thesis is completely original. This research work is carried out under the supervision of **Dr. Gautam V. Soni** at Raman Research Institute, Bengaluru, India. This dissertation is the result of my work unless otherwise stated. No part of this thesis has been submitted elsewhere for the award of any degree, diploma, membership, fellowship, or any other similar title of any university or institution. I also declare that this thesis has been passed through the **DrillBit** software to check for plagiarism.



Signature of the Supervisor

Dr. Gautam V. Soni

Soft Condensed Matter Department

Raman Research Institute

Bengaluru 560080

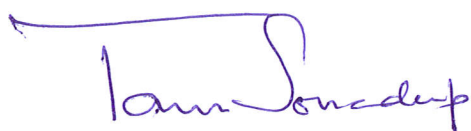


Signature of the Student

Saurabh Kaushik

Thesis Certificate

This is to certify that the work contained in the thesis titled '**Quantitative Mechanics of Biological Cells**', submitted by **Saurabh Kaushik** to **Jawaharlal Nehru University, Delhi, India** for the award of the degree of **Doctor of Philosophy** in his original work. The results embodied in the thesis have not been submitted to any other university or institute for the award of any degree or diploma.



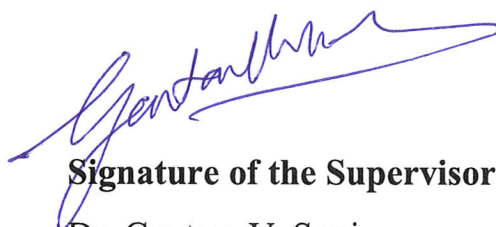
Signature of the Director

Prof. Tarun Souradeep

Director

Raman Research Institute

Bengaluru 560080



Signature of the Supervisor

Dr. Gautam V. Soni

Soft Condensed Matter Group

Raman Research Institute

Bengaluru 560080

Dedicated to

*My spiritual master HH Shree Ashutosh Maharaj Ji for shedding his
divine blessings and enlightening my inner self, which helped me in
both the dark and bright moments of my journey*

&

*My caring mother and father for their love, support, patience, and all
the sacrifices they have made for me while I was en route on this
journey*

Acknowledgment

There have been a lot of ups and downs in my life during my entire PhD journey, but there have been many individuals who supported, motivated, and inspired me to keep my spirits high. Since a Ph.D. is one's path guided by the supervisor, I believe that there was no better person for me than Gautam to take up this role. His work ethic, guidance, and approach towards research have been extremely exhaustive, which in the beginning seemed very annoying and unnecessary, but with time I have learned that all these things are what all young researchers should definitely be exposed to. I could not summarize what I have learned from him in limited words, but the discussions with him after his golden statement: "Let's have a walk and talk" have done wonders every time I had a tough time in my professional as well as personal life. In time I have learned from him that, just being great at science is not a sign of a great Ph.D. supervisor, rather training the students to bring the best out of him and keeping the environment positive is. I admire his consistent positive outlook towards life, and keeping the thinking process as elementary as possible. At the end of my journey, I can say I have learned from the best.

The meetings with my Ph.D. advisory committee members, Promod and Sayantan, have helped me to get a new and holistic perspective on my thesis projects. I want to thank Promod, Sayantan, Raghu, Ranjini, Sandeep, Sadiq, and EEG group members for their kindness in allowing me to use their lab facilities wherever needed. I also want to thank Admin and Academics members including Naresh, Suresh, C.S.R. Murthy, Radha, Harini, Shailaja, Gayatri, and Vidya for taking care of various administrative aspects of my Ph.D; Chaitanya and KRK for managing the lab purchases and conference-related management activities; Mechanical workshop for helping with the fabrication of various custom components for my experiments; Electrical department (Muneeshwaran) for electrical issues in the lab; Purchase, Accounts and Library for various aspects at the institute; and finally the hostel cooks (Padma ji, Uma ji, Sharada ji, etc) for providing healthy food at the hostel and all the hostel and RRI security guards, for keeping the work and residential safe.

I thank Sumanth, Manohar, Mahesh, and Koushik for training me on various experimental setups during my initial days at the lab. They all have been a great support to me and we had some good scientific discussions. I also thank Prabhakaran and Arka for their support in various experiments. I thank Serene for taking care of all the lab order purchases required for the lab. I thank Serene and Divya for the basic molecular biology training, and helping and guiding me for many bio-related work in the lab. I thank

Sukanya, Punit, Shubham, Rajshekhar, Lavanya, Subhash, Mayofik, and Nagesh for being great lab mates. I want to especially thank Yatheendran for all the help and training in performing the AFM, Confocal, and SEM experiments.

I thank my collaborators; Dr. Cecil Ross, Dr. Roshan C. Ross, Dr. Sweta Srivatsawa, Dr. Pavana, and Dr. Varadharajan Sundaramurthy for their help and support in completing my various thesis projects by allowing me to use their lab facility and providing the samples for the experiments.

The COVID-19 pandemic was hard for many, but I am thankful to Anand, Sukhi, Nancy, Chandu, Noman, Intezar, and Palak for creating a jolly environment during those hard times. I thank them all for the cooking, gambling, gully cricket, and occasional physical fitness during the lockdown. I want to thank other colleagues at the institute; Sebanti, Vishnu, Arsalan, Sachi, Aashish, Manish, Mukesh, Shashank, Vaibhav, Ghadai, Shreyas, Mari, Swamy, Subbu, Sachin, and many others for various sports activities at the Institute.

I thank Sachin Kaushik, Lalit, Vivek, Shivam, Shristi, Harshita, Sakshi, Monica, Shashank, Rashmi, Reshma, Jaismeen, Aditya, Sayantan Adak, Panda, and Navdeep; my friends from high school, graduation, and master for various activities including preparing for entrance exams, trips and memorable fun time. I also thank my Master's Thesis supervisor Dr. Rahul Marathe for exposing me to the research work for the very first time. I also want to thank my teachers, Avinish Sasexa Sir, Sinha Sir, Tiwari Sir, Meetu Mam, Mrinal Mam and Meera Mam for their guidance during my high school and graduation.

Special Thanks

I am extremely thankful for my family's support and sacrifices. I have stayed away from home for a very long time, but my parents have always supported me with all they had. They have always kept their problems hidden from me, so that I can focus on my career, and both of them have always motivated me to aim higher and higher. No words can express how much I love or care for them, I only hope that I have made them proud and wish to make them even prouder in the future. Although the love of my life joined me at the end of this journey, but my wife, Nishu has done her best in her power to create a homely environment for us, which was missing for all the years I stayed away from my parents. She has spoiled me with her amazing cooking skills, because of which I have also become a food critic. Time spent with my nephew (Reyansh), sister (Ruchi), and brother-in-law (Sumit Jiju) in person or over the call, has always been refreshing for me, the family trip to Kerala with them was a well-needed break. My father-in-law has also played a crucial part in supporting many personal aspects of my life lately. I have had the best family one can expect. I thank them all for all the things they have done for me over the years.

I have had another family; without which I could not have kept my energy high. The members of my DJJS family gave me a purpose and an escape from normal life, which has helped me to recharge myself now and then. I want to thank, my spiritual master HH Shree Ashutosh Maharaj Ji for shedding his divine blessings and enlightening my inner self, which helped me in both the dark and bright moments of my journey. I want to thank Sadhavi Manisha Bharti Ji, Mridula Bharti Ji, Nishanka Bharti Ji, Ritu Bharti Ji, Dr. Deepa Bharti Ji, and Rachita Bharti Ji, for the most needed guidance when needed. I also want to thank, Swamy Dr. Sarveshanand Ji, Adityanand Ji, Narendrand Ji, and Anil Bhaiya for the motivational discussions and talks inspiring me to work hard on my actual life goals. I have many brothers from my YPSS family, who have stood with me at times when no one would; I am grateful to have brothers like, Rajat, Animesh, Ravi, Sachin, Kapil, Laala, Bhupi Bhaiya, Meet, Nikhil Bhaiya, Shushank, Roshan, Nitesh Bhaiya, Mangal Bhaiya, Ranjeet, Shiv, Mohit, Shashank, Vinayak, Pavan Bhaiya, Pankaj Bhaiya, Mihir, Mayank, Manoj Bhaiya and many many more. Rajat, Animesh, and Sachin Kaushik have always been there for me at different stages of my life, they are the most dependable souls for me out there. I can never thank enough the god or MJ, for surrounding me with such great souls. All these people have made a crucial contribution in carving me into the person I have grown to be today.

Abstract

Morphological changes and the effective mechanical response of cells are potent markers for various diseases and an understanding of cellular growth and their development cycles. A quantitative understanding of these morphological (volume or surface area) and mechanical (stiffness) changes caused by different pathogens or chemicals/drugs can be vital for disease diagnosis in large-scale population screening in low-resource conditions. studies. All the biological systems are extremely complex and their morphology, as well as mechanics, are sensitive to their environment (pH, Tonicity, Temperature). The understanding of these physical parameters in soft materials also have promising applications in various pharmaceuticals industries, including optimizing small-molecule delivery capsules or vesicles used in various cell-response. In this thesis work, we use resistive pulse sensing-based custom electro-fluidic devices, atomic force spectroscopy measurements, and various microscopy techniques to quantitatively study the cellular mechanical and/or physiology of model cells and biological cells. The research work presented in this thesis is divided into the following parts:

Chapter 1 introduces the background of cellular mechanosensing scientific research work required for this thesis. We also give a brief introduction about the different approaches used across the globe for cellular qualitative or quantitative mechanical as well as physiological studies. Here, we also explain the biochemical aspect of a cell's interior to establish an understanding of how cells respond to different types of probing methods to give different mechanical and physiological responses. The ambiguity in various measurement techniques giving different quantitative values is also discussed in this chapter. We also provide a brief overview of important topics related to the upcoming chapters, followed by an outline of various problems addressed in this thesis.

Chapter 2 provides all the details on the sample preparation protocols, and the procedures involved in procuring and handling the biological samples, drugs, and chemicals used. The working principle of the Resistive Pulse Technique (RPT) and the Atomic Force Microscopy (AFM) force spectroscopy measurements, extensively used in this thesis work are detailed in this chapter. A review of different theoretical models used to understand the data acquired using the resistive pulse technique is also briefed here. I next describe the steps involved in fabricating the custom-made micropore device for RPT experiments. This is followed by a description of the sample incubation chamber made in the lab for AFM force spectroscopy study on cells. We also provide a thorough detail on all instruments, their required

settings along with troubleshooting tips we learnt while performing these experiments. This chapter is intended a guidebook for anyone starting fresh on resistive pulse technique and AFM force spectroscopy.

Chapter 3 establishes the electro-fluidic measurement principle used in this thesis work. First, we measure the volumetric changes in red blood cells in physiologically relevant alcohol concentrations. Alcohol exposure has been postulated to adversely affect the physiology and function of the red blood cells (RBCs). The global pervasiveness of alcohol abuse, causing health issues and social problems, makes it imperative to resolve the physiological effects of alcohol on RBC physiology. Alcohol consumed recreationally or otherwise almost immediately alters cell physiology in ways that are subtle and still unresolved. In this chapter, we demonstrate high-resolution quantitative electrofluidic measurement of changes in RBC volume upon alcohol exposure. We find an RBC shrinkage of 5.3% at 0.125% ethanol (the legal limit in the United States) and a shrinkage of 18.5% at 0.5% ethanol (the lethal limit) exposure. Further, we also measure the time dependence of cell volume shrinkage (upon alcohol exposure) and then recovery (upon alcohol removal) to quantify shrinkage and recovery rates of RBC volumes. This work presents the first direct quantification of temporal and concentration-dependent changes in red blood cell volume upon ethanol exposure. We present a universally applicable high-resolution and high-throughput platform to measure changes in cell physiology under native and diseased conditions.

Chapter 4 presents a lab-made cost-effective (~3500 INR) trans-impedance amplifier compatible with our electro-fluidic micropore devices for resistive pulse sensing of Biologicals samples. In Chapter 3, we show that our electro-fluidic measurements require a low-noise trans-impedance amplifier. The required commercial amplifiers cost as much as 4 to 12 lakh INR. Here, we introduce our low-cost and portable trans-impedance amplifier and characterize the maximum range, absolute error percentage, and RMS noise of the amplifier in the measured current signal, along with the amplifier's bandwidth, and compare these characteristics with the commercial amplifiers. Using our home-built amplifier, we demonstrate a high throughput detection of ~1300 cells/second and resolve cell diameter changes down to 1 μm . Finally, we demonstrate the measurement of cell volume changes in *E. coli* bacteria when exposed to ethanol (5% v/v), which is otherwise difficult to measure via imaging techniques. Our low-cost amplifier (~100-fold lower than commercial alternatives) is battery-run and completely portable for point-of-care applications.

Chapter 5 establishes an empirical formulation for the estimation of cellular elastic modulus using a high-throughput label-free approach. We first establish the quantitative measurement of cell stiffness using the softening effect of the actin inhibitor drug (Latrunculin-A) as a control parameter. We correlate our electro-

fluidic quantitative measurement with the cellular elasticity measurements using atomic force microscopy on red blood cells. The concentration of the available actin reduces in the presence of the Lat-A drug as it binds to the actin monomers near the nucleotide-binding cleft and prevents actin monomers from polymerizing. The decrease in the polymerizing rate of actin monomers affects the whole cell stiffness. We make use of the AFM force spectroscopy measurements and various electro-fluidic experimental data to establish an empirical model for elastic modulus estimation. This approach allows us to estimate the relative elastic modulus of soft samples solely based on our electro-fluidic measurements. Next, we demonstrate the medical application of our electro-fluidic system by screening sickle cell disease (SCD) patients. We show that our experimental device can be used at the point-of-care, by performing all measurements on-site at the St. Johns Medical College Hospital. The stiffness measurements of the patient RBC cells were correlated with the patient's pathology reports. We show a linear correlation of the cell stiffness with the patient's HbS content. Our measurements allow us to use whole-cell stiffness as a preliminary screening parameter for sickle cell disease patients and also screening possibilities for many other hematological conditions. Our label-free stiffness detection approach also has future applications in areas such as tumor cell identification, veterinary sciences as well as hydrogel technologies.

Chapter 6 summarizes our understanding of all the problems addressed in previous chapters and highlight a few unaddressed or open questions to explore in the future.

Signature of the Supervisor

Dr. Gautam V. Soni

Soft Condensed Matter Department

Raman Research Institute

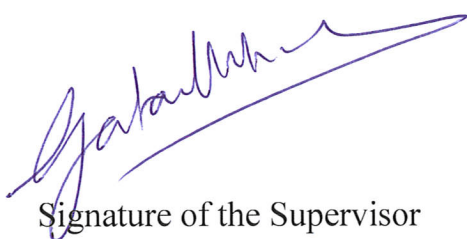
Bengaluru 560080

Signature of the Student

Saurabh Kaushik

List of Publications

1. **Kaushik S**, Mahadeva M, Murugan KD, Sundaramurthy V, Soni GV. Measurement of Alcohol-Dependent Physiological Changes in Red Blood Cells Using Resistive Pulse Sensing. ACS Sensors. 2020; 5: 3892–3901.
2. **Kaushik S**, Selvanathan P, Soni GV Customized low-cost high-throughput amplifier for electro-fluidic detection of cell volume changes in point-of-care applications. PLoS ONE 17(4): e0267207.
3. B. Sinha, A. Biswas, **S. Kaushik** & G.V. Soni. Cellular and Nuclear Forces: An Overview. [Invited Book Chapter – "Molecular Motors" (Springer: Methods in Molecular Biology series)]
4. **Kaushik, S.**, A., Mishra, Ross C. R., Srivastava, S., Ross C., and Soni, G. V. Novel high-throughput label-free screening of sickle cell disease patients based on their red blood cell stiffness. **(In Submission)**



Signature of the Supervisor

Dr. Gautam V. Soni

Soft Condensed Matter Department

Raman Research Institute

Bengaluru 560080



Signature of the Student

Saurabh Kaushik

CONTENTS

Declaration	iii
Thesis Certificate	v
Acknowledgments	ix
Special Thanks	xi
Abstract	xiii
List of Publications	xvii
List of Figures	xv
List of Tables	xxxi
CHAPTER 1: Introduction	1
1.1 Microfluidics-based Cellular Mechanosensing	3
1.1.1 Quantitative Deformability Cytometry (q-DC)	3
1.1.2 Dimensionless Indexing of Cellular Stiffness-based Deformability	6
1.1.3 Constricted Suspended Microchannel Resonator	9
1.1.4 Real-Time Shear Flow Deformability Cytometry (RT-DC)	10
1.1.5 Hydrodynamic Extensional Flow Deformability Cytometry	11
1.1.6 Resistive Pulse Electrofluidic Measurements	12
1.2 Cellular Membrane-Based Mechanosensing	14
1.2.1 Micropipette Aspiration	14
1.2.2 Membrane Tether Extraction using Optical Tweezer	16
1.3 Rheology Based Cellular Mechanosensing	17
1.3.1 Parallel Plate Rheometers	17

1.3.2 Laser Tracking Rheology	19
1.4 Dual Optical Stretching	21
1.5 Conclusion	22
1.6 References	23
CHAPTER 2: Experimental Techniques	29
2.1 Resistive Pulse Sensing Technology	30
2.1.1 History of Resistive Pulse Technique	31
2.1.2 Micropore Forging Protocol	41
2.1.3 Micropore Device Preparation	44
2.1.4 Data Acquisition	45
2.1.5 Micropore Characterization	47
2.1.6 Data Analysis	49
2.2 Atomic Force Microscopy	51
2.2.1 History of Atomic Force Microscopy	51
2.2.2 AFM Imaging	52
2.2.3 AFM Force Spectroscopy Measurements	56
2.3 Conclusion	59
2.4 References	60

CHAPTER 3: Measurement of Alcohol-Dependent Physiological Changes in Red Blood Cells Using Resistive Pulse Sensing **65**

3.1 Introduction	66
3.2 Materials and Methods	68
3.2.1 Fabrication of Electrofluidic Devices	68
3.2.2 Sample Preparation	68
3.2.3 Electrofluidic Measurements	69
3.3 Results and Discussion	70
3.3.1 Principal of Electro-fluidic Measurements	70
3.3.2 Signal Contrast and Resolution of the Micropore Device	73
3.3.3 Volume Quantification of Model Cells	75
3.3.4 Detection of Ethanol Dependent Changes in Red Blood Cells	78
3.3.5 Reversibility of RBC Volume Changes	80
3.3.6 Time Dependence of RBC Volume Changes upon Ethanol Exposure	82
3.4 Conclusion	84
3.5 References	85

CHAPTER 4: Customized low-cost high-throughput amplifier for electro-fluidic detection of cell volume changes in Point-of-Care applications **93**

4.1 Introduction	94
4.2 Materials and Methods	96
4.3 Results	98
4.3.1 Amplifier Characteristics	98
4.3.1.1 Current Range	98

4.3.1.2 Absolute Error and Root Mean Square (RMS) Noise in Current	99
4.3.1.3 Bandwidth of lab amplifier	100
4.3.2 Translocation Measurements	102
4.3.2.1 Detection of model cells using lab-amplifiers and electro-fluidic devices	102
4.3.2.2 Resolving and quantifying mixed sample population	104
4.3.2.3 Effect of alcohol on bacterial cell volume	107
4.4 Conclusion	109
4.5 References	110
CHAPTER 5: Novel high-throughput and label-free screening of sickle cell disease patients based on their red blood cell stiffness	117
5.1 Introduction	118
5.2 Materials and Methods	121
5.2.1 Micropore Device Fabrication	121
5.2.2 Sample Preparation	121
5.2.3 Electro-Fluidic Measurements	122
5.2.4 Changes in RBC Stiffness using Lat-A	124
5.2.5 AFM based cell stiffness Measurements	124
5.3 Results and Discussion	126
5.3.1 Detection of Cell Volume and Cell Stiffness in Micropore Experiments	126
5.3.2 Measurement of varying cell stiffness of RBCs	128
5.3.3 RBC Elastic Modulus Estimation	129
5.3.4 Empirical correlation between constricted micropore dwell times and Cellular Stiffness	130

5.3.5 Screening SCD Patients Based on RBC Stiffness	132
5.4 Conclusion	135
5.5 References	136
CHAPTER 6: Summary and Future Directions	139
6.1 Cellular porosity under small applied voltages	141
6.2 Translocation of Cells through a dual micropore device for stiffness estimation	142
6.3 Studying the cellular membrane fluctuations during cell translocation through a constriction micro-channel	143
Appendix 1: Basic Rules for Writing and Plotting Experimental Data	145
A1.1 Using correct significant figures to avoid false resolution in presenting experimental data	145
A1.2 Importance of using the standard deviations for correctly fitting the experimental data	147
Appendix 2: Pressure in a Cylindrical and Conical Geometry	151
Appendix 3: Analytical calculation of volume change in Red Blood Cells	153
Appendix 4: AFM force spectroscopy data analysis	157
Appendix 5: Additional Experimental Data used in the chapter 3	161
Appendix 6: Additional Experimental Data used in the chapter 4	169
Appendix 7: Additional Experimental Data used in the chapter 5	177
Appendix 8: MATLAB Codes and Igor Scripts	201
A8.1 MATLAB code for analyzing the AFM force spectroscopy data	201
A8.2 MATLAB function ‘Parabolic_Cantilever’ used in the previous section	207
A8.3 Igor scripts to extract the AFM force spectroscopy data to be used in MATLAB	209
A8.4 Igor scripts used for micropore data analysis	213

Appendix 9: Additional Experiments Performed	235
A9.1 Effect of software filtering on the measured ΔG values	235
A9.2 Effect of Bovine Albumin Serum on EtOH-treated RBCs	236
A9.3 Electrofluidic detection of RBCs infected with malaria Parasite	237

List of Figures

Figure 1.1 Physical parameters associated with the cellular mechanosensing	2
Figure 1.2 Quantitative Deformability Cytometry (q-DC)	5
Figure 1.3 Dimensionless Indexing of Cellular Stiffness-based Deformability	8
Figure 1.4 Constricted Suspended Microchannel Resonator (SMR)	10
Figure 1.5 Real-Time Flow Deformability Cytometry	11
Figure 1.6 Hydrodynamic Extensional Flow Deformability Cytometry	12
Figure 1.7 Resistive Pulse Sensing Electro-fluidic Measurements	13
Figure 1.8 Cellular Membrane-Based Mechanosensing	15
Figure 1.9 Rheology-based Cellular Mechanosensing	19
Figure 1.10 Dual Optical Stretching	21
Figure 2.1 Schematic of the Coulter Counter design	32
Figure 2.2 Schematic of a spherical particle inside a conducting cylinder	34
Figure 2.3 Quantifying the volume of latex polystyrene particles	35
Figure 2.4 Oscillograms of resistive pulse signals for human red blood cells	36
Figure 2.5 Electric field distortion due to a non-conducting sphere inside a conducting fluid in a cylindrical tube	37
Figure 2.6 Resistive pulse signals on the oscilloscope and the change in resistance v/s volume for polystyrene particles	40
Figure 2.7 Steps involved in forging a micropore from a glass capillary	43
Figure 2.8 Images of steps involved in micropore device preparation	45
Figure 2.9 Interface of the record trace LabVIEW code	46
Figure 2.10 Interface of the IV Curve LabVIEW sub-VI	48

Figure 2.11 Interface of the Translocation Event Analysis LabVIEW Code	50
Figure 2.12 Laser cantilever alignment on the PSD	53
Figure 2.13 Contact mode AFM images of a DVD	54
Figure 2.14 Tapping mode AFM images of a DVD	55
Figure 2.15 Schematic of force spectroscopy measurements using an atomic force microscope	56
Figure 2.16 Shape of different AFM cantilever tips	57
Figure 3.1 Detection principle	71
Figure 3.2 Proof of concept, signal contrast, and resolution of micropore device	74
Figure 3.3 Volume quantification of model cells	76
Figure 3.4 Effect of Alcohol on Red Blood Cells	80
Figure 3.5 Reversibility of RBC volume changes with ethanol exposure	81
Figure 3.6 Time-dependent relative volume shrinkage of RBC	83
Figure 4.1 Schematic and construction of low-cost portable amplifier	98
Figure 4.2 Comparison of absolute percentage error and RMS noise in current	100
Figure 4.3 Bandwidth measurement of lab-amplifiers	101
Figure 4.4 High throughput detection of model cells using lab amplifiers	103
Figure 4.5 Resolving and Quantifying mixed sample population	105
Figure 4.6 Measurement of changes in bacterial relative volumes using lab amplifier	107
Figure 5.1 Schematic of electrofluidic device detection principle and signals for measurement of stiffness and size through the micropore device	124
Figure 5.2 Demonstration of cell volume and stiffness detection using Micropore Devices	127
Figure 5.3 Effect of the actin inhibitor drug (Latrunculin-A) on the stiffness of red blood cells	129

Figure 5.4 Empirical formulation for modeling the cellular stiffness using the electrofluidic experimental data	132
Figure 5.5 Cellular stiffness estimation of sickled RBCs of the SCD patients using microfluidic devices	134
Figure 6.1 RBC porosity effect under applied voltages	141
Figure 6.2 Translocation of RBCs through a single glass capillary dual micropore device	142
Figure A1.1 Manual Fitting options in Igor software	148
Figure A1.2 Difference in fitting results due to weights and constraints	149
Figure A2.1 Schematic of a cylindrical region	151
Figure A2.2 Schematic of a truncated conical region	152
Figure A3.1 Analytical Volume of RBC	153
Figure A4.1 AFM force-distance curve for RBCs	157
Figure A4.2 Estimating the contact point between the sample and cantilever	158
Figure A4.3 Fitting the force vs indentation data with the hertz model	159
Figure A5.1 Conductance of micropore devices	161
Figure A5.2 Representative electrical events	161
Figure A5.3 Scatter plot and dwell time data	162
Figure A5.4 Quantitative detection of populations in a mixed sample	163
Figure A5.5 Image library of micropores	164
Figure A5.6 Image library of micropores	165
Figure A6.1 Optical Image Library of micropores	172
Figure A6.2: Schematic of the micropore setup	173
Figure A6.3: Effect of Filter frequency on ΔG values	174
Figure A6.4: Demonstration of constant ΔG with changing ethanol concentration	175

Figure A7.1 Steps involved in forging a micropore from a glass capillary	181
Figure A7.2 Image Library of constricted micropores	182
Figure A7.3 Image library of constricted micropores	183
Figure A7.4 Image library of free-flight micropores	184
Figure A7.5 AFM Sample Fluid Cell	185
Figure A7.6 Effect of incubation temperature on translocation experiment	186
Figure A7.7 Effect of Amplifier Bandwidth on TL Data	187
Figure A7.8 Image library of bright field image of RBCs used for AFM force spectroscopy measurements	188
Figure A7.9 Schematic of AFM force-indentation experiment	188
Figure A7.10 Effect of Lat-A on the constricted and free-flight ΔG of RBCs	189
Figure A7.11 Effect of flow rate on the Δt values of RBCs treated with different concentrations of Lat-A	190
Figure A7.12 Δt histogram with the Gaussian fit for RBCs treated with different concentrations of Lat-A at different fluid flow	191
Figure A7.13 Effect of Lat-A on RBCs from different donors	191
Figure A7.14 Effect of sample size on the translocation experiment	192
Figure A7.15 Hospital Setup	193
Figure A7.16 Image library of Red blood cells acquired from healthy donors and SCD patients	194
Figure A7.17 Translocation data for sickle cell anemia patient-1 and patient-2	195
Figure A7.18 Translocation data for sickle cell anemia patient-3 and patient-4	196
Figure A7.19 Translocation data for sickle cell anemia patient-5 and patient-6	197
Figure A7.20 Translocation data for sickle cell anemia patient-7 and patient-8	198
Figure A7.21 Translocation data for sickle cell anemia patient-9	199

Figure A7.22 Translocation data for sickle cell anemia patient-10	200
Figure A7.23 Summary of Δt values of the constricted micropore data acquired for healthy donors and SCD patients	200
Figure A9.1 Effect of software filtering on the measured ΔG values	235
Figure A9.2 Effect of Bovine Albumin Serum on EtOH-treated RBCs	236
Figure A9.3 Electrofluidic detection of RBCs infected with malaria Parasite	237

List of Tables

Table 2.1 Micropipette puller program parameters	41
Table 3.1 Volume quantification of model cells by different methods	78
Table 4.1 Quantification of mixed samples	106
Table A1.1 Incorrect way of writing significant figures	146
Table A1.2 Correct way of writing significant figures	146
Table A5.1 Quantification of mixed bead data	165
Table A5.2 Quantifying model cell volumes for Figure 3.2b	166
Table A5.3 List of L_{eff} values for different pores used in Chapter 3	167
Table A5.4 Summary of mean ΔG values	168
Table A6.1 Total Expenditure	169
Table A6.2 Summary of the comparison between all the amplifiers	170
Table A6.3 RMS Noise values of different amplifiers with a 500 k Ω load resistor	171
Table A6.4 RMS Noise values of different amplifiers with a 1 M Ω load resistor	172
Table A7.1 Mapping RBCs elasticity with the micropore Δt measurements	177
Table A7.2 Fitting R2 Values for AFM force-distance curves	178
Table A7.3 Mapping RBCs elasticity with the micropore Δt measurements at different flow rates	178
Table A7.4 Summary of SCD patient data	179
Table A7.5 Relative elasticity of SCD patients estimated using the empirical equation A7.6	180

CHAPTER 1

INTRODUCTION

ABSTRACT

“Cells are the basic building block of all living things”- German scientists Theodor Schwann and Matthias Jakob Schleiden stated this in the early 1800s¹. Cells are truly considered the essence of life as they harbor the basic structure and functionality of all living organisms. Cells are seemingly simple but quite complex entities as they constantly adapt to their environmental and physiological conditions. Their unique signaling pathways allow them to communicate among themselves and coordinate their activities and responses in orchestrating complex biological processes such as growth and development². A deeper qualitative as well as quantitative understanding of cellular biology is the key to unraveling the molecular mechanism for various human diseases. The understanding of cellular mechanics is the basis of developing novel therapeutic strategies targeting specific cellular pathways and mechanisms. For instance, the unique ability of stem cells to differentiate into various cell types holds immense potential for regenerative procedures, promising the repair of damaged tissues or organs by treating a degenerative disease or injury^{3,4}. The ever-evolving knowledge of various cellular systems has revolutionized the field of medicine for ages, but the key has always been the deeper understanding of cellular mechanics at the molecular level. There are numerous physical parameters that govern the mechanism of all living systems, like the cytoplasmic environment (pH, temperature and chemicals), osmotic pressure, mechanical forces (both internal and external), cellular physiology (shape and size), extracellular matrix dynamics, ion channel response, active and passive cellular motion, deformability, membrane dynamics and enzymatic activity⁵⁻⁷. Note that, these physical parameters have the possibility to interact in complex ways within a single cell. The cells ability to mechanically respond to these complex interactive forces is termed as cellular mechanosensing, various physical parameters associated with it are shown in the schematic in Figure 1.1. Understanding the cellular mechanosensing, is a simple approach to a very complicated system, hence it is widely used for studying the force transmission, signal transduction, gene expression

and cellular and membrane cytoskeleton responses in cells and tissues⁸. In this chapter, we attempt to provide brief details on various measurement systems used by the cellular mechanosensing research community to study the mechanical response and properties of various cellular systems.

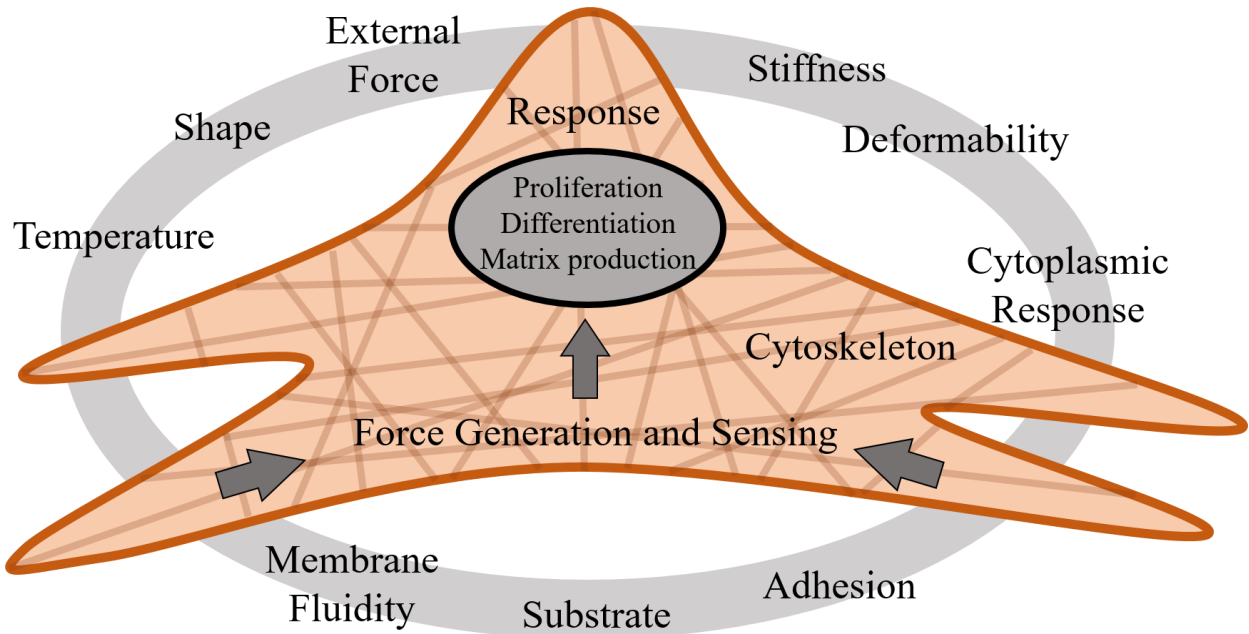


Figure 1.1 : Physical parameters associated with the cellular mechanosensing. Various physical parameters controls the active and passive motion of the cells, which in principle governs all the living systems. The complexity of all these parameters can simply be observed by monitoring the cellular mechanical responses.

1.1 Microfluidics-based Cellular Mechanosensing

Microfluidic systems have been a promising tool in studying cell mechanics with different approaches. In these approaches cells that are suspended in a buffer are probed in microchannels using different fluid flow methods and the cellular response is then sensed with various techniques^{9–18}. These microfluidic studies usually require a flow/pressure system and microchannels, usually made of polydimethylsiloxane (PDMS) using standard lithographic techniques, for the flow. The novelty of the cellular mechanosensing measurements in these approaches lies in the unique channel design integrated with a sensing tool, a fluid system, and the interpretation of the cell's response. In this section, we will review various microfluidic system designs and the associated sensing techniques to measure cellular mechanics, commonly referred to as flow cytometry. Flow cytometry is one of the novel approaches to detect and analyze different mechanical properties of cells as they flow inside a channel with an appropriate buffer solution. For mechanosensing of biological samples, the flow cytometry is often integrated with an imaging setup^{9,11–14,16–18} and/or electrical measurement system^{10,15,19}, where the samples are either probed using high fluid flow, intersecting fluids, and/or interaction with the constricted device surfaces. The changes in the cellular structures are imaged with a high-end fast camera or electrical signals, and temporal or spatial analysis of these cellular changes is modeled to estimate the cell's mechanical properties. In this section, we briefly discuss some of the methods used in this research area for cellular mechanosensing.

1.1.1 Quantitative Deformability Cytometry (q-DC)

Standard soft lithographic techniques are used to fabricate polydimethylsiloxane (PDMS) q-DC devices with 5 μm or 10 μm wide occlusion channels. The q-DC microfluidic system has an extended network of parallel occlusion array channels (See Figure 1.2) and cell passage is monitored using an inverted microscope equipped with 20X/0.4 NA Objective. Cells (HL-60 cells used in this study) are driven through the occlusions with a constant air pressure applied at the inlet, and the pressure is regulated by using a pneumatic valve. A downstream filter is also used in the flow pathway to trap junk or cell aggregates ($> 20 \mu\text{m}$ in size). The images of the cellular deformation through the occlusions are acquired using a CMOS camera at the rate of 200–2000 fps.

The acquired images are used to measure the cell shape, determining the time-dependent circularity of the cells, as they are driven through the constriction. The time-dependent circularity is defined as $C(t)=4\pi A(t)/P(t)^2$, where $A(t)$ and $P(t)$ are time-dependent cross-sectional areas of cells and pressure. The time-dependent strain $\varepsilon(t)$ is measured in terms of change in circularity^{18,20} as:

$$\varepsilon(t) = \frac{C_0 - C(t)}{C_0} \quad (1.1)$$

Here, C_0 is the circularity of the cell before going through the constriction part of the channel.

The time-dependent creep function $J(t)$ is determined as the ratio of the observed time-dependent strain $\varepsilon(t)$ and the time-averaged stress $\bar{\sigma}$

$$J(t) = \frac{\varepsilon(t)}{\bar{\sigma}} \quad (1.2)$$

where the time-averaged stress $\bar{\sigma}$ is defined as:

$$\bar{\sigma} = A * P_{applied} \quad (1.3)$$

where, A is the system calibration factor, which is determined by using agarose particles with elastic moduli estimated using atomic force microscopy. Assuming that the cells and the calibration particles are within the linear elastic regime, the calibration factor ‘ A ’ can be determined by the strain-stress relation at the threshold where $P_{applied} = P_{threshold}$ as:

$$A = \frac{E * \varepsilon_c}{P_{threshold}} \quad (1.4)$$

where E is the elastic moduli of the calibration particle, $P_{threshold}$ is the minimum pressure needed to drive at least 80% of particles through the constriction, and ε_c is the minimum strain induced by the applied stress for the calibration particle transit.

Considering above four equations, we get the expression for the time-dependent creep function as:

$$J(t) = \frac{1}{E \varepsilon_c} \left(\frac{P_{threshold}}{P_{applied}} \right) \left(\frac{C_0 - C(t)}{C_0} \right) \quad (1.5)$$

The Power Law Rheology (PLR) model gives the expression for the time-dependent creep function as follows:

$$J(t) = \frac{1}{E} \left(\frac{t}{\tau} \right)^\beta \quad (1.6)$$

Where E is the elastic modulus, τ is the characteristic timescale (commonly kept 1) and the exponent β reflects the rate of stress dissipation, which also provides a measure of cell fluidity. The above equations can be compared to estimate cellular fluidity. Note that, when $\beta=0$, the creep function reduces to the Hookian model and describes a purely elastic system, whereas when $\beta = 1$, the creep function reduces to the Newtonian liquid-drop model describing the system as purely viscous.

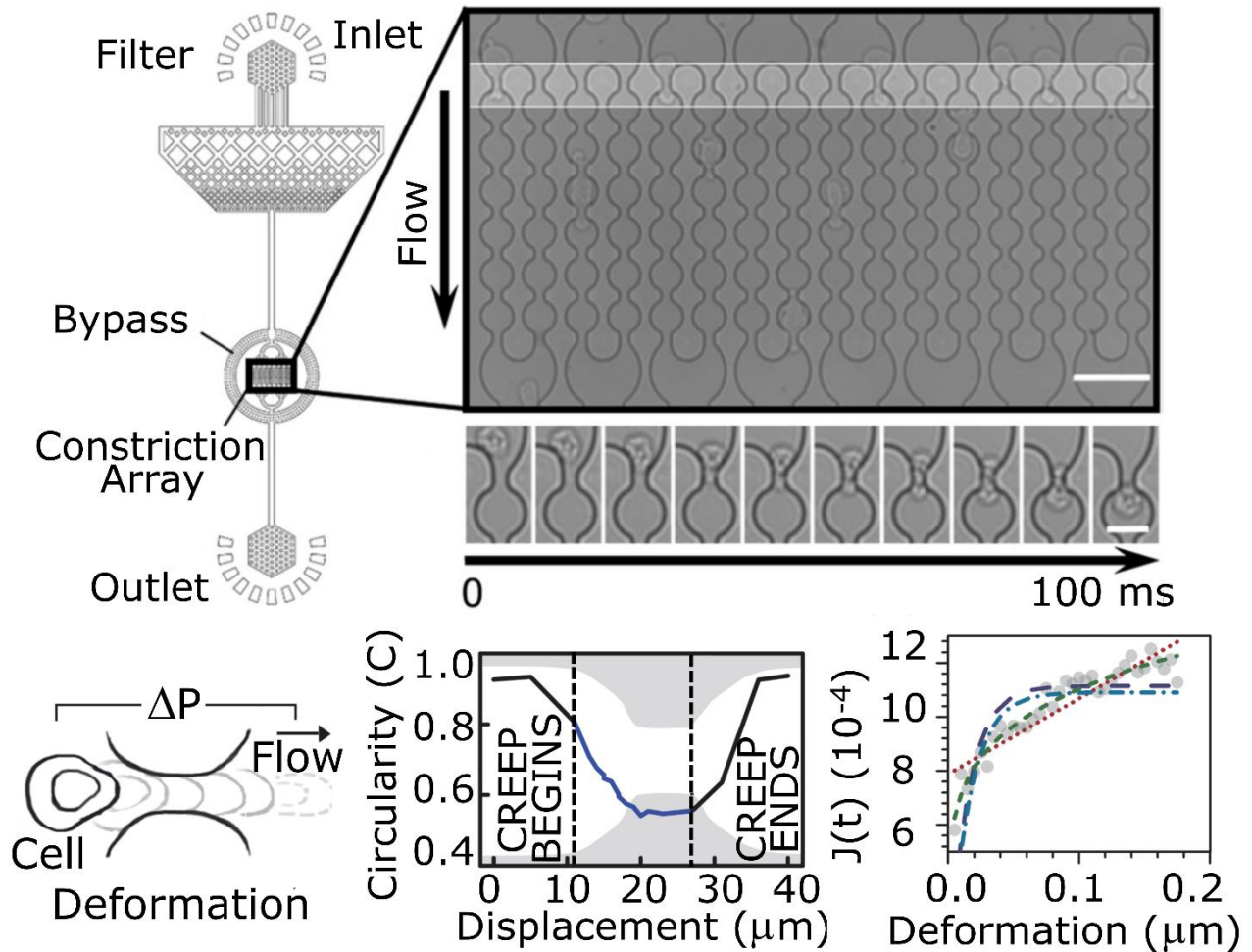


Figure 1.2 Quantitative Deformability Cytometry (q-DC). Schematic of the quantitative deformability cytometry (q-DC) microfluidic system having 16 parallel occlusion array channels and a single cell transiting through the constricted channel by a pressure-driven flow. A microscopic image of the array channels is also shown here. The time-dependent circularity is also shown here, which is used to estimate the beginning and end of the creep. The time-dependent creep trajectory data fitted with Maxwell (red dotted line), Kelvin-Voigt (KV, purple long-dashed line), Standard Linear Solid (blue dot-dashed line), and the Power Law Rheology (green short-dashed line) models fitted for HL-60 cells (gray dots). Figures are reprinted with permission from ^{20,21}.

1.1.2 Dimensionless Indexing of Cellular Stiffness-based Deformability

In this method, dimensionless indexes are introduced in the limiting case where the cells achieve an equilibrium transit velocity (elastic limit approximation) by tracking cell position as it passes through a small constriction channel. As shown in Figure 1.3 the velocity profile of a cell in the constriction has two phases, a non-equilibrium phase followed by a transit point, beyond which an equilibrium phase with a constant velocity. Since cells are viscoelastic they are considered as a combination of springs and dampers. The equilibrium transition point isolates the elastic behavior from the visco-elastic behavior. The Kelvin-Voigt model ⁹ for such a system gives the expression for the total force response as:

$$F = F_s + F_d \quad (1.7)$$

where,

$$F_s = k\delta_s \quad (1.8)$$

$$F_d = D \frac{d\delta_d}{dt} \quad (1.9)$$

Here, F_s and F_d are force responses for the deformed spring and deformed damper, k is the stiffness of the spring, δ_s is the deformation in the spring, D is the damping coefficient and $\frac{d\delta_d}{dt}$ is deformation rate.

The dimensionless indexing is possible only at equilibrium, as the damping coefficient (D) for each cell is difficult to estimate experimentally. Hence, to overcome this limit the channels are designed such that,

$$D_c \ll \lambda_m \quad (1.10)$$

Here, λ_m is the length of the channel and D_c is the undeformed cell diameter. With an additional approximation the ratio between the first and second phase of the velocities is negligible, which means that the average velocity is equal to the equilibrium velocity. With all these approximations and making use of the Thin-Film Lubrication theory ²², Buckingham π theorem ²³, and dimensional analysis, the following dimensionless indexes can be estimated:

$$\hat{\phi} = \left(\frac{k}{u_f * u} \right)^{-1} \quad (1.11)$$

$$\hat{u} = \frac{u_{eq}}{u_f} \quad (1.12)$$

$$\hat{\delta} = \frac{D_c}{w} \quad (1.13)$$

$$\hat{\lambda} = \frac{\lambda}{w} \quad (1.14)$$

Here, k , D_c , λ , u_{eq} , u_f , w , and μ are cell stiffness, cell undeformed diameter, cell in-channel length, equilibrium velocity, fluid velocity, channel width, and fluid viscosity, respectively. See Figure 1.3 for a visual interpretation of these physical parameters. So, the dimensionless index (\widehat{DI}) for the cellular stiffness can be evaluated from its equilibrium velocity and deformation when the flow conditions are known as all the parameters in above equations correlate to the cell deformability as following:

$$\widehat{DI} = \hat{\delta} * \hat{\lambda} * \hat{u} = \frac{D_c \lambda u_{eq}}{w^2 U_f} \quad (1.15)$$

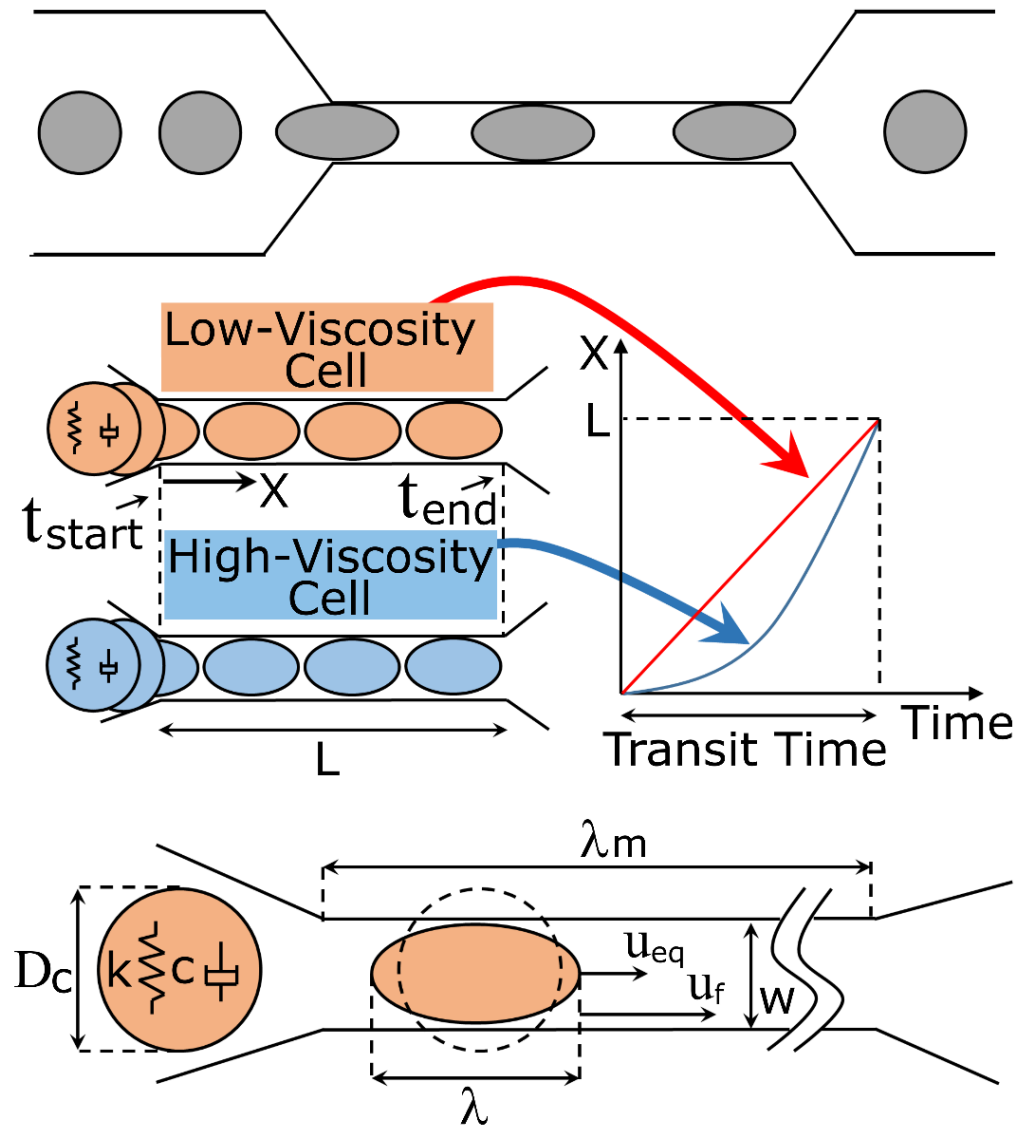


Figure 1.3 Dimensionless Indexing of Cellular Stiffness-based Deformability: A schematic of a series of cells translocating through the constricted channel. (Middle) Schematic of two cells having different viscous properties passing through the constriction taking the same transit time. The low-viscosity cell attains the equilibrium velocity faster compared with a high-viscosity cell. The difference in the cellular viscosity causes the cells to have different velocity profiles, even when the transit time is the same. (Bottom) Shows the schematic of the device and sample parameters used for the dimensional analysis for visual interpretation.

1.1.3 Constricted Suspended Microchannel Resonator

In this method, the buoyant mass of cells is estimated as they flow through the suspended microchannel resonator (SMR) device^{10,17}. The SMR cantilever's vibrations are detected by an optical lever integrated beneath the cantilever along with an electrostatic drive electrode. An oscillator circuit continuously tracks the resonant frequency of the SMR device via the drive electrode. A constricted suspended region is fabricated on the top surface of the cantilever using insulated wafer thinning and dry-etching in silicon. The constriction region has a 6 μm width, 15 μm depth, and 50 μm length, dividing the suspended microchannel into 5 major sections (See Figure 1.4). The peak of the SMR signal (frequency vs. time) recorded within the region 1 and 2 corresponds to the buoyant mass of the cell. The region marked between 3 and 4 is the cellular passage for mechanical response detection. A pressure regulator drives the cells through the entry (region-1) and exit (region-2) of the SMR device by maintaining a constant pressure across the microfluidic channel. The passage time within the constriction (between regions 3 and 4) is divided into entry and transit times. The features of the SMR pulse recorded contain the exact temporal information of the entry and transit time of the cell as it passes through the constriction.

The H1975 cells were treated with Latrunculin-B (LatB) drug and a huge decrease in entry velocities is recorded compared with untreated cells, showcasing that the actin inhibitor drug (LatB) is softening the cell (See Figure 1.4)¹⁰. Although there was no major effect of the drug in the transit velocities for the LatB-treated and untreated cells, the cell's viscoelastic properties were critically reflected in the entry times compared to the transit times of the cell through the constriction. Since the normal friction of the cell against the channel wall is also an important parameter in the passage time, the constriction channels were coated with PLL or PEG. The positively charged PLL coating in the channel increased the overall passage time of the cells,

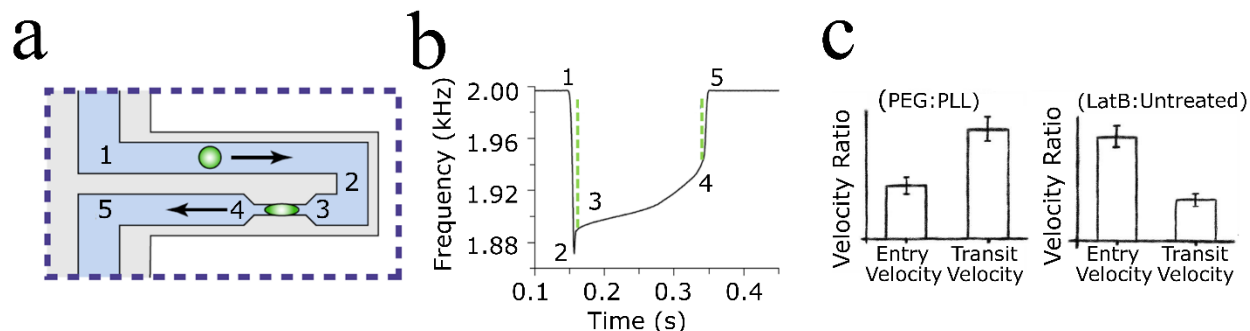


Figure 1.4 Constricted Suspended Microchannel Resonator (SMR). *a* The schematic of the constricted suspended microchannel resonator (SMR) device is shown here. *b* A representative SMR signal is also shown, which is later mapped with the device dimensions to estimate the passage time (entry and transit times) for the cellular stiffness interpretation. *c* The effect of surface coating (PLL and PEG) and cytoskeleton drug inhibitor (LatB) on the entry and transit time of H1975 cells is also shown. Figures are reprinted with permission from ^{10,17}.

whereas the neutral PEG coating did not affect the passage time (See Figure 1.4). The application of the device was also demonstrated by characterizing the deformations and surface friction of metastatic cells translocating through the constriction.

1.1.4 Real-Time Shear Flow Deformability Cytometry (RT-DC)

Fluid flow shear is a common probing approach in microfluidic systems for cell deformation. This approach was used to measure changes in HL-60 cells that were softened with the use of different doses of the cytoskeletal drug (CytoD) ¹². These cells are deformed by using fast shear fluid flow and the deformations were imaged with a high-speed camera at 4000 fps (See Figure 1.5). The microfluidic setup is illuminated with a very high-power LED source used for the required exposure and is mounted on an inverted microscope equipped with 40X/0.75 NA objective lens. The deformation of cells is characterized in terms of the cell's circularity, which is defined as:

$$C = \frac{2\sqrt{\pi A}}{l} \quad (1.16)$$

Where A is the cross-sectional surface area of the cell and l is the perimeter. An automated algorithm is used to process the contour of the cell and then determine the cross-sectional area and the perimeter of the cell. For an undeformed cell, the circularity (C) is 1 and for a deformed cell, it will be less than 1. As the cells deform the circularity of cells will decrease or the deformation (D),

defined as $D = 1 - C$ will increase. It is important to note that the cellular deformations are size dependent, as greater shear stress is experienced by larger cells, hence deform more. An analytical modeling approach was used to decouple the size and deformations and establish the parametric isoelasticity lines of the scatter plots to extract the material properties. These isoelasticity lines isolate the size-deformation plots into identical stiffness regions.

A connection between the cytoskeleton drugs affecting the intermediate filaments (actin and microtubules) to the progression of cells to its different cell cycle stages was demonstrated here as an application of this technique. The isoelasticity data for HL-60 cells with varying doses of Cyto-D using RT-DC shows the characteristic changes in size, and deformation, showing the ability to distinguish between G2 and M-Phases of cell bands (See Figure 1.5). This band usually overlaps and is not resolvable by routine methods such as FACS (Fluorescence Activated Cell Sorting).

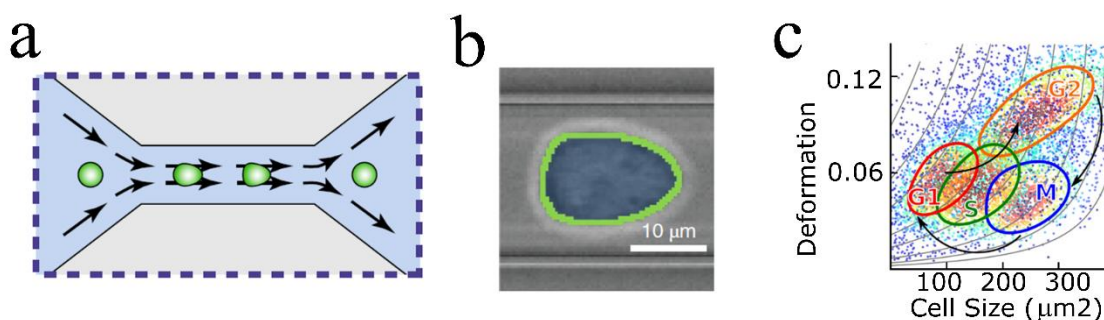


Figure 1.5 Real-Time Flow Deformability Cytometry. *a and b* The schematic of the real-time flow deformability cytometry system is shown here along with a representative image of a HL-60 cell deformed due to the fast shear fluid flow. *c* The isoelasticity data for HL-60 cells with varying doses of Cyto-D using RT-DC shows the characteristic changes in size, and deformation, showing the ability to distinguish between G2 and M-Phases of cell bands. Figures are reprinted with permission from ^{12,17}.

1.1.5 Hydrodynamic Extensional Flow Deformability Cytometry

In the previous technique, a uni-directional fast shear fluid flow was used as a probe to deform cells. In the current method, a hydrodynamic inertial focusing approach is incorporated to deform cells at high strain rates using a uniform extensional fluid flow stretching profile in an intersecting microfluidic channel ^{13,17}. Here, the cells flow through a long channel attaining an inertial motion maintained by the inertial focusers, and then experience a rapid deceleration caused by an opposing fluid flow at the intersection (See Figure 1.6). Inertial forces act on the cells due to the immediate deceleration experienced at the intersection, resulting in the deformation of the cells.

Unlike uni-directional shear fluid flow where the cells undergo only longitudinal deformation, here the extensional fluid stretching profile causes both longitudinal and lateral deformations in the cells. These deformations are captured using a high-speed camera, and the images are analyzed using automated computational methods. The deformability index for each cell is measured as the ratio of the longitudinal (a) and lateral deformations (b) i.e.,

$$D = \frac{a}{b} \quad (1.17)$$

The deformability index (D) of each cell is plotted against its original cellular diameter as a scatter plot. This approach maps the deformability index qualitatively to the cellular mechanical properties, which helps in distinguishing populations of cells within pleural fluids ¹³ (See Figure 1.6). It is important to note that the strain rates applied using the hydrodynamic extensional flow cytometry do not measure the responses to actin cytoskeletal perturbations due to the fluidization of the actin networks caused by very high strain rates.

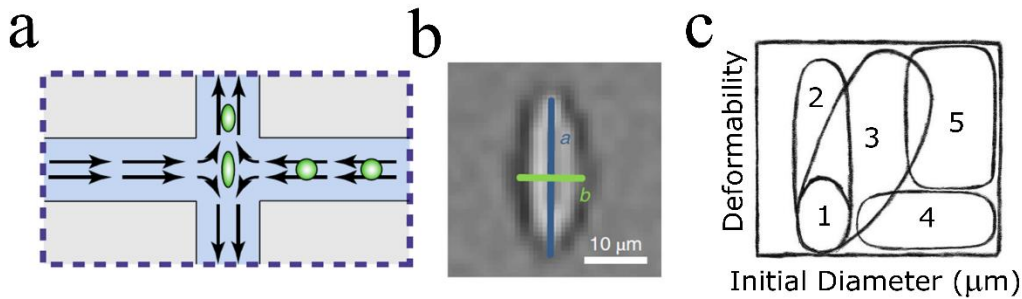


Figure 1.6 Hydrodynamic Extensional Flow Deformability Cytometry. *a and b* The schematic of the intersection hydrodynamic extensional flow deformability cytometry system is shown here along with an image of a cell experiencing inertial force causing the longitudinal and lateral deformations. *c* Distinguishing different populations of cells within pleural fluids based on the deformability index is shown here. Figures are reprinted with permission from ^{13,17}.

1.1.6 Resistive Pulse Electrofluidic Measurements

The resistive pulse sensing technique (RPT) has been used in the medical and research fields for decades for the detection and counting of cells or micron-sized particles ^{24–28}. The technique has existed since the early 1950s and is known as a Coulter counter ²⁹. Many improvements have been employed in this technique for the quantification of the sample size, orientation, and charge. The advanced low-noise data acquisition and signal amplification tools have also opened up applications

in the field of nano-sized biological sample detection, DNA sequencing, branches in biopolymers, and their conformations^{15,19,24,25,30,30–43}. In this section, we propose the application of RPT in the measurement of cellular mechanical properties. Since the measurement signals are electrical and the technique is integrated with microfluidics, it is commonly referred to as electrofluidics.

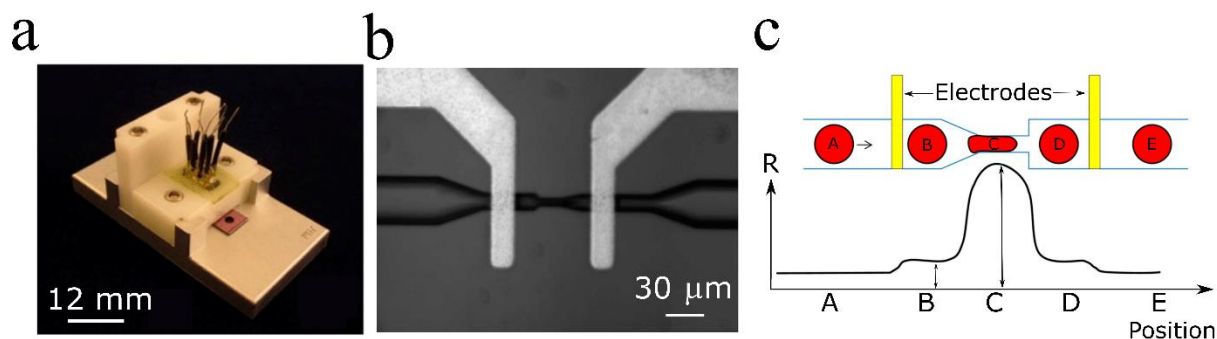


Figure 1.7 Resistive Pulse Sensing Electro-fluidic Measurements. *a and b* Image of a microfluidic device made on a silicon wafer is shown here along with the image of the sensing region of the channel and the electrodes. *c* A schematic electrical resistive pulse signal showcasing the position of the cell and the signal features is also presented here. Figures are reprinted with permission from⁴⁴. Copyright 2012 American Chemical Society.

The sensing part of the electrofluidic devices is commonly made out of glass, polydimethylsiloxane (PDMS), or silicon wafers. The sensing region is a constriction with dimensions smaller than the cell size under consideration. The buffer-filled device (with the micropore constriction at its mouth) is dipped into a fluid cell where the cells are suspended. A pair of electrodes are used to apply voltage and measure current across the micropore. The conductance depends on the ionic buffer conductivity and micropore geometry. The conductance would drop as a cell translocates (due to a flow generated using a syringe pump) through the constriction, giving an electrical pulse⁴⁴ (See Figure 1.7). Since the cell is bigger than the constriction, it will squeeze through, and the time taken by the cell (Δt) to translocate across the sensing region under a constant fluid flow will depend on the whole cell's stiffness. Any change in cellular stiffness, due to physical, chemical, or disease-based reasons can be detected. This technique can be used to detect the effect of drugs, parasites, or genetic mutations causing any change in cellular stiffness. This approach can either be used with or without the need for microscopy as the cell's mechanical information is embedded in the Δt . As mentioned in the previous section a relevant surface coating could help improve the detection and resolution of signal for cells with minuscule stiffness changes.

1.2 Cellular Membrane-Based Mechanosensing

The Cellular membrane is a passive barrier protecting the nucleus and the cytoplasm of the cell. It also has a dynamic structure capable of sensing any mechanical cue from the extracellular environment, and transducing it within the cell using biochemical signals ^{2,8}. Hence, probing the cellular membrane and studying the ability of cells to detect and respond to such mechanical forces is an amazing mechanosensing approach to understanding crucial cellular functions such as cell differentiation, migration, proliferation, and development of tissues ^{1,2,5,6}. In this section of this chapter, we will present a few widely used cellular membrane-based mechanosensing techniques used by the scientific community.

1.2.1 Micropipette Aspiration

A glass capillary with a very small diameter connected with a negative pressure system is used to apply a controlled suction pressure to cells or vesicles (See Figure 1.8a). The deformation in the cellular membrane or the vesicles is quantified with the known applied suction pressure. This entire process is termed as micropipette and is being widely in cell biology and biophysics to measure the mechanical tension of the cell ⁴⁵⁻⁴⁷. The degree of aspiration (part of the cell that enters the pipette) is observed under a microscope for further analysis is done based on these observations. For a spherical soft sample, the pressure across the membrane (ΔP) can be described in terms of the membrane tension (T) and the radius of the sample (R), using Young-Laplace Equation⁴⁵ as:

$$\Delta P = \frac{2T}{R} \quad (1.18)$$

Now, when the sample is aspirated into the micropipette, at the equilibrium between the suction pressure and the restoring force of the membrane, the following expression is observed⁴⁶:

$$\Delta P = \frac{2T}{R_p} \left(1 - \frac{L}{R_p}\right) \quad (1.19)$$

Here, R_p is the radius of the micropipette, and L is the length of the cell inside the micropipette. On using the equations (1.18) and (1.19), the cortical tension (T) of the cell membrane under the applied suction pressure (ΔP) can be calculated as follows:

$$T = \frac{\Delta P R_P}{2\left(1 - \frac{L}{R_P}\right)} \quad (1.21)$$

Now, if the deformations (L) are small compared with the sample size, the behavior of the cell can be assumed to be elastic, and the relationship between the suction pressure and the elastic modulus (E) of the cell can be estimated as⁴⁵:

$$E = \Delta P \frac{3(1-\nu^2)}{2} \left(\frac{R}{L}\right) \quad (1.21)$$

Here, ν is the Poisson's ratio of the cell, and R is the radius of the cell.

The micropipette aspiration technique has applications in understanding the mechanical properties of cells, (stiffness and elasticity), membrane dynamics and structure, and many therapeutic applications in medical research and drug industries.

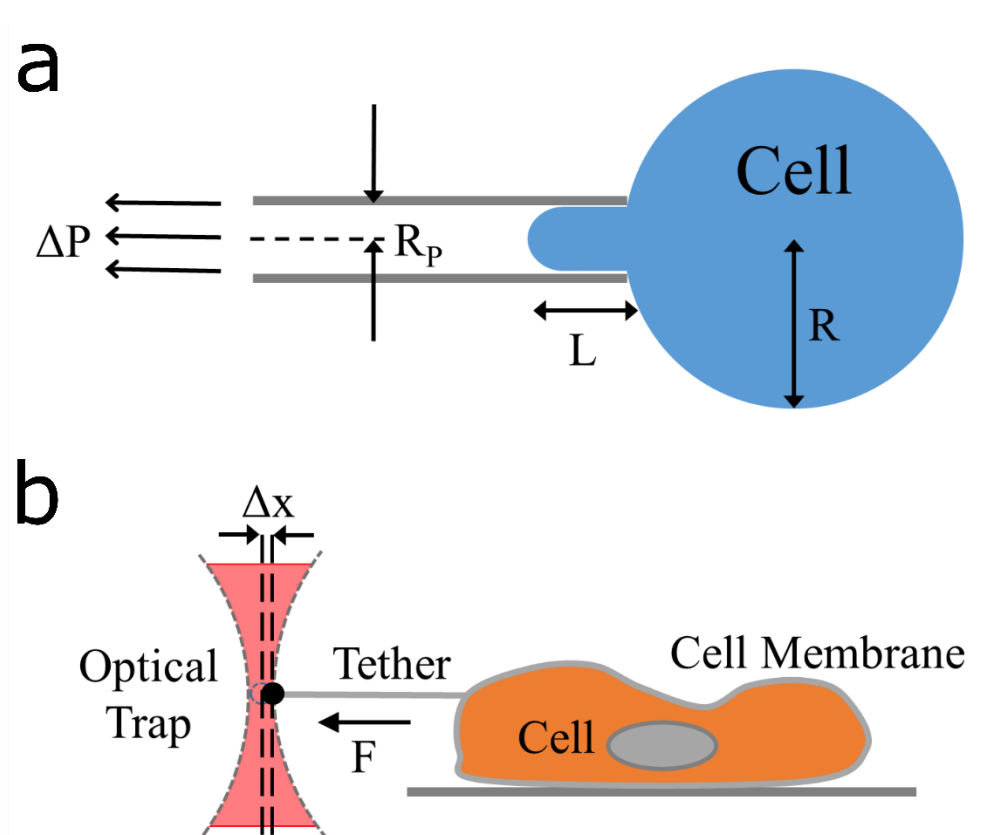


Figure 1.8 Cellular Membrane Based Mechanosensing. *a* Schematic of the micropipette aspiration experiment. Here, R is the cellular radius, L is the aspirated membrane length, R_p is the diameter of the micropipette and ΔP is the negative pressure used to aspirate the cellular membrane. *b* Schematic of the membrane tether extraction using optical tweezer setup. The retraction force and the displacement of the trapped bead due to the tether extraction are shown here.

1.2.2 Membrane Tether Extraction using Optical Tweezer

The radiation pressure of a highly focused laser light is used by the optical tweezer setup to trap and move microscopic objects with great precision⁴⁸⁻⁵¹. The gradient force balances the scattering force near the laser beam's focal point, trapping the particle in a stable position. The optical trap, works like a spring, and if any external force causes any displacement (Δx) of the bead out of the trap, the restoring force (F_{trap}) of the trap will be:

$$F_{trap} = -k_{trap} \Delta x \quad (1.22)$$

Here, k_{trap} , is the spring constant of the trap, which depends on the laser power, wavelength of the laser beam, the numerical aperture of the objective, trapping medium, and the refractive index of the trapping particle and the medium.

Now, the trapped functionalized bead is brought in contact with the cell membrane, the bead then binds with the lipid components on the cell surface. Now on pulling the bead away, a membrane tether extraction can be seen (see Figure 1.8b). The expression of the membrane tension (σ) for the pulled tether in terms of bending rigidity (κ) and force (F) required to maintain the tether is given by⁵²:

$$\sigma = \frac{F^2}{8\pi^2\kappa} \quad (1.23)$$

At equilibrium, the displacement of the bead and the length of the membrane tether becomes stable and the membrane tension for the pulled tether can be estimated by using equations (1.22) and (1.23).

1.3 Rheology Based Cellular Mechanosensing

Cells are viscoelastic materials, and there are various rheological experimental techniques to study their flow (viscosity) and mechanical (elasticity) properties. Broadly, there are two approaches to perform these studies; active and passive rheology^{53,54}. The active rheology-based experiments are performed by applying an external force to probe the cells and study their response. This approach is preferred for controlled measurement to study the system in non-equilibrium. Whereas, passive rheology-based studies involve observing the spontaneous response of the system due to the environmental fluctuations without any external probes. In this section, we present one example of both active and passive rheology-based techniques to study cellular mechanosensing.

1.3.1 Parallel Plate Rheometers

The parallel plate Rheometers consist of two plates, out of which one is stationary (bottom plate or stator), and the other one can rotate or oscillate (top plate or rotor). The sample is placed between these parallel plates (see Figure 1.9a), where the top plate acts as a probe, which can either rotate or oscillate to apply shear stress to the sample. The bottom plate is connected to a sensor to measure the response exerted by the cell in the form of force or torque. Note that, the gap between the two parallel plates plays a crucial role as it controls the shear rate and the accuracy of the measurements is dependent on it. The parallel plate Rheometer can be used in various modes; dynamic and relaxation. In the dynamic mode, the top plate oscillates back and forth, creating a sinusoidal stress. The storage (elasticity, G') and loss (viscosity, G'') modulus of the cells when deformed sinusoidally can be estimated as^{55,56}:

$$G' = \frac{kL_0}{S} \left\{ \frac{D_0}{d_0} \cos(\phi) - 1 \right\} \quad (1.24)$$

$$G'' = -\frac{kL_0}{S} \left\{ \frac{D_0}{d_0} \sin(\phi) + 1 \right\} \quad (1.25)$$

Here, k is the bending stiffness, S is the area of contact, L_0 is the initial length of the cell, d_0 , and D_0 are amplitudes of the bottom plate resulting movement and the imposed sinusoidal displacement to the top plate respectively, and ϕ is the phase lag between top and bottom plate movements. The

dynamic mode measurement can also be used to estimate the time-dependent cell creep function as:

$$J(t) = \frac{D(t)S}{kd_0L_0} \quad (1.26)$$

The equation (1.26) can be used to estimate cellular fluidity by comparing it to the power law rheology equation.

For relaxation mode, a constant strain (D) is applied to the cells by the top plate and the time-dependent deflection in the plate ($\delta(t)$) is measured. To maintain the desired cell strain feedback is applied to the bottom plate (Δ_0). The expression for relaxation modulus is given by:

$$E(t) = \frac{kL_0D(t)}{\Delta_0S} \quad (1.27)$$

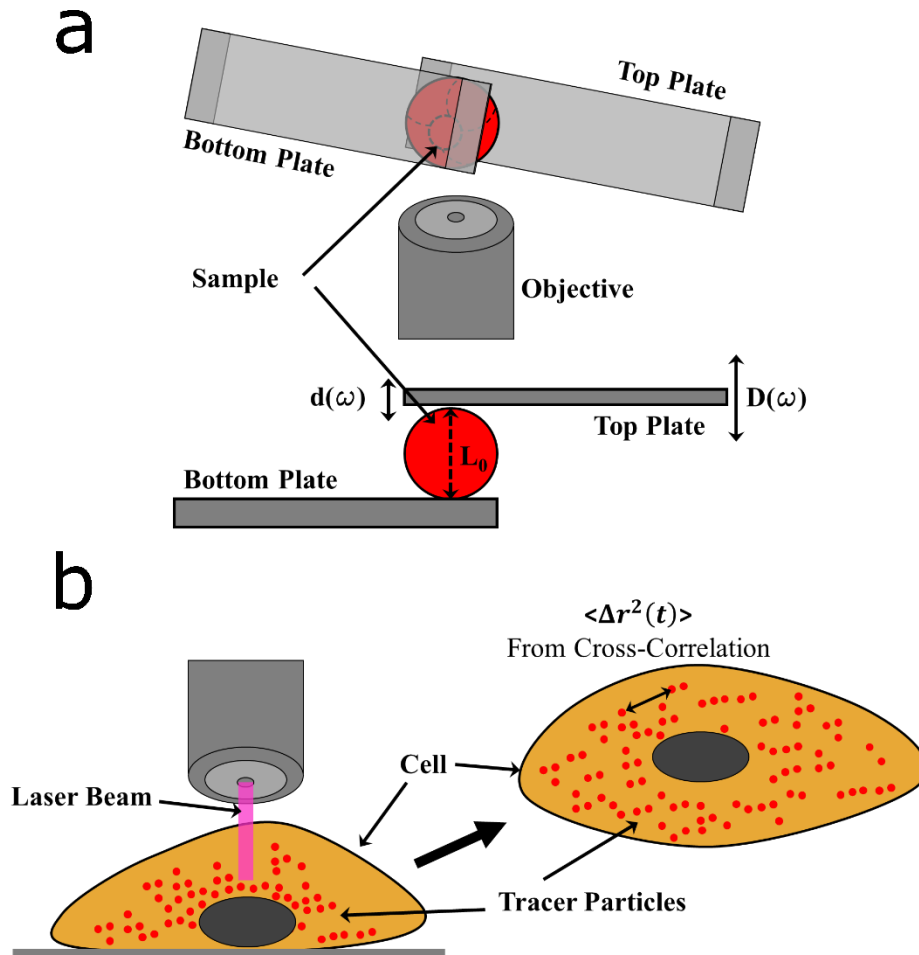


Figure 1.9 Rheology-based Cellular Mechanosensing: **a** Schematic of the parallel plate Rheometer showing the top and bottom plates, the microscope objective, and the displacement by the plates. **b** Schematic of the laser tracking rheology showing the tracer micro beads inside the cells and the laser beam. The cross-correlation between particles gives the mean square displacement.

1.3.2 Laser Tracking Rheology

Laser tracking rheology is a passive technique to measure the mechanical properties of cells by tracking micron-sized tracer particles embedded into the cells (see Figure 1.9b). The tracer particles interact with the cellular cytoplasmic environment and move stochastically^{57,58}. A laser beam is used to illuminate the tracer particles to monitor their movement over time. The tracking of the particles is done using Doppler velocimetry or confocal microscopy. The mean square displacement of the particles is estimated using the acquired data. Note that the thermal energy continuously causes movement of the cytoplasmic structure, imparting random forces on the tracer particles. These frictional forces are proportional to the velocity of the bead and the bead's friction

coefficient inside the cell. The friction coefficient depends on the cytoplasmic viscosity and size of the bead ⁵⁷. From the Stokes-Einstein relation, the diffusion coefficient (D) is given by⁵⁷:

$$D = \frac{k_B T}{\epsilon} \quad (1.28)$$

Where k_B is the Boltzmann constant, T is the temperature, and ϵ is the friction coefficient of the bead expressed as $\epsilon = 6\pi\eta a$, here η is the viscosity of the suspension and a is the radius of the particle.

According to Einstein's expression for diffusion, the relationship between the mean square displacement ($\langle \Delta r^2 \rangle$) and the diffusion coefficient (D) is⁵⁷:

$$\langle \Delta r^2 \rangle = 4Dt \quad (1.29)$$

On using equations (1.28) and (1.29), we get the viscosity of the bead suspension liquid as:

$$\eta = \frac{2k_B T}{3\pi a} \frac{t}{\langle \Delta r^2(t) \rangle} \quad (1.30)$$

By estimating the mean displacement of the tracer particles using the laser tracking rheology, the viscosity of the cellular cytoplasm can be estimated according to the equation (1.30).

1.4 Dual Optical Stretching

A single converging laser beam is used to create an optical trap, whereas, in a dual optical stretching setup, two diverging beams are used to stretch a dielectric soft sample (e.g. cells) as shown in Figure 1.10a. There is a momentum transfer from the laser beam due to the change in the refractive index at the interface of the cell and the suspension medium, which causes the cells to get uniaxially stretched^{48–51,53}. The dual trap setup is integrated with a microfluidic system and a microscope to have better cell delivery and optically measure the deformations in the cells. The stress on the cells is controlled by varying the laser power and is computed with the electromagnetic wave model^{59,60}. The induced force on the cells scales linearly with the incident power of the beam and $(n-1)$, where ‘ n ’ is the sample and medium refractive index ratio. The deformation of the cells is measured in terms of the time-dependent strain from the optical images, and the creep compliance profile of the cell is estimated using the Power Law Rheology (PLR) model according to Equation (1.6). The time-dependent strain and the creep compliance measured for MCF-7 cells using an optical dual trap are shown in Figure 1.10b, which can be used to estimate the composite viscoelasticity of cells.

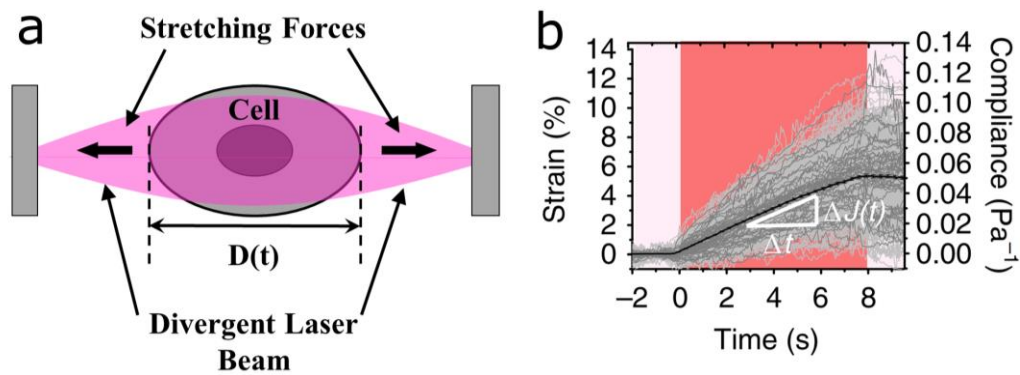


Figure 1.10 Dual Optical Stretching: *a* Schematic of a dual laser optical stretching setup, showing the divergent laser beam, the direction of the stretching force, the stretched cell, and the time-dependent diameter. *b* Time-dependent strain and creep compliance of MCF-7 cells as measured using the optical dual trap. (The Figure 1.10b is used here with permission⁶⁰)

1.5 CONCLUSION

In this chapter, we have discussed various mechanosensing techniques used to study cellular mechanical and physiological properties. We first introduced techniques that involve microfluidics-based systems to make whole-cell measurements. These measurements involve using flow cytometry, micro-resonators, and electrofluidic devices. The cellular membrane-based mechanosensing approaches like micropipette aspiration and membrane tether extraction using optical tweezers were also briefed in this chapter, to understand the membrane mechanical properties. Rheometers are widely used to study soft matter systems, mostly the bulk suspension properties, here we specifically discussed some of the techniques like parallel-plate Rheometers and laser tracking rheology to study and estimate the mechanical properties of cells in active and passive states respectively. Finally, we briefed, how a dual laser system can be used to apply stress and stretch cells using divergent beams, followed by studying the viscoelastic properties of cells in the suspension. This chapter is an overview of various experimental and theoretical approaches used by researchers to quantitatively and qualitatively study the cellular mechanics of cells.

1.6 REFERENCES

- (1) Ribatti, D. An Historical Note on the Cell Theory. *Exp. Cell Res.* **2018**, *364* (1), 1–4.
- (2) Nair, A.; Chauhan, P.; Saha, B.; Kubatzky, K. F. Conceptual Evolution of Cell Signaling. *Int. J. Mol. Sci.* **2019**, *20* (13), 1–44.
- (3) Soufi, K. H.; Castillo, J. A.; Rogdriguez, F. Y.; DeMesa, C. J.; Ebinu, J. O. Potential Role for Stem Cell Regenerative Therapy as a Treatment for Degenerative Disc Disease and Low Back Pain: A Systematic Review. *Int. J. Mol. Sci.* **2023**, *24* (10).
- (4) Munda, M.; Velnar, T. Stem Cell Therapy for Degenerative Disc Disease: Bridging the Gap between Preclinical Promise and Clinical Potential. *Biomol. Biomed.* **2024**, *24* (2), 210–218.
- (5) National Academies of Sciences, Engineering, and M. 2022. *Physics of Life*; 2023.
- (6) Yamada, K. M. R. M. Cell Dynamics in Development, Tissue Remodelling, and Cancer Kenneth. *Curr Opin Cell Biol.* **2016**, *42*, 4–6.
- (7) Scott, S.; Weiss, M.; Selhuber-Unkel, C.; Barooji, Y. F.; Sabri, A.; Erler, J. T.; Metzler, R.; Oddershede, L. B. Extracting, Quantifying, and Comparing Dynamical and Biomechanical Properties of Living Matter through Single Particle Tracking. *Phys. Chem. Chem. Phys.* **2022**, *25* (3), 1513–1537.
- (8) Kollmannsberger, P.; Bidan, C. M.; Dunlop, J. W. C.; Fratzl, P. The Physics of Tissue Patterning and Extracellular Matrix Organisation: How Cells Join Forces. *Soft Matter* **2011**, *7* (20), 9549–9560.
- (9) Tsai, C. D.; Sakuma, S.; Arai, F.; Kaneko, M. A New Dimensionless Index for Evaluating Cell Stiffness-Based Deformability in Microchannel. **2014**, *61* (4), 1187–1195.
- (10) Byun, S.; Son, S.; Amodei, D.; Cermak, N.; Shaw, J.; Ho, J.; Hecht, V. C. Characterizing Deformability and Surface Friction of Cancer Cells. *PNAS* **2013**, *110* (19), 7580–7585.
- (11) Raj, A.; Sen, A. K. Entry and Passage Behavior of Biological Cells in a Constricted Compliant Microchannel. **2018**, 20884–20893.

- (12) Otto, O.; Rosendahl, P.; Mietke, A.; Golfier, S.; Herold, C.; Klaue, D.; Girardo, S.; Pagliara, S.; Ekpenyong, A.; Jacobi, A.; Wobus, M.; Töpfner, N.; Keyser, U. F.; Mansfeld, J.; Fischer-friedrich, E.; Guck, J. Real-Time Deformability Cytometry : On-the-Fly Cell Mechanical Phenotyping. *Br. Commun.* **2015**.
- (13) Gossett, D. R.; Tse, H. T. K.; Lee, S. A.; Ying, Y.; Lindgren, A. G.; Yang, O. O.; Rao, J. Hydrodynamic Stretching of Single Cells for Large Population Mechanical Phenotyping. *PNAS* **2012**, *109* (20).
- (14) Ito, H.; Kaneko, M. On - Chip Cell Manipulation and Applications to Deformability Measurements. *ROBOMECH J.* **2020**.
- (15) Adamo, A.; Sharei, A.; Adamo, L.; Lee, B.; Mao, S.; Jensen, K. F. Micro Fluidics-Based Assessment of Cell Deformability. **2012**.
- (16) Convery, N.; Gadegaard, N. Micro and Nano Engineering 30 Years of Micro Fluidics. **2019**, *2* (May 2018), 76–91.
- (17) Urbanska, M.; Muñoz, H. E.; Bagnall, J. S.; Otto, O.; Manalis, S. R.; Carlo, D. Di; Guck, J. A Comparison of Microfluidic Methods for High-Throughput Cell Deformability Measurements. *Nat. Methods* **2020**, *17*, 587–593.
- (18) Nyberg, K. D.; Scott, M. B.; Bruce, S. L.; Gopinath, A. B.; Bikos, D.; Mason, T. G.; Kim, W.; Sung, H.; Rowat, A. C. The Physical Origins of Transit Time Measurements for Rapid, Single Cell Mechanotyping. *Lab Chip* **2016**, *16*, 3330–3339.
- (19) Kaushik, S.; Mahadeva, M.; Murugan, K. D.; Sundaramurthy, V.; Soni, G. V. Measurement of Alcohol-Dependent Physiological Changes in Red Blood Cells Using Resistive Pulse Sensing. *ACS Sensors* **2020**, *5* (12), 3892–3901.
- (20) Nyberg, K. D.; Hu, K. H.; Kleinman, S. H.; Khismatullin, D. B.; Butte, M. J. Quantitative Deformability Cytometry : Rapid , Calibrated Measurements of Cell Mechanical Properties. *Biophys. J.* **2017**, *113* (7), 1574–1584.
- (21) Nyberg, K. D.; Scott, M. B.; Bruce, S. L.; Gopinath, A. B.; Bikos, D.; Mason, T. G.; Kim, J. W.; Choi, H. S.; Rowat, A. C. The Physical Origins of Transit Time Measurements for Rapid, Single Cell Mechanotyping. *Lab Chip* **2016**, *16* (17), 3330–3339.

- (22) Elrod, H. G. Thin-Film Lubrication Theory for Newtonian Fluids with Surfaces Possessing Striated Roughness or Grooving. *J. Tribol.* **1973**, *95* (4), 484–489.
- (23) Gukhman, A. A. *Introduction to the Theory of Similarity*; New York, Academic Press: New York, NY, USA, 1965.
- (24) Grover, N. B.; Naaman, J.; Ben-Sasson, S.; Doljanski, F. Electrical Sizing of Particles in Suspensions: III. Rigid Spheroids and Red Blood Cells. *Biophys. J.* **1972**, *12* (9), 1099–1116.
- (25) DeBlois, R. W.; Bean, C. P. Counting and Sizing of Submicron Particles by the Resistive Pulse Technique. *Rev. Sci. Instrum.* **1970**, *41* (7), 909–916.
- (26) Sha, J.; Si, W.; Xu, B.; Zhang, S.; Li, K.; Lin, K.; Shi, H.; Chen, Y. Identification of Spherical and Nonspherical Proteins by a Solid-State Nanopore. *Anal. Chem.* **2018**, *90* (23), 13826–13831.
- (27) Grover, N. B.; Naaman, J.; Ben-Sasson, S.; Doljanski, F. Electrical Sizing of Particles in Suspensions: I. Theory. *Biophys. J.* **1969**, *9* (11), 1398–1414.
- (28) Grover, N. B.; Naaman, J.; Ben-Sasson, S.; Doljanski, F.; Nadav, E. Electrical Sizing of Particles in Suspensions: II. Experiments with Rigid Spheres. *Biophys. J.* **1969**, *9* (11), 1415–1425.
- (29) Morrison, P. E. A.; Coulter, W. H.; Springs, M. United States Patent 72). **1971**, No. ii.
- (30) Lan, W. J.; Holden, D. A.; Liu, J.; White, H. S. Pressure-Driven Nanoparticle Transport across Glass Membranes Containing a Conical-Shaped Nanopore. *J. Phys. Chem. C* **2011**, *115* (38), 18445–18452.
- (31) Lan, W. J.; Holden, D. A.; Zhang, B.; White, H. S. Nanoparticle Transport in Conical-Shaped Nanopores. *Anal. Chem.* **2011**, *83* (10), 3840–3847.
- (32) Grover, N. B.; Naaman, J.; Ben-Sasson, S.; Doljanski, F. Electrical Sizing of Particles in Suspensions: III. Rigid Spheroids and Red Blood Cells. *Biophys. J.* **1972**, *12* (9), 1099–1116.
- (33) Soni, G. V.; Dekker, C. Detection of Nucleosomal Substructures Using Solid-State

- Nanopores. *Nano Lett.* **2012**, *12* (6), 3180–3186.
- (34) Bell, N. A. W.; Muthukumar, M.; Keyser, U. F. Translocation Frequency of Double-Stranded DNA through a Solid-State Nanopore. *Phys. Rev. E* **2016**, *93* (2), 1–10.
- (35) Wang, X.; Wilkinson, M. D.; Lin, X.; Ren, R.; Willison, K. R.; Ivanov, A. P.; Baum, J.; Edel, J. B. Single-Molecule Nanopore Sensing of Actin Dynamics and Drug Binding. *Chem. Sci.* **2020**, *11* (4), 970–979.
- (36) Soni, G. V.; Singer, A.; Yu, Z.; Sun, Y.; McNally, B.; Meller, A. Synchronous Optical and Electrical Detection of Biomolecules Traversing through Solid-State Nanopores. *Rev. Sci. Instrum.* **2010**, *81* (1).
- (37) Nanopores, I. U. Handbook of Single-Molecule Biophysics. *Handb. Single-Molecule Biophys.* **2009**, 265–291.
- (38) Bafna, J. A.; Soni, G. V. Fabrication of Low Noise Borosilicate Glass Nanopores for Single Molecule Sensing. *PLoS One* **2016**, *11*, e0157399.
- (39) Kowalczyk, S. W.; Hall, A. R.; Dekker, C. Detection of Local Protein Structures along DNA Using Solid-State Nanopores. *Nano Lett.* **2010**, *10* (1), 324–328.
- (40) Yusko, E. C.; Prangkio, P.; Sept, D.; Rollings, R. C.; Li, J.; Mayer, M. Single-Particle Characterization of A β Oligomers in Solution. *ACS Nano* **2012**, *6* (7), 5909–5919.
- (41) Maheshwaram, S. K.; Sreenivasa, K.; Soni, G. V. Fingerprinting Branches on Supercoiled Plasmid DNA Using Quartz Nanocapillaries. *Nanoscale* **2021**, *13* (1), 320–331.
- (42) Steinbock, L. J.; Otto, O.; Chimere, C.; Gornall, J.; Keyser, U. F. Detecting DNA Folding with Nanocapillaries. *Nano Lett.* **2010**, *10* (7), 2493–2497.
- (43) Yusko, E. C.; Johnson, J. M.; Majd, S.; Prangkio, P.; Rollings, R. C.; Li, J.; Yang, J.; Mayer, M. Controlling Protein Translocation through Nanopores with Bio-Inspired Fluid Walls. *Nat. Nanotechnol.* **2011**, *6* (4), 253–260.
- (44) Adamo, A.; Sharei, A.; Adamo, L.; Lee, B.; Mao, S.; Jensen, K. F. Micro Fluidics-Based Assessment of Cell Deformability. *Anal. Chem.* **2012**, *84*, 6438–6443.
- (45) Lee, L. M.; Liu, A. P. The Application of Micropipette Aspiration in Molecular Mechanics

- of Single Cells. *J. Nanotechnol. Eng. Med.* **2014**, 5 (4), 0408011–0408016.
- (46) Alert, R.; Casademunt, J.; Brugués, J.; Sens, P. Model for Probing Membrane-Cortex Adhesion by Micropipette Aspiration and Fluctuation Spectroscopy. *Biophys. J.* **2015**, 108 (8), 1878–1886.
- (47) Bo, L.; Waugh, R. E. Determination of Bilayer Membrane Bending Stiffness by Tether Formation from Giant, Thin-Walled Vesicles. *Biophys. J.* **1989**, 55 (3), 509–517.
- (48) Guck, J.; Ananthakrishnan, R.; Mahmood, H.; Moon, T. J.; Cunningham, C. C.; Käs, J. The Optical Stretcher: A Novel Laser Tool to Micromanipulate Cells. *Biophys. J.* **2001**, 81 (2), 767–784.
- (49) Dao, M.; Lim, C. T.; Suresh, S. Mechanics of the Human Red Blood Cell Deformed by Optical Tweezers. *J. Mech. Phys. Solids* **2003**, 51 (11), 2259–2280.
- (50) Blakely, B. L.; Dumelin, C. E.; Trappmann, B.; Mcgregor, L. M.; Choi, C. K.; Anthony, P. C.; Duesterberg, V. K.; Baker, B. M.; Steven, M.; Liu, D. R.; Chen, C. S. A DNA-Based Molecular Probe for Optically Reporting Cellular Traction Forces. *Nat Methods* **2014**, 11 (12), 1229–1232.
- (51) Keir C. Neuman; Attila Nagy. Single-Molecule Force Spectroscopy: Optical Tweezers, Magnetic Tweezers and Atomic Force Microscopy. *Nat. Methods* **2008**, 5 (6), 491–505.
- (52) Datar, A.; Bornschlögl, T.; Bassereau, P.; Prost, J.; Pullarkat, P. A. Dynamics of Membrane Tethers Reveal Novel Aspects of Cytoskeleton-Membrane Interactions in Axons. *Biophys. J.* **2015**, 108 (3), 489–497.
- (53) Mao, Y.; Nielsen, P.; Ali, J. Passive and Active Microrheology for Biomedical Systems. *Front. Bioeng. Biotechnol.* **2022**, 10 (July).
- (54) Zia, R. N. Active and Passive Microrheology: Theory and Simulation. *Annu. Rev. Fluid Mech.* **2018**, 50, 371–405.
- (55) Laukkanen, O. V. Small-Diameter Parallel Plate Rheometry: A Simple Technique for Measuring Rheological Properties of Glass-Forming Liquids in Shear. *Rheol. Acta* **2017**, 56 (7–8), 661–671.

- (56) Shuichi Tanoue, Michal K. Zielinski, Naoki Washida, and Y. iemoTo. Evaluation of Parallel Plate Type Rheometer Using an Oscillatory Viscoelastic Flow Simulation. *J. Soc. Rheol.* **2008**, 37 (2), 113–120.
- (57) Wirtz, D. Particle-Tracking Microrheology of Living Cells: Principles and Applications. *Annu. Rev. Biophys.* **2009**, 38 (1), 301–326.
- (58) Yamada, S.; Wirtz, D.; Kuo, S. C. Mechanics of Living Cells Measured by Laser Tracking Microrheology. *Biophys. J.* **2000**, 78 (4), 1736–1747.
- (59) Wottawah, F.; Schinkinger, S.; Lincoln, B.; Ananthakrishnan, R.; Romeyke, M.; Guck, J.; Käs, J. Optical Rheology of Biological Cells. *Phys. Rev. Lett.* **2005**, 94 (9), 1–4.
- (60) Wu, P. H.; Aroush, D. R. Ben; Asnacios, A.; Chen, W. C.; Dokukin, M. E.; Doss, B. L.; Durand-Smet, P.; Ekpenyong, A.; Guck, J.; Guz, N. V.; Janmey, P. A.; Lee, J. S. H.; Moore, N. M.; Ott, A.; Poh, Y. C.; Ros, R.; Sander, M.; Sokolov, I.; Staunton, J. R.; Wang, N.; Whyte, G.; Wirtz, D. A Comparison of Methods to Assess Cell Mechanical Properties. *Nat. Methods* **2018**, 15 (7), 491–498.

CHAPTER 2

EXPERIMENTAL TECHNIQUES

ABSTRACT

In this chapter, we provide details on the working principle of the Resistive Pulse Technique (RPT) and the Atomic Force Microscopy (AFM) force spectroscopy measurements majorly used in this thesis work. Firstly, we present the basics of resistive pulse sensing along with a brief review of various RPT models used during the evolution of RPT over a period of time. We then elaborate steps involved in the fabrication of the custom-made glass micropore device, along with every small learning we had from all the possible mistakes we made and various ways to troubleshoot them. We have made a few geometrical changes to the micropore as per the requirement of the problem, which is also detailed here. Based on our understanding from a detailed review of various RPT models we have used appropriate models for our RPT data in the subsequent chapters. The details of the data acquisition, characterization of the micropore devices, and our understanding of the data are also provided in this chapter. We also present the working principle of atomic force microscope force spectroscopy measurements as it is used for cellular elasticity measurements in this thesis. We then conclude this chapter with our understanding of the experimental techniques and the models used for data analysis in this thesis. Note that the subsequent chapters of this thesis build upon all the experimental techniques presented in this chapter.

2.1 RESISTIVE PULSE SENSING TECHNOLOGY (RPT)

There are numerous methods used to study micron, sub-micron, and nanoscale biological and synthetic objects. The most commonly used ones are bright field, confocal, fluorescent imaging, optical tweezers, atomic force microscopes (AFM), rheometers, electron microscopes (EM), and flow cytometry. All of these techniques have their benefits and drawbacks, for example, optical microscopy has spatial resolution limits, whereas confocal, fluorescence, and EM imaging approaches have better spatial resolution, but require appropriate labels. Optical tweezers and AFM are amazing tools for single molecule force spectroscopy measurements but lack a reasonable throughput. Rheometers are great for the bulk properties of micron-sized particles, but can not be used for single cell level study. Flow cytometry often requires fast imaging systems and post-processing is neither time nor data storage efficient. Note that, it is possible to couple many of these techniques with each other to overcome the underlying drawbacks of just one approach.

In this section, we are going to discuss resistive pulse sensing, a technique that works on the basic principle of Ohm's law and can easily be coupled with flow cytometry, optical tweezers, and various microscopic imaging methods. The technique has existed since the early 1950s and was for the first time used by Coulter for cell counting¹, since then it has been used in the medical and research fields for decades for the detection and counting of cells or micron-sized particles²⁻⁴. Many improvements have been employed in this technique for the quantification of the sample size, orientation, and charges⁵⁻¹⁴. The advanced low-noise data acquisition and signal amplification tools have also opened up applications in the field of nano-sized biological sample detection, DNA sequencing, branches in biopolymers, and their conformations^{7,9,10,15}. The resistive pulse sensing has been an emerging platform for studying and detecting physiological, morphological, conformational, and mechanical properties of various biopolymers and cells^{7,13,16,17}. In RPT the sensing part of the device is an orifice made of materials like silicon oxide^{15,18,19}, silicon nitride^{10,11,20-27}, carbon nanotubes^{28,29}, graphene^{30,31}, glass capillaries^{27,32-35}, biological membrane³⁶, polydimethylsiloxane (PDMS)^{37,38}, and silicon wafers³⁹. These orifice acts as a channel between reservoirs filled with an appropriate ionic buffer. When a particle moves through this channel either due to an external fluid flow or electro-osmosis, under an applied biased voltage the particle displaces ions in the sensing region of the channel, causing the conductance to drop momentarily, which can be recorded as an electrical pulse. These electrical events caused by the presence of a particle in the sensing region contain details about the particle's physiology^{13,17,40}.

Note that on using a low-noise data acquisition, a signal amplification system and appropriate dimensions of the RPT detection device also allow sensing morphological, conformational, and mechanical properties of various biological samples. The developments made in resistive pulse sensing and its evolution over time are detailed in the following sections of this thesis.

2.1.1 History of Resistive Pulse Technique

The Coulter Counter: In the year 1953 Wallace H. Coulter for the very first time demonstrated the resistive pulse technique for counting cells ⁴¹. It could easily be said that Coulter invented the idea of blood count analysis methodology based on the resistive pulse technology, which is widely used in most of diagnostic applications in the modern world. In his work, Coulter separated two reservoirs filled with an electrolyte solution using a membrane, and electrodes were placed in each reservoir connected with the electrical assembly to apply voltage and read the current using an ammeter (see Figure 2.1 (top)). The electrolyte fluid levels in the two reservoirs were maintained to be higher in the left compared to the right reservoir, this was essential to create a pressure difference between the two reservoirs, to allow fluid flow from the left to the right reservoir. The blood samples were added to the right reservoir, and the pressure difference created due to the gravity made the blood cells flow from right to left. When particles with a higher or lower conductivity compared with the conductivity of the electrolyte solution go through the membrane channel, an instantaneous increase (i_1) and decrease (i_2) in currents are observed respectively (see Figure 2.1 (bottom)). The concentration of cells in the suspension is then estimated with the information on how much amount of fluid volume has moved through the channel and the number of spikes that occurred in a fixed amount of time. The magnitude of the current spikes correlates to the cellular volumes, which are then used to distinguish cells of different sizes and types from the whole blood, hence giving a complete blood count, which is commonly known as a CBC test today. More details on the analysis of volume and size estimation based on the resistive pulse technique can be found in the text later.

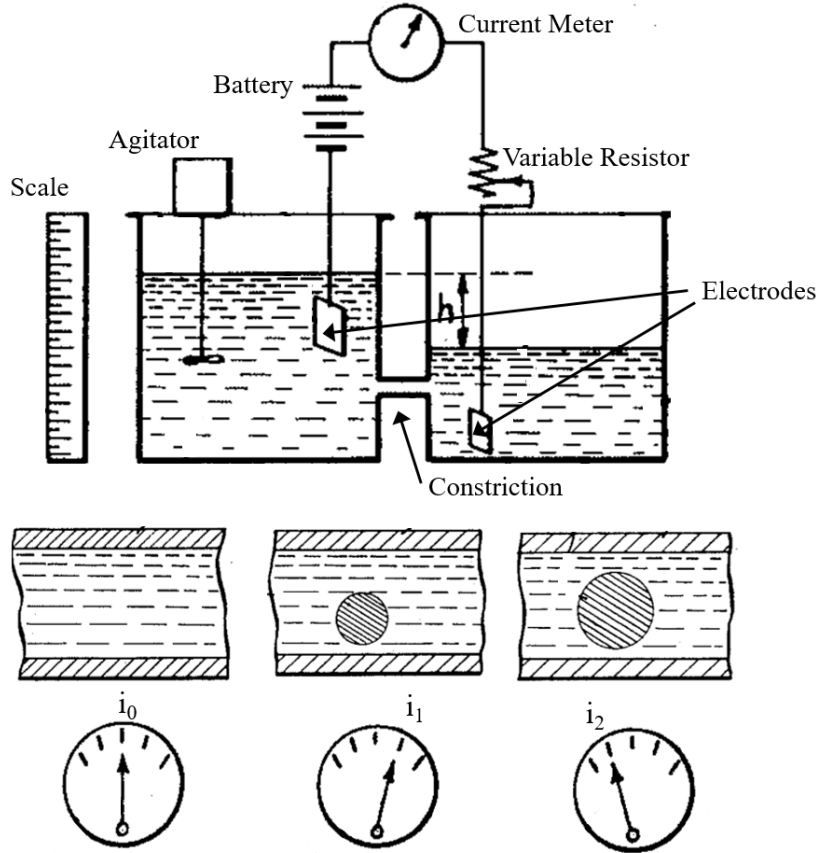


Figure 2.1 Schematic of the Coulter Counter design: A conducting solution is added to the two reservoirs, with two electrodes dipped in each reservoir. A battery is connected to provide a constant voltage, and a current meter is used to detect any changes in the current. The blood sample is added to the left reservoir, and an agitator is used to maintain a homogenous concentration. The height difference in the two reservoirs creates a pressure difference, making the particles to moves through the constriction. In the absence of any particle in the constriction channel, the current meter reads i_0 due to the ionic current flow. Whereas when a particle with higher conductivity compared to the solution, an instantaneous increase in the current is detected as i_1 , and a particle with lower conductivity results in a decrease in the current as i_2 . The schematic of these instantaneous currents drop or rise is shown at the bottom. The figure is adapted from ⁴¹.

Maxwell Model for Resistive Pulse Technique: Inspired by Coulter’s work, in the year 1954, J. C. Maxwell estimated a simple expression for the change in resistance caused by a spherical particle when in suspension in a cylindrical geometry containing a conducting medium. In his book “A Treatise on Electricity & Magnetism” ⁴², Maxwell states that the effective resistivity of the solution in the presence of a non-conducting sphere in the suspension is given by:

$$\rho_{eff} = \rho_o \left(1 + \frac{3}{2}f + \dots \right) \quad (2.1)$$

Here, ρ_o is the suspension medium’s resistivity and f is the volume fraction of the sphere (i.e. the ratio of the sphere and the sensing part of the cylinder) which is expressed as following :

$$f = \left(\frac{4}{3} \pi \left(\frac{d}{2} \right)^3 \right) \cdot \left(\frac{1}{\pi L \left(\frac{D}{2} \right)^2} \right) \quad (2.2)$$

$$f = \frac{2d^3}{3D^2L} \quad (2.3)$$

Now, since the expression for the resistance of a conducting cylinder in terms of the resistivity (ρ), cross-sectional area (A), and length (L) is:

$$R_0 = \frac{\rho L}{A} = \frac{4\rho L}{\pi D^2} \quad (2.4)$$

The effective resistance (R_{eff}) of the same cylinder with a spherical particle of diameter 'd' in the suspension (see Figure 2.2) will be:

$$R_{eff} = \frac{4L}{\pi D^2} \rho_{eff} \quad (2.5)$$

Now, on combining equations 2.2, 2.3, 2.4, and 2.5, the expression for the change in resistance ($\Delta R = R_{eff} - R_0$) caused by the presence of the spherical particle in the conducting medium will be:

$$\Delta R = \frac{4L\rho_0}{\pi D^2} \left[1 + \frac{3}{2}f + \dots - 1 \right] \quad (2.6)$$

Assuming that the length of the cylinder is very large compared to the diameter (i.e. $L \gg D$) and the diameter of the spherical particle is very small compared to the diameter of the cylinder (i.e. $d \ll D$), equation 2.6 can be approximated to:

$$\Delta R \approx \frac{4\rho d^3}{\pi D^4} \quad (2.7)$$

It is important to note that the second order term in ' ρ_{eff} ' gets neglected and the L dependence can be accounted for in the equation by considering the higher order terms in ' ρ_{eff} '.

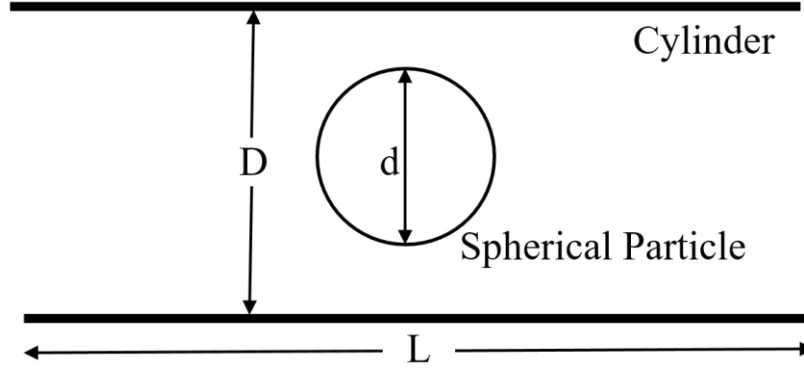


Figure 2.2 Schematic of a spherical particle inside a conducting cylinder: A non-conducting spherical particle of diameter 'd' suspended inside a cylinder of diameter 'D' and length 'L' containing a conduction fluid of resistivity 'ρ' is shown here.

Grover's Model: Inspired by Maxwell's work on estimating the change in resistance of a channel caused by a spherical non-conducting sphere, in the year 1969 Grover et.al made use of synthetic rubies with cylindrical holes to precisely quantify the volume of latex particles²⁻⁴. The following expression of relative current change in the pore was obtained to estimate the volume of the latex particles:

$$\frac{\Delta I}{I} = 1.5 \left(\frac{\delta}{1-\delta} \right) \quad (2.8)$$

Here, δ is the ratio of particle volume and the pore channel volume, which is expressed in terms of the effective pore length (L_{eff}), pore diameter (D_p), and pore channel conductance (G) as $\delta = \frac{4 \cdot V_{particle}}{\pi D_p^2 L_{eff}}$, where the L_{eff} , for a pore is measured as:

$$L_{eff} = \frac{\pi D_p^2}{\rho G} \quad (2.9)$$

Here, ρ is the resistivity of the pore channel containing the conducting medium. A comparison of the latex particle's volume measured using the resistive pulse technique and electron microscopy is shown in Figure 2.3².

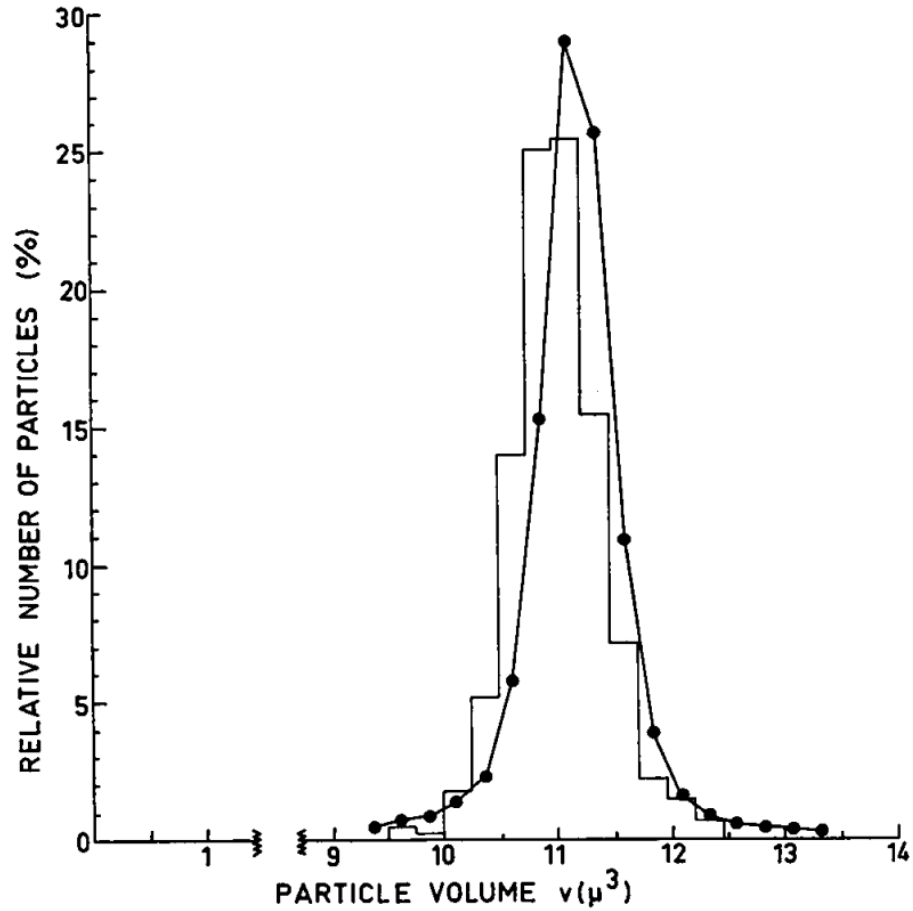


Figure 2.3 *Quantifying the volume of latex polystyrene particles: Volume distribution of the polystyrene latex particles as determined electrically (broken line) and with an electron microscope (histogram). Reprinted with permission from ².*

Note that, so far all the models considered the sample particles to be a sphere, hence when experiments were performed with non-spherical samples like RBCs, instead of a single type of electrical signal, two types of signals were recorded as shown in Figure 2.4. One type of the signal was showing a sudden peak during their passage through the pore channel (See Figure 2.4), these sudden peaks were explained to be a result of the non-symmetric shape of the sample. The theoretical studies performed by Fricke ^{43,44} showed that the orientation and shape of a particle inside the pore channel along the direction of the ionic flow changes the channel current, hence the relative change in the current caused by a non-symmetric particle passing through the pore channel is given by the equation ^{43,44}:

$$\frac{\Delta I}{I} = \gamma \left(\frac{\delta}{1-\delta} \right) \quad (2.10)$$

Here, γ is the shape factor, and the expression for the shape factor for ellipsoidal particles as obtained by Fricke⁴⁴ and experimentally verified by Velick and Gorin⁴⁵ are:

$$\frac{1}{\gamma} = \begin{cases} \frac{m \cos^{-1} m}{(1-m^2)^{\frac{3}{2}}} - \frac{m^2}{1-m^2} & \text{Oblate Spheroid} \\ \frac{m^2}{m^2-1} - \frac{m \cosh^{-1} m}{(m^2-1)^{\frac{3}{2}}} & \text{Prolate Spheroid} \end{cases} \quad (2.11)$$

Here, m is the ratio of the principle axes 'a' and 'b', i.e. $m=a/b$. for an oblate spheroid $m<1$, whereas for a prolate spheroid $m>1$. It is important to note that the expression in equation 2.11 is valid only if the direction of principle axis 'a' is along the electric field, otherwise, the expression for γ will be replaced by:

$$\gamma' = \frac{2\gamma}{2\gamma-1} \quad (2.22)$$

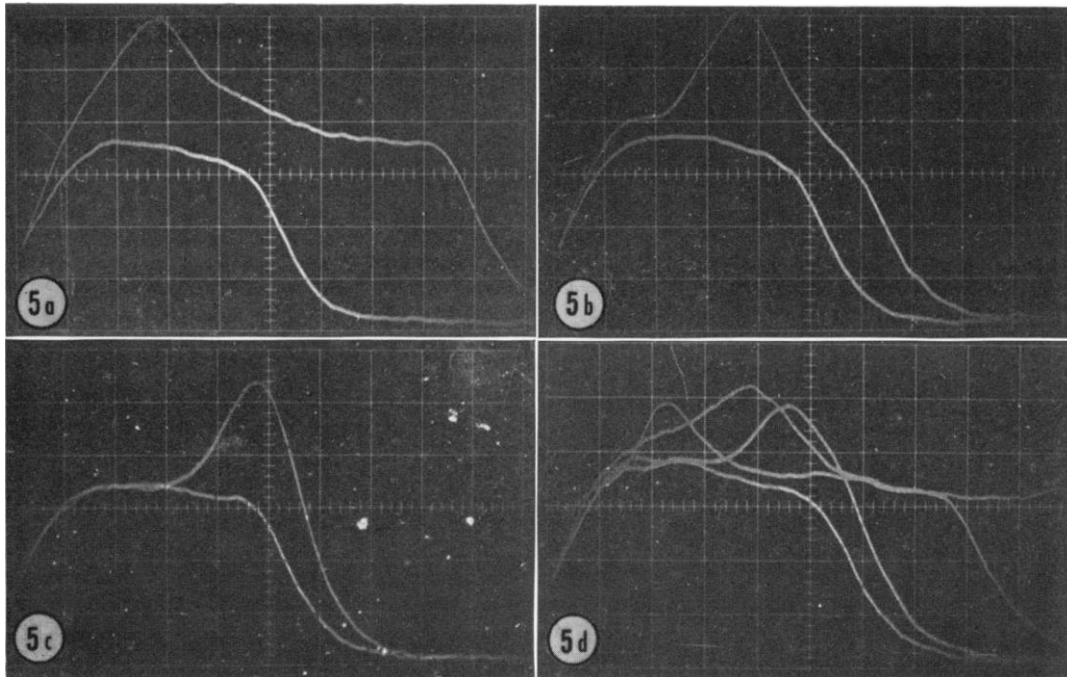


Figure 2.4 Oscillograms of resistive pulse signals for human red blood cells: The electric pulse of RBCs passing through an orifice of $50 \times 50 \mu\text{m}$ dimensions at a glow rate of 450 cm/sec . The open current is $170 \mu\text{A}$ and the oscillograms are taken with a sweep of $5.0 \mu\text{sec/division}$. Reprinted with permission from³.

Deblois-Bean Model: In the studies mentioned so far, the resistive pulse technique was used to detect particles in the micron-sized range. In this study sub-micron, polystyrene particles are driven through pores solely by the applied electric field, without using any external fluid flow or

pressure ⁵. The electrophoretic and electro-osmotic forces come into play to drive the particles through the pore channel. In this work, Deblois and Bean have provided a classical approach to understanding the translocation of the non-conducting particles under the applied electric field. On considering a sphere in a uniform field (see Figure 2.5), Laplace's equation for Voltage in polar coordinates is given by,

$$V(r, \theta) = \left(A \cdot r + \frac{B}{r^2} \right) \text{Cos}\theta \quad (2.23)$$

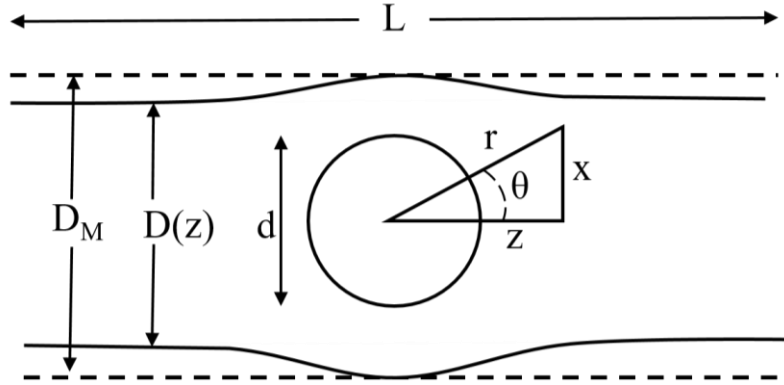


Figure 2.5 Electric field distortion due to a non-conducting sphere inside a conducting fluid in a cylindrical tube: $D(Z)$ shows the axial cross-section of an electric field streamline tube of length 'L', as distortion by insertion of a non-conducting sphere of diameter 'd', placed in a conducting fluid with an originally uniform field along the Z axis. D_M represents the cross-section of a uniform tube with a diameter equal to that of the distorted tube at its maximum bulge. Reprinted with permission from ⁵.

For a non-conducting sphere, the field normal to the sphere vanishes at the surface, i.e.

$$-\frac{\partial V}{\partial r} \Big|_{r=\frac{d}{2}} = 0 \Rightarrow B = \frac{d^3 A}{16} \quad (2.24)$$

Hence,

$$V(r, \theta) = A \left(r + \frac{d^3}{16r^2} \right) \cdot \text{Cos}\theta \quad (2.25)$$

The axial component of the electric field will be:

$$E_z = -\frac{dV(r, \theta)}{d(r, \theta)} = -\frac{\partial V}{\partial r} \text{Cos}\theta + \frac{1}{r} \frac{\partial V}{\partial \theta} \text{Sin}\theta \quad (2.26)$$

Now according to Ohm's Law the total current 'I' through any cross-section of diameter 'D' and distance 'Z' along the axis from the Centre of the axis will be:

$$I = \frac{2\pi}{\rho} \int^{D/2} E_z x dx , \quad (2.27)$$

Here, x is the distance from the central axis. Now, on substituting E_z from equation (2.26) and integrating we'll get:

$$I(z) = -\pi A \frac{D^2}{4\rho} \left\{ 1 - \left(\frac{d^3}{(D^2+4z^2)^{\frac{3}{2}}} \right) \right\} \quad (2.28)$$

At $z=0$ $D = D_m$, which gives us,

$$I(0) = -\frac{\pi A D^2}{4\rho} \left[1 - \left(\frac{d}{D_m} \right)^3 \right] \quad (2.29)$$

Far from the bulge, I will be constant and independent of the variable D , and $I(z)=I(0)$ resulting:

$$D^2 \left[1 - \frac{d^3}{(D^2+4z^2)^{\frac{3}{2}}} \right] = D_m^2 \left[1 - \left(\frac{d}{D_m} \right)^3 \right] \quad (2.30)$$

The resistance across the channel with the sphere in it will be:

$$R_2 = \frac{[v(-\frac{L}{2}) - v(\frac{L}{2})]}{I(0)} \quad (2.31)$$

On using the equation (2.25) and (2.31), we get:

$$R_2 = \frac{4\rho L}{\pi D_m^2} \left[1 + \frac{d^3}{16r^3} \right] \cdot \left[1 - \left(\frac{d}{D_m} \right)^3 \right]^{-1} \quad (2.32)$$

In the limits $d \ll L$, ' r ' can be replaced with $L/2$, hence the expression for R_2 will be:

$$R_2 = \frac{4\rho L}{\pi D_m^2} \left[1 + \frac{d^3}{2L^3} \right] \cdot \left[1 - \left(\frac{d}{D_m} \right)^3 \right]^{-1} \quad (2.33)$$

Now for R_1 , the approximation for resistance of a tube having varying cross-section is given by:

$$R = \rho \frac{\int dz}{A(z)}, \quad \text{where } A(z) = \frac{\pi D^2}{4}$$

On substituting the D^2 from equation (2.30) we get,

$$R_1 = \frac{4\rho L}{\pi D_m^2} \left[1 - \left(\frac{d}{D_m} \right)^3 \right]^{-1} \cdot \left[1 - \frac{2}{L} \int_0^{\frac{L}{2}} \frac{d^3 dz}{D^2 + 4z^2} \right]^{\frac{3}{2}} \quad (2.34)$$

And, $\Delta R = R_2 - R_1$

Hence, from eqn (7) and eqn (8), we get,

$$\Delta R = \frac{4\rho}{\pi D_m^2} \left[1 - \left(\frac{d}{D_m} \right)^{-1} \right] \cdot \left[\frac{d^3}{2L^2} + 2 \int_0^{\frac{L}{2}} \frac{d^3 dz}{(D^2 + 4z^2)^{\frac{3}{2}}} \right] \quad (2.35)$$

Now in limits $d \ll D_m$, we can approximate $D = D_m$, and we get

$$\Delta R_{\left\{ \left(\frac{D_m}{L} \right) < 1 \right\}, \frac{d}{D_m} \ll 1} = \frac{4\rho d^3}{\pi D_m^4} \left[1 + \frac{3}{8} \left(\frac{D_m}{L} \right)^4 + \dots \dots \right] \quad (2.36)$$

For finite values of $\frac{d}{D_m}$ the following expression can be evaluated numerically:

$$\Delta R_{\left\{ \left(\frac{D_m}{L} \right) \ll 1 \right\}} = \frac{4\rho d^3}{\pi D_m^4} F \left(\frac{d^3}{D_m^3} \right) \quad (2.37)$$

Where,

$$F \left(\frac{d^3}{D_m^3} \right) = 1 + 1.26_8 \frac{d^3}{D_m^3} + 1.1_7 \frac{d^6}{D_m^6} \quad (2.38)$$

The experimental data for beads of diameter 91 nm, 109 nm, 121 nm, 176 nm, 234 nm, and 357 nm using a pore of diameter 454 nm, in terms of ΔR (M Ω) v\ s Volume of the beads (μm^3) are shown in Figure 2.6. The best-fit analysis for the experimental data shown in Figure 2.6 is used to get the following empirical equation:

$$\Delta R = \frac{4\rho d^3}{\pi D_m^4} \left[1 + 0.73 \left(\frac{d^3}{D_m^3} \right) \right] \quad (2.39)$$

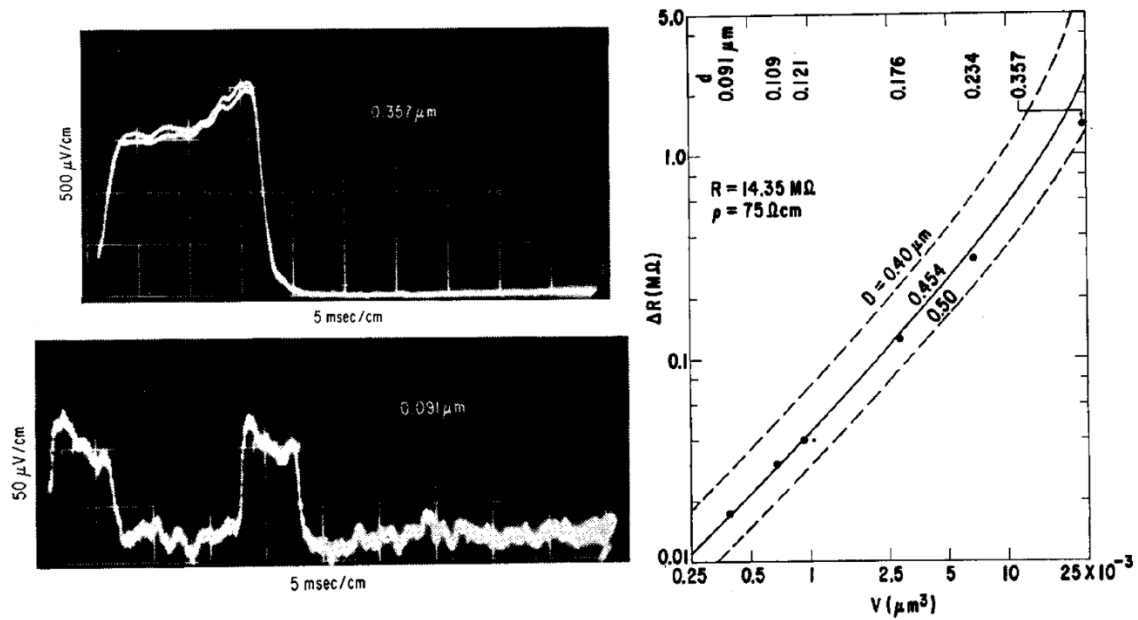


Figure 2.6 Resistive pulse signals on the oscilloscope and the change in resistance v/s volume for polystyrene particles: Resistive pulse signal for 0.357 and 0.091 μm polystyrene particles through a $0.49 \times 0.45 \mu\text{m}$ plastic membrane is shown on the left. The plot of resistive pulse ΔR vs the volume of beads of diameter 91 nm, 109 nm, 121 nm, 176 nm, 234 nm, and 357 nm using a pore of diameter 454 nm. The solid line is the theoretical upper limit for a 454 nm pore that best matches the experimental data. Reprinted with permission from ⁵.

Access Resistance: We have discussed different approaches to estimate the resistive pulse effect considering the geometry of the pore channel, properties of the buffer, and the sample. In all of these approaches, the problem of the edge effects caused due to the electro-diffusive limitation experienced by the ions passing through a small confinement is not taken into account. This edge effect which increases the open pore resistance was initially thought to be more dominant in confinements made of biological membranes, but as shown by Hall in the year 1975, the problem of the edge effect is due to a flat pore mouth offering an additional resistance, hence famously known as ‘Access Resistance’⁴⁶. Hall provided a theoretical expression for the access resistance for a pore of diameter D_p with the solution conductivity ‘ σ ’ as:

$$R_{access} = \frac{1}{2\sigma D_p} \quad (2.40)$$

Note, that the access resistance and the bulk resistance of the pore are in series, hence they add up. Hence, the effective conductance (G_{eff}) of the pore in terms of bulk and access resistance can be written as:

$$G_{eff} = [R_{bulk} + R_{access}]^{-1} \quad \text{or} \quad G_{eff} = \left[\frac{1}{G_{bulk}} + \frac{1}{G_{access}} \right]^{-1} \quad (2.41)$$

The contribution of the access resistance in the effective open pore conductance is inversely proportional to the diameter of the pore channel. Hence, it is observed that the access resistance effect can easily be neglected while working with large pores. The resistive pulse technique-based experiments performed for this work were done on pore channels having diameters in the range of 2 – 10 μm , hence the effect of access resistance terms has been neglected.

2.1.2 Micropore Forging Protocol

For all the resistive pulse experiments performed in this thesis work, two types of borosilicate glass capillaries (OD = 1 mm, ID = 0.75 mm or 0.50 mm, length = 150 mm or 75 mm) (Sutter Instrument) were used to make the micropores. The glass capillaries are initially cleaned using ethanol and acetone, then nitrogen-dried. The cleaned glass capillaries are then pulled using a micropipette puller (model P-2000, Sutter Instrument), using the following parameters:

S.no	Micropore	Heat	Filament	Velocity	Delay	Pull
1	Free Flight	300	0	15	128	250
2	Constricted	350	0	25	150	200

Table 2.1 Micropipette puller program parameters: Two different sets of micropipette puller programs are used to pull the capillaries for free flight and constricted micropores respectively.

The pulled capillaries (see Figure 2.7 a) are then cut and shrunk to the desired micropore geometry using a flame polisher instrument (MF-900, Micro Forge, Narshige). We have used two types of micropores in this thesis work; micropores for free flight and constricted flight experiments. The free-flight micropores are forged using a simple V-shaped filament (see Figure 2.7 b). Firstly, the pulled capillary (shown in Figure 2.7 c) is brought on top of the V-shaped filament with a small glass bead attached to it, and gentle contact is made between the glass bead on the filament and the

capillary, note that the inner diameter of the capillary at the contact is roughly 60-80 μm . The filament is then heated using a high voltage for a fraction of a second, which cuts the capillary as shown in the Figure 2.7 d. The cut capillary is then brought in front of the filament, and then high voltage is again used to heat the filament to get the desired micropore diameter (see Figure 2.7 e-g). An objective of 35X magnification and a cross-hair are used constantly to monitor the diameter of the micropore during the entire forging procedure. Now, the constricted flight micropores are forged using an omega-shaped (Ω) filament (see Figure 2.7 h). The pulled capillary is carefully placed symmetrically at the center of the omega-shaped filament, avoiding any contact as shown in Figure 2.7 g. A high voltage is used to heat the filament to forge the capillary to get a long cylindrical constriction of the desired diameter (see Figure 2.7 j). An objective of 10X magnification and the cross-hair are used this time to monitor the diameter and the shape of the capillary. It is important to note that sometimes the forging causes asymmetry in the capillaries, so the capillary is then carefully rotated during the forging to correct for any asymmetry. Once we get the desired geometry and diameter, the omega-shaped filament is then removed, and the V-shaped filament is mounted. The protocol used for free-flight micropore forging is used to cut and shrink the access glass capillary to get the final constricted micropore (see Figure 2.7 k-n). Note that all the micropores are later imaged and checked for any asymmetry under a commercial bright-field microscope, only the symmetric micropores were considered for the experiments. Images of all the intermediate steps involved while forging the free-flight and the constricted micropores are shown in Figure 2.7.

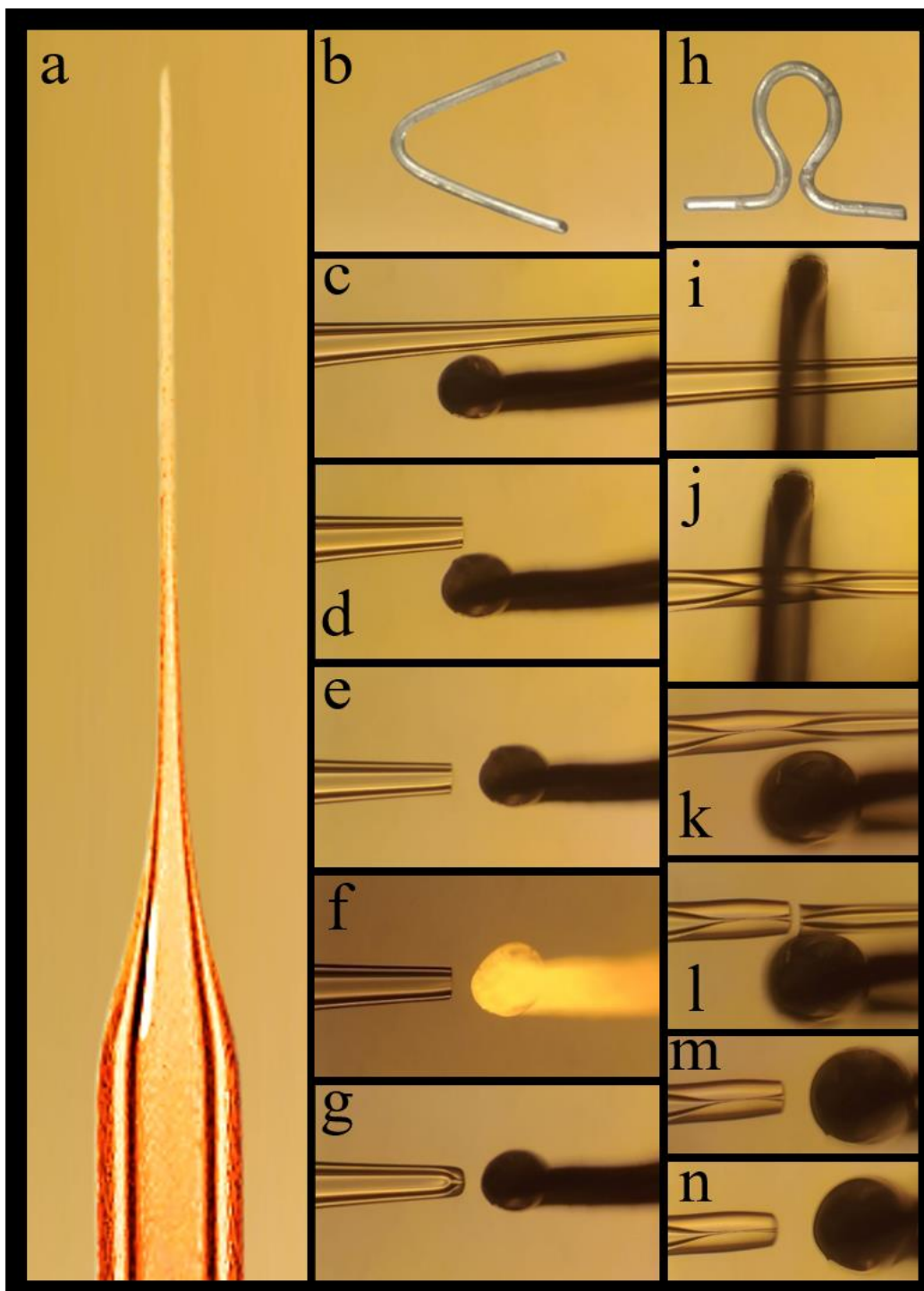


Figure 2.7 Steps involved in forging a micropore from a glass capillary: (a) The image of the glass capillary pulled using the Shutter Puller instrument is shown here. (b-g) Images of a 'V' shaped filament and the steps involved in forging a free-flight micropore are shown. (h-n) Images of an omega-shaped (Ω) filament and the steps involved in forging a constricted micropore are shown. Note that these images are not to be scaled. Note that this figure is also used in Chapter 5, for the sake of the continuity of the discussion.

2.1.3 Micropore Device Preparation

To mount a micropore, firstly a 4 cm long TYGON Masterflex tubing (ID=0.025” and OD 0.095”) is cut, and a 100 μ L pipette tip is inserted inside it and left for about 20-30 mins (see Figure 2.8 a). Insertion of pipette tip expands to tubing and avoids any scratched debris blocking the device while inserting the glass micropore in the Masterflex tubing. A pair of AgCl electrodes is made by chlorinating two 1-inch pieces of pure silver by keeping them half-dipped in a Clorox bleach solution for 12-15 hours. We then insert the desired micropore of appropriate length and an electrode inside the Masterflex tubing. The entire assembly is then mounted in a glass-bottom Teflon fluid chamber, and a polymer glue (Ecoflex 5) is used for this step (see Figure 2.8 b). We then melt a 100 μ L pipette tip from its center using a spirit lamp and then pull it to make our custom pipette filler (see Figure 2.8 c). We attach the pipette filler with a syringe, insert the elongated part of the pipette filler inside the micropore assembly, and fill the micropore with the electrolyte buffer (1 X PBS or RPMI 1640). Note that the pipette filler is brought extremely close to the micropore orifice while filling the electrolyte buffer to make sure no air bubbles are left. Now, one end of a long PTFE tubing (~30 cm) is connected to the back of the Masterflex tubing, and the other end is attached with a syringe mounted on a syringe pump (Pico Elite, Harvard Apparatus).

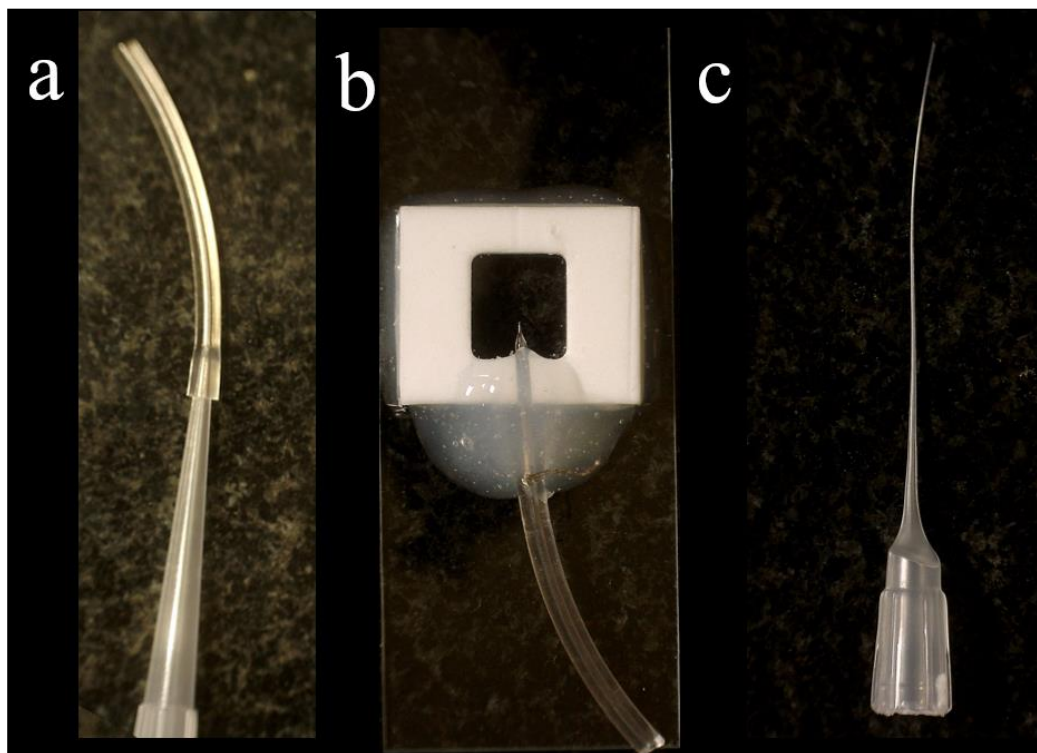


Figure 2.8 Images of steps involved in micropore device preparation: (a) Elongation of the Masterflex tubing using a 100 μL pipette tip. (b) Micropore mounted in a glass-bottom Teflon fluid chamber with an AgCl electrode inserted at the back. (c) Image of our custom-made pipette filler made from a 100 μL pipette tip is shown here.

2.1.4 Data Acquisition

A custom LabVIEW code is used to acquire the electrical data through an amplifier connected to the micropore experimental setup (See Figure XXX). We have used various data acquisition (DAQ) systems from National Instruments to control our LabVIEW code. The specific details of the bandwidth setting, filter frequency, DAQ system, and the amplifier used in this thesis work for different projects are provided in the subsequent chapters. In Figure 2.9, we show a screenshot of the LabVIEW code acquiring the electrical data. The marked region 1 shows the controllers for applied voltage, sample rate, filter frequency, DAQ physical channels, etc. The sample rate and filter frequency for all the experiments while acquiring the data in this thesis work were kept at 100k and 10k respectively. The save file control switch, directory, size, and counters are highlighted in Region 2. The maximum file size is 10 MB, containing 640k points. The peak detection factor, event counter, and counter reset controls are shown in Region 3. The live electrical data is highlighted in Region 4. Region 5 shows the mean and standard deviation values of the measured current (nA) and voltage (mV) across the micropores. The instantaneous measured

resistance is also shown in region 5, which is later verified by taking an IV curve. The controllers for the amplifier voltage gain (α) and head stage gain (β) values are shown in Region 5. IV Curve Boolean switch marked in region 6 opens a new sub-VI, and a screenshot of this sub-VI is shown in Figure 2.10. While recording the data, the channel blockage due to any junk is observed as a sudden step decrease in the current, to unblock the micropore in such a situation, small pulses of reverse flow are applied using the syringe pump until the original open pore current is attained.

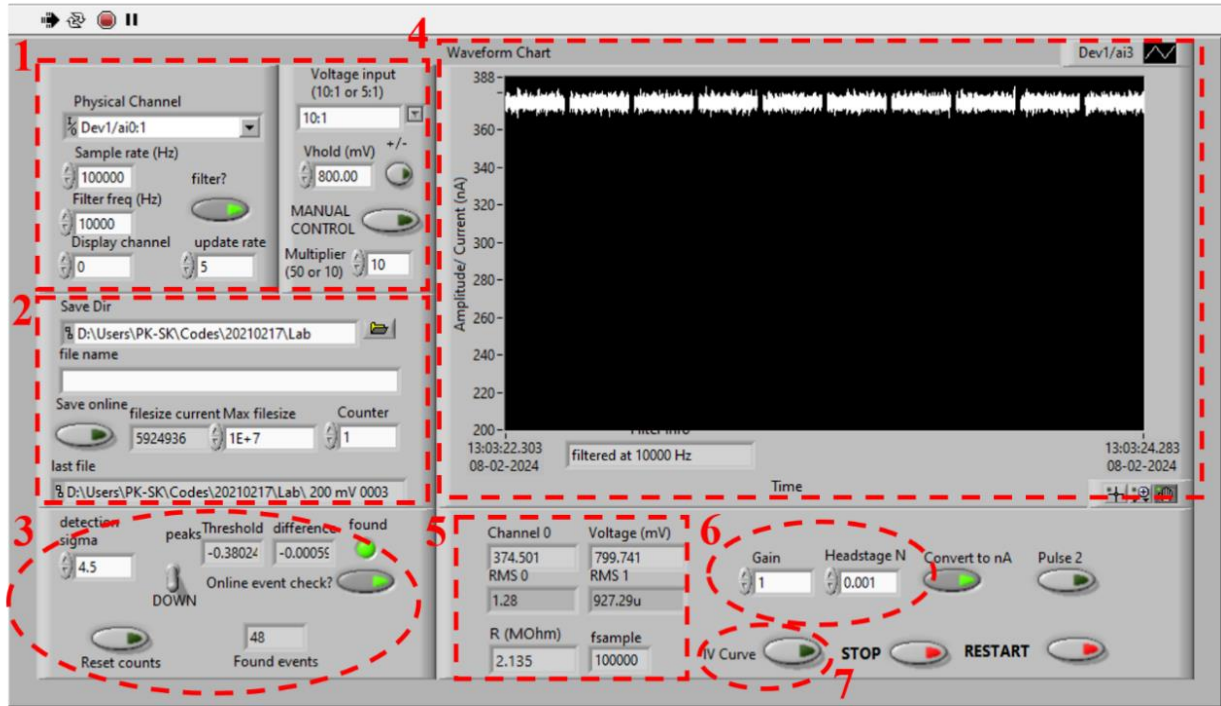


Figure 2.9: Interface of the record trace LabVIEW code: The control input parameters for setting the analog input channels, sample rate, and filter frequency are highlighted in Region 1. The controllers in Region 2 are used to set the file save directory, file size, and file number, the save online Boolean switch is used to start recording the data. The peak detection factor along with the Online event check controllers marked in Region 3 are used record files only if an event occurs. This feature of the code is used only if there event rate is extremely low. The live electrical data showing the current through the micropore at a constant applied voltage is shown in Region 4. The panels in Region 5 show the voltage, current, and measured resistance across the micropore. The amplifier voltage gain (α) and head stage gain (β) controllers are highlighted in Region 6. The Boolean switch shown in region 6 is used to open a new sub-VI for IV curve measurement. Note this LabVIEW code builds on what was used in Dekker lab and is re-written and customized for our experiments

2.1.5 Micropore Characterization

Since the micropores act as a variable resistor, the characterization of each micropore is performed by taking an IV curve. For this, the IV Curve sub-VI of our custom LabVIEW code is used and the various control panels of this VI are shown in Figure XXX. The highlighted region 1 in Figure 2.10 has controls to set the DAQ channels for applied voltage and measured current, region 2 has controls for the start voltage, voltage step values, and number of total steps between the voltages. The wait time between voltage jumps and making the measurement, the total number of points to be recorded, and the DAQ scanning rate are marked in Region 3. Region 4 graphically shows the recorded voltage corresponding to the current at different applied voltages, these voltages are then converted into current by using the amplifier gain values Alpha (α) and Beta (β), and the converted current (nA) vs applied voltage are plotted and fitted with a linear function in the graph shown in region 5. The resistance and conductance are estimated using the results of the fitting and are shown in the marked region 6. The panel shown in Region 7 is for setting the file directory to save the IV curve data.

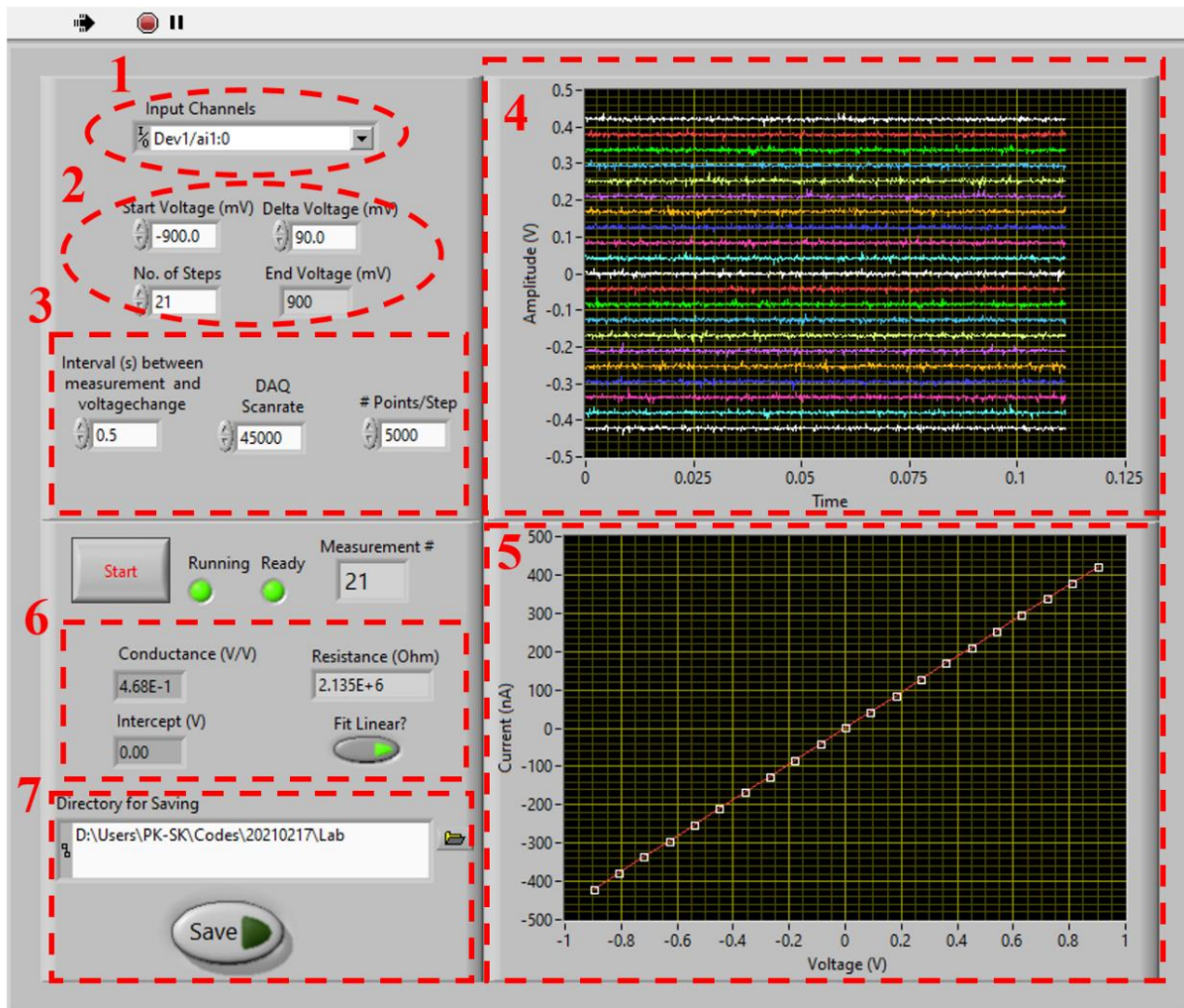


Figure 2.10 Interface of the IV Curve LabVIEW sub-VI: The controls for analog input channels to read the voltages corresponding to the applied voltage and current are shown in Region 1. Controls for giving signals in defined steps to the analog output channels to change voltages are marked in Region 2. The time between voltage change and measurement, sample rate to record points, and number of points to be recorded are controlled using panels highlighted in Region 3. The voltage corresponding to each applied voltage is shown in panel 4. Current vs applied voltage and the IV curve fitting are shown in Region 5. The measured resistance and the conductance from the fitting results are shown in the indicators in Region 6. The IV curve file save directory controller is marked in region 7.

2.1.6 Data Analysis

We use another custom-written LabVIEW code for analyzing the recorded translocation events. A screenshot of this code is shown in Figure 2.11, where Region 1 shows a 6.4 sec long electrical data recorded. The directory controls used to access the recorded binary files by the record trace LabVIEW code are highlighted in marked region 2. The software second-order Butterworth filter option is marked by the highlighted region 3. The voltage to current conversion control factor (product of α and β) set during data acquisition is in region 4. The parameters to identify and detect a translocation event like peak detection factor, and minimum and maximum dwell time allowed are marked in Region 5. The intricate details of detecting an event using the peak detection factor and baseline are provided in the next chapter. An indicator of the number of events found in a single file and the sum of all the events found in all the files are shown in Region 6. The graphical panel shown in Region 7 shows the concatenated events found in a file that is being analyzed. Finally, the graphical panel in Region 8 shows the entire raw trace concatenated events found in all the recorded files. The analyzed data is exported to a text file, which is then further used for statistical interpretation and understanding using custom macros written in Igor software.

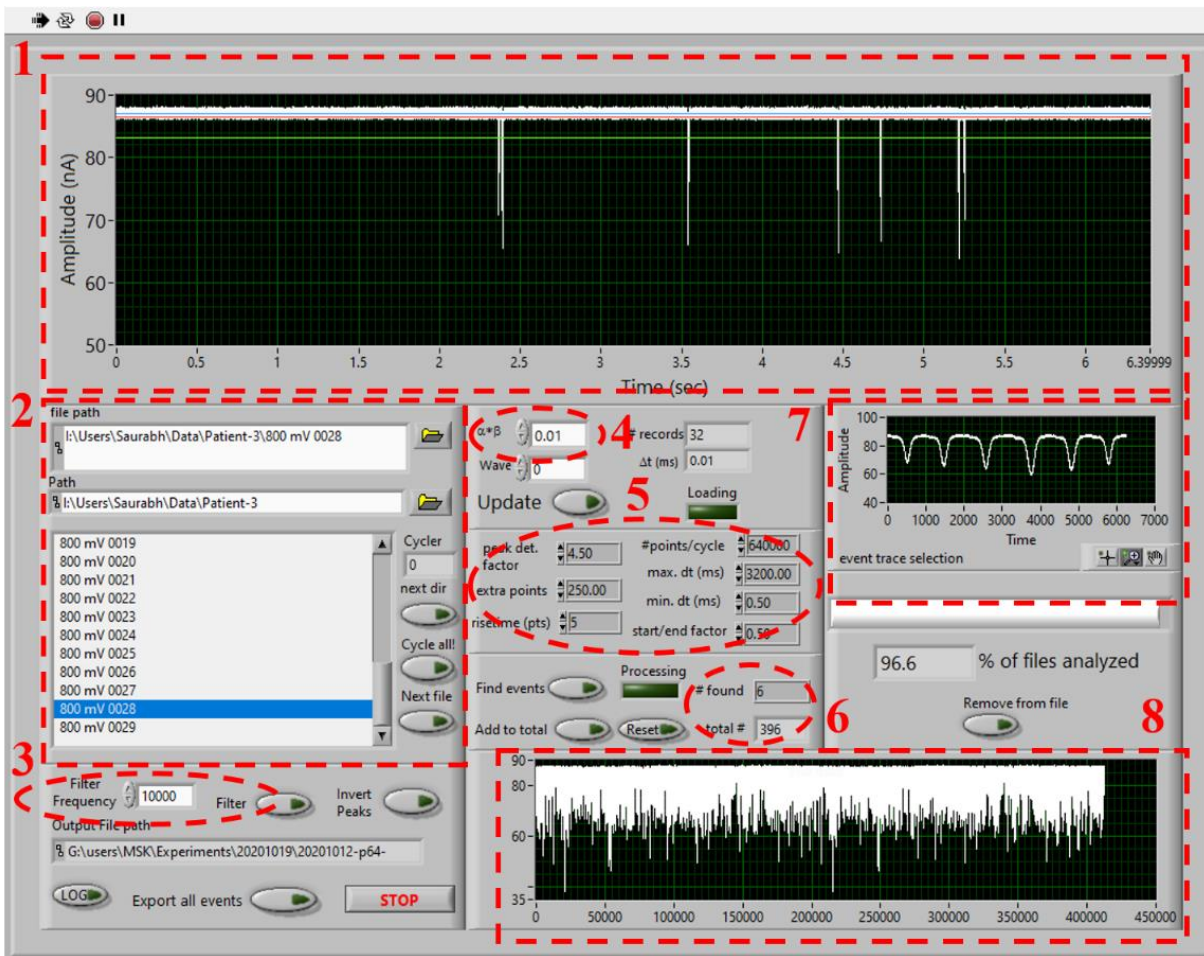


Figure 2.11 Interface of the Translocation Event Analysis LabVIEW Code: All the controls for input parameters for analyzing the recorded translocation events are shown in the highlighted regions 2, 3, 4, and 5. The graphical representation of the electrical event time trace, and concatenated events in a single file and all the files are shown in regions 1, 7, and 8 respectively. The indicator for the number of events found in a single file and the sum of all the number of events is highlighted in Region 6.

2.2 ATOMIC FORCE MICROSCOPY

Microscopes have been a crucial instrument for monitoring and studying various microscopic systems for centuries. The earliest reports of a working microscope are found to be a compound microscope made by two Dutch lens-crafters in the 1590s⁴⁷. Galileo built a similar magnifying system of lenses in the year 1609, and named it ‘Occhiolino’⁴⁷. Later Faber for the very first time used the term ‘Microscope’ for a system of lenses capable of providing a 30 times magnification⁴⁷. The origin of the word is Greek, where ‘Micron’ means small, and ‘Skopein’ means to look at. The first detailed treatise on microscopy and imaging on cells was illustrated by the British scientist Robert Hooke in his *Micrographia* using his compound microscope also famously known as modern microscope⁴⁷. Since the invention of microscopes in the 16th century, the field of microscopy has gone through a lot of advancement. There is a whole list of microscopy, which are commonly grouped into three categories; optical, electron, and scanning probe microscopy. Bright field, dark field, fluorescence, phase contrast, confocal, and polarized microscopy are various techniques considered under optical microscopy. Transmission electron microscope (TEM), scanning electron microscope (SEM), field emission scanning electron microscopes (FESEM), and reflection electron microscope (REM) are categorized under electron microscopy techniques. Whereas, scanning tunneling microscopy, scanning electrochemical microscopy, magnetic force microscopy, and atomic force microscopy are considered under scanning probe microscopy. In this section of the chapter, we are only going to focus on atomic force microscopy. We are going to briefly explore the history of atomic force microscopy, followed by the two major imaging modes and the force spectroscopy measurements.

2.2.1 History of Atomic Force Microscopy

Gerd Binnig and Heinrich Rohrer laid the foundational work for Atomic Force Microscopy (AFM) in the 1970s with the development of the Scanning Tunneling Microscopy (STM)⁴⁸. The STM was designed to image conducting surfaces at the atomic level by scanning a sharp tip over the conducting surface, the measured tunneling current between the sample and the sharp tip was then used to create the surface morphology electronically⁴⁸. The 1986 Nobel Prize in physics was awarded to Gerd Binnig and Heinrich Rohrer for their invention of STM. Later, they invented AFM, which was capable of imaging non-conducting materials, unlike STM. They devised a system to detect the forces between a sharp tip and sample surface and image various materials. Since the

invention of AFM in 1986, numerous developments have been incorporated to improve its resolution and sensitivity. Commercialization of AFM has also brought in competition which hugely contributed to further advancement of the instrument, pitching in various modes like tapping mode, contact mode, dynamic force microscopy (DFM), phase imaging, force spectroscopy, lateral force or frictional force microscopy, electrical modes and magnetic force microscopy (MFM)⁴⁸. These advanced modes with specially functionalized cantilevers have revolutionized the scientific community, enabling researchers to study mechanical properties, surface properties, and molecular interactions with remarkable precision. Although AFM has a huge versatility of modes and applications, the most widely used modes by the scientific community are the tapping and contact mode imaging and force spectroscopy measurements. In the following section, we are going to provide some details and the associated mathematical models used for these modes.

2.2.1 AFM Imaging

The accurate measurements of the topological, morphological, and mechanical properties of the samples primarily depend on the precise alignment of a laser beam on the cantilever used to scan the sample surface. A visible near-infrared laser beam is directed on the back of the cantilever, which reflects the laser beam towards a position-sensitive photodetector (PSD), which is capable of detecting very small changes in the position of the cantilever based on any deflection of the laser spot falling on it (see Figure 2.12 a). The PSD consists of a semiconductor material and when the incident laser beam light falls on it, electron-hole pairs are generated, creating a current between the electrodes. This current (measured in the form of potential difference) is used to determine any change in the position and direction of the incoming laser beam, followed by estimating the precise position of the cantilever. Hence, a proper alignment of the laser beam is essential for precise cantilever motion detection. As demonstrated in Figure 2.12 b, any deflection in the cantilever deflects the laser beam and PSD immediately detects this deflection. Note that, a proper calibration (β -calibration) has to be performed to quantitatively establish the relationship between the cantilever deflection and the change in the PSD voltages (nm/mV). All the commercial instruments have their established modules to perform the β -calibration, but one of the most common mistakes made by an experimentalist while working with samples in liquid is that the β -calibration is performed in air, but the β -calibration changes in liquid. There is a feedback controller in the AFM, which monitors the cantilever deflections in real-time and performs the needed positional changes

in the cantilever according to the user's commands. These commands can maintain any one of the following parameters constant: cantilever deflection, force, indentation, and PSD deflection voltage. Now, since we understand the basics of the AFM laser alignment, β -calibration, and feedback controls, we will see their role in imaging samples in contact and tapping mode.

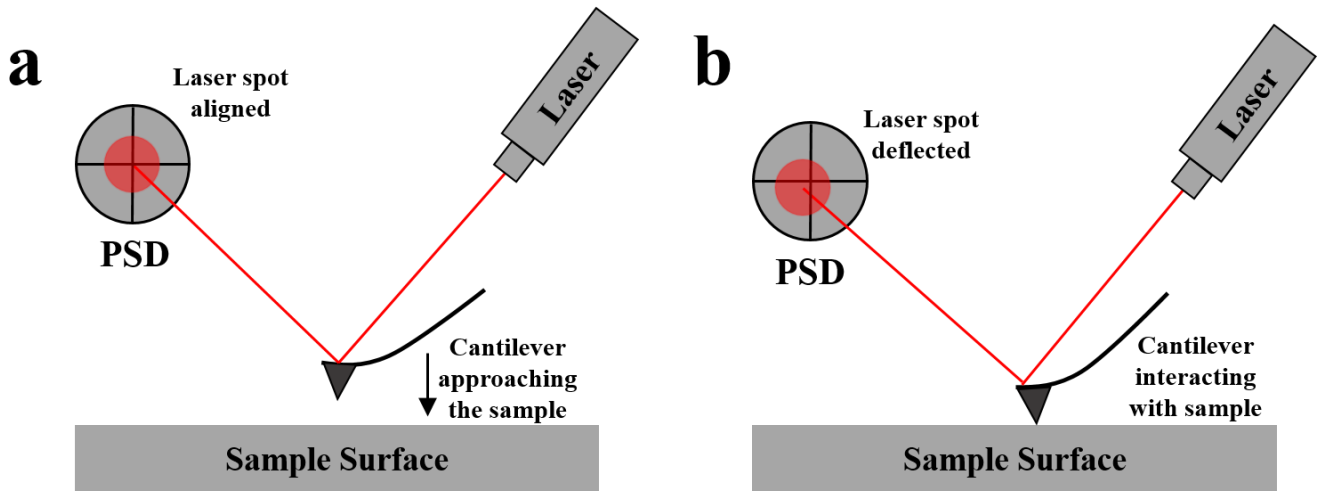


Figure 2.12 Laser cantilever alignment on the PSD: (a) The laser is aligned on the PSD symmetrically as the cantilever approaches the sample surface. (b) The spot gets deflected from the center of the PSD when the cantilever interacts with the sample.

Contact Mode: Although contact mode is the oldest mode of AFM, it is still widely used due to its simplicity. The cantilever tip constantly maintains contact with the sample surface as it scans. The AFM scanner's feedback controller adjusts the height to keep the deflection constant, maintaining a constant interaction force between the sample and the cantilever tip. The tip-sample interaction depends on factors like surface chemistry, adhesion and roughness. Derjaguin Muller and Toporov (DMT) and Hertz models are the most common complex models used to quantify this interaction, but the simple Hookes's law expressed with the following equation describes this interaction force well enough for imaging purposes:

$$F = k * X \quad (2.42)$$

Here, k is the spring constant of the cantilever and x is the deflection. The movement made by the cantilever in the vertical direction, to maintain the constant deflection is recorded to generate the topographical image of the surface. A contact mode image of the surface of a computer DVD is shown in Figure 2.13.

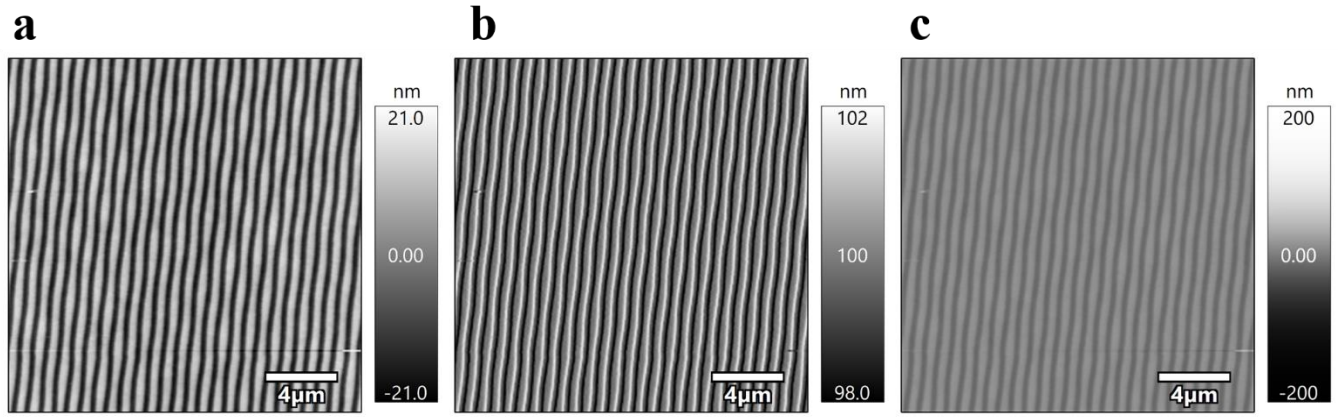


Figure 2.13 Contact mode AFM images of a DVD: The images of the surface of a computer DVD created using the AFM contact mode with the height (a), deflection (b), and the Z sensor (c) signals are shown here.

Tapping Mode: The constant interaction between the sample and the cantilever tip in contact mode imaging often causes lateral force on the sample and it can lead to damaging delicate samples and/or the cantilever tip itself while using samples with huge topological features. Hence, tapping mode imaging is preferred while working with single molecule systems or soft samples, as it offers reduced sample-tip interaction and minimal sample damage. In tapping mode, the cantilever oscillates near its natural resonance frequency, which depends on the material and geometry of the cantilever. The amplitude and the frequency of the cantilever oscillations are affected as it approaches the sample surface. These changes in the cantilever's oscillations are dependent on the sample cantilever interaction forces, which can be measured using the following simple equation, assuming that the AFM cantilever tip is acting like a harmonic oscillator:

$$m \frac{d^2z}{dt^2} + c \frac{dz}{dt} + k(z - z_0) = F_{st} \quad (2.43)$$

Here, m is the effective mass of the cantilever, c is the damping coefficient, k is the spring constant of the cantilever tip, z is the cantilever position, z_0 is the cantilever equilibrium position and F_{st} is the interaction force between the sample and the cantilever tip. So, when the cantilever oscillating near its natural frequency approaches the sample surface the interaction force (F_{st}) changes, causing a change in the cantilever's amplitude or frequency, which is used to devise the information about the sample topography. A tapping mode AFM image of the surface of a computer DVD is shown in Figure 2.14.

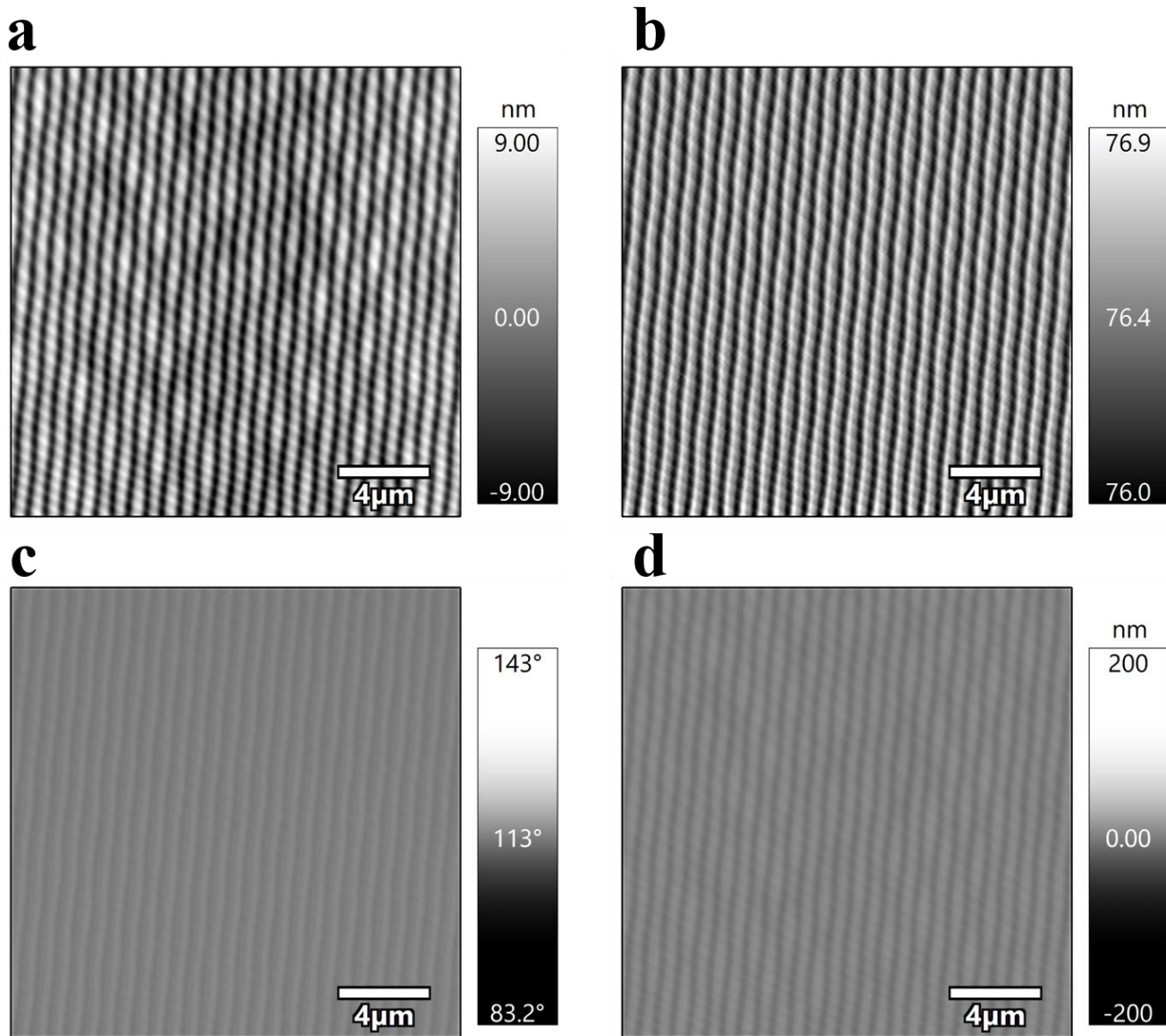


Figure 2.14 Tapping mode AFM images of a DVD: An image of the surface of a computer DVD created using the AFM tapping mode with the height (a), amplitude (b), phase (c), and Z sensor (d) signals are shown here.

2.2.2 AFM Force Spectroscopy Measurements

To estimate the mechanical properties of any material, it has to be probed with an external force and the material responds to the applied external force. The applied force and the response to it by the material are used to estimate various physical mechanical properties of the material. The force spectroscopy mode of AFM is used to probe the sample at the nanoscale by using the cantilever tip. The AFM force spectroscopy measurement is performed in the contact mode and involves interaction between the cantilever tip and the sample (See Figure 2.15 a). The interaction results in the force-distance (f - x) curve shown in Figure 2.15 b. Since we have already assumed that the cantilever is a spring, the most common and simple mathematical model to interpret the f - x curve data is the Hertz model for linear elastic materials. For adhesive interactions, the Derjaguin-Muller-Toporov (DMT) model is considered, whereas for complex contact mechanics, the Johnson-Kendall-Roberts (JKR) model is accounted for. Since the AFM force spectroscopy work in this thesis was used to estimate the elasticity of red blood cells, we are only going to discuss the Hertz model.

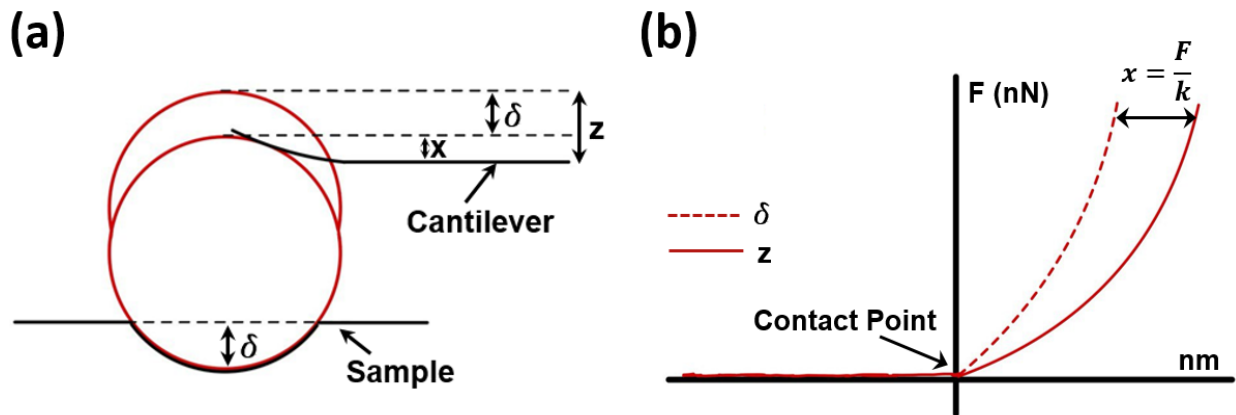


Figure 2.15 Schematic of force spectroscopy measurements using an atomic force microscope: (a) The schematic of a spherical bead attached to a cantilever probing a soft sample is demonstrated here. The cantilever's piezo position (z), deflection in the cantilever (d), and the indentation in the sample (x) are also presented in the schematic. (b) A representative force-distance curve is shown along with the sample-cantilever contact point, the cantilever's piezo position (solid line), and the deflection in the cantilever (dashed line).

The Hertz model stands correct for the following assumptions; (i) The sample is linear elastic material, i.e. it deforms under external force but regains its original shape when the force is removed. (ii) The deformation made by the cantilever is smaller than the characteristic length of the sample. (iii) The cantilever loading is axisymmetric, i.e. the force is applied perpendicular to the sample surface. (iv) The sample is homogeneous, with uniform elasticity throughout. Initially,

there was one more assumption that the cantilever tip should be perfectly spherical and the radius of the spherical cantilever must be smaller than the characteristic length of the sample. Later several extensions and modifications in the hertz model were made based on the shape of the cantilever tip. Most commonly used AFM cantilever tips are sharp conical, but for cellular AFM force spectroscopy measurements customized spherical cantilever tips are recommended to avoid damage to the cellular membrane if sharp tips are used.

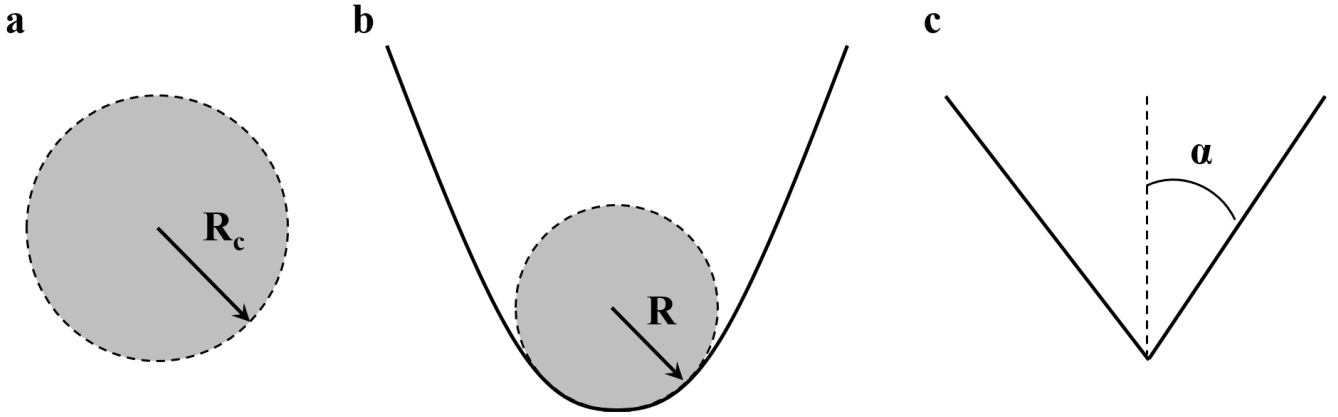


Figure 2.16 Shape of different AFM cantilever tips: (a) A spherical cantilever tip having radius R_c . (b) For very small indentations a spherical cantilever can be assumed to be a parabola-shaped cantilever (c) A sharp conical-shaped cantilever tip having a half angle of α .

If the Poisson's ratio (ν) of the sample is known, then the mathematical expression for the hertz model using a spherical cantilever tip (see Figure 2.16 a) is⁴⁹:

$$F = \frac{E}{1-\nu^2} \left[\frac{a^2+R^2}{2} \ln \left(\frac{R+a}{R-a} \right) - aR \right] \quad \text{where,} \quad \delta = \frac{a}{2} \ln \left(\frac{R+a}{R-a} \right) \quad (2.44)$$

Here, F is the external force applied by the spherical cantilever of radius ' R ' on the sample of elasticity ' E ' causing an indentation ' δ '. Now, if the characteristic length of the sample is larger than the spherical cantilever, then for small indentations the sample sees a very small arc of the spherical cantilever, hence the cantilever can be assumed to be a parabolic cantilever (see Figure 2.16 b). Hence, the expression for the hertz model for a parabolic cantilever is given by⁴⁹:

$$F = \frac{4\sqrt{R_c}}{3} \frac{E}{1-\nu^2} \delta^{\frac{3}{2}} \quad (2.45)$$

Since customizing a spherical bead to a regular cantilever is extremely expensive, most of the research groups use a traditional contact mode sharp conical cantilever (see Figure 2.16 c), and the hertz expression for a conical cantilever tip with a half angle ‘ α ’ is given by⁴⁹:

$$F = \frac{E}{1-\nu^2} \frac{2 \tan(\alpha)}{\pi} \delta^2 \quad (2.46)$$

Note that for all the AFM force spectroscopy work done for this thesis, we have used spherical cantilevers, and since the indentations are very small, we have used the parabolic hertz equation for estimating the elasticity of our samples. We have written a custom MATLAB code to find the contact point in the f-x curve from the experiments and to estimate the cellular elasticity.

2.3 CONCLUSION

In this chapter, we have first discussed the development of the resistive pulse technique and understood its basic working principle. The fabrication of the resistive pulse device and various mathematical models used to understand the resistive pulse signals were discussed in detail. We have also provided thorough information on the custom-written LabVIEW codes for resistive pulse data recording, data analysis, and micropore device characterization. The significance of laser alignment to atomic force microscopy imaging is discussed in this chapter. We have also explained the two most commonly used imaging modes of AFM; contact and tapping mode. The difference in the images taken by both modes is also demonstrated in this chapter. We have then discussed the linear hertz model for the estimation of the elasticity of the sample using AFM force spectroscopy measurements. The content of this chapter has laid down all the details about the experimental techniques used in the subsequent chapter.

2.4 REFERENCES

- (1) Morrison, P. E. A.; Coulter, W. H.; Springs, M. United States Patent 72). **1971**, No. ii.
- (2) Grover, N. B.; Naaman, J.; Ben-Sasson, S.; Doljanski, F.; Nadav, E. Electrical Sizing of Particles in Suspensions: II. Experiments with Rigid Spheres. *Biophys. J.* **1969**, *9* (11), 1415–1425.
- (3) Grover, N. B.; Naaman, J.; Ben-Sasson, S.; Doljanski, F. Electrical Sizing of Particles in Suspensions: III. Rigid Spheroids and Red Blood Cells. *Biophys. J.* **1972**, *12* (9), 1099–1116.
- (4) Grover, N. B.; Naaman, J.; Ben-Sasson, S.; Doljanski, F. Electrical Sizing of Particles in Suspensions: I. Theory. *Biophys. J.* **1969**, *9* (11), 1398–1414.
- (5) DeBlois, R. W.; Bean, C. P. Counting and Sizing of Submicron Particles by the Resistive Pulse Technique. *Rev. Sci. Instrum.* **1970**, *41* (7), 909–916.
- (6) Lan, W. J.; Holden, D. A.; Liu, J.; White, H. S. Pressure-Driven Nanoparticle Transport across Glass Membranes Containing a Conical-Shaped Nanopore. *J. Phys. Chem. C* **2011**, *115* (38), 18445–18452.
- (7) Bell, N. A. W.; Muthukumar, M.; Keyser, U. F. Translocation Frequency of Double-Stranded DNA through a Solid-State Nanopore. *Phys. Rev. E* **2016**, *93* (2), 1–10.
- (8) Wang, X.; Wilkinson, M. D.; Lin, X.; Ren, R.; Willison, K. R.; Ivanov, A. P.; Baum, J.; Edel, J. B. Single-Molecule Nanopore Sensing of Actin Dynamics and Drug Binding. *Chem. Sci.* **2020**, *11* (4), 970–979.
- (9) Steinbock, L. J.; Otto, O.; Chimere, C.; Gornall, J.; Keyser, U. F. Detecting DNA Folding with Nanocapillaries. *Nano Lett.* **2010**, *10* (7), 2493–2497.
- (10) Kowalczyk, S. W.; Hall, A. R.; Dekker, C. Detection of Local Protein Structures along DNA Using Solid-State Nanopores. *Nano Lett.* **2010**, *10* (1), 324–328.
- (11) Nanopores, I. U. Handbook of Single-Molecule Biophysics. *Handb. Single-Molecule Biophys.* **2009**, 265–291.

- (12) Bafna, J. A.; Soni, G. V. Fabrication of Low Noise Borosilicate Glass Nanopores for Single Molecule Sensing. *PLoS One* **2016**, *11*, e0157399.
- (13) Kaushik, S.; Mahadeva, M.; Murugan, K. D.; Sundaramurthy, V.; Soni, G. V. Measurement of Alcohol-Dependent Physiological Changes in Red Blood Cells Using Resistive Pulse Sensing. *ACS Sensors* **2020**, *5* (12), 3892–3901.
- (14) Yusko, E. C.; Johnson, J. M.; Majd, S.; Prangkio, P.; Rollings, R. C.; Li, J.; Yang, J.; Mayer, M. Controlling Protein Translocation through Nanopores with Bio-Inspired Fluid Walls. *Nat. Nanotechnol.* **2011**, *6* (4), 253–260.
- (15) Maheshwaram, S. K.; Sreenivasa, K.; Soni, G. V. Fingerprinting Branches on Supercoiled Plasmid DNA Using Quartz Nanocapillaries. *Nanoscale* **2021**, *13* (1), 320–331.
- (16) Bulushev, R. D.; Marion, S.; Petrova, E.; Davis, S. J.; Maerkl, S. J.; Radenovic, A. Single Molecule Localization and Discrimination of DNA-Protein Complexes by Controlled Translocation Through Nanocapillaries. *Nano Lett.* **2016**, *16* (12), 7882–7890.
- (17) Kaushik, S.; Selvanathan, P.; Soni, G. V. Customized Low-Cost High-Throughput Amplifier for Electro-Fluidic Detection of Cell Volume Changes in Point-of-Care Applications. *PLoS One* **2022**, *17* (4), e0267207.
- (18) Smeets, R. M. M.; Kowalczyk, S. W.; Hall, A. R.; Dekker, N. H.; Dekker, C. Translocation of RecA-Coated Double-Stranded DNA through Solid-State Nanopores. *Nano Lett.* **2009**, *9* (9), 3089–3095.
- (19) Storm, A. J.; Chen, J. H.; Zandbergen, H. W.; Dekker, C. Translocation of Double-Strand DNA through a Silicon Oxide Nanopore. *Phys. Rev. E* **2005**, *71* (5), 051903.
- (20) Bulushev, R. D.; Marion, S.; Radenovic, A. Relevance of the Drag Force during Controlled Translocation of a DNA-Protein Complex through a Glass Nanocapillary. *Nano Lett.* **2015**, *15* (10), 7118–7125.
- (21) Soni, G. V.; Dekker, C. Detection of Nucleosomal Substructures Using Solid-State Nanopores. *Nano Lett.* **2012**, *12* (6), 3180–3186.
- (22) Soni, G. V.; Singer, A.; Yu, Z.; Sun, Y.; McNally, B.; Meller, A. Synchronous Optical and

- Electrical Detection of Biomolecules Traversing through Solid-State Nanopores. *Rev. Sci. Instrum.* **2010**, *81* (1).
- (23) Krueger, E.; Shim, J.; Fathizadeh, A.; Chang, A. N.; Subei, B.; Yocham, K. M.; Davis, P. H.; Graugnard, E.; Khalili-Araghi, F.; Bashir, R.; Estrada, D.; Fologea, D. Modeling and Analysis of Intercalant Effects on Circular DNA Conformation. *ACS Nano* **2016**, *10* (9), 8910–8917.
- (24) Tabard-Cossa, V.; Trivedi, D.; Wiggin, M.; Jetha, N. N.; Marziali, A. Noise Analysis and Reduction in Solid-State Nanopores. *Nanotechnology* **2007**, *18* (30).
- (25) Steinbock, L. J.; Bulushev, R. D.; Krishnan, S.; Raillon, C.; Radenovic, A. DNA Translocation through Low-Noise Glass Nanopores. *ACS Nano* **2013**, *7* (12), 11255–11262.
- (26) Yusko, E. C.; Prangko, P.; Sept, D.; Rollings, R. C.; Li, J.; Mayer, M. Single-Particle Characterization of A β Oligomers in Solution. *ACS Nano* **2012**, *6* (7), 5909–5919.
- (27) Steinbock, L. J.; Krishnan, S.; Bulushev, R. D.; Borgeaud, S.; Blokesch, M.; Feletti, L.; Radenovic, A. Probing the Size of Proteins with Glass Nanopores. *Nanoscale* **2014**, *6* (23), 14380–14387.
- (28) Fakhri, N.; Wessel, A. D.; Willms, C.; Pasquali, M.; Klopfenstein, D. R.; MacKintosh, F. C.; Schmidt, C. F. High-Resolution Mapping of Intracellular Fluctuations Using Carbon Nanotubes. *Science* (80-.). **2014**, *344* (6187).
- (29) Liu, L.; Yang, C.; Zhao, K.; Li, J.; Wu, H. C. Ultrashort Single-Walled Carbon Nanotubes in a Lipid Bilayer as a New Nanopore Sensor. *Nat. Commun.* **2013**, *4*, 2989.
- (30) Heerema, S. J.; Dekker, C. Graphene Nanodevices for DNA Sequencing. *Nature Nanotechnology*. Nature Publishing Group February 1, 2016, pp 127–136.
- (31) Schneider, G. F.; Kowalczyk, S. W.; Calado, V. E.; Pandraud, G.; Zandbergen, H. W.; Vandersypen, L. M. K.; Dekker, C. DNA Translocation through Graphene Nanopores. *Nano Lett.* **2010**, *10* (8), 3163–3167.
- (32) Li, W.; Bell, N. A. W.; Hernández-Ainsa, S.; Thacker, V. V.; Thackray, A. M.; Bujdoso,

- R.; Keyser, U. F. Single Protein Molecule Detection by Glass Nanopores. *ACS Nano* **2013**, 7 (5), 4129–4134.
- (33) Bafna, J. A.; Soni, G. V. Fabrication of Low Noise Borosilicate Glass Nanopores for Single Molecule Sensing. *PLoS One* **2016**, 11 (6), e0157399.
- (34) Steinbock, L. J.; Steinbock, J. F.; Radenovic, A. Controllable Shrinking and Shaping of Glass Nanocapillaries under Electron Irradiation. *Nano Lett.* **2013**, 13 (4), 1717–1723.
- (35) Steinbock, L. J.; Bulushev, R. D.; Krishnan, S.; Raillon, C.; Radenovic, A. DNA Translocation through Low-Noise Glass Nanopores. *ACS Nano* **2013**, 7 (12), 11255–11262.
- (36) Arkhangelsky, E.; Sefi, Y.; Hajaj, B.; Rothenberg, G.; Gitis, V. Kinetics and Mechanism of Plasmid DNA Penetration through Nanopores. *J. Memb. Sci.* **2011**, 371 (1–2), 45–51.
- (37) Shimada, T.; Fujino, K.; Yasui, T.; Kaji, N.; Ueda, Y.; Fujii, K.; Yukawa, H.; Baba, Y. Resistive Pulse Sensing on a Capillary-Assisted Microfluidic Platform for On-Site Single-Particle Analyses. **2023**.
- (38) Xu, R.; Ouyang, L.; Shaik, R.; Zhang, G.; Zhe, J. Multiplexed Resistive Pulse Sensor Based on Geometry Modulation for High-Throughput Microparticle Counting. *Sensors and Actuators Reports* **2023**, 5 (November 2022), 100140.
- (39) Liu, Q.; Wu, H.; Wu, L.; Xie, X.; Kong, J.; Ye, X.; Liu, L. Voltage-Driven Translocation of DNA through a High Throughput Conical Solid-State Nanopore. *PLoS One* **2012**, 7 (9).
- (40) Reinhart, W. H.; Chien, S. Roles of Cell Geometry and Cellular Viscosity in Red Cell Passage through Narrow Pores. *Am. J. Physiol. - Cell Physiol.* **1985**, 17 (3).
- (41) Coulter, W. H. Means for Counting Particles Suspended in a Fluid. US Patent, 2656508, 1953.
- (42) Maxwell, J. C. *A Treatise on Electricity & Magnetism (Volume 1)*, 3rd ed.; Dover Publications, 1954.
- (43) James, W. B.; Harbor, C. S. The Maxwell-Wagner Dispersion in a Suspension of Ellipsoids. **1953**, 57, 934–937.

- (44) Fricke, H. A MATHEMATICAL TREATMENT OF THE ELECTRIC CONDUCTIVITY AND CAPACITY OF DISPERSE SYSTEMS. *Phys. Rev.* **1924**, 24, 575.
- (45) Velick, B. Y. S.; Gorin, M. The Electrical Conductance of Suspensions of Ellipsoids and Its Relation to the Study of Avian Erythrocytes. *J. Gen. Physiol.* **1940**, 23, 753.
- (46) Hall, J. E. Access Resistance of a Small Circular Pore. *J. Gen. Physiol.* **1975**, 66 (4), 531–532.
- (47) Sushmasusik, M. S. History of Microscopes. **2015**, 3 (3).
- (48) Giessibl, F. J. Advances in Atomic Force Microscopy. **2003**, 75 (July).
- (49) Lin, D. C. Robust Strategies for Automated AFM Force Curve Analysis — I. Non-Adhesive Indentation of Soft ., **2007**, 129 (May).

CHAPTER 3

Measurement of alcohol-dependent physiological changes in red blood cells using resistive pulse sensing

ABSTRACT

Alcohol exposure has been postulated to adversely affect the physiology and function of the red blood cells (RBCs). The global pervasiveness of alcohol abuse, causing health issues and social problems, makes it imperative to resolve the physiological effects of alcohol on RBC physiology. Alcohol consumed recreationally or otherwise, almost immediately alters cell physiology in ways that is subtle and still unresolved. In this paper, we introduce a high-resolution device for quantitative electro-fluidic measurement of changes in RBC cell volume upon alcohol exposure. We present an exhaustive calibration of our device using model cells to measure and resolve volume changes down to 0.6 fL. We find RBCs shrinkage of 5.3% at 0.125% ethanol (legal limit in USA) and a shrinkage of 18.5% at 0.5 % ethanol (lethal limit) exposure. Further, we also measure the time dependence of cell volume shrinkage (upon alcohol exposure) and then recovery (upon alcohol removal) to quantify shrinkage and recovery of RBC volumes. This work presents the first direct quantification of temporal and concentration-dependent changes in red blood cell volume upon ethanol exposure. Our device presents a universally applicable high-resolution & high-throughput platform to measure changes in cell physiology under native and diseased conditions.

3.1 INTRODUCTION

Morphological changes or responses of red blood cells (RBCs) are powerful markers for a variety of diseases and haematological disorders¹⁻³. Given the global reach of alcoholism, there have been major efforts in understanding responses of RBCs upon exposure to alcohol¹⁻⁸. Changes intrinsic to the blood cells have been studied extensively and the role of alcohol in the suppression of blood cell precursors (pancytopenia) in the bone marrow, formation of fluid-filled cavities (vacuoles)⁸ or iron deposits in them and their role in elevating the risk of liver cancer is documented. Investigation of alterations in RBCs caused by alcohol exposure is widely investigated by methods like electron paramagnetic resonance spectroscopy^{1,9,10}, fluorescence anisotropy¹¹⁻¹⁵, gas chromatography¹⁶, laser diffraction ektacytometry^{1,6}, micro-size mesh filtration⁵, electrical impedance cytometry¹⁷ and flow cytometry in-vitro and in-vivo^{7,18-23}. These studies extensively addressed qualitative morphological, biochemical, rheological or mechanical alterations in alcohol introduced RBCs. However, the morphological changes studied by these methods were reported for too high alcohol concentrations or too long incubation times, which are beyond physiological levels. Non-physiological levels of ethanol were introduced to RBCs because detecting small changes with these conventional techniques for physiological conditions is challenging and has resulted in reports showing increase²⁴⁻²⁷, decrease^{2,7} or no change^{4,28} in RBC size in the presence of alcohol. The most recent study addressing the cell-volume changes using Common-path diffraction optical tomography reported measurements of 3D refractive index tomograms and membrane dynamic fluctuations to simultaneously study morphological, biochemical and biomechanical properties of RBCs subjected to physiologically relevant ethanol concentrations (0.0 to 0.5% v/v)⁴. Although this study showed changes in the mean surface area and sphericities of RBCs, they were unable to report on quantitative volumetric changes in RBCs exposed to different ethanol concentrations. Although they also do not deny the possibility of any such volumetric changes demonstrating sensitivity limitation and low throughput of the method.

In this work, we show, for the first time, high resolution quantitative measurement of changes in cell volume of red blood cells (RBCs) after ethanol exposure in the physiological range. We confirm these changes in cell volume by monitoring its recovery after the removal of ethanol from the RBC solution. We also measure the shrinkage and recovery time constants of RBC for different exposure times and concentrations. We achieve this by developing a custom-made high-throughput electro-fluidic platform that uses resistive pulse technique for accurate electrical read-

out of changes in cell volumes as they single-file translocate through a micropore. This is a single-cell measurement which can sample hundreds and thousands of cells in a few minutes. Resistive pulse sensing is a technique widely used to count and measure the size of particles^{29,30,39-48,31,49-52,32-38}. We show a complete calibration of our high-resolution high-throughput resistive pulse technique (RPT) based micropore device for volume measurements. We used model cells (microbeads in the size range of typical biological cells) to test the principle and resolution limits of our device. After demonstrating this, we further apply this platform to measure quantitative volumetric changes in RBCs when introduced to physiologically relevant ethanol concentrations (0.0 to 0.5% v/v). We observed a decrease in the RBCs volume on introducing ethanol and a further decrease if incubated for longer in ethanol. This study also reports the time constants for the shrinkage and recovery of RBCs from shock due to ethanol addition and removal respectively.

3.2 MATERIAL AND METHODS

3.2.1 Fabrication of Electrofluidic Devices

Borosilicate glass capillaries (OD= 1 mm, ID= 0.75 mm, length= 150 mm) (Sutter Instrument) were used to fabricate micropores. Glass capillaries were cleaned by ultrasonication in ethanol, acetone and then ethanol again for 5 min each. Clean glass capillaries were pulled using a micropipette puller (Model P – 2000, Sutter Instrument), using the following parameters: Heat: 300, Filament: 0, Velocity: 15, Delay: 128, Pull: 250. These pulled capillaries were cut and shrunk to the desired micropore size using a flame polisher instrument (MF – 900, Micro Forge, Narshige). The micropore was then mounted in a glass-bottom Teflon fluid chamber (~100 μ L) using curable silicone glue as shown in Figure 3.1a. The micropore end of the capillary was within the Teflon chamber and the other end was connected to a syringe pump (Picoplus Elite, Harvard Apparatus), using PTFE tubing, to generate flow. Micropore diameters are estimated by measuring the smallest opening in the optical image of the pore cross-section, see Figure 3.1a (inset). Images of all the micropores used in this study are listed in Appendix Figure A5.5 and A5.6.

3.2.2 Sample Preparation

For model cells, polystyrene beads, of varying diameters, 1.0, 1.9, 2.0, 2.1, 2.8, 3.0, 4.0, 4.3, 4.98, 6.0, 7.03 and 8.0 μ m (Sigma and microParticles GmbH) were used. After washing beads in ultrapure (Milli-Q, Millipore) water, beads were suspended in 1X Phosphate-buffered saline, PBS (137 mM NaCl, 2.7 mM KCl, 4.3 mM Na₂HPO₄, 1.47 mM KH₂PO₄ at pH 7.4) to dilute the stock concentration to about 1.3×10^5 to 8.3×10^7 particles/ml. Beads were used in translocation experiments with no further processing. Red Blood Cells (RBCs) were obtained from human volunteers following the institutional human ethics committee approval from National Centre for Biological Sciences. For RBC experiments, 20 μ L of the whole blood sample from the donor was diluted by adding 500 μ L of RPMI-1640 (RPMI buffer, Sigma #SLBT0197) (pH=7.4). RPMI buffer is used here to keep the RBCs healthy for long duration^{53,54} and the salt content of the buffer⁵⁵ makes it an excellent electrolyte for translocation measurements. RBCs were then isolated from blood plasma and other cells by centrifuging three times at 600 rcf for 3 min at 4°C and resuspending RBC pellets in RPMI buffer. After the isolation step, RBCs were diluted 50-100 times for further experiments. For every experiment, isolated RBCs were checked for health and debris under an

optical microscope. For time-dependent experiments, the RBCs were stored at 4°C between measurements. For RBC volume measurements in the presence of ethanol, cells were incubated in RPMI buffer containing ethanol of different volume fractions for specific times (see text). To test the recovery of RBC volume, cells were resuspended in ethanol free RPMI buffer.

3.2.3 Electrofluidic Measurements

PBS or RPMI buffer was used as the electrolyte for ionic current measurements through the micropore. All experiments with model cells (beads) were done in PBS buffer. All RBC measurements were done in RPMI buffer. The glass bottom fluid chamber, microcapillary, and microfluidic PTFE tubing were filled with buffer. The current signals were acquired using Ag/AgCl electrodes, one dipped into the buffer in the fluid chamber and the other inserted into the tubing. The entire flow cell assembly was mounted on an optical microscope inside a Faraday cage to reduce electrical noise. For all measurements, the sample was pulled into the micropore by a syringe pump at a constant withdrawal rate of 0.5 $\mu\text{l}/\text{min}$. A Chem-Clamp low noise amplifier (Dagan Corp.) with 10 kHz bandwidth was used to apply a voltage (see text) across the micropore and record the open pore current and translocation events. Each measurement dataset contains 500-3000 events. $N \geq 3$ datasets would mean each sample is measured at least 3 times to get the mean ΔG and standard deviation of mean. The line frequencies in the signal were eliminated using Hum-Bug noise eliminator (Quesst Scientific). The signals were acquired and stored using a data acquisition card (National Instruments, NI myDAQ) and a custom-written LabVIEW code. Events are isolated in real-time from the continuous measurement of pore current (baseline) whenever current event crosses the threshold-1 (set at 4.5 times standard deviation of the baseline current) for at least 0.01 ms duration (see Fig 1e). For every, isolated event, the start (t_{start}) and end (t_{end}) of the event are then determined as the time points where the event signal crosses threshold-2 (0.5 times standard deviation of the baseline current). For every event, ΔG is then calculated as the maximum conductance drop (between t_{start} and t_{end}) from the baseline and Δt is calculated as the time between t_{start} and t_{end} ⁵⁶⁻⁶².

3.3 RESULTS AND DISCUSSION

3.3.1 Principle of Electro-fluidic Measurements

Our devices work on the resistive pulse technique. Under an applied potential across the micropore, the buffer ions flow through the pore (open pore conductance) and are displaced (current blockades) whenever a particle flows through it. This results in characteristic electrical pulses for every particle translocating through the pore. The devices were first electrically characterized by recording I-V curves. Linear I-V characteristics of the devices were measured for all micropore diameters as shown in Figure 3.1b. The pore conductance (G , nS) increases with pore diameter (see Figure 3.1b inset) as well as the electrolyte conductivity (see Appendix Figure A5.1), as expected. We find that a simple cylindrical geometry describes all the salient features of our measurements. We model open pore conductance of our pores by⁵¹

$$G = \sigma \frac{\pi D_P^2}{4 L_{Cond}} \quad (3.1)$$

where, σ is electrolyte conductivity, D_P is the micropore diameter and L_{Cond} is the length (conductance length) across which the entire pore resistance drops. From the linear fit to the equation (3.1) shown in Figure 3.1b (inset) we find,

$$L_{Cond} = (3.6 \pm 0.11) \times D_P \quad (3.2)$$

This would mean, for example, a typical micropore of $D_P = 6 \mu\text{m}$ will have its $L_{Cond} = 21.6 \mu\text{m}$. This matches reasonably well with the visual observation of micropore images. After confirming stable open pore signal at the applied voltage (Figure 3.1c), samples were added to the fluid chamber and pulled into the micropore by maintaining constant flow using a syringe pump. Sample (beads/cells) translocating through the micropore were detected in the form of current pulses corresponding to individual particles passing through the pore. In Figure 3.1d we show a typical time trace of recorded electrical events for

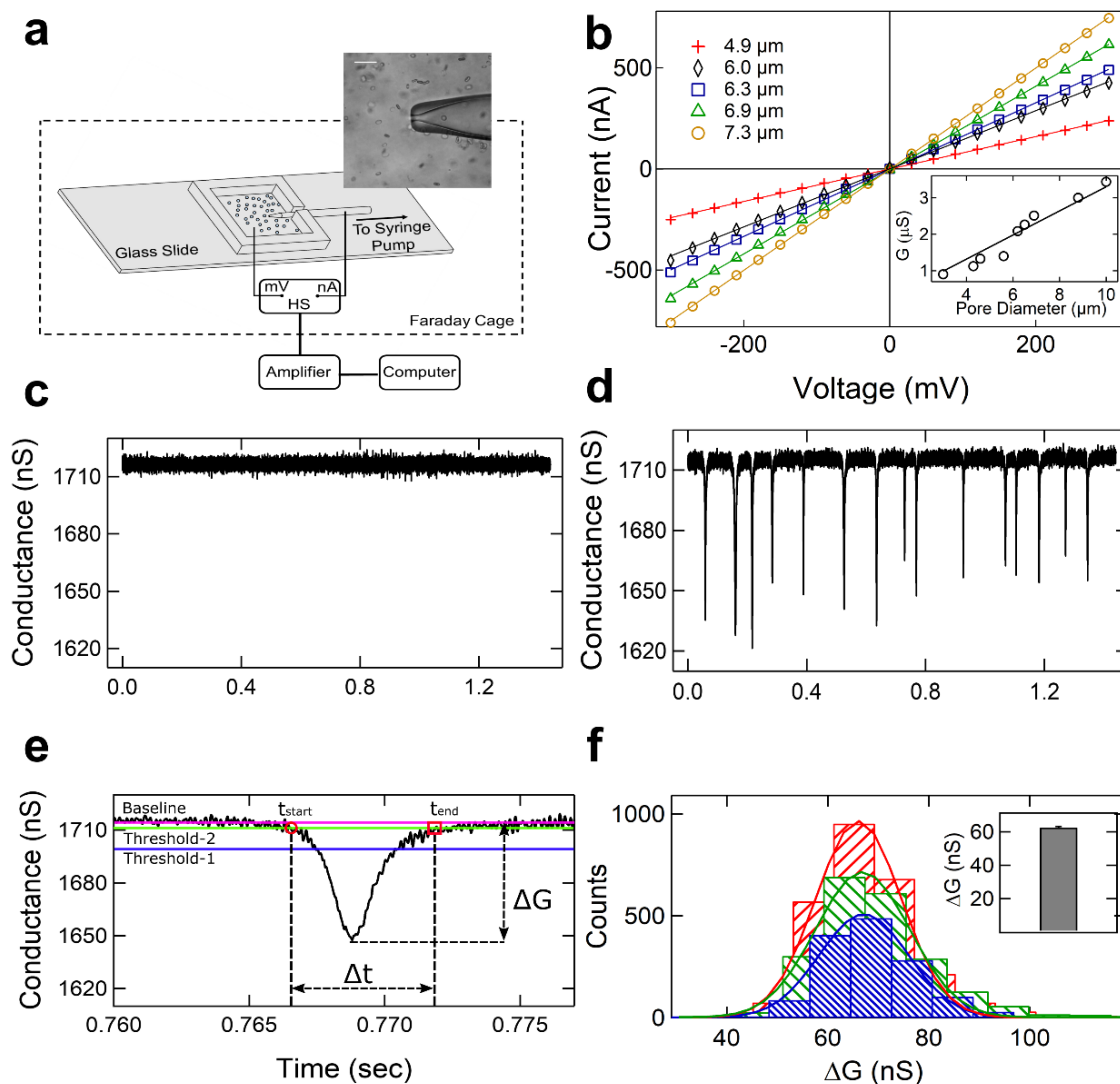


Figure 3.1 Detection principle. **a** Schematic of the experimental setup. A micropore is mounted in the fluid chamber with buffer and sample. The sample is translocated through the micropore using a syringe pump. Translocation events are recorded by the amplifier (HS: Amplifier Head Stage). The inset is the optical microscope image of an $8.3 \mu\text{m}$ micropore with red blood cells as sample (Scalebar is $30 \mu\text{m}$). **b** I-V characteristics of micropores of different pore diameters (Plus: $4.9 \mu\text{m}$, Diamond: $6.0 \mu\text{m}$, Square: $6.3 \mu\text{m}$, Triangle: $6.9 \mu\text{m}$ & Circle: $7.3 \mu\text{m}$) as measured in $1X$ PBS buffer. The resistance values measured are 1.25 , 0.70 , 0.61 , 0.48 and $0.40 \text{ M}\Omega$ respectively. Inset shows the open pore conductance measured as function of micropore diameter (see Results). **c-e** shows current traces of the micropore as a function of time (seconds) before **(c)** any sample is added and events seen after **(d)** the sample is added. **e** shows the zoom of one representative translocation event, where Threshold-1 (Blue) and threshold-2 (Green) are used to identify the start and end of the event (see methods and materials). Here translocation time (Δt) is the time between t_{start} and t_{end} and (ΔG) is the maximum conductance drop from the baseline (Pink). **f** shows ΔG histograms from three independent measurements of RBC cells translocating through the $8.3 \mu\text{m}$ pore. The inset shows the mean of the three measurements in the form of a bar graph where the error bar is the standard deviation of the mean values.

individual red blood cells translocating through a 8.3 μm micropore device. Under our experimental conditions, we routinely detect ~ 1300 RBCs/ μl . The Figure 3.1e shows a zoom of one of the representative events. We note that, under our experimental conditions we find both, the spherical beads as well as discotic RBCs, produce symmetric electrical events when the sample translocates through the micropore. Linear IV curves and symmetric nature of the translocation events confirm that the internal geometrical asymmetry of the pore (if any) does not play a role in our measurement conditions. For every translocation event, the translocation time and the current drop were measured. We characterized each event with two parameters: conductance drop (ΔG , nS) and its characteristic event translocation time (Δt , ms) (see Fig 1e). Here the conductance drop (ΔG) represents the blockage of micropore current caused by the presence of a particle in the pore and the translocation time represents the time it takes to translocate through the sensing region of the micropore. For every sample, typically 500-3000 translocation events were recorded and analysed (see Appendix Figure A5a). To show the reproducibility of our measurements, the Figure 3.1f shows ΔG histograms of three independent measurements of RBCs translocating through the 8.3 μm micropore with the variation in the mean value shown in the inset. The ΔG histograms are fitted with Gaussian distribution to find mean values^{39,42,63,64}. These histogram fits are used to compare mean conductance drop values between multiple samples.

We next compare electrical events of different sized beads translocating through the same pore. In Figure 3.2a (inset) we show representative events for beads of 3.0, 4.0, 4.3, 6.0 and 8.0 μm diameter translocating through a 10.0 μm micropore device. Figure 3.2a shows the mean values of ΔG histograms ($N \geq 3$ data sets) measured for different bead sizes. We observed that the conductance drop in the micropore device is dependent on the size of the translocating sample. To confirm this, we also measured ΔG for a sample when translocating through micropores of different sizes. Appendix Figure A5.2a shows representative events of 3.0 μm beads translocating through micropores of diameter: 10.0, 8.8, 6.9, 5.6, 4.6 and 4.3 μm and Figure A5.2b shows ΔG values for the same conditions. All error bars in ΔG values are the standard deviation of means obtained from Gaussian fits of multiple datasets. Figure 3.2a and Figure A5.2 showed that the detection signal depends on the relative sizes of the translocating particle and the micropore. The amplitude of the pulse (event) corresponds to the number of ions displaced by the excluded

volume of the particle. This allows us to not only detect particles in our sample solution as electrical events but also estimate the volumes of individual particles from their ΔG values. The fit in Figure 3.2a supports our model that the measured ΔG values depend on particle volume²⁹. We also note that the signal to noise ratio (S/N) for detected events depend on the ratio of sample diameter and the micropore diameter. Closer the particle diameter to the micropore diameter, larger is the effect of excluded volume on the conductance drop (ΔG). We further use this platform to detect particles/cells of different sizes. In our experiments, we could not see any systematic trends in the translocation times of the particles of different sizes across a micropore device (see Appendix Figure A5.3b). This is because our translocation time estimates from Δt histograms have large variability, possibly due to off-center trajectories of particle through the pore, particle-wall interactions, syringe pump stability, and the role of pressure changes near the pore mouth in the presence of particles which are significant fraction of the pore size³². To understand the time dynamics of particle translocation further investigations are ongoing in our laboratory.

3.3.2 Signal Contrast and Resolution of the Micropore Device

To measure signal-to-noise of our device, we compared ΔG values for $4.0 \pm 0.1 \mu\text{m}$ beads with $4.30 \pm 0.13 \mu\text{m}$ beads translocating across micropores of different sizes. In Figure 3.2b we show the signal contrast when measured with devices with different pore sizes and show that signal contrast increases as the micropore diameter used are closer to the model cells being measured. Inset of Figure 3.2b shows ΔG histogram measured for the two bead sizes through a $6.5 \mu\text{m}$ micropore showing ΔG values of $120 \pm 20 \text{ nS}$ and $170 \pm 20 \text{ nS}$ for 4.0 and $4.3 \mu\text{m}$ beads respectively.

To demonstrate a limiting case of signal resolution, we show in Figure 3.2c, the ΔG measurements of 39 ± 2 , 47 ± 2 and $58 \pm 3 \text{ nS}$ respectively for beads of diameters 1.90 ± 0.04 , 2.00 ± 0.04 and 2.1 ± 0.3

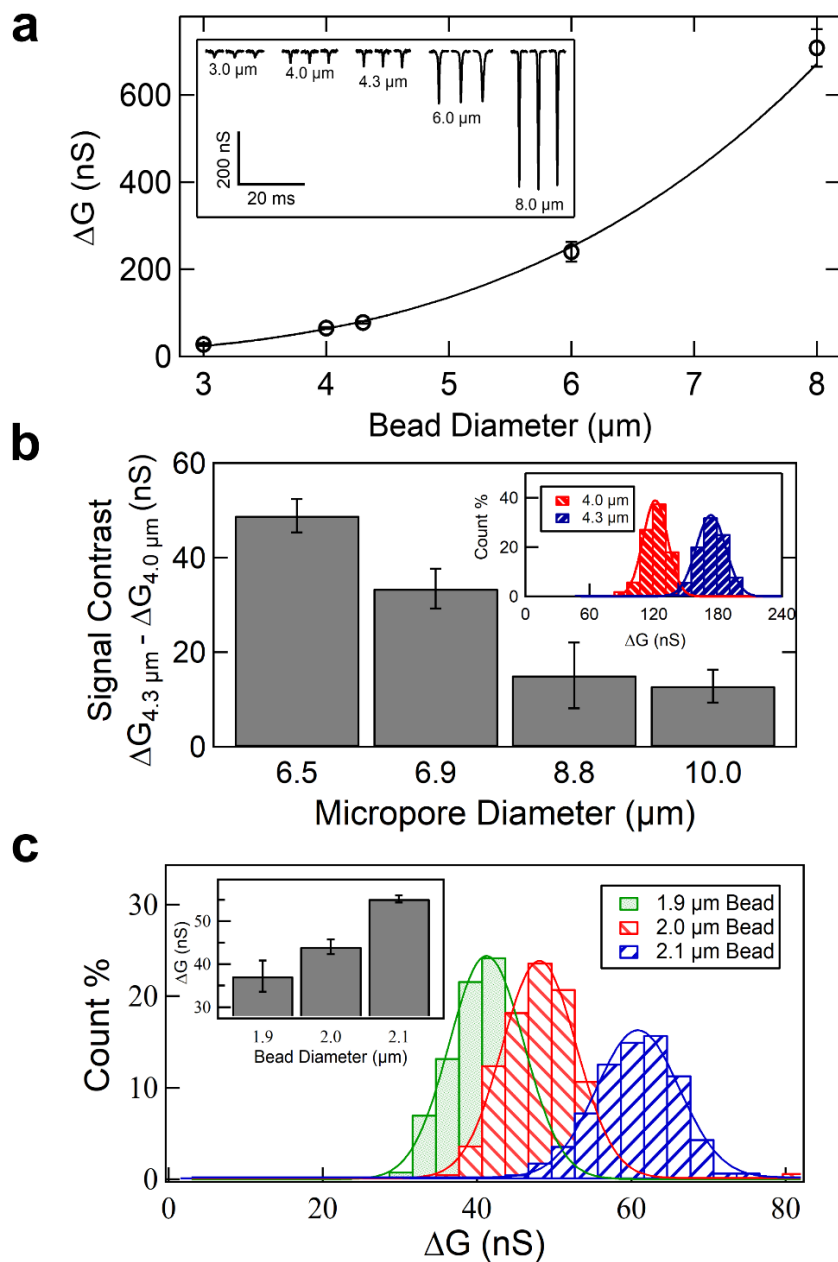


Figure 3.2 Proof of concept, signal contrast and resolution of micropore device. *a* ΔG values measured for different bead diameters ($N \geq 3$ datasets for each bead diameter) translocating through a $10.0 \mu\text{m}$ micropore device. The solid line is a power function with exponent fit of 3.4. Inset shows representative electrical events for beads of diameter $3.0 \mu\text{m}$, $4.0 \mu\text{m}$, $4.3 \mu\text{m}$, $6.0 \mu\text{m}$ and $8.0 \mu\text{m}$ translocating through a $10.0 \mu\text{m}$ micropore device under a constant flow rate of $0.5 \mu\text{l}/\text{min}$. *b* Bar plot shows the signal contrast in ΔG for beads differing in diameters by 300 nm ($4.3 \mu\text{m}$ and $4.0 \mu\text{m}$), translocating through $6.5 \mu\text{m}$, $6.9 \mu\text{m}$, $8.8 \mu\text{m}$ and $10.0 \mu\text{m}$ micropore devices. The inset shows ΔG histogram with Gaussian fits for beads with diameter $4.3 \mu\text{m}$ and $4.0 \mu\text{m}$ translocating through a $6.5 \mu\text{m}$ micropore device. *c* ΔG histogram shows the change in the signal for the beads with diameters $1.9 \mu\text{m}$, $2.0 \mu\text{m}$ and $2.1 \mu\text{m}$. Solid lines are Gaussian fits to the histograms. Inset is bar plot of ΔG signal for three beads with diameters $1.9 \mu\text{m}$, $2.0 \mu\text{m}$ and $2.1 \mu\text{m}$ translocating through a $3.0 \mu\text{m}$ micropore device ($N \geq 3$ datasets for each bead).

μm translocating through a $3.0 \mu\text{m}$ micropore. Average of multiple measurements of these beads are shown in the inset. Here we successfully show, for the first time, contrast between particles which differ by 100 nm in diameter or 0.6 fL in volume in particles of cellular length scales.

We also used our electro-fluidic platform to resolve individual populations in a mixed sample. Beads of three different diameters, 2.0 , 3.0 and $4.0 \mu\text{m}$, were mixed in known number ratio and measured with a $6.5 \mu\text{m}$ micropore device. We were able to successfully find signatures of three distinct size clusters from our micropore analysis where the measured cluster size number matched quantitatively with the number ratio of the mixed sample (see Appendix Figure A5.4 and Table A5.1).

3.3.3 Volume Quantification of Model Cells

We have shown that the change in the micropore conductance depends on the relative size of the translocating particle and the micropore. Here we show that the conductance drop caused by particle translocation is dependent on the volume excluded (V_{excl}) by the particle of diameter (D_{Bead}) inside a micropore of diameter (D_{Pore}) with geometric sensing length (effective length, L_{eff}). Note that the L_{eff} takes into account the internal pore geometry and particle size/shape. We calculate the volume of the same batch of sample particles by three different methods. In the first method, we estimate the L_{eff} for a typical $8.8 \mu\text{m}$ diameter micropore by measuring the ΔG values for different calibration beads (see Figure 3.3a, crosses). For particle sizes smaller than the pore length, we use

$$\Delta G = \sigma \frac{V_{\text{excl}}}{L_{\text{eff}}^2} \quad (3.3)$$

to estimate excluded volume from the measured ΔG values³⁷. According to equation (3.3), a linear fit to the data gave $L_{\text{eff}}^{8.8 \mu\text{m}} = 25.5 \pm 0.6 \mu\text{m}$. From this effective length we estimated the bead volumes by measuring ΔG values for two test beads of diameters $4.3 \mu\text{m}$ and $6.0 \mu\text{m}$ in the same pore (Figure 3.3a, circles) and compared it to the manufacturer's data (Figure 3.3a, dotted lines and Table 3.1. In the second

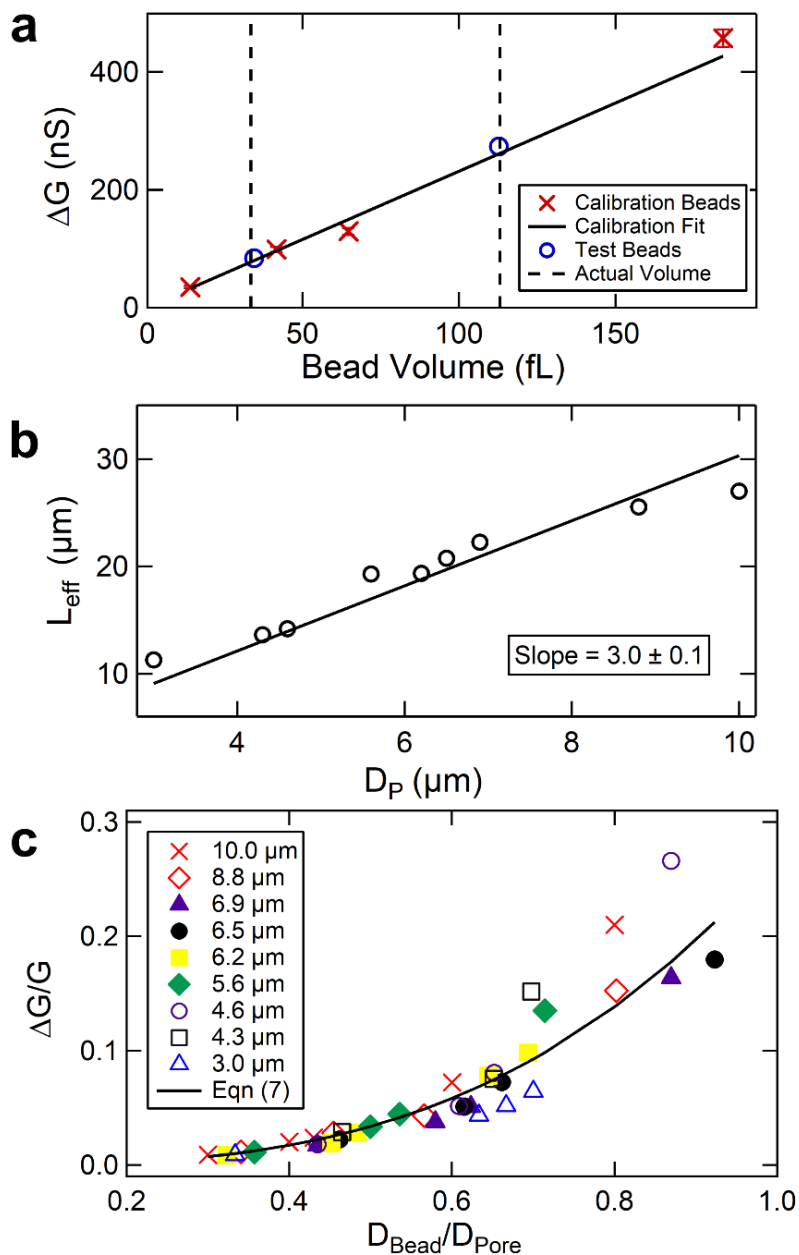


Figure 3.3 Volume quantification of model cells. *a* Conductance drops (ΔG) for calibration beads (model cells) (crosses) are plotted against bead volumes. The solid line is the fit to equation (3.3) giving L_{eff} for the 8.8 μm device to be $25.5 \pm 0.6 \mu\text{m}$. The volumes of unknown (test beads) model cells as estimated from their ΔG values are plotted (circles). True volumes of test beads (dotted line), as estimated from manufacturer data, are also plotted. *b* Effective length vs micropore diameter for different devices is plotted here to establish a global relationship between D_p and L_{eff} . *c* Normalized signal $\Delta G/G$ vs ratio of bead diameter and micropore diameter is plotted. Solid line is the plot of equation (3.7), not a fit.

method, we measured L_{eff} for all our micropore devices (see Appendix Table A5.3) and found that, globally, L_{eff} depends linearly on the pore diameter (see Figure 3.3b). The linear fit in Figure 3.3b was found to be:

$$L_{eff}^{Global} = (3.0 \pm 0.1) \times D_p \quad (3.4)$$

Now, the volumes of test beads were calculated by using both estimates of L_{eff} ($L_{eff}^{8.8 \mu m}$ and L_{eff}^{Global}) for 8.8 μm micropore and found them to be in excellent agreement with each other as well as the value from manufacturer's data (Table 3.1). Note that, the parameters quantifying the L_{eff} will change depending on individual lab's micropore fabrication conditions. However, when following a reproducible recipe for micropore fabrication, L_{eff}^{Global} can be used. Table 3.1 (column 4 & 5) compares the volume measurements using the above two methods. In the third method, we note that equation (3.3) predicts ΔG to be directly proportional to the excluded volume. If a calibrated sample of known volume (V_{excl_1}) is measured through the same micropore, the excluded volume of the unknown sample (V_{excl_2}) can be directly measured using the following equation:

$$V_{excl_2} = \frac{\Delta G_2}{\Delta G_1} * V_{excl_1} \quad (3.5)$$

This direct method was used to estimate the bead volumes and the results are in excellent agreement to the previous methods (see Column 6 & 7 in Table 3.1 and Appendix Table A5.2). We note that this method also takes into account particle shape (spherical or non-spherical) and pore geometry as long as the calibration sample and the unknown sample are of same shape and are measured through the same pore.

To check the universality of our model, all of our measured translocation data, across multiple micropore devices and multiple particle diameters were modelled simultaneously using equations (3.1) and (3.3) (see Appendix Table A5.3 and A5.4) giving the expression for $\Delta G/G$ to be:

$$\frac{\Delta G}{G} = \frac{4}{\pi} \cdot \frac{L_{Cond}}{L_{eff}^2 D_p^2} \cdot V_{excl} \quad (3.6)$$

On substituting equation (3.3), (3.4) and using $V_{exc} = \frac{4}{3}\pi \left(\frac{D_{Bead}}{2}\right)^3$ we get:

$$\frac{\Delta G}{G} = (0.27 \pm 0.01) \times \left(\frac{D_{Bead}}{D_{Pore}} \right)^3 \quad (3.7)$$

This is a parameter-free equation. In Figure 3.3c we plot the normalized conductance drop values ($\Delta G/G$) against the ratio of bead diameter to micropore diameter (D_{Bead}/D_{Pore}) for micropores of 10.0, 8.8, 6.9, 6.5, 6.2, 5.6, 4.6, 4.3 and 3.0 μm diameters (see Appendix Table A5.3). We note that all normalized datasets for different micropore-bead combinations converge to a universal curve. The solid line is the plot (not a fit) of equation (3.7) describing universal behaviour of our devices.

Bead Diameter (μm)	ΔG (nS)	V_{Bead} (fL) Manufacturer Data	$V = \frac{\Delta G}{\sigma} * L_{eff(8.8 \mu\text{m})}^2$ (fL)	$V = \frac{\Delta G}{\sigma} * L_{eff}^{Global2}$ (fL)	$V = \frac{\Delta G_{sample}}{\Delta G_{3.0 \mu\text{m}}} * V_{3.0 \mu\text{m}}$ (fL)	$V = \frac{\Delta G_{sample}}{\Delta G_{7.03 \mu\text{m}}} * V_{7.03 \mu\text{m}}$ (fL)
4.0	84 ± 4	33.5 ± 0.3	36 ± 3	39 ± 2	34 ± 4	33 ± 3
6.0	270 ± 30	113.1 ± 0.6	120 ± 20	120 ± 10	110 ± 20	110 ± 20

Table 3.1 Volume quantification of model cells by different methods: Columns 1 and 3 are parameters as given by the manufacturer. ΔG values measured ($N \geq 3$ datasets) are in column 2. Bead volumes are then compared by multiple methods: from L_{eff} calculated for 8.8 μm pore data (column 4), L_{eff}^{global} calculated from Figure 3.4c (column 5) and using equation (3.5) in columns 6 and 7 with 3.0 and 7.03 μm beads as the control samples respectively. The error bars are the standard deviation in the ΔG mean values as measured for multiple ($N \geq 3$) datasets.

3.3.4 Detection of Ethanol Dependent Changes in Red Blood Cells

We now use our high-resolution cell size measurement technique to measure changes in RBC size on exposure to alcohol (ethanol). For these experiments, RBC samples from three different donors were measured using our electro-fluidic device. RBCs were incubated for 10 minutes in RPMI buffer with different volume fractions (v/v %) of ethanol: 0.0%, 0.125%, 0.25%, 0.375% and 0.5%. Figure 3.4a shows optical images of the RBCs incubated with different concentrations of ethanol. These samples are indistinguishable under visual observation (see Fig S7b) or other techniques^{4,65}. To quantitatively measure the relative change in the RBC sizes upon increasing concentrations of ethanol exposure, we translocated these samples through our electro-fluidic device of 7.1 μm diameter micropore. The relative volumes of RBCs measured at different v/v % ethanol concentrations are shown in Figure 3.4b. Relative volumes are estimated by

comparing ΔG values of RBCs with different concentrations of ethanol to ΔG values of RBCs with no ethanol measured in the same device (see equation (3.5)). In multiple measurements, the order of the alcohol concentration being tested, were randomized to ascertain that the linear drop in relative volumes is solely due to ethanol exposure and not due to any other reason, for example cell ageing between measurements or ethanol dependent changes in the device (see Fig S7a). We show that RBC reduces in volume by 5.3% at 0.125 % ethanol (legal limit in USA⁶⁶) incubation and by 18.5 % at 0.5% ethanol (lethal limit)⁴. This is the first report on the quantitative measurement of changes in RBC volumes upon ethanol exposure. Although one can easily see changes in RBC sizes under a microscope at very high (non-physiological, 20% v/v or above) concentrations of ethanol, there has been multiple references showing elevation²⁴⁻²⁷, reduction^{2,7} or no change^{4,28} in RBC volume upon ethanol exposure at physiological concentrations. Main reason for this ambiguity has been the limitation of the techniques used⁶⁷⁻⁶⁹, hence the long-standing nature of the problem. Our work quantitatively shows these changes in RBC physiology at physiologically relevant ethanol concentrations. Possible reason for this effect is that the alcohol increases the osmolality of the RBC solution^{70,71} resulting in shrinkage of RBC cells due to loss of water^{7,72,73}. The reduction in the RBC volume in the presence of ethanol shown in our work supports studies that reported a significant decrease in Hemoglobin (Hb) content in the presence of ethanol⁴. The decreased Hb content and changes in RBC volume may be associated with the existing reports of blurred vision, muscular incoordination and stupor state of alcohol abuse. There is a possibility that the symptoms related to alcohol abuse may be due to reduced O₂ carrying capacity of RBCs with reduced volume. A detailed study in this direction is required.

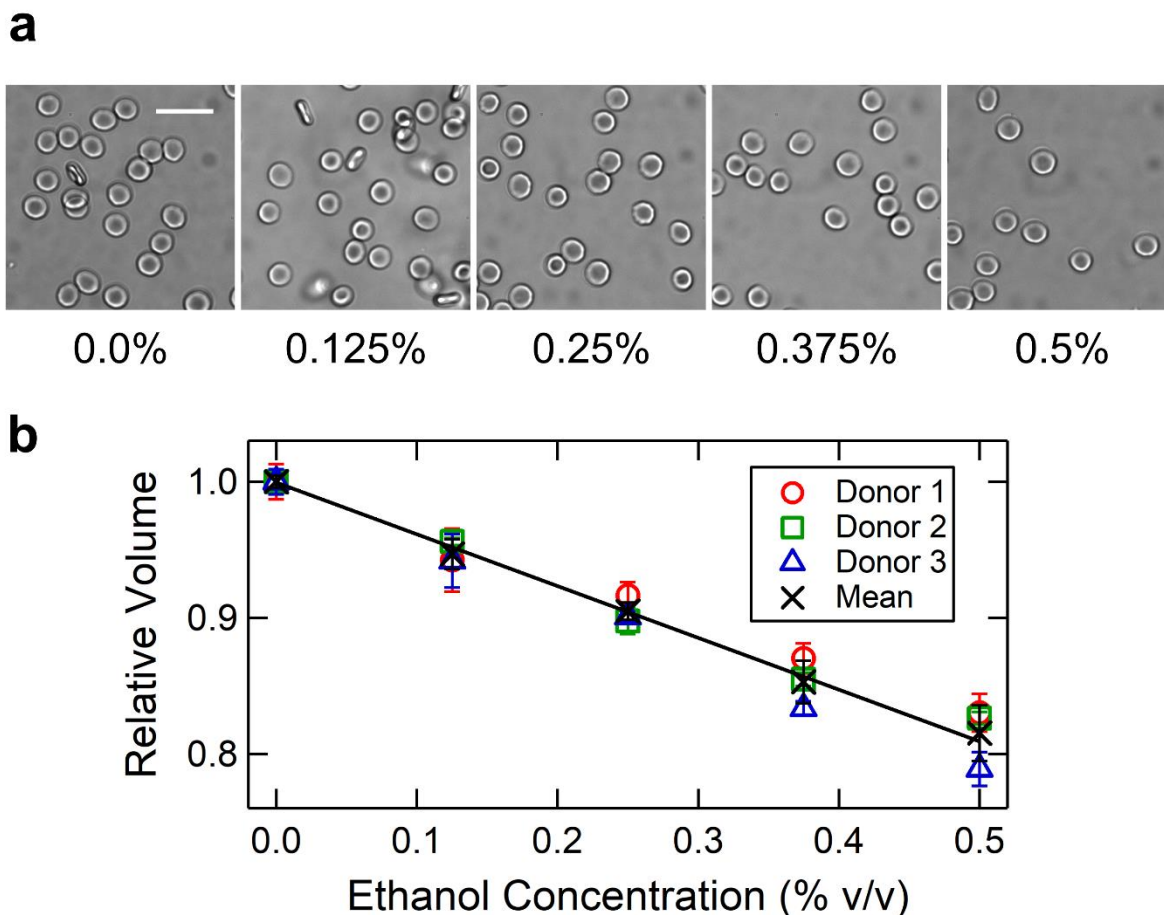


Figure 3.4 Effect of alcohol on Red Blood Cells. **a** Images of RBCs incubated for 10 mins at different concentrations of ethanol (% v/v) in RPMI buffer (Scalebar is 20 μm). **b** The plot shows the relative volume of Red Blood Cells at different concentrations of ethanol (% v/v) in RPMI buffer measured for 3 different donors. Crosses are the mean values (with error bars) and solid black line is the linear fit to the mean (crosses). A 7.1 μm micropore was used for this experiment.

3.3.5 Reversibility of RBC Volume Changes

We next measure the recovery of RBC cell volumes upon removal of ethanol. In Figure 3.5a we successively add and remove ethanol to RBCs and measure changes in their relative cell volumes using a 7.8 μm micropore device. We see a 24.4% reduction in cell volume when RBCs were exposed to 0.5% ethanol for 10 minutes. Upon removal of ethanol, RBCs regain their volume up to 94.7% within 10 minutes. This process is repeatable as shown in the next cycle of addition and then removal of ethanol. We note that there is a lower recovery (87.9%) of cell volume (within 10 minutes) in the second round. To understand the time dependent response of RBC's cell volume

recovery, we measured relative changes in RBC volumes, after ethanol removal, as a function of time. Figure 3.5b shows relative RBC cell volumes as measured by a 7.9 μm micropore device. We note that longer incubation of RBCs in ethanol reduces their volume by a larger fraction. We also note that after ethanol removal RBCs recover their volumes in two steps: the first fast recovery (within 10 minutes) and then a slow recovery up to the measured 4 hours. In Figure 3.5c we quantify the slow recovery step of RBC volume with time. We have modeled the recovery process by the following equation

$$Y(t) = 1 - Ae^{-t/\tau_r} \quad (3.8)$$

and found the slow recovery time constant (τ_r) is 120 ± 20 minutes.

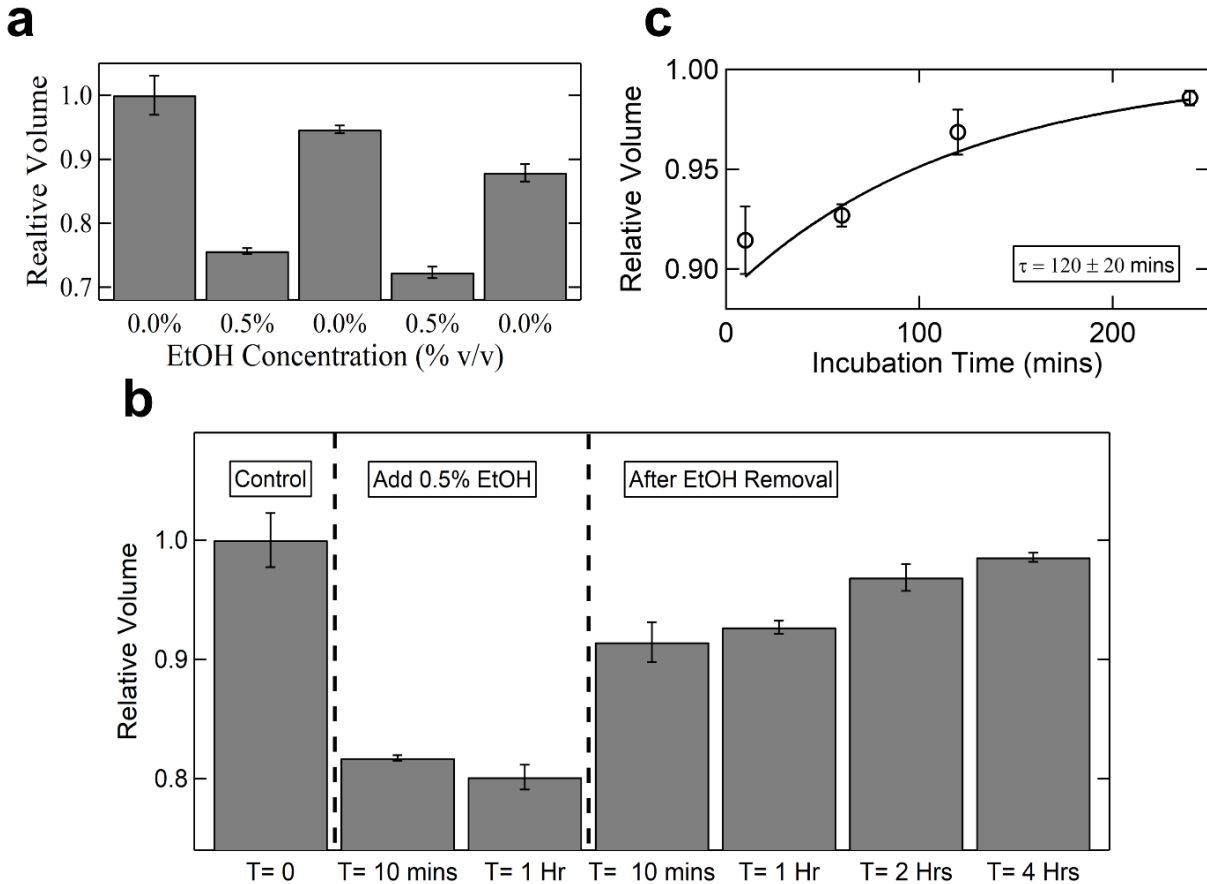


Figure 3.5 Reversibility of RBC volume changes with ethanol exposure. **a** Bar plot shows relative volume changes (measured in 7.8 μm pore) in RBCs after incubating successively in buffers with and without 0.5% v/v ethanol. Error bars are standard deviation in mean values for 3 different data sets. **b** Shows the time dependent recovery of RBCs in RPMI buffer after 1 hr incubation in 0.5% v/v ethanol containing RPMI buffer, as measured in a 7.9 μm pore. **c** Shows quantification of recovery of RBCs as shown in **b**. The solid line is fit to equation (3.8), giving a time constant of $\tau = 120 \pm 20$ mins.

3.3.6 Time Dependence of RBC Volume Changes upon Ethanol Exposure

Finally, to measure time dependent response to ethanol exposure, RBCs were incubated in different ethanol percentages for extended periods of time (10 mins, 4 hours and 8 hours). Figure 3.6a shows ethanol dependent changes in RBC cell volumes for different incubation times. We note that longer the ethanol exposure, the larger is the change in the cell's relative volume. In Figure 3.6b we plot the time course of relative volumes upon incubation in different ethanol concentrations. We model the time course of RBC's volume change with:

$$Y(t) = Y_0 + Ae^{-t/\tau_s} \quad (3.9)$$

and find that the shrinkage time constant (τ_s) depends on the ethanol concentration used. At the highest ethanol concentration of 0.5% v/v, we find the shrinkage time constant to be 63.1 ± 0.1 minutes, whereas at the lowest concentration of 0.125% v/v we found the shrinkage time constant to be 1038.9 ± 0.1 minutes.

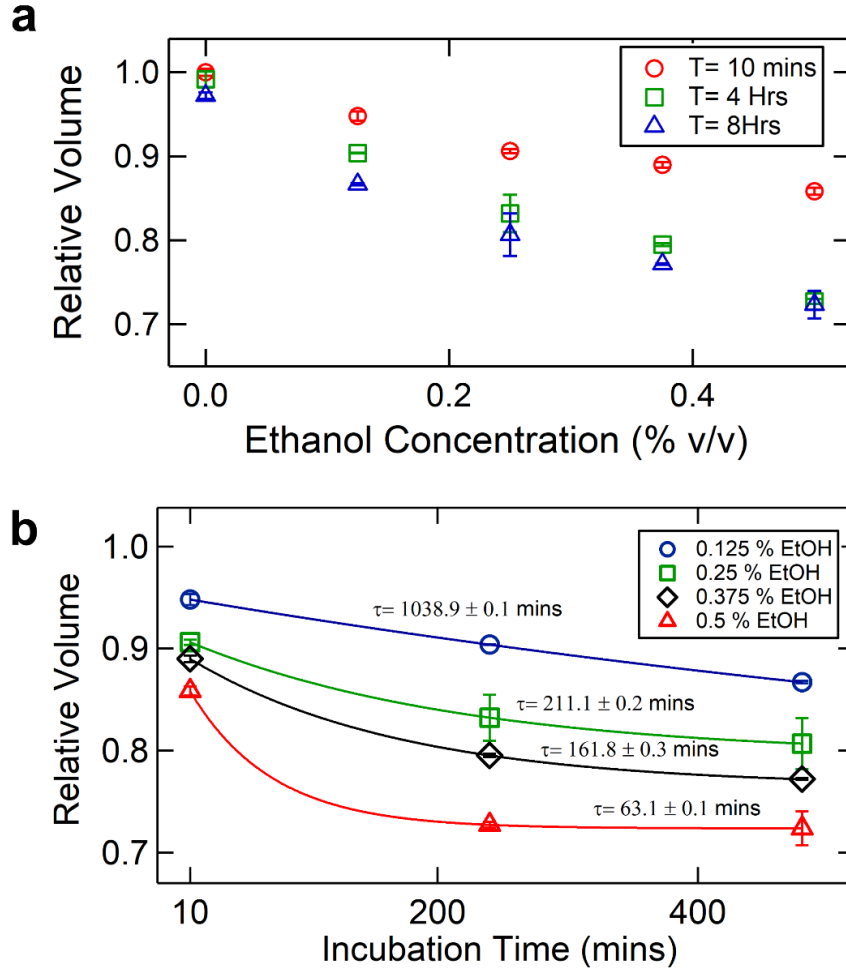


Figure 3.6 Time-dependent relative volume shrinkage of RBC. **a** The plot shows relative volume changes in RBCs at different percentages of ethanol in the RPMI buffer with 10 mins, 4 hrs and 8 hrs incubation time. **b** The plot shows the time course of volume shrinkage at different concentrations of ethanol (%v/v). The solid lines are fit to equation (3.9) giving the decay constants for 0.125%, 0.25%, 0.375% and 0.5% ethanol (v/v) as 1038.9 ± 0.1 mins, 211.1 ± 0.2 mins, 161.8 ± 0.3 mins, 63.1 ± 0.1 mins, respectively.

3.4 CONCLUSION

In this work, we demonstrate the use of our electrofluidic micropore devices and accurately estimate small changes in concentration, size and volume. With this device we could detect particles with different sizes in the correct ratios they were present in a well-mixed sample. We also showed that changes in micron sized particles as small as 100 nm in diameter or 0.6 fL in volume were detected with a micropore device of appropriate geometry. The resolution of the device depends on the ratio of particle size and micropore diameter, i.e. particles with their sizes of the order of micropore diameter are resolved better. In this paper, we use our electro-fluidic platform to measure the physiological changes in RBC by quantitatively measuring relative changes in the RBC volume when exposed to ethanol. These small changes in relative volume were not observed in the microscopic images of RBCs, but we're able to detect these changes using resistive pulse technique with our micropore device. We showed that the fast RBC shrinkage caused by ethanol is reversible after removing ethanol from the RBC's suspension buffer. After the initial fast recovery, the reversal has a long time constant and may take up to 4 hrs of incubation at 4°C to attain 98% of the native state volume of RBC. Accurate measurement of volume changes of RBC has applications in detection as well as mechanistic studies in diseases such as sickle cell anaemia & malaria where shape changes of RBC's play a major role. Similarly small but detectable volume changes of RBC could be indicators of nutritional states of the cell, such as iron deficiency. With this work, we envisage that our high-resolution platform, is a versatile tool, and can be used to screen multiple diagnostically relevant RBC dependent haematological conditions⁷⁴⁻⁷⁸.

3.5 REFERENCES

- (1) Sonmez, M.; Ince, H. Y.; Yalcin, O.; Ajdžanović, V.; Spasojević, I.; Meiselman, H. J.; Baskurt, O. K. The Effect of Alcohols on Red Blood Cell Mechanical Properties and Membrane Fluidity Depends on Their Molecular Size. *PLoS One* **2013**, *8* (9), 1–12.
- (2) Chi, L. M.; Wu, W. guey. Mechanism of Hemolysis of Red Blood Cell Mediated by Ethanol. *BBA - Biomembr.* **1991**, *1062* (1), 46–50.
- (3) Ballard, H. S. The Hematological Complications of Alcoholism. *Alcohol Research and Health*. 1997, pp 42–52.
- (4) Lee, S. Y.; Park, H. J.; Best-Popescu, C.; Jang, S.; Park, Y. K. The Effects of Ethanol on the Morphological and Biochemical Properties of Individual Human Red Blood Cells. *PLoS One* **2015**, *10* (12), 1–14.
- (5) Oonishi, T.; Sakashita, K. Ethanol Improves Decreased Filterability of Human Red Blood Cells Through Modulation of Intracellular Signaling Pathways. *Alcohol. Clin. Exp. Res.* **2000**, *24* (3), 352–356.
- (6) Palmieri, V. O.; Cicco, G.; Minerva, F.; Portincasa, P.; Grattagliano, I.; Memeo, V.; Palasciano, G. Red Blood Cells (RBC) Deformability and Aggregability: Alterations in Alcoholism. In *Advances in Experimental Medicine and Biology*; Springer New York, 2006; Vol. 578, pp 125–131.
- (7) Fehr, M.; Galliard-Grigioni, K. S.; Reinhart, W. H. Influence of Acute Alcohol Exposure on Hemorheological Parameters and Platelet Function in Vivo and in Vitro. In *Clinical Hemorheology and Microcirculation*; 2008; Vol. 39, pp 351–358.
- (8) Ballard, H. S. The Hematological Complications of Alcoholism. *Alcohol Res. Heal.* **1997**, *21* (1), 42–52.
- (9) Chin, J. H.; Goldstein, D. B. Effects of Low Concentrations of Ethanol on the Fluidity of Spin-Labeled Erythrocyte and Brain Membranes. *Mol. Pharmacol.* **1977**, *13* (3), 435–441.
- (10) Wood, W. G.; Lahiri, S.; Gorka, C.; Armbrrecht, H. J.; Strong, R. In Vitro Effects of Ethanol on Erythrocyte Membrane Fluidity of Alcoholic Patients: An Electron Spin

- Resonance Study. *Alcohol. Clin. Exp. Res.* **1987**, *11* (4), 332–335.
- (11) Beaugé, F.; Stibter, H.; Borg, S. Abnormal Fluidity and Surface Carbohydrate Content of the Erythrocyte Membrane in Alcoholic Patients. *Alcohol. Clin. Exp. Res.* **1985**, *9* (4), 322–326.
- (12) Beaugé, F.; Stibler, H.; Borg, S. Alterations of Erythrocyte Membrane Organization in Alcoholics. *Alcohol Alcohol Suppl.* **1987**, *1*, 561–565.
- (13) Benedetti, A.; Birarelli, A. M.; Brunelli, E.; Curatola, G.; Ferretti, G.; Jezequel, A. M.; Orlandi, F. Effect of Chronic Ethanol Abuse on the Physico-Chemical Properties of Erythrocyte Membranes in Man. *Pharmacol. Res. Commun.* **1986**, *18* (11), 1003–1014.
- (14) Beaug, F.; Gallay, J.; Stibler, H.; Borg, S. Alcohol Abuse Increases the Lipid Structural Order in Human Erythrocyte Membranes. A Steady-State and Time-Resolved Anisotropy Study. *Biochem. Pharmacol.* **1988**, *37* (20), 3823–3828.
- (15) Stibler, H.; Beauge, F.; Leguicher, A.; Borgt, S. Biophysical and Biochemical Alterations in Erythrocyte Membranes from Chronic Alcoholics. *Scand. J. Clin. Lab. Invest.* **1991**, *51* (4), 309–319.
- (16) Hrelia, S.; Lercker, G.; Biagi, P. L.; Bordoni, A.; Stefanini, F.; Zunarelli, P.; Rossi, C. A. Effect of Ethanol Intake on Human Erythrocyte Membrane Fluidity and Lipid Composition. *Biochem. Int.* **1986**, *12* (5), 741–750.
- (17) Liu, J.; Qiang, Y.; Alvarez, O.; Du, E. Electrical Impedance Characterization of Erythrocyte Response to Cyclic Hypoxia in Sickle Cell Disease. *ACS Sensors* **2019**, *4* (7), 1783–1790.
- (18) Spencer, D.; Morgan, H. High-Speed Single-Cell Dielectric Spectroscopy. *ACS Sensors* **2020**, *5* (2), 423–430.
- (19) Bernabini, C.; Holmes, D.; Morgan, H. Micro-Impedance Cytometry for Detection and Analysis of Micron-Sized Particles and Bacteria. *Lab Chip* **2011**, *11* (3), 407–412.
- (20) Nyberg, K. D.; Scott, M. B.; Bruce, S. L.; Gopinath, A. B.; Bikos, D.; Mason, T. G.; Kim, J. W.; Choi, H. S.; Rowat, A. C. The Physical Origins of Transit Time Measurements for

- Rapid, Single Cell Mechanotyping. *Lab Chip* **2016**, *16* (17), 3330–3339.
- (21) Tomaiuolo, G.; Barra, M.; Preziosi, V.; Cassinese, A.; Rotoli, B.; Guido, S. Microfluidics Analysis of Red Blood Cell Membrane Viscoelasticity. *Lab Chip* **2011**, *11* (3), 449–454.
- (22) Zheng, Y.; Shojaei-Baghini, E.; Azad, A.; Wang, C.; Sun, Y. High-Throughput Biophysical Measurement of Human Red Blood Cells. *Lab Chip* **2012**, *12* (14), 2560–2567.
- (23) Bow, H.; Pivkin, I. V.; Diez-Silva, M.; Goldfless, S. J.; Dao, M.; Niles, J. C.; Suresh, S.; Han, J. A Microfabricated Deformability-Based Flow Cytometer with Application to Malaria. *Lab Chip* **2011**, *11* (6), 1065–1073.
- (24) Mutlag, S. H.; Abdulhussein, A. J.; Najim, S. M.; Taher, M. A. The Assessment of Alcohol Effects on Red Blood Cell Indices in Rats. **2018**, *10* (January), 3153–3158.
- (25) Eschwege, E.; Papoz, L.; Lellouch, J.; Claude, J. R.; Cubeau, J.; Pequignot, G.; Richard, J. L.; Schwartz, D. Blood Cells and Alcohol Consumption with Special Reference to Smoking Habits. *J. Clin. Pathol.* **1978**, *31* (7), 654–658.
- (26) Bitsch, I.; Mazhari, S.; Klapp Kunsemueller, E. Acute Effects of Ethanol on Hematologic Parameters and Acid Base Metabolism of Rats. *Nutr. Metab.* **1977**, *21* (sup.1), 152–154.
- (27) Benedetti, A.; Birarelli, A. M.; Brunelli, E.; Curatola, G.; Ferretti, G.; Jezequel, A. ; Orlandi, F. Effect of Chronic Ethanol Abuse on the Physio-Chemical Properties of Erythrocyte Membrane in Man. **1986**, *18* (11), 1003–1010.
- (28) Hillbom, M. E.; Kaste, M.; Tarssanen, L.; Johnsson, R. Effect of Ethanol on Blood Viscosity and Erythrocyte Flexibility in Healthy Men. *Eur. J. Clin. Invest.* **1983**, *13*, 45–48.
- (29) Lan, W. J.; Holden, D. A.; Zhang, B.; White, H. S. Nanoparticle Transport in Conical-Shaped Nanopores. *Anal. Chem.* **2011**, *83* (10), 3840–3847.
- (30) Skinner, G. M.; Van Den Hout, M.; Broekmans, O.; Dekker, C.; Dekker, N. H. Distinguishing Single-and Double-Stranded Nucleic Acid Molecules Using Solid-State Nanopores. *Nano Lett.* **2009**, *9* (8), 2953–2960.
- (31) Butler, T. Z.; Gundlach, J. H.; Troll, M. A. Determination of RNA Orientation during

- Translocation through a Biological Nanopore. *Biophys. J.* **2006**, *90* (1), 190–199.
- (32) Lan, W. J.; Holden, D. A.; Liu, J.; White, H. S. Pressure-Driven Nanoparticle Transport across Glass Membranes Containing a Conical-Shaped Nanopore. *J. Phys. Chem. C* **2011**, *115* (38), 18445–18452.
- (33) Yusko, E. C.; Bruhn, B. R.; Eggenberger, O. M.; Houghtaling, J.; Rollings, R. C.; Walsh, N. C.; Nandivada, S.; Pindrus, M.; Hall, A. R.; Sept, D.; Li, J.; Kalonia, D. S.; Mayer, M. Real-Time Shape Approximation and Fingerprinting of Single Proteins Using a Nanopore. *Nat. Nanotechnol.* **2017**, *12* (4), 360–367.
- (34) Miles, B. N.; Ivanov, A. P.; Wilson, K. A.; Doğan, F.; Japrun, D.; Edel, J. B. Single Molecule Sensing with Solid-State Nanopores: Novel Materials, Methods, and Applications. *Chem. Soc. Rev.* **2013**, *42* (1), 15–28.
- (35) Li, W.; Bell, N. A. W.; Hernández-Ainsa, S.; Thacker, V. V.; Thackray, A. M.; Bujdoso, R.; Keyser, U. F. Single Protein Molecule Detection by Glass Nanopores. *ACS Nano* **2013**, *7* (5), 4129–4134.
- (36) Grover, N. B.; Naaman, J.; Ben-Sasson, S.; Doljanski, F. Electrical Sizing of Particles in Suspensions: III. Rigid Spheroids and Red Blood Cells. *Biophys. J.* **1972**, *12* (9), 1099–1116.
- (37) Wang, X.; Wilkinson, M. D.; Lin, X.; Ren, R.; Willison, K. R.; Ivanov, A. P.; Baum, J.; Edel, J. B. Single-Molecule Nanopore Sensing of Actin Dynamics and Drug Binding. *Chem. Sci.* **2020**, *11* (4), 970–979.
- (38) Steinbock, L. J.; Bulushev, R. D.; Krishnan, S.; Raillon, C.; Radenovic, A. DNA Translocation through Low-Noise Glass Nanopores. *ACS Nano* **2013**, *7* (12), 11255–11262.
- (39) Kowalczyk, S. W.; Hall, A. R.; Dekker, C. Detection of Local Protein Structures along DNA Using Solid-State Nanopores. *Nano Lett.* **2010**, *10* (1), 324–328.
- (40) Grover, N. B.; Naaman, J.; Ben-Sasson, S.; Doljanski, F. Electrical Sizing of Particles in Suspensions: I. Theory. *Biophys. J.* **1969**, *9* (11), 1398–1414.

- (41) M. Wanunu, G. V. S. & A. M. Analyzing Individual Biomolecules Using Nanopores. In *Handbook of Nanophysics: Nanomedicine and Nanorobotics*; Sattler, E. K. D., Ed.; CRC Press, 2010.
- (42) Steinbock, L. J.; Otto, O.; Chimere, C.; Gornall, J.; Keyser, U. F. Detecting DNA Folding with Nanocapillaries. *Nano Lett.* **2010**, *10* (7), 2493–2497.
- (43) Bafna, J. A.; Soni, G. V. Fabrication of Low Noise Borosilicate Glass Nanopores for Single Molecule Sensing. *PLoS One* **2016**, *11* (6), e0157399.
- (44) Bell, N. A. W.; Keyser, U. F. Digitally Encoded DNA Nanostructures for Multiplexed, Single-Molecule Protein Sensing with Nanopores. *Nat. Nanotechnol.* **2016**, *11* (7), 645–651.
- (45) Sha, J.; Si, W.; Xu, B.; Zhang, S.; Li, K.; Lin, K.; Shi, H.; Chen, Y. Identification of Spherical and Nonspherical Proteins by a Solid-State Nanopore. *Anal. Chem.* **2018**, *90* (23), 13826–13831.
- (46) Wanunu, M.; Soni, G. V.; Amit, M. Single-Molecule Studies of Nucleic Acid Interactions Using Nanopores. *Handb. Single-Molecule Biophys.* **2009**.
- (47) Grover, N. B.; Naaman, J.; Ben-Sasson, S.; Doljanski, F.; Nadav, E. Electrical Sizing of Particles in Suspensions: II. Experiments with Rigid Spheres. *Biophys. J.* **1969**, *9* (11), 1415–1425.
- (48) Yusko, E. C.; Prangkio, P.; Sept, D.; Rollings, R. C.; Li, J.; Mayer, M. Single-Particle Characterization of A β Oligomers in Solution. *ACS Nano* **2012**, *6*, (7), 5909–5919.
- (49) Soni, G. V.; Singer, A.; Yu, Z.; Sun, Y.; McNally, B.; Meller, A. Synchronous Optical and Electrical Detection of Biomolecules Traversing through Solid-State Nanopores. *Rev. Sci. Instrum.* **2010**, *81* (1).
- (50) Schneider, G. F.; Kowalczyk, S. W.; Calado, V. E.; Pandraud, G.; Zandbergen, H. W.; Vandersypen, L. M. K.; Dekker, C. DNA Translocation through Graphene Nanopores. *Nano Lett.* **2010**, *10* (8), 3163–3167.
- (51) Smeets, R. M. M.; Keyser, U. F.; Krapf, D.; Wu, M.-Y.; Dekker, N. H.; Dekker, C. Salt

- Dependence of Ion Transport and DNA Translocation through Solid-State Nanopores. *Nano Lett.* **2006**, *6* (1), 89–95.
- (52) DeBlois, R. W.; Bean, C. P. Counting and Sizing of Submicron Particles by the Resistive Pulse Technique. *Rev. Sci. Instrum.* **1970**, *41* (7), 909–916.
- (53) Arora, M. Cell Culture Media: A Review. *Labome*. 2013, pp 1–29.
- (54) Moore, G. E.; Gerner, R. E.; Franklin, H. A. Culture of Normal Human Leukocytes. *JAMA J. Am. Med. Assoc.* **1967**, *199* (8), 519–524.
- (55) Areman, E. M.; Dickerson, S. A.; Kotula, P. L.; Spitzer, T. R.; Sacher, R. A. Use of a Licensed Electrolyte Solution as an Alternative to Tissue Culture Medium for Bone Marrow Collection. *Transfusion* **1993**, *33* (7), 562–566.
- (56) Plesa, C.; Dekker, C. Data Analysis Methods for Solid-State Nanopores. *Nanotechnology* **2015**, *26* (8).
- (57) Smeets, R. M. M.; Keyser, U. F.; Krapf, D.; Wu, M. Y.; Dekker, N. H.; Dekker, C. Salt Dependence of Ion Transport and DNA Translocation through Solid-State Nanopores. *Nano Lett.* **2006**, *6* (1), 89–95.
- (58) Raillon, C.; Granjon, P.; Graf, M.; Steinbock, L. J.; Radenovic, A. Fast and Automatic Processing of Multi-Level Events in Nanopore Translocation Experiments. *Nanoscale* **2012**, *4* (16), 4916.
- (59) Iqbal, S. M.; Akin, D.; Bashir, R. Solid-State Nanopore Channels with DNA Selectivity. *Nat. Nanotechnol.* **2007**, *2* (4), 243–248.
- (60) Han, A.; Creus, M.; Schürmann, G.; Linder, V.; Ward, T. R.; De Rooij, N. F.; Stauer, U. Label-Free Detection of Single Protein Molecules and Protein-Protein Interactions Using Synthetic Nanopores. *Anal. Chem.* **2008**, *80* (12), 4651–4658.
- (61) Heng, J. B.; Aksimentiev, A.; Ho, C.; Marks, P.; Grinkova, Y. V.; Sligar, S.; Schulten, K.; Timp, G. The Electromechanics of DNA in a Synthetic Nanopore. *Biophys. J.* **2006**, *90* (3), 1098–1106.
- (62) Sexton, L. T.; Horne, L. P.; Sherrill, S. A.; Bishop, G. W.; Baker, L. A.; Martin, C. R.

- Resistive-Pulse Studies of Proteins and Protein/Antibody Complexes Using a Conical Nanotube Sensor. *J. Am. Chem. Soc.* **2007**, *129* (43), 13144–13152.
- (63) Soni, G. V.; Dekker, C. Detection of Nucleosomal Substructures Using Solid-State Nanopores. *Nano Lett.* **2012**, *12* (6), 3180–3186.
- (64) Bafna, J. A.; Soni, G. V. Fabrication of Low Noise Borosilicate Glass Nanopores for Single Molecule Sensing. *PLoS One* **2016**, *11*, e0157399.
- (65) Zachée, P.; Snauwaert, J.; Vandenberghe, P.; Hellemans, L.; Boogaerts, M. Imaging Red Blood Cells with the Atomic Force Microscope. *Br. J. Haematol.* **1996**, *95* (3), 472–481.
- (66) Plate, L.; Federal, M.; Angeles, L. DrunkDrivingLaws_040418_0. **2018**, No. April, 1–4.
- (67) Nguyen, A.; Wahed, A. Sources of Errors in Hematology and Coagulation Testing. In *Accurate Results in the Clinical Laboratory: A Guide to Error Detection and Correction*; Dasgupta, A., Sepulveda, J. L., Eds.; Elsevier Inc., 2013; pp 305–314.
- (68) Strauchen, J. A.; Alston, W.; Anderson, J.; Gustafson, Z.; Fajardo, L. F. Inaccuracy in Automated Measurement of Hematocrit and Corpuscular Indices in the PResence of Severe Hyperglycemia. *Blood* **1981**, *57* (6), 1065–1067.
- (69) Wennecke, G. Hematocrit - a review of different analytical methods
<https://acutecaretesting.org/-/media/acutecaretesting/files/pdf/hematocrit--a-review-of-different-analytical-methods.pdf>.
- (70) G. Robinson, A.; N. Loeb, J. Ethanol Ingestion - Commonest Cause of Elevated Plasma Osmolality? *N Engl J Med* **1971**, *284* (22), 1253–1255.
- (71) Champion, H. R.; Baker, S. P.; Benner, C.; Fisher, R.; Caplan, Y. H.; Long, W. B.; Cowley, R. A.; Gill, W. Alcohol Intoxication and Serum Osmolality. *Lancet* **1975**, *305* (7922), 1402–1404.
- (72) Reinhart, W. H.; Chien, S. Roles of Cell Geometry and Cellular Viscosity in Red Cell Passage through Narrow Pores. *Am. J. Physiol. - Cell Physiol.* **1985**, *17* (3).
- (73) Meiselman, H. J.; Merrill, E. W.; Gilliland, E. R.; Pelletier, G. A.; Salzman, E. W. Influence of Plasma Osmolarity on the Rheology of Human Blood. *J. Appl. Physiol.* **1967**,

22 (4), 772–781.

- (74) Gardner, R. V. Sickle Cell Disease: Advances in Treatment. *Ochsner J.* **2018**, *18* (4), 377–389.
- (75) Miller, J. L. Iron Deficiency Anemia: A Common and Curable Disease. *Cold Spring Harb. Perspect. Med.* **2013**, *3* (7), 1–13.
- (76) Kotepui, M.; Piwkham, D.; PhunPhuech, B.; Phiwklam, N.; Chupeerach, C.; Duangmano, S. Effects of Malaria Parasite Density on Blood Cell Parameters. *PLoS One* **2015**, *10* (3), 1–11.
- (77) Patnaik, M. M.; Tefferi, A. The Complete Evaluation of Erythrocytosis: Congenital and Acquired. *Leukemia* **2009**, *23* (5), 834–844.
- (78) Madu, A. J.; Ughasoro, M. D. Anaemia of Chronic Disease: An In-Depth Review. *Med. Princ. Pract.* **2017**, *26* (1), 1–9.

CHAPTER 4:

Customized low-cost high-throughput amplifier for electro-fluidic detection of cell volume changes in Point-of-Care applications

ABSTRACT

Physical parameters of the pathogenic cells, like their volume, shape, and stiffness, are important biomarkers for diseases, chemical changes within the cell, and overall cell health. The response of pathogenic bacteria and viruses to different chemical disinfectants is studied widely. Some of the routinely employed techniques to measure these changes require elaborate and expensive equipment which limits any study to a non-mobile research lab facility. Recently, we showed a micropore-based electro-fluidic technique to have great promise in measuring subtle changes in cell volumes at high throughput and resolution. This method, however, requires commercial amplifiers, which makes this technique expensive and incompatible for in-field use. In this paper, we develop a home-built amplifier to make this technique in-field compatible and apply it to measure changes in bacterial volumes upon alcohol exposure. First, we introduce our low-cost and portable trans-impedance amplifier and characterize the maximum range, absolute error percentage, and RMS noise of the amplifier in the measured current signal, along with the amplifier's bandwidth, and compare these characteristics with the commercial amplifiers. Using our home-built amplifier, we demonstrate a high throughput detection of ~ 1300 cells/second and resolve cell diameter changes down to $1 \mu\text{m}$. Finally, we demonstrate the measurement of cell volume changes in *E. coli* bacteria when exposed to ethanol (5% v/v), which is otherwise difficult to measure via imaging techniques. Our low-cost amplifier (~ 100 -fold lower than commercial alternatives) is battery-run and completely portable for point-of-care applications, and the electro-fluidic devices are currently being tested for in-field applications.

4.1 INTRODUCTION

Diagnosis of a disease is the first critical step for finding a cure for a patient¹⁻⁴. Lack of in-field diagnostic facilities or diagnosis tools has caused numerous casualties in past⁵⁻⁷. The diagnostic industry includes X-ray, flow cytometry, ultrasound, coagulation analyzers, CT-scan, MRI, cell counters, micro sedimentation centrifuges, platelet aggregometers, enzyme assay kits, and many associated consumables⁸⁻²². The urban population has access to these facilities via multi-specialist hospitals, door-to-door ambulance services, private clinics, and even online medical assistance, whereas in many rural areas around the globe, the nearest medical help or essential medical equipment are miles away²³⁻²⁶. Diseases like Tuberculosis, Tetanus, Cholera, Anthrax, Pneumonia, etc., are caused by bacterial infection, which has been fatal for centuries²⁷⁻³⁶. Certain alcohol-based disinfectants are used to kill bacterial cells and can help prevent infections^{37,38}. Disinfectants cause denaturation, and the bacterial cells lose their structural integrity by the breakdown of membrane proteins³⁹⁻⁴². There are pathogens that resist certain disinfectants⁴³⁻⁴⁶, and hence a quantitative study of alcohol-based physiological changes can lead to a better understanding of how these cells evolve to develop such resistance.

In this work, we present our electro-fluidic device to measure alcohol-dependent changes in bacterial cells. This device makes a high resolution and high throughput electrical measurement which directly corresponds to changes in cell volume. We start with introducing a low-cost portable amplifier (referred to as “lab-amplifier”) customized with a microfluidic platform which is easy to build, plug and play in use, portable to be used in the field, and about a 100-fold lower in cost than the existing commercial amplifiers. Accurate electrical readout of cell volume changes is recorded with the lab amplifier with high resolution as the cells translocate through the microfluidic device (micropore). The calibration of the micropore device to estimate the volume is based on resistive pulse technique⁴⁷⁻⁵⁶. The lab amplifier is characterized for the maximum range, absolute error, and RMS noise in the measured current signals. We have two series of lab amplifiers (L1 and L10 series), and both are characterized to have different bandwidths with different current gains. Lab amplifier with higher bandwidth (L1 series) works better for higher throughput but at the cost of slightly higher noise than the L10 series. L1 series amplifiers are more suitable for larger cells with large resistive pulse signals⁴⁸, whereas the L10 series amplifiers are more suitable to measure subtle changes in cell volumes with higher resolution. All the electrical characterization of the lab

amplifier is compared with two commercial amplifiers under identical experimental conditions. Using model cells, we demonstrate resolution and high throughput detection of up to ~1300 model cells/sec using our lab amplifier. Finally, we apply our device to quantitatively measure volumetric changes in cells (*E. Coli* bacteria) caused due to mild ethanol exposure in the suspension buffer. These subtle changes in cell physiology were not detectable using typical fluorescence or bright field microscopy imaging but were resolved successfully using our electro-fluidic device with lab-amplifier-based detection. There have been previous reports of making customized amplifiers for resistive pulse sensing, however, those designs are not suitable for measurement in cellular changes as they are aimed at molecular detection insteads⁵⁷⁻⁶³. Given the custom design of our lab amplifiers, we have made our portable measurement system low-cost, high throughput, and demonstratively aimed towards measuring changes in cell sizes. We foresee its multiple applications in hospitals and in-field rural settings.

4.2 MATERIAL AND METHODS

Our custom lab amplifier is designed with an inverting mode operational amplifier (Op-amp) (IC AD820) which is powered by two 9V DC batteries ($+V_{cc}$ and $-V_{cc}$) at IC pins 7 and 4, respectively. The feedback resistor (R_F) and capacitor (C_F) are connected across pins 2 and 6 of the Op-amp in parallel. We use a data acquisition card (National Instruments, NI myDAQ) to apply a constant DC input voltage (V_{in}) across the load resistor (R_P) in a virtual ground configuration. It is important to note that the input voltage (V_{in}) can also be applied from a third DC battery with a voltage regulator circuit. The analog signal across the input (V_{in} and ground) and output (pin 6 and ground) terminals were recorded by the DAQ system using a custom-written LabVIEW code. All ground cables were connected to the Aluminum box to keep the electrical noise low. The schematic of the above-mentioned electrical circuit is shown in Figure 4.1a. Two BNCs for connecting the load resistor (R_P), a DB9 connector for sending and receiving the signal from DAQ, an On/Off DPST toggle switch connected to the batteries to power the amplifier, the circuit board, and a power LED are shown in the interior of the lab amplifier in Figure 4.1b. Simulations for these amplifiers were done using Tina-TI simulation tool. During cell experiments, the load resistor R_P is replaced by the micropore device. In Figure 4.1c, we show two lab amplifiers (L10 and L1 series) enclosed in an aluminum box, with the feedback resistor, bandwidth, and maximum measurable current labeled. A microfluidic device and a one rupee coin are shown in the image for size references. The description and cost of all the electronics parts used in making lab amplifiers are mentioned in supplementary Table A6.1. Borosilicate glass capillaries (Part # B100-50-10, Sutter Instruments) were pulled using a micropipette puller (P-2000, Shutter Instrument) and then polished using a flame polisher (MF-900, Micro Forge, Narishige) to fabricate the desired micropores (electro-fluidic device). The detailed information on the fabrication of the micropores (electro-fluidic device), sample preparation, and electro-fluidic measurements are presented in our previous work⁴⁸. The schematic and brief details on how the micropore devices are prepared is included in the supplementary information file (see Fig S2). The two commercial amplifiers used in this work as a standard comparison are Dagan Chem Clamp and AM Systems Model 2400 (See Table A6.2 for detail). Latex beads of different diameters (see text) were used as model cells for testing the signal-to-noise, throughput, and resolution. Events in the conductance traces are detected using at least 1.5σ (1.5 times the standard deviation of baseline noise) thresholding from the baseline. DH5 α strain of *E. coli* bacteria were grown overnight in Luria broth at 37 °C, and 180 rpm overnight. Cells

were washed with 1X-PBS (137 mM NaCl, 4.3 mM Na₂HPO₄, 2.7 mM KCl, and 1.47 mM KH₂PO₄ at pH 7.4) buffer before its cell volume measurements. Bacterial cells were stained with FM4-64 (Cat # T13320 Invitrogen) dye to a final concentration of 10 μM and imaged using Andor iXon DU-885K-CS0 camera (Oxford Instruments) and fluorescent lamp illumination on an IX-73 Olympus microscope with 100X objective. For testing the effect of alcohol on the cell volumes, 1000 μl of *E. coli* bacterial culture was incubated with 50 μl of ethanol (EtOH) (5 % v/v) for 30 minutes before measurement.

4.3 RESULTS

4.3.1 Amplifier Characteristics

4.3.1.1 Current Range: To measure the current range of our L1 series (gain = 0.001 mV/pA, $R_F = 1 \text{ M}\Omega$, $C_F = 4.7 \text{ pF}$) and L10 series (gain = 0.01 mV/pA, $R_F = 10 \text{ M}\Omega$, $C_F = 1.5 \text{ pF}$) amplifiers, we measure their I-V characteristics for different R_P load resistors. The I-V characteristics of L1A, L1B and D001-1 amplifiers (all with $R_F = 1 \text{ M}\Omega$) for R_P values of 50 k Ω , 100 k Ω , 500 k Ω , and 1 M Ω electrical resistors are shown in the Figure 4.1d.

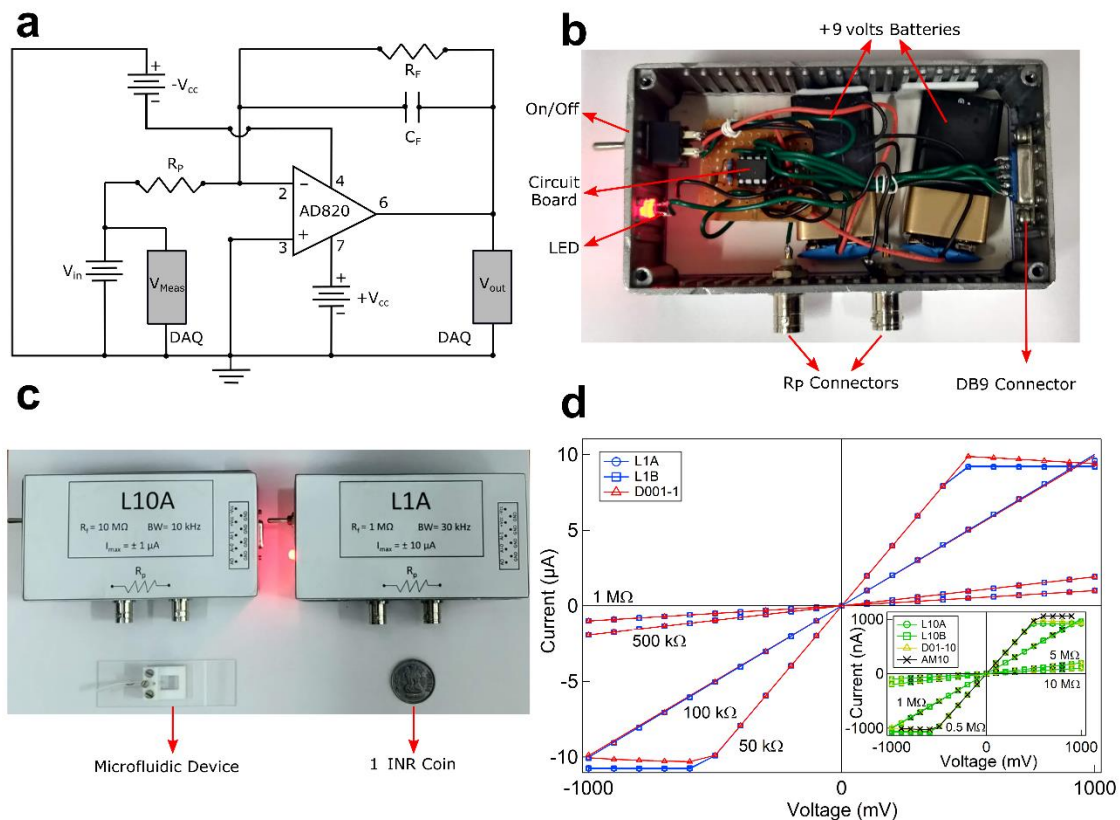


Figure 4.1 Schematic and construction of low-cost portable amplifier. (a) Schematic of the electrical circuit of the amplifier. (b) Image of the soldered circuit board inside the amplifier box with labeled circuit board, On/Off switch, LED, R_P connectors (to device) and DB9 connector. The amplifier is powered by two 9 volts DC batteries. (c) Shows two lab amplifiers (L1 and L10 series), enclosed in an aluminum box with labels showing individual specifications. The micropore device on a glass slide and a 1 INR coin is also shown for size reference. (d) I-V characteristics of electrical resistors measured with our amplifiers (L1 and L10 (inset), with ± 10 volts VCC) series where A & B suffix are 2 copies of the same amplifier design) is compared with commercial amplifiers (D and AM series).

The inset shows the I-V characteristics of L10A and L10B compared with commercial amplifiers D01-10 and AM10 ($R_F=10\text{ M}\Omega$) for R_P values of 0.5, 1, 5, and 10 $\text{M}\Omega$ electrical resistors. The current across $R_P = 50\text{ k}\Omega$ resistor with L1A, L1B, and D001-1 amplifiers saturates at $\pm 10\text{ }\mu\text{A}$, and for $R_P = 500\text{ k}\Omega$ the L10A, L10B, D01-10, and AM10 amplifiers saturate at $\pm 1000\text{ nA}$. The current range is limited by the saturation voltage of the Op-amps in the amplifiers. The values of the current ranges for all the amplifiers are listed in Table A6.2.

4.3.1.2 Absolute Error and Root Mean Square (RMS) Noise in Current: Current was measured across load resistors of values 100 $\text{k}\Omega$, 500 $\text{k}\Omega$, 1 $\text{M}\Omega$, 5 $\text{M}\Omega$, 10 $\text{M}\Omega$, 50 $\text{M}\Omega$ and 500 $\text{M}\Omega$ at voltages $\pm 200\text{ mV}$, $\pm 400\text{ mV}$, $\pm 600\text{ mV}$, $\pm 800\text{ mV}$, and $\pm 1000\text{ mV}$. The absolute error percentages, as defined by equation 1, in the current was calculated at all the measured voltages (Note: the current values in the saturation region (beyond measurable current range) were neglected for all the amplifiers):

$$\text{Absolute Error \%} = \text{Abs} \left(\frac{I_{Th} - I_{Meas}}{I_{Th}} \right) * 100 \quad (4.1)$$

Here, I_{Th} is the theoretically expected current, and I_{Meas} is the experimentally measured current for a known load resistor R_P . Figure 4.2a shows a semi-log plot of the absolute percentage error vs. the theoretically expected current values for different lab and commercial amplifiers. The dotted regions in the plot show the electrical resistor used as the load. We note that the current measured by our lab amplifiers has an error of less than 6% and does as good as (or better than) the commercial amplifiers. The load resistance of our microfluidic devices used for cell volume measurements is in the range of $\sim 1\text{ M}\Omega$, where we find the absolute percentage errors to be less than 1%. We next recorded the current at $\pm 300\text{ mV}$ for electrical resistors 500 $\text{k}\Omega$ and 1 $\text{M}\Omega$ (our experimental range) and measured the RMS noise in current at 1 kHz filter frequency. As seen in Figure 4.2b and 4.2c, in the experimental range of load resistances (R_P), our lab amplifiers show RMS noise of $< 200\text{ pA}$ (L1 series) and $< 80\text{ pA}$ (L10 series).

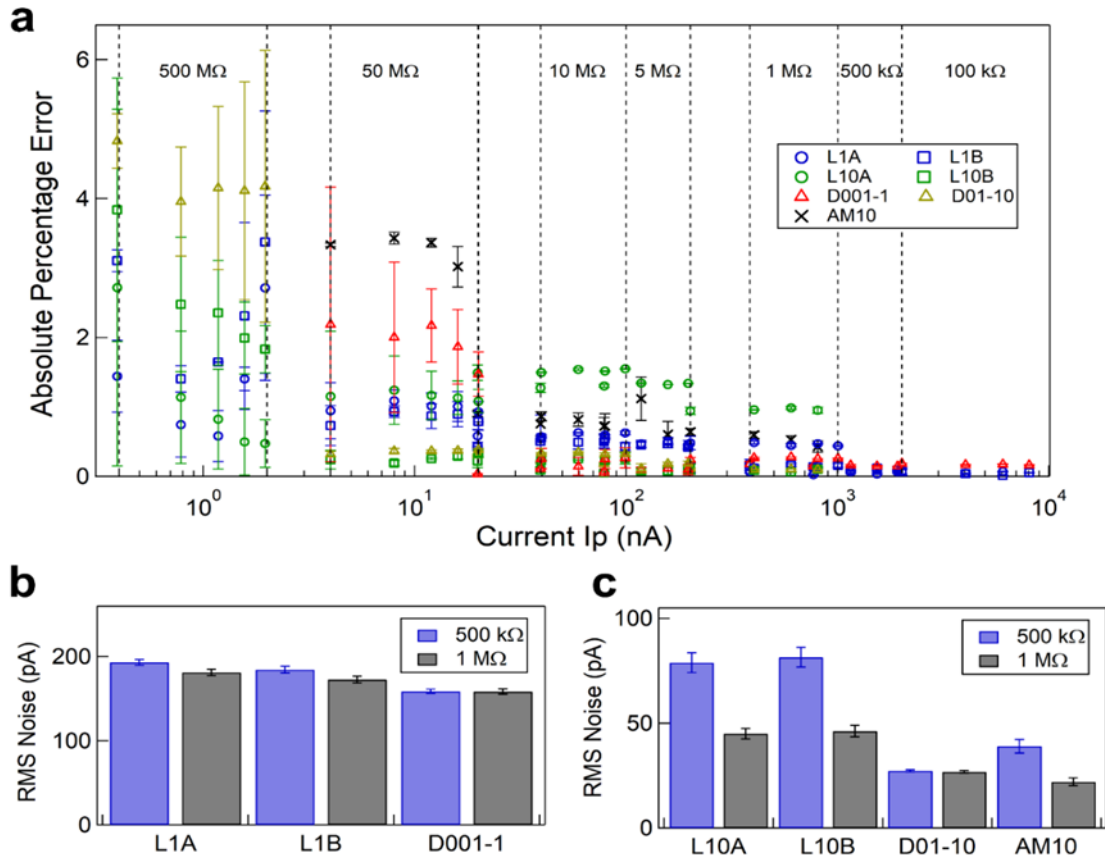


Figure 4.2 Comparison of absolute percentage error and RMS noise in current: (a) Absolute error percentage in the measured current as defined in equation (1) is plotted against the expected current for different amplifiers. Note that the current was measured at both positive and negative voltages to get an absolute mean current value and errorbars. Blue and green markers are for lab amplifiers and red, yellow and black are for commercial amplifiers. (b) and (c) show RMS noise and the error bar values (at 1 kHz) in the current, measured at ± 300 mV for $RP = 500$ k Ω (blue) and 1 M Ω (grey), by different amplifiers with feedback resistor (RF) values 1 M Ω (b) and 10 M Ω (c). A 600 ms current series was recorded at 100k sample/sec, 10 such sets at ± 300 mV were used for estimation of RMS noise and respective errorbars.

The RMS noise values at other filter frequencies are shown in supplementary Table A6.3 and A6.4. We note that the RMS noise values of our lab amplifiers (comparable to the commercial amplifiers) and the large signal-to-noise (see later in Figure 4.4a) in the cell measurements demonstrates suitability of our devices for such measurements.

4.3.1.3 Bandwidth of lab amplifier: We next calibrated the frequency response of our lab amplifiers. The low-pass cutoff frequency decides the time response of the amplifier, which in turn decides the maximum throughput of cells that can be measured per second. The Gain (dB)-

Frequency (Hz) response curves of different lab amplifiers (with $R_P = 500 \text{ k}\Omega$) is shown in Figure 4.3, where the black horizontal dotted line shows the -3dB decrease in the gain value. For this measurement, a data acquisition card (DAQ) with a maximum sampling rate of 2 MHz was used to apply a clean sine signal of 150 mV amplitude (V_{in}) of different frequencies and then recorded the output sine signal (V_{out}). The Gain (dB) was measured as $20 \times \log\left(\frac{V_{out}}{V_{in}}\right)$, for each frequency.

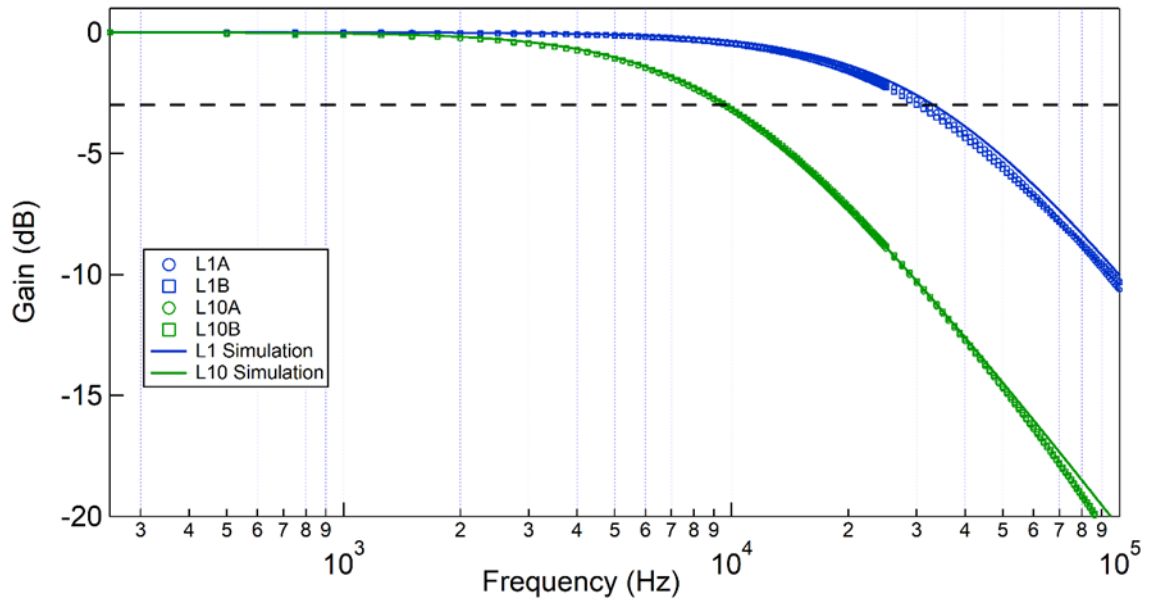


Figure 4.3 Bandwidth measurement of lab-amplifiers. Frequency response of the constructed amplifiers are shown here. The horizontal black dotted line is the 3dB drop in signal. A 500 k Ω resistor was used for all the measurements. L1 (A&B) and L10 (A&B) amplifiers show bandwidths of $30.9 \pm 0.8 \text{ kHz}$, and $9.55 \pm 0.05 \text{ kHz}$ respectively.

The blue (circle- L1A, square- L1B) and green (circle- L10A, square- L10B) markers are experimental data, whereas the solid blue (L1) and green (L10) lines are simulation results of the lab amplifier frequency response. The y-axis is scaled so that maximum gain appears at 0 dB. The cutoff frequencies were estimated from the graph at the intersection point of the -3dB line (horizontal black dotted line) and the response curve, and the values are listed in Table A6.2. We show that L1-series amplifiers have a relatively higher bandwidth of $\sim 30 \text{ kHz}$, whereas the L10 series amplifiers are of $\sim 10 \text{ kHz}$ bandwidth.

4.3.2 Translocation Measurements

4.3.2.1 Detection of model cells using lab-amplifiers and electro-fluidic devices: We next show cell volume detection capabilities using model cells measured with our electro-fluidic device and lab-amplifiers. Our devices make electrical measurements of cell volumes, with single-cell resolution, as individual cells translocate through the micropore under an applied flow and electrical potential⁴⁸. Figure 4.4a shows 1.5 sec long time series of translocation events caused by 4.98 μm beads translocating through a 6.8 μm micropore device as measured using the L1A (blue), L10A (green) and D001-1 (red) amplifiers. Schematic of a typical micropore (inset (right)) and a measurement device (inset (left)) is shown in Figure 4.4b. Translocation of the model cells was maintained by a 500 nL/min constant fluid flow and an applied potential of 300 mV. Ions in the 1X-PBS buffer move across the unobstructed micropore resulting in an open pore conductance. As the model cells translocate through the micropore, they block the pore conductance (ΔG (nS)) for the duration of translocation (dwell time, Δt (ms)). An electrical conductance drop (ΔG) signals the translocation of a single cell and is directly proportional to the cell volume^{48,51,52,54}. In each dataset, we collect electrical conductance blockage events for 500 cells or more that translocate through the pore to measure population average cell volumes and changes in it, if any. Figure 4.4b shows the population average of ΔG histograms. We show high signal-to-noise measurements on the same device and sample using the L1 and L10 lab amplifiers and compare it with the D001-1 commercial amplifier. The identical and overlapping histograms in Figure 4.4b show numerically identical ΔG values for the model cell population when measured using any amplifier.

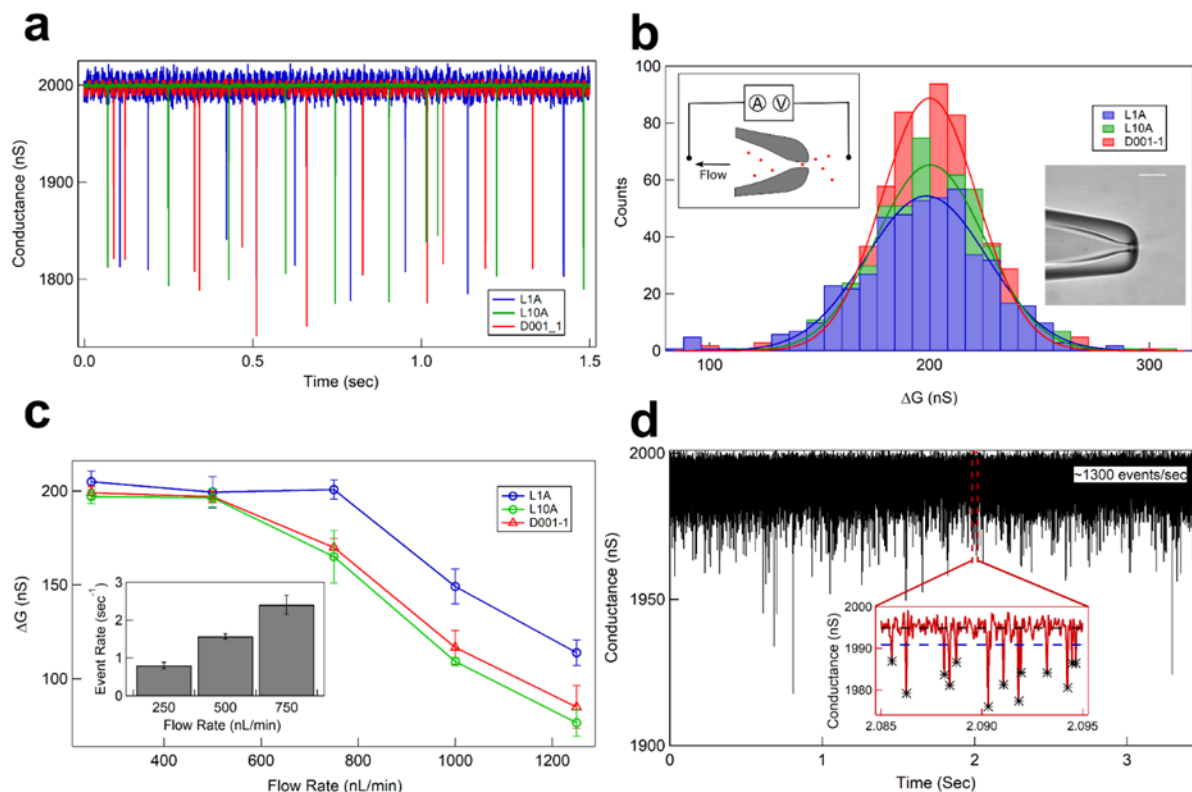


Figure 4.4 High throughput detection of model cells using lab amplifiers: (a) The plot shows 1.5 sec time series of open pore conductance baseline and the translocation events of $4.98 \mu\text{m}$ beads translocating through a $6.8 \mu\text{m}$ micropore device as measured using the L1A (blue), L10A (green) and D001-1 (red) amplifiers. Measurement was done at constant fluid flow of 500 nL/min . (b) ΔG histograms of detection events measured from the three different amplifiers are shown. Inset-left shows the schematic of the micropore experiment where the fluid flow is generated by a syringe pump and pore current across the micropore is measured by the amplifier. Inset-right shows optical microscope image of a typical micropore fabricated from a glass capillary. (c) Shows the mean signal (ΔG) of the translocation events as a function of fluid flow rates measured using different amplifiers. The inset shows the change in event rates for different flow rates for L1A amplifier. (d) Demonstrates typical detection throughput of our lab amplifier (L10A). $4.06 \mu\text{m}$ beads were detected through the same $6.8 \mu\text{m}$ micropore device at a fluid flow of $50 \mu\text{L/min}$ with the average event rate of $1308.4 \text{ particles/sec}$. The inset shows a 10 ms zoom of the times series and the detected events are marked by black stars. The baseline and the detection thresholds are shown by black and blue dashed lines, respectively..

We demonstrate the effect of the bandwidth of the amplifier on the measured signal by translocating the $4.98 \mu\text{m}$ latex beads through the same $6.8 \mu\text{m}$ micropore at different fluid flow rates. At larger flow rates, the event rate of cells translocating through the device increases dramatically (see Figure 4.4c inset). The ΔG values of model cells measured at different flow rates are shown in Figure 4.4c. We show that the amplifiers maintain the correct ΔG values up to certain throughput, after which, although the cells are detected successfully, the measured ΔG values drops. This is due to the low pass filtering of the amplifiers. We show in Figure 4.4c that the L1 amplifier

(30 kHz bandwidth) maintains the measured ΔG values up to much higher flow rates (750 nL/min of fluid flow), whereas for other amplifiers (L10 and D00-1, both with 10 kHz bandwidth) ΔG values drop after 500 nL/min of fluid flow. The choice of amplifier bandwidth is important to accurately quantify the translocation dynamics. For the translocation of particles and cells used in our study, 10 kHz bandwidth was found sufficiently high so as not to affect the ΔG conductance drop values (see Fig S3). Hence, the amplifier and the measurements were optimized to be recorded by 10 kHz bandwidth so that the signal doesn't experience any distortion at the fluid flow rates used for experiments in this paper. Our amplifiers can be used in two different modes. The sensitivity mode (see Fig 4b and later in Fig 5) where the translocation speeds are more controlled and the current drop amplitudes correspond to cell volumes and the high-throughput mode where the cells are detected at a very high speed. We demonstrate the high-throughput detection of model cells in Figure 4.4d. We use the 6.8 μm micropore device to translocate 4.06 μm model cells at a fluid flow of 50 $\mu\text{L}/\text{min}$ and demonstrate a detection event rate of ~ 1300 particles per second. In Figure 4.4d, we show a conductance trace of ~ 3.5 seconds (using an L10A amplifier), showing such a high detection throughput. The inset of Figure 4.4d shows a 10 ms zoom of the time series along with the baseline (dotted black line), detection threshold (dotted blue line), and the detected events are marked (black stars).

4.3.2.2 Resolving and quantifying mixed sample population: We next demonstrate the resolution of our measurement electronics by resolving model cells that differ in diameter by 1 μm . In Figure 4.5a, we show the conductance blockade events corresponding to model cells of diameters 4.06 μm (blue), 4.98 μm (red), and a mixture of both 4.06 and 4.98 μm (black) translocating through a 7.6 μm micropore device. A comparison of the translocation time (Δt) and change in conductance (ΔG) along with the respective lognormal (inset) and Gaussian fits for the same samples are shown in Figure 4.5b respectively. Although the two different model cells are not resolvable in the Δt histogram, they are very well resolved in the ΔG histograms (red and blue histograms). In the mixed sample experiment, the ΔG histogram shows two clear well-separated populations (Fig 5b, black histogram) corresponding to individual populations of 4.06 μm and 4.98 μm model cells. In Figure 4.5c, we also show the ΔG - Δt scatter plot that also clearly shows the presence of two distinct cell size populations.

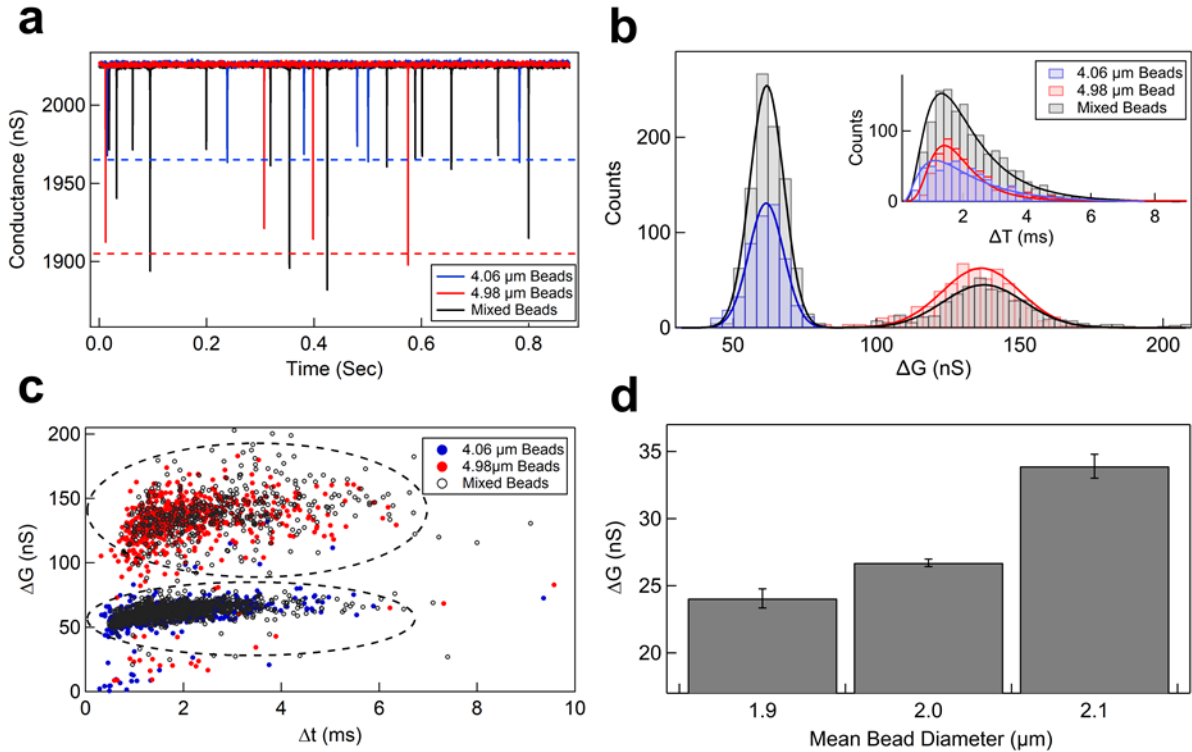


Figure 4.5 Resolving and Quantifying mixed sample population: (a) shows translocation events for 4.98 and 4.06 μm beads translocating through a 7.6 μm micropore device measured using L10A amplifier. Blue and red data is for individual sample measurements and black data is for a mixed beads sample. (b) Shows the Δt (inset) and ΔG histograms of individual and mixed sample translocation experiments with their respective lognormal and Gaussian fits. (c) The ΔG - Δt scatter plot shows the two populations of the beads. The result of the quantification of the population ratios of mixed beads is shown in Table 4.1. Online version in color. (d) Bar plot of ΔG values ($N \geq 3$ data sets for each bead size) for beads with diameters 1.9, 2.0, and 2.1 μm translocating through a 3.0 μm micropore device.

We further quantify the mixed sample data by comparing the number-ratio of events in each population histogram to the number-ratio in which the mixed sample was prepared. Since there is a random chance of any type of cell to translocate through the pore, the two ratios must be equal. The two populations were isolated by fitting Gaussian peaks (with no y-offset) to the histograms (Fig 5b) and estimating number of events in each peak. The quantitative data for the mixed sample is shown in Table 4.1 (average of three independent experiments). The first column of each set is the ΔG value and the spread in the histogram, and the second column is the number of events corresponding to the respective latex beads. The last column shows the sample concentration used in the experiment from the bead manufacturer’s numbers. The 4.06 and 4.98 μm beads were mixed in a known ratio of 2.5:1, the last row of the Table 4.1 shows the event ratio measured from the

translocation experiment. The average of the event ratio from three sets gives us (2.49 ± 0.08) : 1, which is remarkably close to the ratio in which the beads were mixed. Thus, our devices, along with our custom amplifiers, may be used in the field for testing multiple types of cells that differ in size and concentrations. In Fig 5d, we demonstrate the resolution capabilities of our system by detecting changes in particle volumes as low as 0.6 femtoliter. The bar plot in this figure shows comparison of measured ΔG values of 24.1 ± 0.7 , 26.7 ± 0.3 and 33.9 ± 0.9 nS respectively, for beads of diameter 1.90 ± 0.04 , 2.00 ± 0.04 , and 2.1 ± 0.3 μm translocating through a 3.0 μm micropore device. In our previous work, we have shown similar contrast between particles using commercial amplifiers⁴⁸, Fig 5d demonstrates that in terms of resolutions, our custom made lab-amplifier compares very well to the commercial amplifiers.

Bead Size (μm)	Set1		Set2		Set3		Manufacturer's Data (# x $10^9/\mu\text{l}$)
	ΔG (nS)	# Events	ΔG (nS)	# Events	ΔG (nS)	# Events	
4.06	60 ± 8	940	60 ± 8	964	60 ± 9	1468	1.365
4.98	140 ± 20	397	140 ± 20	375	140 ± 20	583	0.547
Events Ratio	2.37 : 1		2.57 : 1		2.52 : 1		2.5 : 1

Table 4.1 Quantification of mixed samples: ΔG and number of events detected corresponding to 4.06 and 4.98 μm latex beads in a 7.6 μm micropore device for three sets of translocation experiments is shown in the table. The 4.06 and 4.98 μm beads mixed in a known ratio of 2.5:1, and the experimental values of the detected ratio for 3 sets are mentioned in the last row.

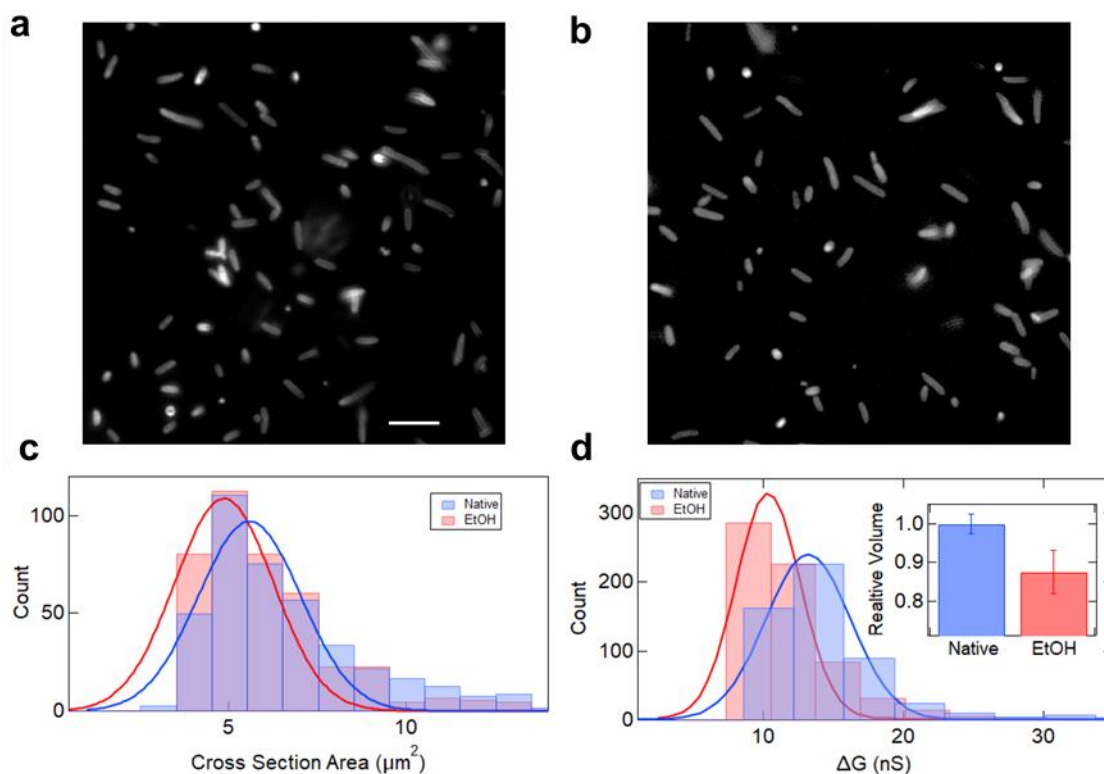


Figure 4.6 Measurement of changes in bacterial relative volumes using lab amplifier. (a) and (b) are fluorescent images of DH5a strain of *E. coli* bacteria in 1X PBS buffer with and without ethanol exposure respectively (scale bar is 10 μm). The histogram in (c) shows the projected area estimated from the fluorescent images for bacterial cells. (d) compares the ΔG histograms of *E. coli* cells measured in a 2.1 μm micropore device. The inset is a bar plot showing relative change in cell volumes when cells are treated with 5% (v/v) ethanol when compared to their native state in 1X PBS buffer (average of 4 experiments).

4.3.2.3 Effect of alcohol on bacterial cell volume: Finally, we apply our measurement system with the lab amplifier (L10 series) to quantitatively understand the effect of ethanol on bacterial cell physiology. The FM4-64 stained fluorescent images of the cells suspended in 1X PBS buffer, exposed with and without ethanol, are shown in Figure 4.6a and 6b, respectively. Particle analyzer plugin of ImageJ software was used post thresholding to estimate the projected area for the bacteria in the fluorescent images. The histogram in Figure 4.6c shows the projected area estimated from ~ 400 bacteria cells each with and without alcohol exposure. The Gaussian fit to the histograms estimates the values as $5.09 \pm 0.14 \mu\text{m}^2$ and $4.87 \pm 0.12 \mu\text{m}^2$ for native and ethanol exposed state of bacteria, respectively. The changes in the cell's projected area are hard to quantify when measured using imaging techniques. The electrical measurement data, on the other hand, shows excellent contrast in the cell volumes of these two cell populations. The ΔG histogram in Figure 4.6d shows the change in signal for bacterial translocation through a 2.1 (see Figure A6. 1 for

image) μm micropore device. The ΔG value from the Gaussian fits are 11.4 ± 4.3 (Blue- Native) and 8.7 ± 3.2 nS (Red- 5% EtOH exposed). Relative change in the ΔG values directly corresponds to the relative change in cell volume⁴⁸ using the following equation:

$$\text{Relative volume (RV)} = \frac{\Delta G_{\text{Sample}}}{\Delta G_{\text{Control}}} \quad (4.2)$$

Here, the $\Delta G_{\text{Control}}$ is the measured value for the native cells, and ΔG_{Sample} is the measured value for cells exposed to 5% ethanol. The bar plot in the inset shows the relative change in volume when the cells are treated with ethanol for 30 minutes, with respect to their native state. We note a 12.6 % reduction (average of 4 experiments) in bacterial cell volume upon exposure to just 5% ethanol solution. It is important to note that all the pulse measurements are made relative to the baseline and the reduction in bacterial size is solely due to the shrinkage of cells in the presence of ethanol and not due to the decrease in absolute conductivity of the solution as shown in Figure A6.4a. In order to demonstrate this, we translocate $4.0 \mu\text{m}$ beads through a $6.1 \mu\text{m}$ diameter micropore (See Figure A6. 4b) and, 1.9 and $2.1 \mu\text{m}$ beads through a micropore of $3.0 \mu\text{m}$ diameter (See Figure A6.4c and d) in suspension buffers containing different concentrations of ethanol. The constant ΔG values for different ethanol concentrations in Figure A6.4b, c and d for solid latex particles confirms that the change in conductance measured for bacterial cells is solely due to shrinkage of cells. We have demonstrated the ability of our electro-fluidic device, along with the custom-made lab-amplifiers, to detect cells with high throughput and measured changes in cell volumes with high resolution.

4.4 CONCLUSION

In this work, we present an in-field point-of-care compatible system which is cost-effective, portable, and has simple-to-build electronics. This system consists of electrical measurements using a microfluidic device and a lab-made amplifier (L1 and L10 series). The lab amplifier is characterized for the maximum current range, absolute error, RMS noise in the measured current signals, and bandwidth. All the electrical characterization demonstrate that the lab amplifiers perform comparable to the commercially available amplifiers. Using our lab amplifiers, we showed high throughput detection of up to 1300 cells/sec, demonstrating its potential as a cell counter device. We demonstrate the high resolution of our system by measuring cell size differences down to 100 nm. Estimation of absolute volumes of the translocating particles from the measured ΔG values, require detailed modeling of particle and pore's internal geometry. However, the relative change in cell volume, upon exposure to ethanol, is straight forwardly estimated provided the particle and pore shape remains the same. We finally presented a real-world measurement example by quantitatively measuring small physiological changes in the bacterial cells upon mild alcohol exposure. We report a 12.6 % decrease in bacterial volume upon ethanol exposure of 5 % v/v. The quantitative knowledge of cell shrinkage upon mild alcohol exposure is a vital step in understanding the adaptive behaviour of bacterial cells which they use to maintain their cellular integrity against certain alcohol-based disinfectants. The measurement of changes in bacterial volume is presented here as proof of concept for sensitive detection of volume-change in cells, using our lab-amplifiers. The simple design of our lab amplifier, its low cost, portability, high throughput, and resolution makes it a promising device for large-scale population screening applications in hospital and in-field rural areas. We envisage possible application of this system for red blood cell-based population screening for disease that directly affect cell size, such as, malaria and sickle cell anemia.

4.5 REFERENCES

- (1) Land, K. J.; Boeras, D. I.; Chen, X. S.; Ramsay, A. R.; Peeling, R. W. REASSURED Diagnostics to Inform Disease Control Strategies, Strengthen Health Systems and Improve Patient Outcomes. *Nat. Microbiol.* **2019**, *4* (1), 46–54.
- (2) Bruno, P. The Importance of Diagnostic Test Parameters in the Interpretation of Clinical Test Findings: The Prone Hip Extension Test as an Example. *J. Can. Chiropr. Assoc.* **2011**, *55* (2), 69–75.
- (3) Croft, P.; Altman, D. G.; Deeks, J. J.; Dunn, K. M.; Hay, A. D.; Hemingway, H.; LeResche, L.; Peat, G.; Perel, P.; Petersen, S. E.; Riley, R. D.; Roberts, I.; Sharpe, M.; Stevens, R. J.; Van Der Windt, D. A.; Von Korff, M.; Timmis, A. The Science of Clinical Practice: Disease Diagnosis or Patient Prognosis? Evidence about “What Is Likely to Happen” Should Shape Clinical Practice. *BMC Med.* **2015**, *13* (1), 1–8.
- (4) Wurcel, V.; Cicchetti, A.; Garrison, L.; Kip, M. M. A.; Koffijberg, H.; Kolbe, A.; Leeftang, M. M. G.; Merlin, T.; Mestre-Ferrandiz, J.; Oortwijn, W.; Oosterwijk, C.; Tunis, S.; Zamora, B. The Value of Diagnostic Information in Personalised Healthcare: A Comprehensive Concept to Facilitate Bringing This Technology into Healthcare Systems. *Public Health Genomics* **2019**, *22* (1–2), 8–15.
- (5) Williamson, E. J.; Walker, A. J.; Bhaskaran, K.; Bacon, S.; Bates, C.; Morton, C. E.; Curtis, H. J.; Mehrkar, A.; Evans, D.; Inglesby, P.; Cockburn, J.; McDonald, H. I.; MacKenna, B.; Tomlinson, L.; Douglas, I. J.; Rentsch, C. T.; Mathur, R.; Wong, A. Y. S.; Grieve, R.; Harrison, D.; Forbes, H.; Schultze, A.; Croker, R.; Parry, J.; Hester, F.; Harper, S.; Perera, R.; Evans, S. J. W.; Smeeth, L.; Goldacre, B. Factors Associated with COVID-19-Related Death Using OpenSAFELY. *Nature* **2020**, *584* (7821), 430–436.
- (6) Kruk, M. E.; Gage, A. D.; Joseph, N. T.; Danaei, G.; García-Saisó, S.; Salomon, J. A. Mortality Due to Low-Quality Health Systems in the Universal Health Coverage Era: A Systematic Analysis of Amenable Deaths in 137 Countries. *Lancet* **2018**, *392* (10160), 2203–2212.
- (7) Newman-Toker, D. E.; Wang, Z.; Zhu, Y.; Nassery, N.; Saber Tehrani, A. S.; Schaffer, A.

- C.; Yu-Moe, C. W.; Clemens, G. D.; Fanai, M.; Siegal, D. Rate of Diagnostic Errors and Serious Misdiagnosis-Related Harms for Major Vascular Events, Infections, and Cancers: Toward a National Incidence Estimate Using the “Big Three.” *Diagnosis* **2021**, 8 (1), 67–84.
- (8) Paiva, B.; Vidriales, M. B.; Pérez, J. J.; Mateo, G.; Montalbán, M. A.; Mateos, M. V.; Bladé, J.; Lahuerta, J. J.; Orfao, A.; San Miguel, J. F. Multiparameter Flow Cytometry Quantification of Bone Marrow Plasma Cells at Diagnosis Provides More Prognostic Information than Morphological Assessment in Myeloma Patients. *Haematologica* **2009**, 94 (11), 1599–1602.
- (9) Tekkesin, N.; Kilinc, C. Optical and Mechanical Clot Detection Methodologies: A Comparison Study for Routine Coagulation Testing. *J. Clin. Lab. Anal.* **2012**, 26 (3), 125–129.
- (10) Alcaide Martín, M. J.; Altimira Qeral, L.; Sahuquillo Frías, L.; Valiña Amado, L.; Merino, A.; García de Guadiana-Romualdo, L. Automated Cell Count in Body Fluids: A Review. *Adv. Lab. Med. / Av. en Med. Lab.* **2021**, 2 (2), 149–161.
- (11) Vlachos, L.; Trakadas, S.; Gouliamos, A.; Lazarou, S.; Mourikis, D.; Ioannou, R.; Kalovidouris, A.; Papavasiliou, C. Resonance Imaging in the Differentiation of Tumors of the Liver. **1990**, 106, 102–106.
- (12) Kao, L. Y.; Scheinfeld, M. H.; Chernyak, V.; Rozenblit, A. M.; Oh, S.; Dym, R. J. Beyond Ultrasound: CT and MRI of Ectopic Pregnancy. *Am. J. Roentgenol.* **2014**, 202 (4), 904–911.
- (13) Takashima, T.; Okamura, M.; Yeh, T. wen; Okano, T.; Yamashita, M.; Tanaka, K.; Hoshino, A.; Mitsuiki, N.; Takagi, M.; Ishii, E.; Imai, K.; Kanegane, H.; Morio, T. Multicolor Flow Cytometry for the Diagnosis of Primary Immunodeficiency Diseases. *J. Clin. Immunol.* **2017**, 37 (5), 486–495.
- (14) Kinn Rød, A. M.; Harkestad, N.; Jellestad, F. K.; Murison, R. Comparison of Commercial ELISA Assays for Quantification of Corticosterone in Serum. *Sci. Rep.* **2017**, 7 (1), 1–5.
- (15) Stratmann, J.; Karmal, L.; Zwinge, B.; Miesbach, W. Platelet Aggregation Testing on a

- Routine Coagulation Analyzer: A Method Comparison Study. *Clin. Appl. Thromb.* **2019**, 25.
- (16) Koltai, K.; Kesmarky, G.; Feher, G.; Tibold, A.; Toth, K. Platelet Aggregometry Testing: Molecular Mechanisms, Techniques and Clinical Implications. *Int. J. Mol. Sci.* **2017**, 18 (8), 1–21.
- (17) Forchelet, D.; Béguin, S.; Sajic, T.; Bararpour, N.; Pataky, Z.; Frias, M.; Grabherr, S.; Augsburger, M.; Liu, Y.; Charnley, M.; Déglon, J.; Aebersold, R.; Thomas, A.; Renaud, P. Separation of Blood Microsamples by Exploiting Sedimentation at the Microscale. *Sci. Rep.* **2018**, 8 (1), 1–9.
- (18) Mohammadi Aria, M.; Erten, A.; Yalcin, O. Technology Advancements in Blood Coagulation Measurements for Point-of-Care Diagnostic Testing. *Front. Bioeng. Biotechnol.* **2019**, 7 (December), 1–18.
- (19) Smith-Bindman, R.; Kwan, M. L.; Marlow, E. C.; Theis, M. K.; Bolch, W.; Cheng, S. Y.; Bowles, E. J. A.; Duncan, J. R.; Greenlee, R. T.; Kushi, L. H.; Pole, J. D.; Rahm, A. K.; Stout, N. K.; Weinmann, S.; Miglioretti, D. L. Trends in Use of Medical Imaging in US Health Care Systems and in Ontario, Canada, 2000-2016. *JAMA - J. Am. Med. Assoc.* **2019**, 322 (9), 843–856.
- (20) Chen, H.; Rogalski, M. M.; Anker, J. N. Agents. **2013**, 14 (39), 13469–13486.
- (21) Betters, PhD, RN, D. M. Use of Flow Cytometry in Clinical Practice. *J. Adv. Pract. Oncol.* **2015**, 6 (5), 435–440.
- (22) Ruiz-García, R.; Lermo-Rojo, S.; Martínez-Lostao, L.; Mancebo, E.; Mora-Díaz, S.; Paz-Artal, E.; Ruiz-Contreras, J.; Anel, A.; González-Granado, L. I.; Allende, L. M. A Case of Partial Deficiency of Cytokines 8 Deficiency with Altered Effector Phenotype and Impaired CD8+ and Natural Killer Cell Cytotoxicity. *J. Allergy Clin. Immunol.* **2014**, 134 (1).
- (23) Cyr, M. E.; Etchin, A. G.; Guthrie, B. J.; Benneyan, J. C. Access to Specialty Healthcare in Urban versus Rural US Populations: A Systematic Literature Review. *BMC Health Serv. Res.* **2019**, 19 (1), 1–17.

- (24) Daniel E Shumer, N. J. N. N. P. S. 乳鼠心肌提取 HHS Public Access. *Physiol. Behav.* **2017**, *176* (12), 139–148.
- (25) Bearden, A.; Fuller, A. T.; Butler, E. K.; Tran, T.; Makumbi, F.; Luboga, S.; Muhumuza, C.; Ssennono, V.; Galukande, M.; Haglund, M.; Smith, E. R. Rural and Urban Differences in Treatment Status among Children with Surgical Conditions in Uganda. *PLoS One* **2018**, *13* (11), 1–13.
- (26) Hisham, R.; Liew, S. M.; Ng, C. J. A Comparison of Evidence-Based Medicine Practices between Primary Care Physicians in Rural and Urban Primary Care Settings in Malaysia: A Qualitative Study. *BMJ Open* **2018**, *8* (7), e018933.
- (27) Murray, J. F. A Century of Tuberculosis. *Am. J. Respir. Crit. Care Med.* **2004**, *169* (11), 1181–1186.
- (28) Goel, A. K. Anthrax: A Disease of Biowarfare and Public Health Importance. *World J. Clin. Cases* **2015**, *3* (1), 20.
- (29) Phelps, M.; Perner, M. L.; Pitzer, V. E.; Andreasen, V.; Jensen, P. K. M.; Simonsen, L. Cholera Epidemics of the Past Offer New Insights into an Old Enemy. *J. Infect. Dis.* **2018**, *217* (4), 641–649.
- (30) Brundage, J. F.; Shanks, G. D. Deaths from Bacterial Pneumonia during 1918-19 Influenza Pandemic. *Emerg. Infect. Dis.* **2008**, *14* (8), 1193–1199.
- (31) Chan, C. H.; Tuite, A. R.; Fisman, D. N. Historical Epidemiology of the Second Cholera Pandemic: Relevance to Present Day Disease Dynamics. *PLoS One* **2013**, *8* (8).
- (32) Turnbull, P. C. B. Introduction : Anthrax History , *Koehler T.M. Anthrax. Curr. Top. Microbiol. Immunol.* **2002**, *271*, 1–19.
- (33) Kyu, H. H.; Mumford, J. E.; Stanaway, J. D.; Barber, R. M.; Hancock, J. R.; Vos, T.; Murray, C. J. L.; Naghavi, M. Mortality from Tetanus between 1990 and 2015: Findings from the Global Burden of Disease Study 2015. *BMC Public Health* **2017**, *17* (1), 1–17.
- (34) Tiemersma, E. W.; van der Werf, M. J.; Borgdorff, M. W.; Williams, B. G.; Nagelkerke, N. J. D. Natural History of Tuberculosis: Duration and Fatality of Untreated Pulmonary

- Tuberculosis in HIV Negative Patients: A Systematic Review. *PLoS One* **2011**, 6 (4).
- (35) Cook, T. M.; Protheroe, R. T.; Handel, J. M. Tetanus: A Review of the Literature. *Br. J. Anaesth.* **2001**, 87 (3), 477–487.
- (36) Thomson, P. S. Proceedings of the Royal Society of Medicine ! Ection of Tbe Lbtitorp of Flebictne The History of the 1832 Cholera Epidemic in Yorkshire. **1935**, 5–18.
- (37) Ribeiro, M. M.; Neumann, V. A.; Padoveze, M. C.; Graziano, K. U. Efficacy and Effectiveness of Alcohol in the Disinfection of Semi-Critical Materials: A Systematic Review. *Rev. Lat. Am. Enfermagem* **2015**, 23 (4), 741–752.
- (38) Boyce, J. M. Alcohols as Surface Disinfectants in Healthcare Settings. *Infect. Control Hosp. Epidemiol.* **2018**, 39 (3), 323–328.
- (39) Huffer, S.; Clark, M. E.; Ning, J. C.; Blanch, H. W.; Clark, D. S. Role of Alcohols in Growth, Lipid Composition, and Membrane Fluidity of Yeasts, Bacteria, and Archaea. *Appl. Environ. Microbiol.* **2011**, 77 (18), 6400–6408.
- (40) Ingram, L. O. Mechanism of Lysis of Escherichia Coli by Ethanol and Other Chaotropic Agents. *J. Bacteriol.* **1981**, 146 (1), 331–336.
- (41) Nwugo, C. C.; Arivett, B. A.; Zimbler, D. L.; Gaddy, J. A.; Richards, A. M.; Actis, L. A. Effect of Ethanol on Differential Protein Production and Expression of Potential Virulence Functions in the Opportunistic Pathogen Acinetobacter Baumannii. *PLoS One* **2012**, 7 (12).
- (42) Soufi, B.; Krug, K.; Harst, A.; Macek, B. Characterization of the E. Coli Proteome and Its Modifications during Growth and Ethanol Stres. *Front. Microbiol.* **2015**, 6 (FEB), 1–11.
- (43) Pidot, S. J.; Gao, W.; Buultjens, A. H.; Monk, I. R.; Guerillot, R.; Carter, G. P.; Lee, J. Y. H.; Lam, M. M. C.; Grayson, M. L.; Ballard, S. A.; Mahony, A. A.; Grabsch, E. A.; Kotsanas, D.; Korman, T. M.; Coombs, G. W.; Robinson, J. O.; Da Silva, A. G.; Seemann, T.; Howden, B. P.; Johnson, P. D. R.; Stinear, T. P. Increasing Tolerance of Hospital Enterococcus Faecium to Handwash Alcohols. *Sci. Transl. Med.* **2018**, 10 (452).
- (44) Ochwoto, M.; Muita, L.; Talaam, K.; Wanjala, C.; Ogeto, F.; Wachira, F.; Osman, S.; Kimotho, J.; Ndegwa, L. Anti-Bacterial Efficacy of Alcoholic Hand Rubs in the Kenyan

- Market, 2015. *Antimicrob. Resist. Infect. Control* **2017**, 6 (1), 1–6.
- (45) Fair, R. J.; Tor, Y. Antibiotics and Bacterial Resistance in the 21st Century. *Perspect. Medicin. Chem.* **2014**, No. 6, 25–64.
- (46) Ciotti, C.; Ferrao, B.; Garrigues, I.; Nérome, S. Bacteria Which Are Highly Resistant to Antibiotics Are Not Resistant Hydro-Alcoholic Products. *Med. Mal. Infect.* **2020**, 51, 77–80.
- (47) Soni, G. V.; Dekker, C. Detection of Nucleosomal Substructures Using Solid-State Nanopores. *Nano Lett.* **2012**, 12 (6), 3180–3186.
- (48) Kaushik, S.; Mahadeva, M.; Murugan, K. D.; Sundaramurthy, V.; Soni, G. V. Measurement of Alcohol-Dependent Physiological Changes in Red Blood Cells Using Resistive Pulse Sensing. *ACS Sensors* **2020**, 5 (12), 3892–3901.
- (49) Soni, G. V.; Singer, A.; Yu, Z.; Sun, Y.; McNally, B.; Meller, A. Synchronous Optical and Electrical Detection of Biomolecules Traversing through Solid-State Nanopores. *Rev. Sci. Instrum.* **2010**, 81 (1).
- (50) Bafna, J. A.; Soni, G. V. Fabrication of Low Noise Borosilicate Glass Nanopores for Single Molecule Sensing. *PLoS One* **2016**, 11, e0157399.
- (51) Maheshwaram, S. K.; Sreenivasa, K.; Soni, G. V. Fingerprinting Branches on Supercoiled Plasmid DNA Using Quartz Nanocapillaries. *Nanoscale* **2021**, 13 (1), 320–331.
- (52) DeBlois, R. W.; Bean, C. P. Counting and Sizing of Submicron Particles by the Resistive Pulse Technique. *Rev. Sci. Instrum.* **1970**, 41 (7), 909–916.
- (53) Yusko, E. C.; Johnson, J. M.; Majd, S.; Prangko, P.; Rollings, R. C.; Li, J.; Yang, J.; Mayer, M. Controlling Protein Translocation through Nanopores with Bio-Inspired Fluid Walls. *Nat. Nanotechnol.* **2011**, 6 (4), 253–260.
- (54) Grover, N. B.; Naaman, J.; Ben-Sasson, S.; Doljanski, F. Electrical Sizing of Particles in Suspensions: III. Rigid Spheroids and Red Blood Cells. *Biophys. J.* **1972**, 12 (9), 1099–1116.
- (55) Kowalczyk, S. W.; Hall, A. R.; Dekker, C. Detection of Local Protein Structures along

- DNA Using Solid-State Nanopores. *Nano Lett.* **2010**, *10* (1), 324–328.
- (56) Steinbock, L. J.; Otto, O.; Chimerel, C.; Gornall, J.; Keyser, U. F. Detecting DNA Folding with Nanocapillaries. *Nano Lett.* **2010**, *10* (7), 2493–2497.
- (57) Hu, Z. L.; Ying, Y. L.; Huo, M. Z.; Kong, X. F.; Yu, X. D.; Zhang, J. R.; Long, Y. T. A Course of Hands-On Nanopore Experiments for Undergraduates: Single-Molecule Detection with Portable Electrochemical Instruments. *J. Chem. Educ.* **2020**, *97* (12), 4345–4354.
- (58) Abbasi, U.; Chowdhury, P.; Subramaniam, S.; Jain, P.; Muthe, N.; Sheikh, F.; Banerjee, S.; Kumaran, V. A Cartridge Based Point-of-Care Device for Complete Blood Count. *Sci. Rep.* **2019**, *9* (1), 1–16.
- (59) Pérez, P.; Huertas, G.; Maldonado-Jacobi, A.; Martín, M.; Serrano, J. A.; Olmo, A.; Daza, P.; Yúfera, A. Sensing Cell-Culture Assays with Low-Cost Circuitry. *Sci. Rep.* **2018**, *8* (1), 1–11.
- (60) Watanabe, M. Faraday Discussions. *J. Japanese Assoc. Cryst. Growth* **2008**, *34* (4), 240–241.
- (61) Rouzrokh, A.; Ebrahimi, S. A.; Mahmoudian, M. Construction, Calibration, and Validation of a Simple Patch-Clamp Amplifier for Physiology Education. *Am. J. Physiol. - Adv. Physiol. Educ.* **2009**, *33* (2), 121–129.
- (62) Yan, B. Y.; Gu, Z.; Gao, R.; Cao, C.; Ying, Y. L.; Ma, W.; Long, Y. T. A Low Noise Amplifier System for Nanopore-Based Single Molecule Analysis. *Chinese J. Anal. Chem.* **2015**, *43* (7), 971–976.
- (63) Gu, Z.; Wang, H.; Ying, Y. L.; Long, Y. T. Ultra-Low Noise Measurements of Nanopore-Based Single Molecular Detection. *Sci. Bull.* **2017**, *62* (18), 1245–1250.

CHAPTER 5

Novel high-throughput and label-free screening of sickle cell disease patients based on their red blood cell stiffness

ABSTRACT

Understanding the morphological and mechanical changes in red blood cells are important for diagnostic and treatment methods in various hematological diseases. Sickle Cell Disease (SCD) is one of many such hematological genetic diseases that is caused by point mutation of the Hemoglobin β -globin (HBB) gene. The mutated hemoglobin (HbS) has a propensity to aggregate inside the red blood cells, making them rigid and, in extreme cases, sickle-shaped. The stiffened RBCs have been in general reported to block the blood flow and break apart, causing chronic anemia, episodes of pain, and multiple organ damage. High-Performance Liquid Chromatography (HPLC) is the most widely used technique for the screening of the hemoglobin variants present in the RBCs. The effect of the HbS gene (heterozygous and homozygous) is variable both in prevalence and the clinical manifestations. In this work, we present a label-free, cost-effective, high-throughput electro-fluidic technique to study changes in the mechanical and morphological characteristics of red blood cells. We apply our device to quantify the mechanical properties of RBCs as a function of RBC cell volume, storage time & temperature, as well as dependence on the stiffness-altering drug (Latrunculin-A). Further, we demonstrate the on-site application of our system by screening SCD patients. Identification was based on their RBC stiffness changes and a possible correlation with the patient's HbS content. Hence, the quantification of the mechanical properties may help in explaining the variability and identification of the high-risk patients for whom specific therapies could be targeted. Our measurements open the possibility for the whole cell stiffness to be used as a preliminary screening parameter for many haematological conditions. This shows promise of applications in other areas such as tumor cell identification, veterinary sciences as well as hydrogel technologies.

5.1 INTRODUCTION

Sickle cell disease is a group of genetic disorders caused by at least a 1-point mutation of the Hemoglobin β -globin (HBB) gene ¹⁻⁹. The mutated hemoglobin proteins can form a long polymeric chain, then causing aggregates inside the red blood cells, making them rigid and sickle-shaped ^{1,2,5-8,10}. The deformability, self-aggregation, and adherence of RBCs to the endothelial cells of the blood vessel walls have been a prominent factor for blood vessel occlusion (vaso-occlusions) during microcirculation. In SCD patients sickled RBCs, cause severe vaso-occlusion of the blood flow and the RBCs break apart quickly. The mean life span of RBCs reduces to 17 days from their natural life span of 120 days ⁵, which causes the state of anemia. The interruption of blood flow and the anemia cause episodes of chronic pain and multiple organ damage respectively ^{1,2,4-6,10-13}. There are multiple types of SCD, the specific type depends on which HBB gene mutation was inherited from the parents. A few most common SCDs are HbAS, HbSC, HbS β -thalassemia, HbSD, HbSE, and HbSO. Here, 'A' represents the normal hemoglobin gene, whereas, 'S', 'C', 'D', 'E', and 'O' represent the abnormal hemoglobin genes ^{5,6,8,9,14}. It is also important to note that, the sickling phenomenon in most of the SCD types mentioned above is enhanced in the oxygen-deprivation state ^{1-3,5-8,10-12}.

There has been a steady advance in SCD management ¹⁰⁻¹² and in the year 2003, the first approved drug for sickle cell anemia treatment, Hydroxyurea showed a significant decrease in the severity and number of chronic attacks in SCD patients ^{4-6,8-11,13}. Hydroxy urea reactivates the production of RBC cells with fetal hemoglobin (HbF) in the bone marrow, replacing the RBC cells with sickle hemoglobin (HbS) ^{2,10}. Currently, the most commonly used treatment methods for SCD patients include monitored administration of drugs like Hydroxyurea, N-acetylcysteine (NAC), Voxelotor, L-glutamine oral powder, Crizanlizumab, blood transfusion, and bone marrow transplant ¹⁵⁻¹⁷. The bone marrow transplants have proven to be quite effective in children ⁹. Blood transfusion is considered one of the last resorts medical experts use in most critical cases. It is important to note that the blood's storage temperature and time affect the inherited properties of RBCs compared with freshly drawn blood ^{18,19}, hence the efficacy of the blood transfusion might vary.

Although, there are numerous treatment drugs and medical procedures available for sickle cell patients, but one of the crucial challenges in dealing with this genetic disease is screening the population for SCD. Peripheral blood smear, solubility sickling test, isoelectric focusing, Lateral

Flow Immunoassay and high-performance liquid chromatography (HPLC) are the currently available commercial techniques for sickle cell disease diagnosis⁸. Lateral Flow Immunoassay²⁰ and solubility sickling tests²¹ have been reported inadequate in reporting sickle cell traits (HbAS) and often giving false negative and positive results respectively, hence causing unnecessary follow-up testing⁸. Among all, HPLC is a test that detects various variants of hemoglobin, hence considered the most accurate diagnostic tool for sickle cell patients, and is preferred by hematologists^{22,23}. Note, that although HPLC is considered quite accurate, it is quite expensive to be used for population-wide screening of SCD. Considering the limitations of other diagnostic approaches mentioned earlier in the text, a better label-free diagnostic platform is needed for the preliminary screening of patients showing hematological anomalies that can indicate towards sickle cell condition. The life expectancy of a person suffering from sickle cell disease (SCD) in men and women with constant medical assistance is reported 42 and 48 years respectively^{5,6}. About 300,000 babies are born every year with sickle cell anemia globally, although SCD cases are reported all across the world, most cases are reported in Nigeria, the Democratic Republic of the Congo, and India^{5,6,14}. The SCD has majorly affected India's Southern-central rural regions, due to which the Indian Government has announced the 'National Sickle Cell Anaemia Elimination Mission' in the 2023-24 budget²⁴. This research work is inspired to deal with at least three key elements and objectives of this mission set to eliminate SCD by 2047. In India, the prevalence of the HbS gene varies from 0 to 34% in different (tribal and urban) population groups. These sickle cell anemia patients and carriers have coexisting iron and other deficiencies, which is not picked up by HPLC. Hence the mechanical and morphological indices may be able to identify the high risk SCD patients who might have other asymptomatic underlying conditions²⁵. Here, we present a label-free, cost-effective, high-throughput electro-fluidic platform to screen SCD patients based on the changes in their red blood cell's mechanical and morphological characteristics. We propose an analytical approach to estimate cell stiffness. We show sensitive measurements of mechanical changes in cells caused due to either a disease or drugs. To establish the detection principle of our platform, we use Latrunculin-A (Lat-A) (actin inhibitor drug) treated RBCs to artificially and controllably soften the RBC samples taken from otherwise healthy donor. We then quantitatively relate our electro-fluidic measurements to changes in the cell stiffness by comparing with single-cell AFM force spectroscopy measurements. Further, we test our electro-fluidic experiments to show the dependence of parameters like cellular volume, sample incubation time & temperature, fluid flow

rates, and the device geometry to devise an analytical understanding of our measurements on cellular stiffness. Finally, we demonstrate on-site applications of our platform by screening the RBCs of SCD patients at the local hospital. We show distinct signal, based on their RBC stiffness, that allows us to categorically separate RBCs of SCD patients from the control group. Here we also show weak correlation between RBC stiffness and the lab measured HbS content in the RBCs of SCD patients. Note that, the detection of any mechanical changes in the sample does not confirm the disease, it may only function as a platform for preliminary screening for SCD detection. At the current stage samples must be tested via HPLC test for confirmation. The whole cell stiffness has been an overlooked parameter in the diagnostics industry, primarily due to lack of resolution and high throughput. We propose that our technique can be a promising platform for preliminary screening for various hematological conditions, tumor cell identification, veterinary sciences, and hydrogel technologies.

5.2 MATERIAL AND METHODS

5.2.1 Micropore Device Fabrication

Borosilicate capillaries (OD = 1 mm, ID = 0.5 mm, length = 75 mm) (Sutter Instrument) are used to fabricate micropores. Two types of devices were fabricated in this work: first type of devices with large micropores (pore dia (D_P) > cell size) for free-flight experiments and the second type with small micropores (pore dia < cells size) for constricted-flight experiments. The glass capillaries were cleaned by ultrasonication in ethanol, acetone, and then ethanol for 2 mins each. We then used a micropipette puller (Model P – 2000, Sutter Instrument) with the following parameters to pull the cleaned capillaries: Heat: 350, Filament: 0, Velocity: 25, Delay: 150, Pull: 200. For a free-flight micropore a conventional ‘V-shaped’ filament is mounted on a flame polisher instrument (MF – 900, Micro Forge, Narshige), to heat-shrink the pulled capillaries further to a desired dimension ($D_P >$ cell size). For devices with a long-constricted micropore, we mounted an ‘omega-shaped’ (Ω) filament on the flame polisher instrument to shrink the pulled capillaries to our desired micropore dimensions ($D_P <$ cell size). Then the omega-shaped (Ω) filament is replaced with the conventional ‘V-shaped’ filament to cut the glass capillary's extra front region and, flame polish the cut region. See Figure A7.1 for the images of the two types of filaments and the steps involved in fabricating these micropores. The images of all the free-flight and constricted-flight micropores used in this work are shown in Figure A7.2-A7.4. After flame polishing, it was also ensured that the micropores remained circularly symmetric before mounting them in a glass-bottom Teflon fluid chamber (~250 μ L) using curable silicone glue. The pore diameter (D_P) was estimated from the smallest opening in the side-view optical image of the pore cross-section. The micropore was then connected to a syringe pump (Picoplus Elite, Harvard Apparatus), using a PTFE tubing to generate stable fluid flow.

5.2.2 Sample Preparation

The blood samples for the study were acquired from human volunteers and SCD patients with institutional ethical board approval. For experiments, about 10 μ L of the whole blood (from a finger prick) was diluted by adding 500 μ L of RPMI-1640 (RPMI buffer, Sigma #SLBT0197) (pH = 7.4). The solution was then centrifuged three times at 600 rcf for 3 min at 4°C, and the RBCs were isolated from blood plasma and other cells, followed by resuspension of the RBC pellets in

1500 μL of RPMI (Sample stock concentration). After the isolation step for every experiment, RBCs were checked for health and debris under an optical microscope.

To measure drug-dependent changes in cell stiffness, aliquots of the actin depolymerizing drug Latrunculin A (Lat-A) (Cat# L5163, Sigma) were made in DMSO buffer to 1 mM stock concentration. An appropriate concentration of this aliquot was then used to treat the RBCs for different experiments in our study (see text). We incubated the cells in Lat-A for at least 5 minutes at room temperature before performing the experiments.

For AFM-based force spectroscopy experiments on RBC cells, we first made a 100 μL circular fluid cell using silicone glue on a glass slide (see Figure A7.5). This glass slide was cleaned by ultra-sonication in 20% Extran (Part# 34022090-5L Merck), ultrapure water twice (Milli-Q, Millipore), acetone, and ethanol for 5 min each. The glass slide was finally rinsed with ultrapure water to make sure there is no leftover ethanol from the last cleaning step. We then used Nitrogen to dry the fluid cell completely and immediately added 50 μL drop of 0.001% PLL for 30 min incubation on the glass surface. We then removed the PLL using vacuum line and immediately added 50 μL of RBC sample stock and incubated it for 30 min. The fluid cell was then gently washed with 3-5 mL of fresh RPMI buffer to make sure that all the floating cells were removed. After all these steps, the fluid cell is checked for RBC adherence under an optical microscope and then force spectroscopy measurements are performed using the AFM. Since the RBC stiffness was found to be dependent on the storage temperature and storage duration^{18,19} (see Figure A7.6), all experiments mentioned in this work were performed within 150 minutes of sample preparation.

5.2.3 Electro-Fluidic Measurements

The fluid cell design and experiment procedure is described elsewhere in detail^{26,27}. Briefly, microcapillary with the micropore at its tip was filled with RPMI buffer and glued on the fluid chamber. A PTFE tubing was connected at the back of the capillary to a syringe pump. RPMI buffer was filled in the glass bottom fluid chamber, micro-capillary, and microfluidic PTFE tubing avoiding air bubbles everywhere. The RPMI buffer works as the electrolyte for ionic current measurements through our device. A pair of Ag/AgCl electrodes, on either side of the micropore, were used to acquire the current signals, one dipped in the teflon fluid chamber and the other inserted in the tubing. A syringe pump (in withdraw mode) was used to pull samples into the micropore device maintaining a constant fluid flow (500 nL/min). The device was kept inside an

aluminum Faraday cage to reduce electrical noise. Low noise amplifier AM Systems (Model 2400), with 40 kHz bandwidth, and Dagan Chem-Clamp with 10 kHz bandwidth are used in this study, to apply a voltage across the devices and record the open pore current and translocation events. A noise eliminator (Hum-Bug, Quesst Scientific) was also used to eliminate the input source line frequencies in the signal. Data acquisition cards from National Instruments were used to acquire and store the signals using a custom-written LabVIEW code. All the experiments performed in the lab and the hospital, used NI PCIe-6363 and NI myDAQ data acquisition cards respectively, with data sampling done at 100 kHz. The recorded data was then low pass filtered at 10 kHz and analyzed using an offline custom-written LabVIEW code. A representative quantification of an event showing the drop in conductance (ΔG) and the dwell time (Δt) of a recorded electrical event is shown in Figure 5.1c. The ΔG values in free-flight micropores are used to quantify any physiological changes in RBCs²⁶ as shown in the schematic Figure 5.1d. In contrast, the Δt values from the constricted micropores indicate a change in the cellular stiffness as represented in Figure 5.1e. A more detailed quantitative estimation of the cellular stiffness is later in the text. The constricted-flight and free-flight experiments were performed on patient RBC samples simultaneously to avoid any aging effects. The equivalence of the two separate amplifiers used in this study was independently confirmed (see Figure A7.7). All datasets shown in this study are measured in triplicate (on same pore and same sample) and their mean and error of mean values of ΔG and Δt histograms is plotted.

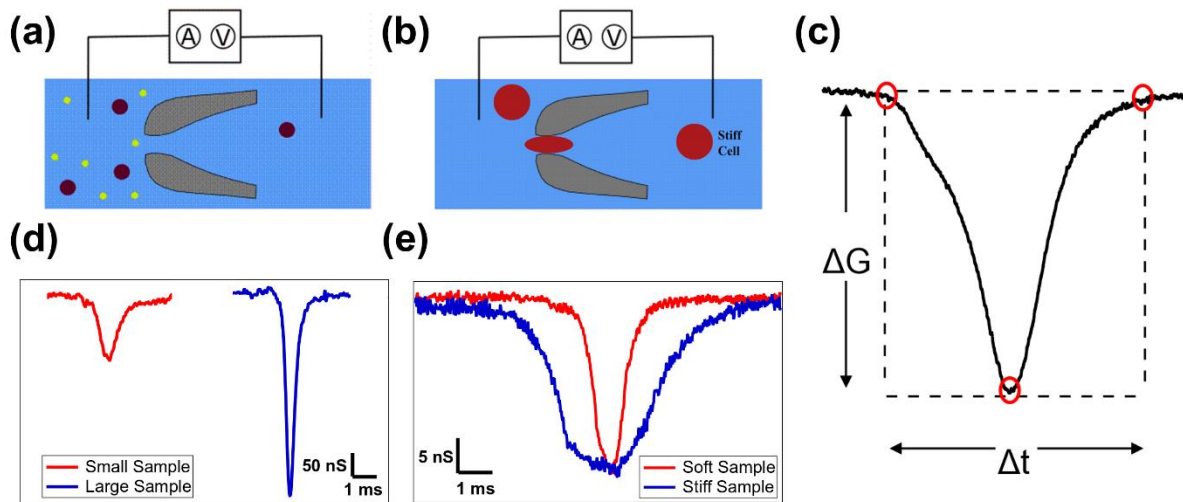


Figure 5.1 Schematic of electrofluidic device detection principle and signals for measurement of stiffness and size through the micropore device. (a) and (b) shows the schematics of cells translocating through a free flight and a constricted micropore device respectively. (c) A representative electrical event recorded when a cell translocates through the micropore is shown. The start, end and peak of the event is marked with red circles. The change in conductance (ΔG) and the dwell time (Δt) for the event is also shown here. (d) Representative events of free-flight experiment for a small (red) and a large (blue) model cells translocating through a 7.0 μm pore are shown here. Respective ΔG_{ff} values that corresponds to the difference in their sizes can be seen. (e) Representative electrical events of constricted-flight experiments is shown here. A comparison of ΔG_{cf} and Δt signals for a stiff (blue) and soft (red) samples are shown.

5.2.4 Changes in RBC stiffness using LatA

For experiments with controlled changes in RBC cell stiffness, the cells were incubated in RPMI buffer with appropriate concentration (see text) of the Latrunculin-A (Lat-A) drug. All stiffness comparison experiments were performed on the same device. The sample fluid chamber was washed thoroughly with 3 - 5 mL of filtered RPMI in between experiments with different drug concentrations ensuring no RBCs were left from the previous experiment.

5.2.5 AFM based cell stiffness Measurements

We used MFP-3D Infinity Bio (Asylum Research AFM, Oxford Instruments) AFM system mounted on an IX73 inverted Olympus microscope for cell stiffness measurements of RBCs. Contact mode silicon nitride cantilevers attached with a spherical polystyrene bead of 4.5 μm diameter (PT.PS.SN.4.5, Novascan) were used for taking F-X curves in this study. RBCs were adhered on the glass substrate fluid cells as briefed previously and the AFM tip was optically

centred on the RBC for every measurement. The RPMI buffer in the fluid cell was then gently washed with 1 mL (20 steps of 50 μ L each) RPMI with the appropriate Lat-A concentration needed for the study. This step was repeated for all the different Lat-A concentrations. It is important to note that another camera with a 60X objective was used to visually ensure the same cell was probed for all the Lat-A concentrations (see Figure A7.8). A schematic of a spherical bead attached to a cantilever probing a soft sample is shown in Figure A7.9 along with the cantilever's piezo position (z), deflection of the cantilever (d), and the indentation into the sample (x). The cantilever had a resonant frequency of 15 kHz, length of 225 μ m, width of 25 μ m, and spring constant of 0.03 N/m. Each cantilever was calibrated for the spring constant (k , pN/nm) and sensitivity (β , nm/V) using the thermal fluctuation mode of the AFM and taking an F-X curve on the glass surface in RPMI, respectively. On each cell, at least 10 F-X curves were recorded with a dwell time of 2 seconds between consequent curves. The data was recorded at a sample rate of 10 kHz and low pass filtered at 5 kHz, with a total vertical travel distance of 500 nm. During the approach curve, trigger in deflection value to stop and retrace was set at 100 nm. For F-X curve analysis and stiffness estimation, a custom-written MATLAB code was used to find the cantilever-sample contact point from the force-distance curve, a representative schematic of the contact point is shown in Figure A7.9. To ensure that our AFM experiments are well within the hertz model limit and to achieve reproducible fits, indentation depth of 50 nm was fixed for all curve fits.

5.3 RESULTS AND DISCUSSION

5.3.1 Detection of Cell Volume and Cell Stiffness in Micropore Experiments.

We first show the two modes (free-flight and constricted-flight) of micropore experiments which detect changes in cell volume and whole cell stiffness, respectively. Figure 5.2a shows electrical events corresponding to free-flight translocation of model cells (spherical polystyrene beads) of diameter 6.0 (blue) and 4.3 μm (red), through a micropore of 7.0 μm diameter. While the dwell time (Δt) corresponds to duration of translocation, the event depth (ΔG_{ff}) of these events correspond to the volume of the translocating model cells. The translocation events, scatter plot (ΔG_{ff} vs Δt) of events of a population of model cells and the ΔG_{ff} histograms are shown in Figures 5.2a, 5.2b, and 5.2c respectively. We see that model cells of different cell volumes correspond to distinct ΔG_{ff} histograms (see Figure 5.1d, 5.2a and 5.2c). A detailed study of cell volume estimation, its resolution and throughput characteristics has been described elsewhere ²⁶. In constricted-flight experiments, red blood cells (typical diameter ($\sim 8 \mu\text{m}$)) are translocated through a micropore of smaller diameter, using a syringe pump. In Figure 5.2d we show concatenated translocation events corresponding to native (blue) and soft (red, LatA treated) RBCs, translocating through a 3.6 μm micropore. The changes in event depths (ΔG_{cf}) and event duration (Δt) is shown as a scatter plot in Figure 5.2e. We see that in constricted-flight experiments, the event duration (Δt) corresponds to whole cell stiffness that allows the cells to squeeze through the constriction. Cells of different stiffness, as shown in Figure 5.2f, are identified with their distinct Δt histograms.

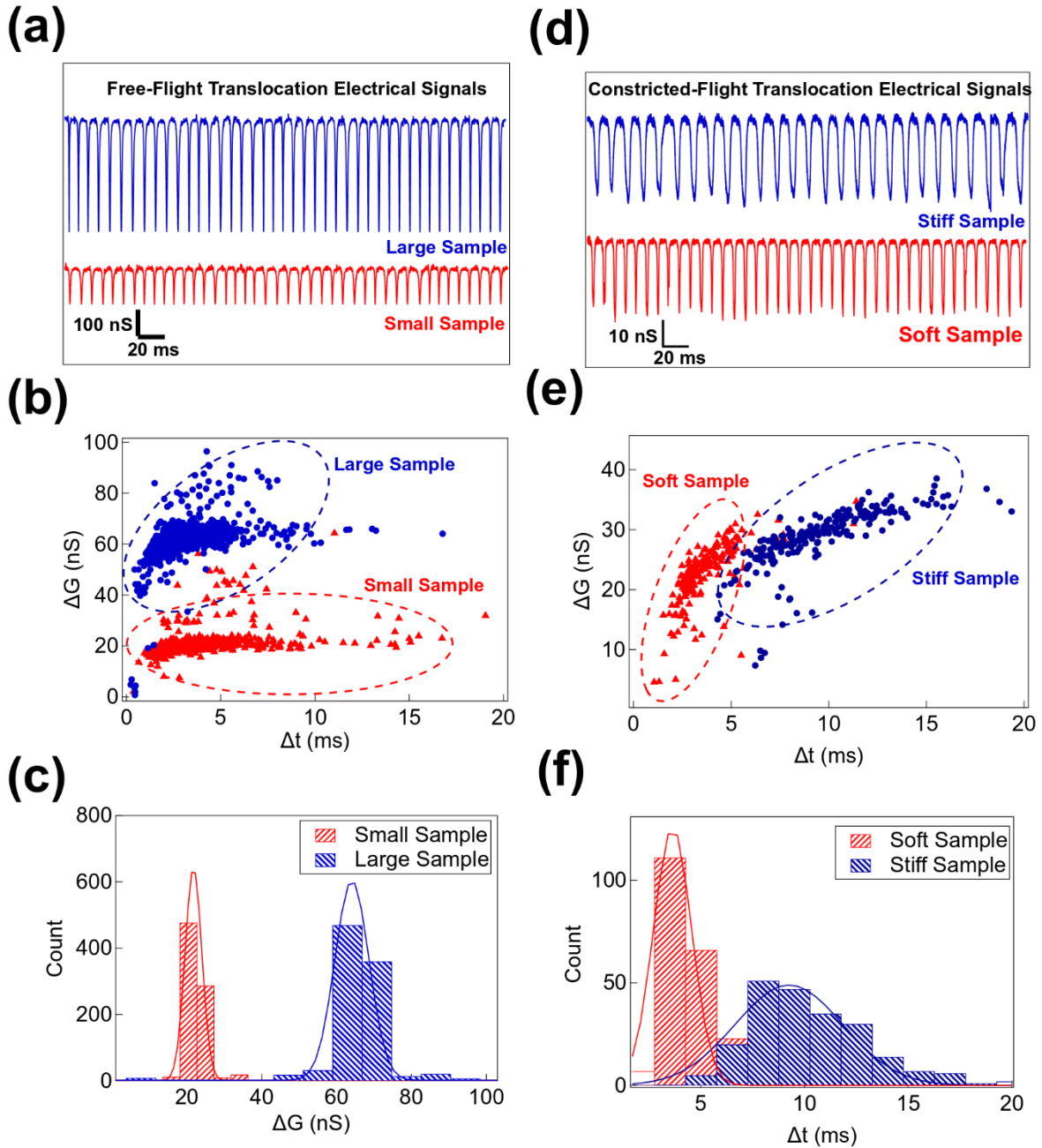


Figure 5.2: Demonstration of cell volume and stiffness detection using Micropore Devices. (a), (b) and (d) show translocation electrical signals, ΔG vs Δt scatter plot, and the Δt histograms for $6.0 \mu\text{m}$ (blue) and $4.3 \mu\text{m}$ (red) polystyrene beads recorded using a $7.0 \mu\text{m}$ micropore device respectively. (d), (e) and (f) show translocation electrical signals, ΔG vs Δt scatter plot, and the Δt histograms for Native (blue) and $1.0 \mu\text{M}$ Lat-A treated (red) RBCs were recorded using a $3.6 \mu\text{m}$ micropore device respectively.

5.3.2 Measurement of varying cell stiffness of RBCs

Next, we show constricted-flight measurement of RBCs that are softened to varying degree using the Lat-A drug. Latrunculin A is known to soften cells, in a concentration dependent manner, by binding to actin monomers near the nucleotide-binding cleft and thus sequestering them from actin polymerization in cells^{28,29}. This actin-spectrin scaffolding inside the inner membrane of RBCs gets affected due to the depolymerization of actin, which results in the softening of the entire cell³⁰⁻³². Red blood cells from a healthy donor were incubated in different concentrations of Lat-A and the effect of the drug on RBC sample was measured with constricted-flight experiments using micropores. Note, to avoid device dependent artifacts, experiments with all Lat-A concentrations were performed, back-to-back, on the same device, with thorough washing of fluid-cell between experiments and randomizing the order of Lat-A concentrations. The translocation events on a 3.6 μm diameter constricted micropore are shown in Figure 5.3a. It shows that the effect of reduced whole cell stiffness by incubation in Lat-A, translates to longer translocation times (Δt). Since Lat-A treated RBCs show no change in cell size/volume (see Figure A7.10), the increase in constricted-flight translocation times is attributed to reduction in cell stiffness. We confirmed this result with constricted flight experiments done on multiple devices. The constricted flight Δt data for RBCs treated with five different Lat-A concentrations and measured using 3.0, 3.2, 3.6, 3.8, and 3.9 μm diameter micropores is shown in Figure 5.3b. We observe a systematic decrease in the Δt with the increasing Lat-A concentrations.

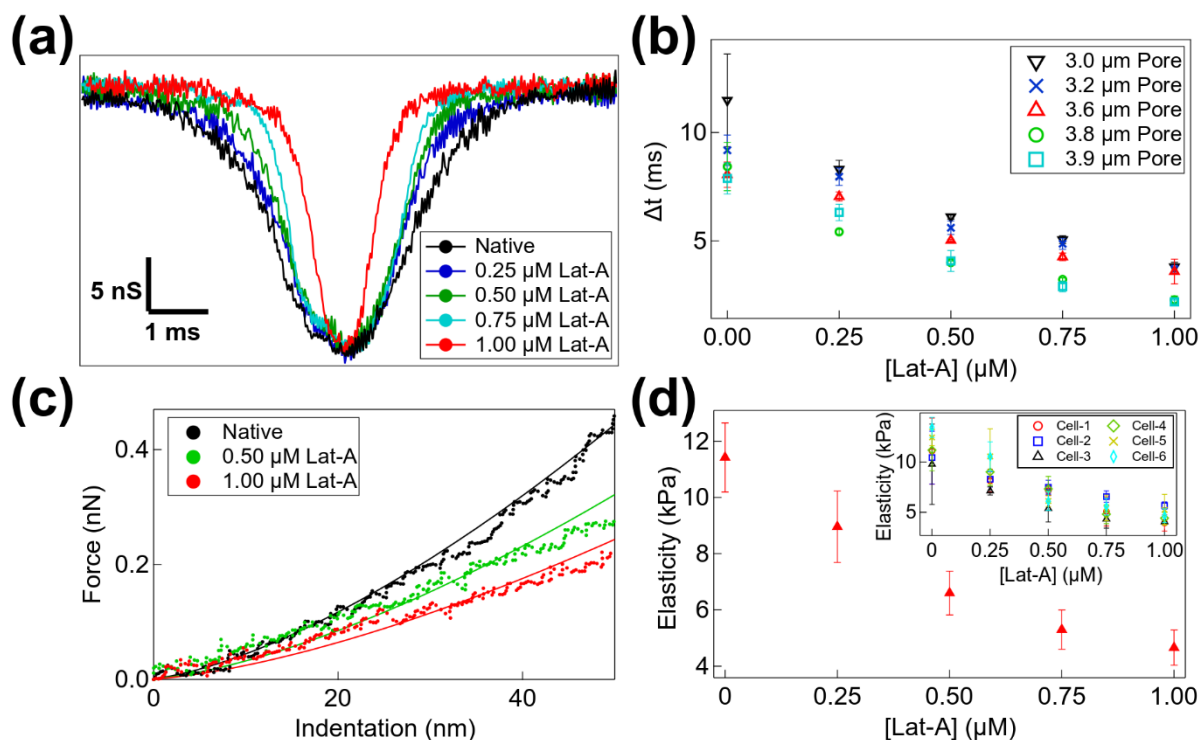


Figure 5.3: Effect of the actin inhibitor drug (Latrunculin-A) on the stiffness of red blood cells. (a) Translocation electrical signals for healthy RBCs (black) and RBCs treated with 0.50 (green) and 1.00 μM Lat-A drug, showing a decrease in the dwell time (Δt) translocating through the 3.6 μm micropore device. (b) Here we present the constricted flight dwell time (Δt) data, measured in 3.0, 3.2, 3.6, 3.8, and 3.9 μm diameters micropores, for red blood cells treated with Lat-A. For this experiment, RBC samples were obtained from a healthy donor (with 90.2 fL mean corpuscular volume, MCV, from pathology test). (c) AFM force-distance curve with the respective Hertz model fits (equation 5.1) for healthy RBCs (black) and RBCs treated with 0.50 (green) and 1.00 μM Lat-A drug. (d) The elasticity of red blood cells, incubated with different amounts of Lat-A as measured using the AFM force spectroscopy is shown here. A spherical (4.5 μm) cantilever having a spring constant of 0.03 N/m was used for the study. The inset shows the effect of Lat-A on six individual cells.

5.3.3 RBC Elastic Modulus Estimation

The reduction in whole cell stiffness by Lat-A is well documented^{28,29,33–37}. However, to compare the cell stiffness changes in the cell population being measured using the micropore, we directly quantify the change in their elastic modulus using an atomic force microscope (AFM) mounted on an inverted optical microscope. The AFM cantilever with a microsphere attached to the tip was optically aligned on top of the red blood cell and force-indentation curves were obtained by pressing the microsphere on the AFM tip into the cell (see Figure A7.9). From the force

indentation curves (see Figure 5.3c), the elastic modulus of RBCs was estimated using the Hertz Model given by:

$$F = \frac{4\sqrt{R_C}}{3} \frac{E}{1-\nu^2} \delta^{\frac{3}{2}} \quad (5.1)$$

Here, F , R_C , E , ν , and δ are force, the radius of the spherical probe, the elastic modulus of the sample, Poisson's ratio of RBC and indentation respectively. In Figure 5.3c, the force-indentation curves with the respective Hertz model fits for untreated RBC (black) and then same cell treated with 0.50 μM (green) and 1.0 μM (red) Lat-A drug, successively, are shown. The experiment is repeated for all Lat-A concentrations and the resulting changes in the elastic modulus of that same red blood cell is plotted in Figure 5.3d inset. These experiments are repeated on multiple cells. The Lat-A concentration-wise average (over all measured cells) of the AFM measurement of cell elasticity is plotted in Figure 5.3d. As expected, AFM measurements show systematic decrease in elastic modulus (E , kPa) with increasing Lat-A concentrations.

5.3.4 Empirical correlation between constricted micropore dwell times and Cellular Stiffness

We next establish qualitative dependence of dwell times (Δt , ms) of constricted-flight micropore experiments of RBCs with AFM-based elastic modulus (E , kPa) measurements. We note that both the micropore Δt measurements (Figure 5.3b), as well as their elastic modulus (Figure 5.3d), decrease similarly with different concentrations of Lat-A. This direct dependence is plotted in Figure 5.4a. We find, empirically, a linear dependence of constricted-flight translocation time, Δt , on the elastic modulus, E , of the translocating cell. We confirm this dependence for multiple devices with different micropore diameters (3.0, 3.2, 3.6, 3.8, and 3.9 μm) (see Figure 5.4a inset). The values of the linear fits are summarized in Table A7.1, with an average slope of 1.15 ± 0.12 . This suggests that the RBCs elastic modulus (E) and the constricted-flight micropore dwell times are directly proportional:

$$\Delta t \propto E \quad (5.2)$$

The constricted-flight dwell times may depend on the flow rate (Q , nL/min) (See Figure A7.11 and S12). We find that the linear dependence of Δt on the elastic modulus (E) is maintained across multiple Q values (see Figure 5.4b). The dwell time for constricted-flight experiments may also depend on the cell size/volume. Although Lat-A doesn't change the cell volume (Figure A7.10), this dependence should be considered when RBC from different donors (see below) is compared.

To establish this dependence, we acquired red blood cells from different healthy donors, with different mean cell volumes (as measured from pathology reports) and compared their free-flight ΔG_{FF} (corresponds to cell volume)²⁶ values to their constricted-flight Δt values. We used 4.3 and 8.0 μm micropore devices for constricted and free flight experiments respectively and the measured data is shown in Figure 5.4c. The dotted red line is a power-law fit giving the following relationship:

$$\Delta t \propto (\Delta G_{FF})^{2.37} \quad (5.3)$$

Here, since all RBC samples are from different healthy donors, we assume they differ only in their cell volume. The constricted-flight dwell times, Δt , also depend on the experimental parameters (such as fluid flow rate (Q), applied voltage (V_m), fluid viscosity (μ) and temperature (T)) as well as geometrical parameters (Length (L_p) and Diameter (D_p) of the micropore).

On combining all the parameters discussed above, we get an empirical relation:

$$\Delta t \propto E \times (\Delta G_{FF})^{2.37} \times f(L_p, V_m, D_p, Q, \mu, T) \quad (5.4)$$

The expression for Δt can now be written as:

$$\Delta t = k * E * (\Delta G_{FF})^{2.37} \quad (5.5)$$

Here, k is the proportionality constant. Note, that experiments that compare control and sample cells are performed using the same micropore (i.e. same L_p and D_p), a constant fluid flow (i.e. same Q and μ), and experimental and sample incubation temperature (T). This allows all the terms in $f(L_p, D_p, V_m, Q, \mu, T)$ to be absorbed into the proportionality constant k in the equation (5.5). We can now, directly measure the change in the elastic modulus of unknown samples, relative to the elastic modulus of a control sample:

$$E_{\text{relative}} = \frac{E_{\text{Sample}}}{E_{\text{Control}}} = \left(\frac{\Delta t_{\text{Sample}}}{\Delta t_{\text{Control}}} \right) * \left(\frac{\Delta G_{FF}^{\text{Control}}}{\Delta G_{FF}^{\text{Sample}}} \right)^{2.37} \quad (5.6)$$

Here, E_{relative} is the ratio of the elasticities of the sample and the control cells, whereas Δt and ΔG_{FF} are the constricted-flight dwell times and free-flight conductance change values respectively. We use the above empirical equation to estimate the relative change in RBC cell stiffness upon Lat-A treatment. The E_{relative} estimated for Lat-A treated RBC cells is shown in Figure 5.4d. In the same plot, we also show the change in elastic modulus (measured relative to the native RBC sample) as measured by the AFM for RBCs treated with the same concentrations of Lat-A. The excellent agreement of our micropore empirical approach with the AFM data shown in Figure 5.4d provides strength to our experimental procedure to estimate changes in the elastic modulus of a sample relative to a control.

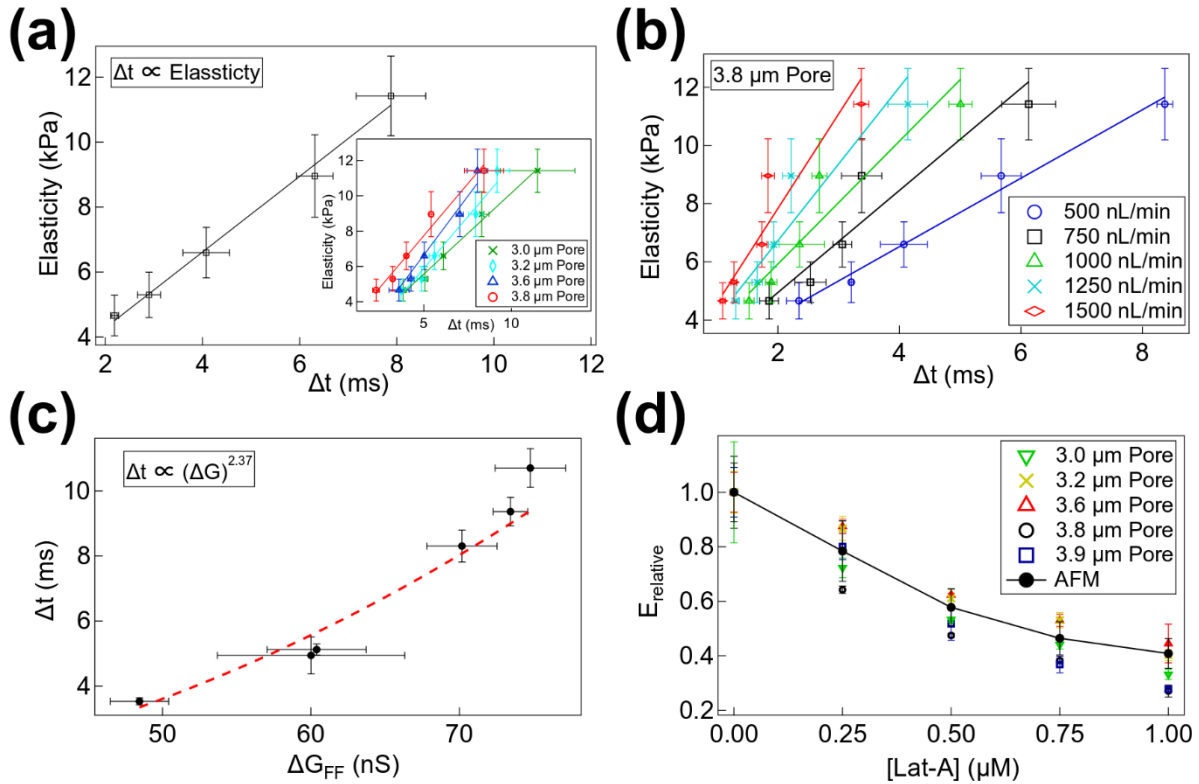


Figure 5.4: Empirical formulation for modeling the cellular stiffness using the electrofluidic experimental data. (a) The elasticity of RBCs obtained from the AFM is plotted with the Δt measurements of electrofluidic devices for cells treated with different concentrations of Lat-A. Note that there is a linear dependency of dwell time on the RBCs elasticity for all the micropores of different diameters used in the experiment. (b) The linear relationship between the elasticity of RBCs treated with different Lat-A concentrations with the constricted Δt measurements at different flow-rates using a $3.8 \mu\text{m}$ micropore device is shown (c) Red blood samples were acquired from different donors and, a 4.3 and $8.0 \mu\text{m}$ micropore device was used for constricted and free flight experiments respectively. Note that the constricted Δt has a power law dependence on the free flight ΔG with an exponent value of 2.37 , where the free flight ΔG corresponds to the volume of the cells. (d) The relative elasticity values from micropore and AFM experiments are shown here, note that both the data show similar trend for RBCs treated with different Lat-A concentrations.

5.3.5 Screening SCD Patients Based on RBC Stiffness

Finally, we apply our micropore device and analysis to compare translocation experiments performed on RBC samples drawn from a healthy donor and sickle cell disease patients, at the hospital (see setup image in Figure A7.15). The two samples, when measured using the same device, showed a clear distinction that the SCD patient RBCs translocated much slowly than the healthy RBCs. This indicates that the SCD RBCs are stiffer than the native healthy RBC cells. Representative plots of the raw electrical translocation signals, the ΔG_{cf} vs Δt scatter plots, and the

Δt histograms (see Figures 5.5a, 5.5b, and 5.5c respectively), show a clear distinction between the RBC samples from a healthy donor (blue) and an SCD patient (red) when detected using a constricted micropore device (4.6 μm). We measure RBC stiffness for 10 SCD patients (available during the time of this study, see Table A7.4). For these experiments, the samples were collected from patients and a healthy donor and the respective RBCs were suspended in RPMI buffer. This was to ensure that every SCD patient's RBC data had in-situ control of the healthy donor RBCs on the same device and experimental conditions. The RBCs were imaged (see Figure A7.16) and split into two batches for simultaneous free-flight (to compare cell volumes) and constricted-flight (to compare cell stiffness) experiments. The constricted-flight Δt bar-plot, the Δt histograms, Δt vs ΔG scatter plots, and the free-flight ΔG_{ff} bar plots for patient and control samples for all the experiments performed on SCD patients at the hospital are shown in Figure A7.17-A7.22 along with the respective constricted and free-flight micropore images used for the experiment. A complete summary of all the micropore experiments performed in the hospital and relevant pathology data from patients and the healthy donor is provided in Table A7.4. We note that, in general, RBCs from SCD patients have a larger distribution in cell volume (as measured by ΔG_{ff}) and take a longer time to translocate through the constricted geometry of the micropore (as measured by constricted-flight dwell times, Δt). This is shown in Figure 5.5d. Here we show the scatter plot of normalized constricted-flight Δt and ΔG_{ff} showing distinct populations for SCD patients (red dotted region) and healthy donors (blue dotted region). Note that the data shown in Figure 5.5d is normalized with a single control (healthy) donor (black triangle). The summary of the constricted-flight Δt values and the normalized Δt estimated for each patient w.r.t the control is shown in Figure A7.23. We then estimate the relative elastic modulus (E_{relative}) of patient RBCs using equation (5.6) and the data is shown in Table A7.5 and Figure 5.5e. The E_{relative} plot demonstrates that the SCD patient RBCs are, in general, always stiffer compared to the healthy donor RBCs by a factor of 2 – 4 and our electrofluidic device detects the SCD patient RBCs with high signal-to-noise ratio and throughput. Since we have HbS% values of the SCD patients from the HPLC-based pathology tests, we compared the relative elastic modulus of the RBCs of all the SCD patients of this study with their HbS % values in Figure 5.5f. We note that other than two data points (possibly belonging to Sickle Cell Trait patients, HbAS trait) the inset of Figure 5.5f shows a linear relationship of E_{relative} with the HbS% content in the cell. We note that given the low patient number of this study, this linear relationship is only empirical.

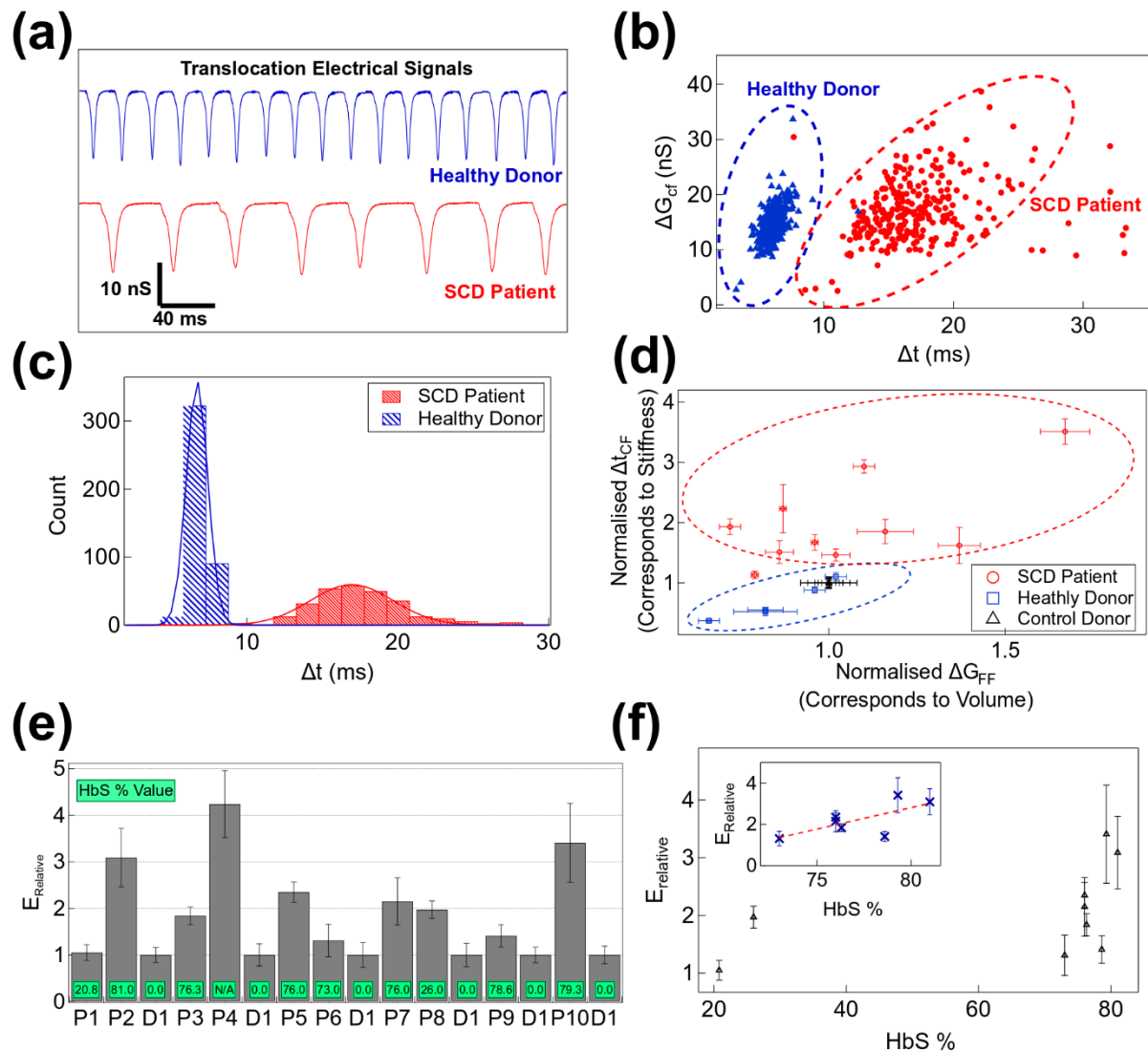


Figure 5.5: Cellular stiffness estimation of sickled RBCs of the SCD patients using microfluidic devices. (a), (b) and (c) show translocation electrical signals, ΔG vs Δt scatter plot, and the Δt histograms for RBCs from a healthy donor (blue) and an SCD patient (red) recorded using a $4.6 \mu\text{m}$ micropore device respectively (d) Scatter plot of Normalized Δt and ΔG from Constricted and free flight experiments respectively, showing distinct signals for SCD patients (red circles), Healthy donors (blue squares), and Control donors (black triangles). (e) shows the bar plot of relative elasticity empirically estimated according to equation 5.6 respectively. (f) Shows the relative elasticity of the SCD patient's samples plotted with their respective HbS % values obtained from the HPLC test. Inset shows an increasing trend of relative elasticity for SCD patients with higher HbS % values.

5.4 CONCLUSION

In this work, we first demonstrate the cell volume and stiffness detection principles using the free-flight and constricted-flight modes of our electro-fluidic micropore devices, respectively. We, then demonstrate that, for a soft sample like a biological cell, the measured dwell time (Δt) through a constricted micropore, corresponds to the stiffness of the sample. For this, we drew RBCs from a healthy donor and treated the cells with different concentrations of Latrunculin A drug which artificially soften the whole cell. The elastic moduli and the dwell time (Δt) values measured using AFM and micropore respectively, showed similar trends for RBCs treated with the same Lat-A concentrations. We found a linear relationship between the RBCs elastic moduli and the dwell times (Δt) measured using different micropore devices; the slope was 1.15 ± 0.12 at 500 nL/min. Next, we established an empirical expression for relative elasticity (equation (5.6)) of samples w.r.t to a control sample taken from a healthy donor. We found an excellent agreement of the relative elasticity measured using micropores with the normalised elastic modulus for Lat-A treated RBCs, where the control was native untreated RBCs. Finally, we demonstrated the application of micropores as a preliminary screening tool for Sickle Cell Disease (SCD) patients. Micropore translocation experiments were performed to compare RBCs from healthy and SCD patients. The Δt values of RBCs from the SCD patients were distinctively different from those of healthy donors. The relative elasticity of all patients was found to be always more than that of a healthy donor (see Figure 5.5e). We also found a weak linear relationship between the relative elasticity and the HbS% for SCD patients. It is important to note that the medication regimen of the participating patients could not be accounted for in our study. Our approach can identify SCD RBCs based on mechanical changes even in the absence of or way before the visual signatures of sickling of the blood cells, hence a better tool for population-wide preliminary screening. Although, any mechanical abnormality found in a sample doesn't guarantee a sickle cell disease, but surely confirms a possible haematological condition that would require more tests. Our research work will be crucial in achieving cost-effective mass population screening to assist in the Indian Government's 'National Sickle Cell Anemia Elimination Mission'. Our cellular mechanical sensing system is not limited to detecting mechanical properties of soft materials, but it also supports future applications in the pharmaceutical field as a quality control test, and understanding the underlying basics of cellular growth and its development cycle.

5.5 REFERENCES

- (1) Liu, Jia; Qiang, Yuhao; Alvarez, O. E. Du. Electrical Impedance Characterization of Erythrocyte Response to Cyclic Hypoxia in Sickle Cell Disease. *ACS Sensors* **2019**, *26*, 1783–1790.
- (2) Liu, J.; Qiang, Y.; Alvarez, O.; Du, E. Electrical Impedance Microflow Cytometry with Oxygen Control for Detection of Sickle Cells. *Sensors Actuators, B Chem.* **2018**, *255*, 2392–2398.
- (3) Liu, J.; Qiang, Y.; Du, E. Measurement of Electrical Properties of Sickle Cells from Electrical Impedance of Cell Suspension. *ASME Int. Mech. Eng. Congr. Expo. Proc.* **2017**, *3*, 1–6.
- (4) Tewari, S.; Rees, D. Morbidity Pattern of Sickle Cell Disease in India: A Single Centre Perspective. *Indian J. Med. Res.* **2013**, *138* (SEP), 288–290.
- (5) Obeagu, E. I.; Ochei, K.; Okoro, O. Sickle Cell Anaemia : A Review. *Sch. J. Appl. Med. Sci.* **2015**, *3*, 2244–2252.
- (6) Kato, G. J.; Piel, F. B.; Reid, C. D.; Gaston, M. H.; Ohene-Frempong, K.; Krishnamurti, L.; Smith, W. R.; Panepinto, J. A.; Weatherall, D. J.; Costa, F. F.; Vichinsky, E. P. Sickle Cell Disease. *Nat. Rev. Dis. Prim.* **2018**, *4*, 1–22.
- (7) Desai, D.; Dhanani, H. Sickle Cell Disease: History And Origin. *Internet J. Hematol.* **2012**, *1* (2).
- (8) Arishi, W. A.; Al-hadrami, H. A.; Zourob, M. Techniques for the Detection of Sickle Cell Disease: A Review. *Micromachines* **2021**, *12* (5), 1–22.
- (9) Serjeant, G. R. The Natural History of Sickle Cell Disease. *Cold Spring Harb. Perspect. Med.* **2013**, *3* (10), 1–12.
- (10) Ilyas, S.; Simonson, A. E.; Asghar, W. Emerging Point-of-Care Technologies for Sickle Cell Disease Diagnostics. *Clin. Chim. Acta* **2020**, *501*, 85–91.
- (11) Rees, D. C.; Brousse, V. A. M.; Brewin, J. N. Determinants of Severity in Sickle Cell Disease. *Blood Rev.* **2022**, *56* (June), 100983.
- (12) Shah, N.; Beenhouwer, D.; Broder, M. S.; Bronte-Hall, L.; De Castro, L. M.; Gibbs, S. N.; Gordeuk, V. R.; Kanter, J.; Klings, E. S.; Lipato, T.; Manwani, D.; Scullin, B.; Yermilov, I.; Smith, W. R. Development of a Severity Classification System for Sickle Cell Disease. *Clin. Outcomes Res.* **2020**, *12*, 625–633.

- (13) Marcus, S. J.; Kinney, T. R.; Schultz, W. H.; O’Branski, E. E.; Ware, R. E. Quantitative Analysis of Erythrocytes Containing Fetal Hemoglobin (F Cells) in Children with Sickle Cell Disease. *Am. J. Hematol.* **1997**, *54* (1), 40–46.
- (14) Stanley Davidson, S. *Davidson’s Principles and Practice of Medicine*; 2014.
- (15) Ndefo, U. A.; Maxwell, A. E.; Nguyen, H.; Chiobi, T. L. Pharmacological Management of Sickle Cell Disease. *P T* **2008**, *33* (4), 238–243.
- (16) Brandow, A. M.; Liem, R. I. Advances in the Diagnosis and Treatment of Sickle Cell Disease. *J. Hematol. Oncol.* **2022**, *15* (1), 1–13.
- (17) Abdel-Hadi, L.; Ventura Carmenate, Y.; Marx Castillo-Aleman, Y.; Sheikh, S.; Zakaria, A.; Phillips, J. Treatment of Sickle Cell Disease-Options and Perspective. *Am J Blood Res* **2023**, *13* (2), 61–70.
- (18) Xu, Z.; Zheng, Y.; Wang, X.; Shehata, N.; Wang, C.; Sun, Y. Stiffness Increase of Red Blood Cells during Storage. *Microsystems Nanoeng.* **2018**, *4* (1), 1–6.
- (19) Xu, Z.; Dou, W.; Wang, C.; Sun, Y. Stiffness and ATP Recovery of Stored Red Blood Cells in Serum. *Microsystems Nanoeng.* **2019**, *5* (1).
- (20) Albertolle, M. E. Characteristics of a Rapid, Point-of-Care Lateral Flow Immunoassay for the Diagnosis of Sickle Cell Disease. *Physiol. Behav.* **2017**, *176* (5), 139–148.
- (21) Alli, N. A.; Loonat, S. B. Solubility Tests and the Peripheral Blood Method for Screening for Sickle Cell Disease. *South African Med. J.* **2010**, *100* (10), 616.
- (22) Ou, C. N.; Rognerud, C. L. Diagnosis of Hemoglobinopathies: Electrophoresis vs. HPLC. *Clin. Chim. Acta* **2001**, *313* (1–2), 187–194.
- (23) Fisher, S. I.; Haga, J. A.; Castleberry, S. M.; Hall, R. B.; Thompson, W. C. Validation of an Automated HPLC Method for Quantification of Hemoglobin S. *Clin. Chem.* **1997**, *43* (9), 1667–1669.
- (24) MoHFW. National Sickle Cell Anaemia Elimination Mission
<https://sickle.nhm.gov.in/home>.
- (25) Bhatia, H. M.; Rao, V. R. *Genetic Atlas of the Indian Tribes*; Institute of Immunohaematology, Indian Council of Medical Research, 1986.
- (26) Kaushik, S.; Mahadeva, M.; Murugan, K. D.; Sundaramurthy, V.; Soni, G. V. Measurement of Alcohol-Dependent Physiological Changes in Red Blood Cells Using Resistive Pulse Sensing. *ACS Sensors* **2020**, *5* (12), 3892–3901.

- (27) Kaushik, S.; Selvanathan, P.; Soni, G. V. Customized Low-Cost High-Throughput Amplifier for Electro-Fluidic Detection of Cell Volume Changes in Point-of-Care Applications. *PLoS One* **2022**, *17* (4), e0267207.
- (28) Braet, F.; De Zanger, R.; Jans, D.; Spector, I.; Wisse, E. Microfilament-Disrupting Agent Latrunculin A Induces an Increased Number of Fenestrae in Rat Liver Sinusoidal Endothelial Cells: Comparison with Cytochalasin B. *Hepatology* **1996**, *24* (3), 627–635.
- (29) Fujiwara, I.; Zweifel, M. E.; Courtemanche, N.; Pollard, T. D. Latrunculin A Accelerates Actin Filament Depolymerization in Addition to Sequestering Actin Monomers. *Physiol. Behav.* **2019**, *176* (3), 139–148.
- (30) Gokhin, D. S.; Nowak, R. B.; Khoory, J. A.; De La Piedra, A.; Ghiran, I. C.; Fowler, V. M. Dynamic Actin Filaments Control the Mechanical Behavior of the Human Red Blood Cell Membrane. *Mol. Biol. Cell* **2015**, *26* (9), 1699–1710.
- (31) David S. Gokhin and Velia M. Fowler. Feisty Filaments: Actin Dynamics in the Red Blood Cell Membrane Skeleton. *Curr Opin Hematol.* **2017**, *23* (3), 206–214.
- (32) Leterrier, C.; Pullarkat, P. A. Mechanical Role of the Submembrane Spectrin Scaffold in Red Blood Cells and Neurons. *J. Cell Sci.* **2022**, *135* (16), 1–9.
- (33) Vargas-Pinto, R.; Gong, H.; Vahabikashi, A.; Johnson, M. The Effect of the Endothelial Cell Cortex on Atomic Force Microscopy Measurements. *Biophys. J.* **2013**, *105* (2), 300–309.
- (34) Fischer, T.; Hayn, A.; Mierke, C. T. Effect of Nuclear Stiffness on Cell Mechanics and Migration of Human Breast Cancer Cells. *Front. Cell Dev. Biol.* **2020**, *8* (May), 1–18.
- (35) Fujiwara, I.; Zweifel, M. E.; Courtemanche, N.; Pollard, T. D. Latrunculin A Accelerates Actin Filament Depolymerization in Addition to Sequestering Actin Monomers. *Curr. Biol.* **2018**, *28* (19), 3183-3192.e2.
- (36) Kubitschke, H.; Schnauss, J.; Nnetu, K. D.; Warmt, E.; Stange, R.; Kaes, J. Actin and Microtubule Networks Contribute Differently to Cell Response for Small and Large Strains. *New J. Phys.* **2017**, *19* (9).
- (37) Stack, T.; Vahabikashi, A.; Johnson, M.; Scott, E. Modulation of Schlemm’s Canal Endothelial Cell Stiffness via Latrunculin Loaded Block Copolymer Micelles. *J. Biomed. Mater. Res. - Part A* **2018**, *106* (7), 1771–1779.

CHAPTER 6

CONCLUSION AND FUTURE WORK

In the first chapter of this thesis, we gave a brief introduction to various mechanosensing approaches used for cellular mechanical and physiological studies performed by researchers. We introduced various experimental methods used to understand the whole cell stiffness, membrane mechanical properties, fluidic properties of the cellular cytoplasm, and viscoelastic properties of cells in the suspension. The theoretical aspects and models associated with all these experimental techniques were also discussed in this chapter. In the next chapter, all the details on the sample preparation protocols, and the procedures involved in procuring and handling the biological samples, drugs, and chemicals used are discussed in great detail. The working principle of the Resistive Pulse Technique (RPT) and the Atomic Force Microscopy (AFM) force spectroscopy measurements majorly used in this thesis work are detailed in this chapter. A review of different theoretical models used to understand the data acquired using the resistive pulse technique is also briefed here. The steps involved in fabricating the custom-made micropore device for RPT experiments and the sample incubation chamber made in the lab for AFM force spectroscopy study on cells are introduced here exhaustively. In the third chapter, we demonstrated the high throughput and high-resolution measurement capabilities of our electrofluidic devices by measuring the volume of model cells, followed by the measurement of the volumetric changes in red blood cells in physiologically relevant alcohol concentrations. Since alcohol exposure has been postulated to adversely affect the physiology and function of red blood cells (RBCs), our measurements showed that alcohol consumption recreationally alters cell physiology in ways that are subtle and unresolved with conventional microscopy methods. We also for the first time present the direct quantification of temporal and concentration-dependent changes in red blood cell volume upon ethanol exposure. In the next chapter, we introduce our low-cost and portable trans-impedance amplifier and characterize and compare all its electrical properties with commercial amplifiers, including the maximum range, absolute error percentage, and RMS noise of the amplifier in the measured current signal, and the bandwidth. Our low-cost amplifier (~100-fold lower than commercial alternatives) is battery-run and completely portable for point-of-care applications. In the fifth chapter, we first

establish the quantitative effect of the cytoskeleton inhibitor drug (Latrunculin-A) on cellular elasticity measurements using atomic force microscopy and micropore devices in red blood cells. We perform various control experiments and establish an empirical formulation for measuring the relative elastic modulus of the cell. We then make use of our formulation to demonstrate the diagnostic application of the lab-made electro-fluidic system on sickle cell disease (SCD) patients, the experiments were performed on-site at the St. Johns Medical College Hospital. Identification was based on their RBC stiffness changes and a possible correlation with the patient's HbS content. This thesis work establishes a label-free high-throughput, cost-effective, and microscopy-free experimental approach to quantitatively study the cellular mechanical and physiological properties. The on-site application of SCD patient screening shows that this work promises the possibility for the whole cell stiffness to be used as a preliminary screening parameter for many hematological conditions and applications in other areas such as tumor cell identification, veterinary sciences as well as hydrogel technologies.

There are various plausible extensions of this thesis work, a few of them are discussed later in this chapter.

6.1 Cellular porosity under small applied voltages

Electroporation and ion channels in cells and lipids has been a topic of interest for researchers as well as pharmaceutical industries. These techniques are used for drug testing and delivery, cell engineering and toxicology studies. Short high voltage electrical pulses are used to create temporary pores in the cellular membrane, which allows chemicals or molecules to easily pass across the cell, which normally wouldn't, and these electrical pulses can often cause damage to the membrane. We propose that even small electrical voltages form pores across the cellular membrane, the preliminary data demonstrating this phenomenon is shown in the figure 6.1. We compared the change in the conductance for a hard sphere and RBCs, and show that conductance drop (ΔG) increases with voltage for RBCs and remains almost constant for hard spheres as they translocate through our electro-fluidic device. This suggests that increasing even small voltages (~ 100 mV), causes pore formations at the cellular membrane and the ion transportation and current detection across the electrofluidic device can be measured. Although, these are just postulations, and further investigation is needed in this regard.

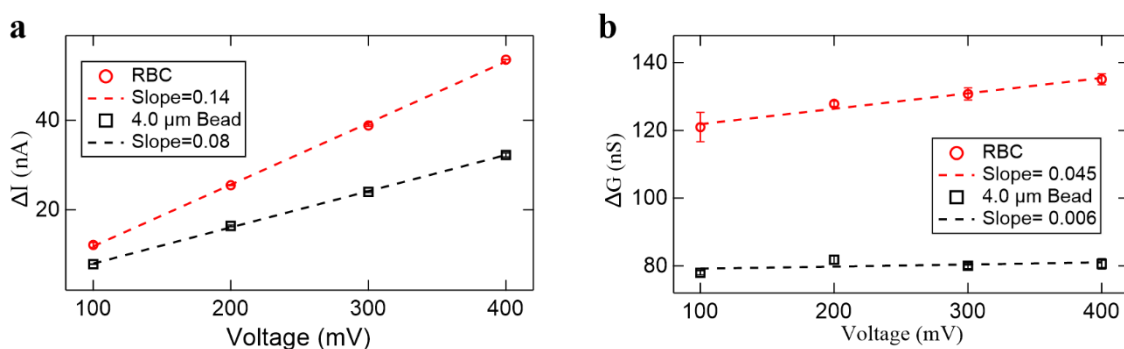


Figure 6.1 RBC porosity effect under applied voltages: **a** The change in open pore current at different voltages caused by translocation of $4.0 \mu\text{m}$ beads (black) and RBCs (red) through an $8.3 \mu\text{m}$ micropore device. **b** The change in the conductance of the micropore device at different voltages caused by the translocation of $4.0 \mu\text{m}$ beads (black) and RBCs. The dotted lines are the linear fit to the data in both graphs.

6.2 Translocation of Cells through a dual micropore device for stiffness estimation

In the fifth chapter, both the free flight and constricted flight experimental data were needed to estimate the relative elastic modulus of the sample using the Equation 5.6. Hence, the free-flight and constricted flight experiments performed simultaneous. We propose that a dual micropore system can be used to measure the cell volume and stiffness in a single device. Such a dual pore device can either be forged using a glass capillary or fabricated using soft lithography. In the Figure 6.2, we present the preliminary experimental data using a glass capillary based dual pore electrofluidic device to perform free-flight and constricted flight experiments.

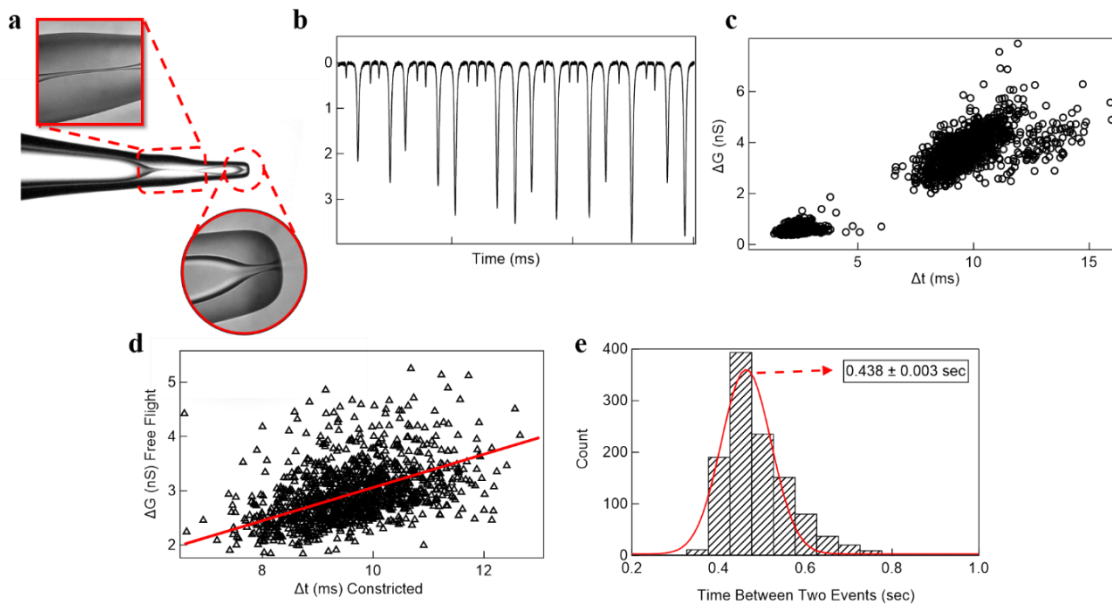


Figure 6.2 Translocation of RBCs through a single glass capillary dual micropore device: **a** Microscopic image of a single glass capillary dual micropore device is shown. The inset shows the magnified image of the constricted (square) and free-flight (circle) micropore regions of the device. **b** The time-series electrical data of the free-flight (small signals) and constricted (large signals) translocation events for RBCs are shown here. Note that the free-flight and constriction events occur in pairs. **c** ΔG vs Δt scatterplot of RBCs translocating through the dual micropore device is shown here. **d** The pair-wise ΔG (free flight) vs Δt (constricted) scatterplot of RBCs translocating through the dual micropore device is shown here. **e** Histogram fitted with the Gaussian for the time between the free flight and constricted electrical pulse for individual RBCs is shown here.

6.3 Studying the cellular membrane fluctuations during cell translocation through a constriction micro-channel.

Here, we propose a simple experimental idea, to detect the cellular membrane fluctuations, as cells translocate through a constricted microchannel. We propose that when a single cell is stuck in the sensing region of the constricted micro-channel, the fluctuations in the cellular membrane will be embedded in the blocked measured current. The Fourier analysis of the blocked current, decoupled from the unblocked current across the sensing region will possibly give the recurrence information of the membrane fluctuations. It is important to note that, the data acquisition sampling rate and the bandwidth of the electrical system used to record the data will be crucial in this experiment. The membrane fluctuation frequency must lie in the flat region of the frequency response curve of the amplifier system to be used, and the data acquisition sampling rate must be at least 10 times of the membrane fluctuation frequency to be able to detect at least the principle frequencies of the fluctuations, without any clamping effects.

APPENDIX 1

Basic Rules for Writing and Plotting Experimental Data

A1.1 Using correct significant figures to avoid false resolution in presenting experimental data

A significant figure is an important parameter in science and writing/mentioning numbers by keeping too many significant numbers can give an incorrect sense of least count of the measurements or resolution of the technique. Hence, while writing a research paper the significant numbers must be mentioned correctly. Consider the following rules in mind to get correct significant numbers:

- Generally, any experimental data is a mean of multiple measurements. Hence, it has to be written as (mean \pm Standard deviation). Please also note that if data is fitted to some function the fitting parameters are mentioned as (Fit value \pm error). So, in general, any experimental value will always be written as (Value \pm error/SD).
- The first step to get the correct significant numbers is to round off the error (or standard deviation) to the first significant digit. Here are some examples:
 - 2.83 has to be rounded off to 3 (Please Note 3 and NOT 3.0).
 - 0.246 will be rounded off to 0.3
 - 12.6 will be rounded off to 10
- After rounding off the error/standard deviation to the first significant digit, the value has to be rounded off to the same place value. Here are some examples:
 - 33.43 ± 2.83 will be written as 33 ± 3
 - 13.56 ± 0.246 will be written as 13.6 ± 0.3
 - 114.56 ± 12.6 will be written as 110 ± 10
- Please note that there is an exception in the rule to round off the error/standard deviation values to the first significant values. If the error value on rounding off to the first significant value ends up to the first decimal place with a value of 1, then the rounding off has to be done up to the second significant figure. Here are some examples:

- 0.126 will be rounded off to 0.13
 - 0.144 will be rounded off to 0.14
 - But 0.15 will be rounded off to 0.2
- Here is an example of writing the numbers with incorrect and then the correct significant numbers:

Bead Diameter (μm)	ΔG (nS)	V _{Bead} ^{Calc} (fL)	$V = \frac{\Delta G}{\sigma} * L_{\text{eff}}^2(8.8 \mu\text{m})$ (fL)	$V = \frac{\Delta G}{\sigma} * L_{\text{eff}}^{\text{Global}^2}$ (fL)	$V = \frac{\Delta G_{\text{sample}}}{\Delta G_{3.0 \mu\text{m}}} * V_{3.0 \mu\text{m}}$ (fL)	$V = \frac{\Delta G_{\text{sample}}}{\Delta G_{7.03 \mu\text{m}}} * V_{7.03 \mu\text{m}}$ (fL)
4.0	83.98 ± 4.38	33.52 ± 0.28	34.57 ± 4.38	34.26 ± 4.46	34.44 ± 4.0	33.43 ± 2.83
6.0	273.74 ± 29.57	113.14 ± 0.63	112.67 ± 20.58	111.68 ± 20.79	112.25 ± 19.32	108.98 ± 15.32

Table A1.1 Incorrect way of writing significant figures: The numbers shown here are obtained after taking an average from multiple experiments, and these averaged numbers with incorrect significant digits give a false sense of instrumental resolution.

Bead Diameter (μm)	ΔG (nS)	V _{Bead} ^{Calc} (fL)	$V = \frac{\Delta G}{\sigma} * L_{\text{eff}}^2(8.8 \mu\text{m})$ (fL)	$V = \frac{\Delta G}{\sigma} * L_{\text{eff}}^{\text{Global}^2}$ (fL)	$V = \frac{\Delta G_{\text{sample}}}{\Delta G_{3.0 \mu\text{m}}} * V_{3.0 \mu\text{m}}$ (fL)	$V = \frac{\Delta G_{\text{sample}}}{\Delta G_{7.03 \mu\text{m}}} * V_{7.03 \mu\text{m}}$ (fL)
4.0	84 ± 4	33.5 ± 0.3	35 ± 4	34 ± 4	34 ± 4	33 ± 3
6.0	270 ± 30	113.1 ± 0.6	110 ± 20	110 ± 20	110 ± 20	110 ± 20

Table A1.2 Correct way of writing significant figures: The numbers shown here are obtained after taking an average from multiple experiments, and these averaged numbers are then written with correct significant digits, avoiding any false sense of instrumental resolution.

It is important to note that an incorrect use of significant figures provides a false sense of precisions or resolutions of the instrument used to record the experimental data. For example, the value of volume in the fourth column for a 6.0 μm bead in the first table reads 112.67 fL, whereas the lowest volume resolution for this technique is reported to be 0.6 fL at cellular sizes. The number ‘112.67’ with incorrect significant figures gives a false sense of precision up to two decimal places, i.e. a resolution of 0.01 fL, which is incorrect.

A1.2 Importance of using the standard deviations for correctly fitting the experimental data

In the experimental research field, multiple sets of experiments are done to make sure that the data obtained is recurrent. The data obtained generally has some error within different experimental sets, hence the values after multiple data sets are written in the form of mean and standard deviation as (Mean \pm Standard Deviation). Now suppose the obtained data is to be fitted to a functional form (say a straight line), then there are two ways to do it:

- Consider only the mean values to fit the data. (Incorrect Method)
- Consider both the mean values as well as the standard deviation to fit the data. (Correct Method)

Why Standard Deviation is important while fitting the data to a functional form:

- Inverse standard deviation is used as weights to fit the data to a function form.
- Please note that weights are an important parameter in fitting, as they decide which data point will contribute more to the fitting relative to other data points.
- We can understand this by an example, suppose we have four Y values for each X, and ΔY is the error in the measurement of Y in multiple sets. If the ΔY_2 is smaller than others, this means the multiple measurements gave Y_2 values very close to each other (i.e. Y_2 value is the most recurrent and must be given more weightage than other Y values while fitting).
- Hence, while fitting data to a functional form we must give three parameters, which are X, Y, and the weight.
- Please note that each software takes the weight values in a specific way. In general, the inverse of the standard deviation is the weight for fitting. But, we need to be careful what column is given as weight to the software (Standard deviation or inverse of standard deviation). For, instance Igor software has both options (see Figure A1.1a).

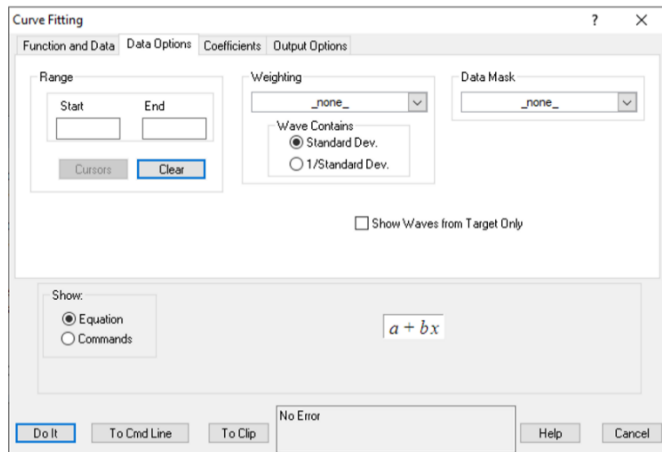
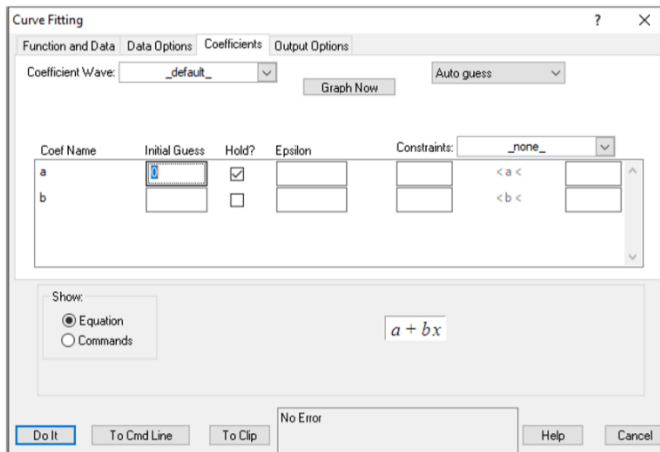
a**b**

Figure A1.1 Manual Fitting options in Igor software: (a) Screenshot of Igor software fitting dialog box, showing the option for choosing the weights for the fitting. (b) Screenshot of Igor software fitting dialog box, showing the option for fitting parameters to be kept fixed or floating.

- In Figures A1.2a and A1.2b we show some examples demonstrating the difference in the slope values obtained by fitting a straight line to data with and with standard deviations as weight
- It is important to understand the behavior of the function form before performing the fitting. This will help us decide whether a fitting parameter should be fixed or floating (see Figure A1.1b).
- Let us understand this with an example, the graphs shown above are fitted with the functional form $\Delta G = k * Volume$. We need to estimate the coefficient k , also it is known that the functional form must have an intercept zero, hence before performing the fit the intercept was fixed to zero. (Note: Always see the function and understand which fitting parameter must be fixed and which must be allowed to float. Softwares are written to give the best fit irrespective of whether the science behind the fit is considered or not. So it's our job to see if science is correct before and after the fit).

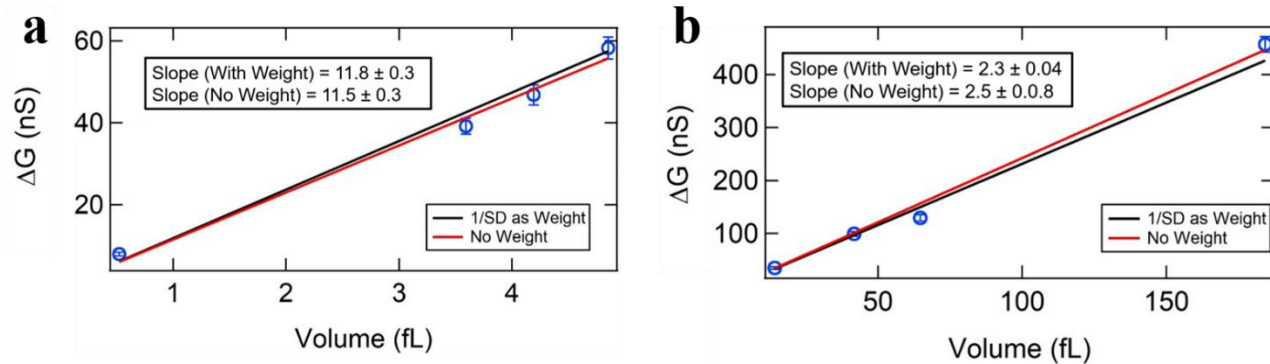


Figure A1.2 *Difference in fitting results due to weights and constraints: (a) and (b) showcase the examples of differences in the values obtained from fitting experimental data to a linear function with and without incorporating the standard deviations as weights.*

APPENDIX 2

Pressure in a Cylindrical and Conical Geometry

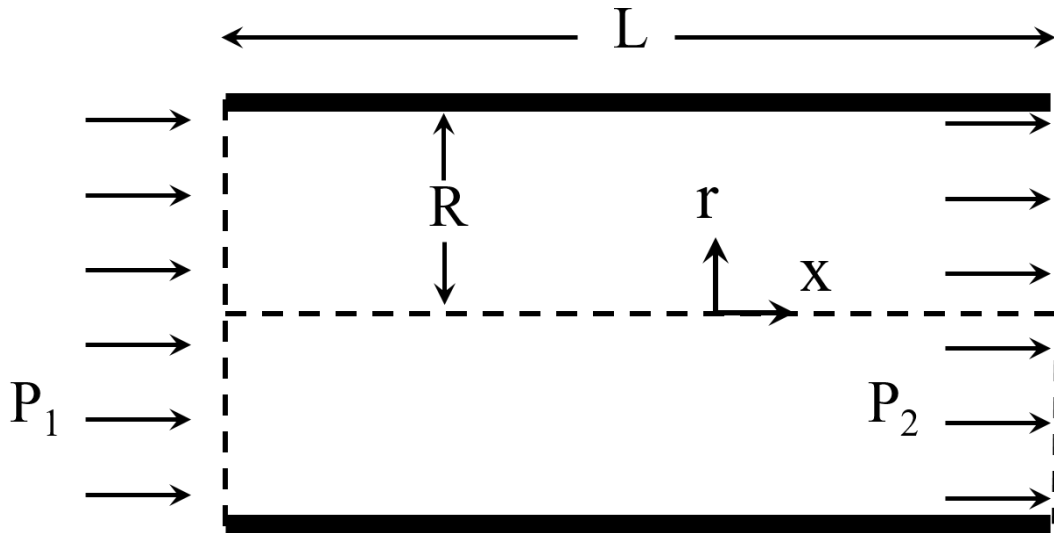


Figure A2.1 Schematic of a cylindrical region: A 2D schematic of a cylindrical region is shown here, showcasing the flow of a fluid at pressures P_1 and P_2 over the length ' L ' and radius ' R '.

The expression for the pressure drop between two points inside a cylindrical capillary can be stated as following using the Hagen-Poiseuille Equation:

$$\Delta P = \frac{8\eta Q}{\pi R^4} L \quad (\text{A2.1})$$

Here, ΔP is the pressure drop ($P_2 - P_1$) over the length ' L ' inside a cylinder of radius ' R ', when a fluid of dynamic viscosity ' η ' is flowing with a constant fluid flow of ' Q '. See Figure A2.1 above for a visual perspective of the geometric parameters used in equation (1).

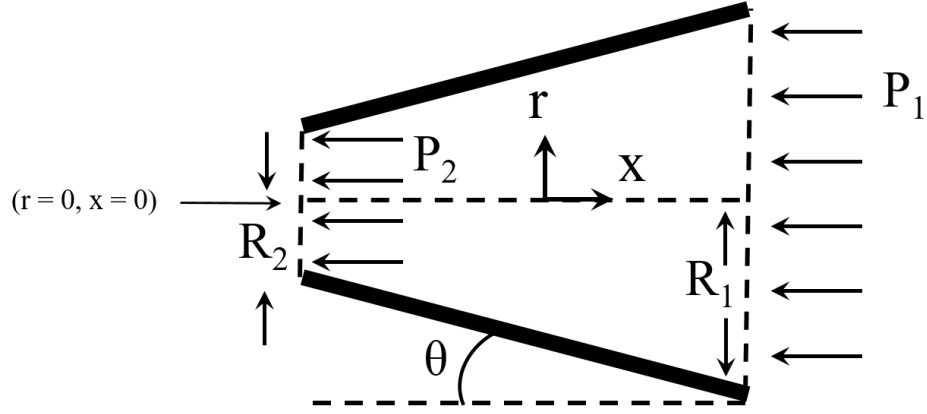


Figure A2.2 Schematic of a truncated conical region: A 2D schematic of a truncated conical region is shown here, showcasing the flow of a fluid at pressures P_1 and P_2 between the region having a half angle ' θ ', and radius ' R_1 ' and ' R_2 '.

Now, we will establish a relationship for the pressure drop across a conical region with the same fluid flowing through it. Firstly, we consider a small cylinder of length ' dX ' and radius ' r ', then according to the equation (1) the expression for pressure drop across dL length will:

$$dP = \frac{8\eta Q}{\pi r^4} dL \quad (A2.2)$$

Here, the dL can be expressed in terms of ' r ' and ' θ ' as:

$$dL = dr \cot \theta \quad (A2.3)$$

Now, on combining equations (2) and (3), we get the following expression:

$$dP = \frac{8\eta Q \cot \theta}{\pi r^4} dr \quad (A2.4)$$

On integrating both sides we get:

$$\int_{P_1}^{P_2} dP = \frac{8\eta Q \cot \theta}{\pi} \int_{R_1}^{R_2} r^{-4} dr$$

$$\Delta P = P_2 - P_1 = -\frac{8\eta Q \cot \theta}{3\pi} (R_2^{-3} - R_1^{-3}) \quad (A2.5)$$

APPENDIX 3

Analytical calculation of volume change in Red Blood Cells

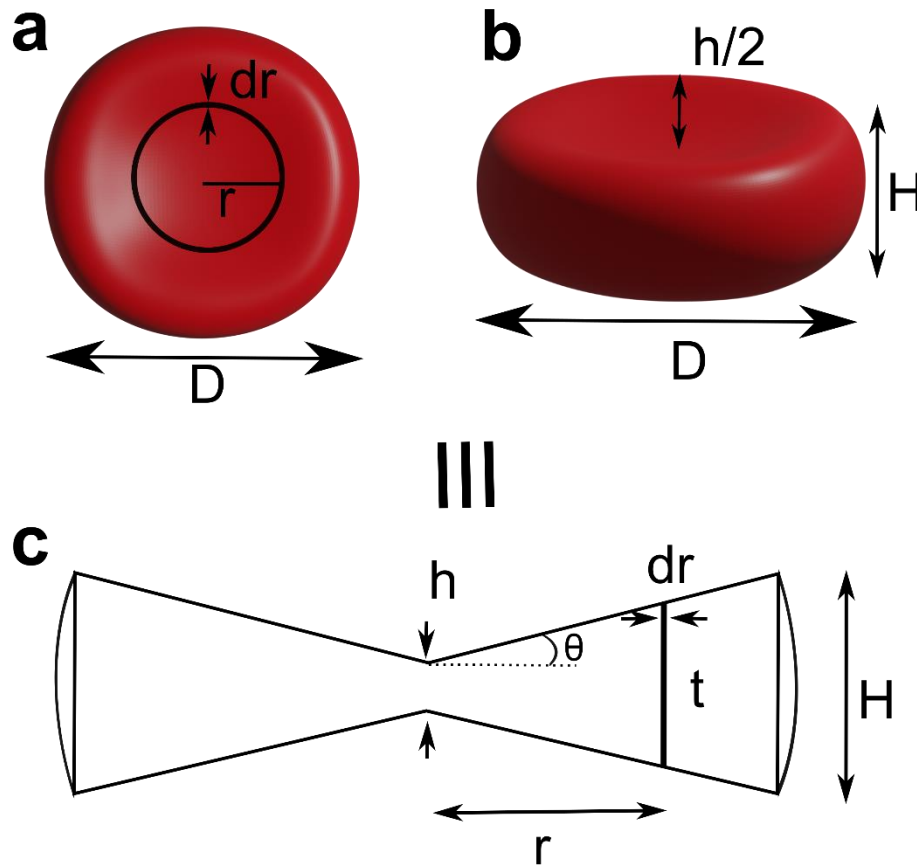


Figure A3.1 Analytical Volume of RBC. (a) Schematic of an RBC with diameter D and a volume element at a radial distance r . (b) Side view of the same RBC schematic showing the dimple height (h), RBC maximum thickness (H) and diameter (D). (c) Dumbbell-shaped disc approximation of an RBC to estimate the volume, with a volume element at a radial distance r and thickness t .

Here we assume that the RBC is a dumbbell-shaped disc of diameter D , maximum height H , and minimum height h (as shown in Figure A2.3c). In Figure A2.3a, the small volume element (dV) can be written as:

$$dV = 2\pi r t \cdot dr \quad (\text{A3.1})$$

Where 't' is the thickness of the volume element. We have the following expressions from Figure A2.3c:

$$t = 2 \left[\frac{h}{2} + r \cdot \text{Tan}(\theta) \right] \quad (\text{A3.2})$$

$$\text{Tan}(\theta) = \frac{H - h}{D} \quad (\text{A3.3})$$

On substituting Equations S2 and S3 in equation S1, we get:

$$dV = 2\pi r h \cdot dr + \frac{4\pi r^2 (H - h)}{D} \cdot dr \quad (\text{A3.4})$$

On integrating the above equation with r going from 0 to D/2, we get the expression for the volume of RBC:

$$V = \frac{\pi D^2 (2H + h)}{12} \quad (\text{A3.5})$$

Typically, RBCs are approximately 7.5 to 8.7 μm in diameter (D), 1.7 to 2.2 μm in thickness (H), and 1 μm thick at the centre (h). So, here we assume that 'D' is 8.0 μm , 'H' is 2.0 μm , and 'h' is 1.0 μm and the volume of RBC following Equation S5 comes out to be 83.8 fL.

Since we observe an 18.5% decrease in the RBC volume at 0.5% (v/v) ethanol concentrations, now we'll calculate the percentage change in the RBC dimensions D, H, and h. Equation S5 can be expressed in the following error formula:

$$\frac{\Delta V}{V} = 2 \cdot \frac{\Delta D}{D} + \frac{\Delta H}{H} + \frac{\Delta h}{h} \quad (\text{A3.6})$$

Note, we are assuming that all the three parameters decrease uniformly, i.e. the percentage of decrease in D, H, and h are the same giving the following relation:

$$X = \frac{\Delta D}{D} = \frac{\Delta H}{H} = \frac{\Delta h}{h} \quad (\text{A3.7})$$

Equations S6 and S7 with $\Delta V/V=0.185$ gives $X \approx 0.046$. Hence,

$$\Delta D = 0.046 * D = 368 \text{ nm} \quad (\text{A3.8})$$

$$\Delta H = 0.046 * H = 92 \text{ nm} \quad (\text{A3.9})$$

$$\Delta h = 0.046 * h = 46 \text{ nm} \quad (\text{A3.10})$$

Such small changes can not be detected under optical images due to diffraction limitations

APPENDIX 4

AFM force spectroscopy data analysis

The trace (red) and retrace (blue) of a force distance curve for a spherical cantilever indenting an RBC are shown in Figure A4.1a. We are only going to make use of the trace of the force spectroscopy data for our analysis, hence it is isolated as shown in Figure A4.1b. Since no force should be experienced by the cantilever before it gets in contact with the RBC, the trace curve is transformed accordingly (see blue curve in Figure A4.1b). We also further transform the trace curve assuming the cantilever starts from a position zero (see black curve in Figure A4.1b).

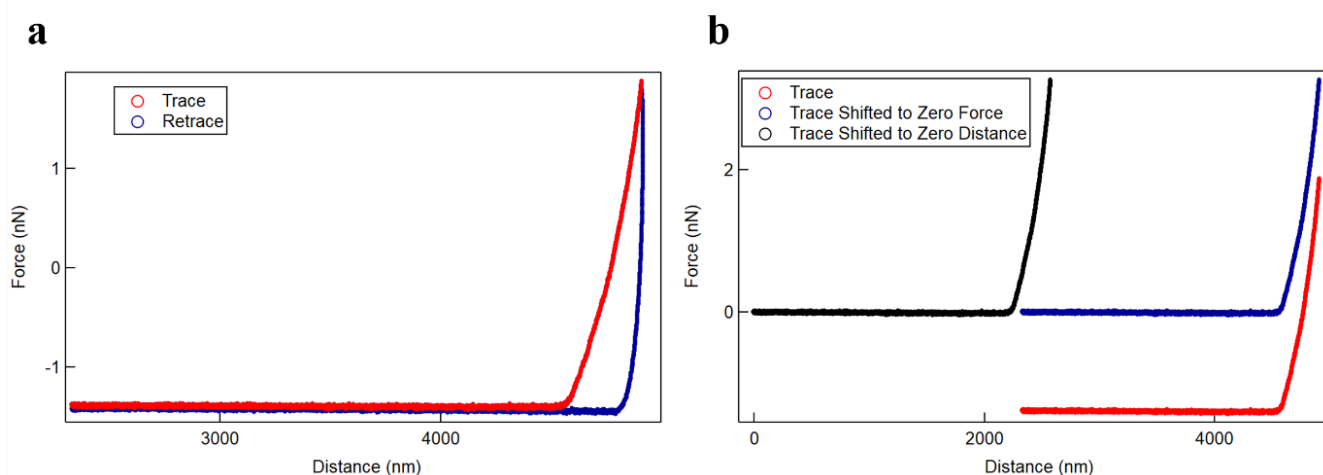


Figure A4.1 AFM force-distance curve for RBCs: (a) The trace (red) and retrace (blue) curve from the force spectroscopy experimental data taken on an RBC sample is shown here. (b) The raw force-distance curve is transformed for no contact and the relative zero position of the cantilever.

Now, the transformed force-distance curve is isolated (see inset Figure A4.2a), we need to find the contact point. For this, we find the slope at all the points in the F-X curve and plot it with the respective distance in the F-X curve as shown in Figure A4.2a (red). Since the data has some noise we also perform a running average for the slope values and the data is plotted in black on the same Figure A4.2a. The first one-third of data from the entire slope data is used to estimate the mean and standard deviation in the slope in the non-contact region. The non-contact slope values are then used to estimate the contact point (see Appendix 6 for the MATLAB code used). The contact between the cantilever and the sample is highlighted in the slope vs distance plot shown in Figure A4.2b.

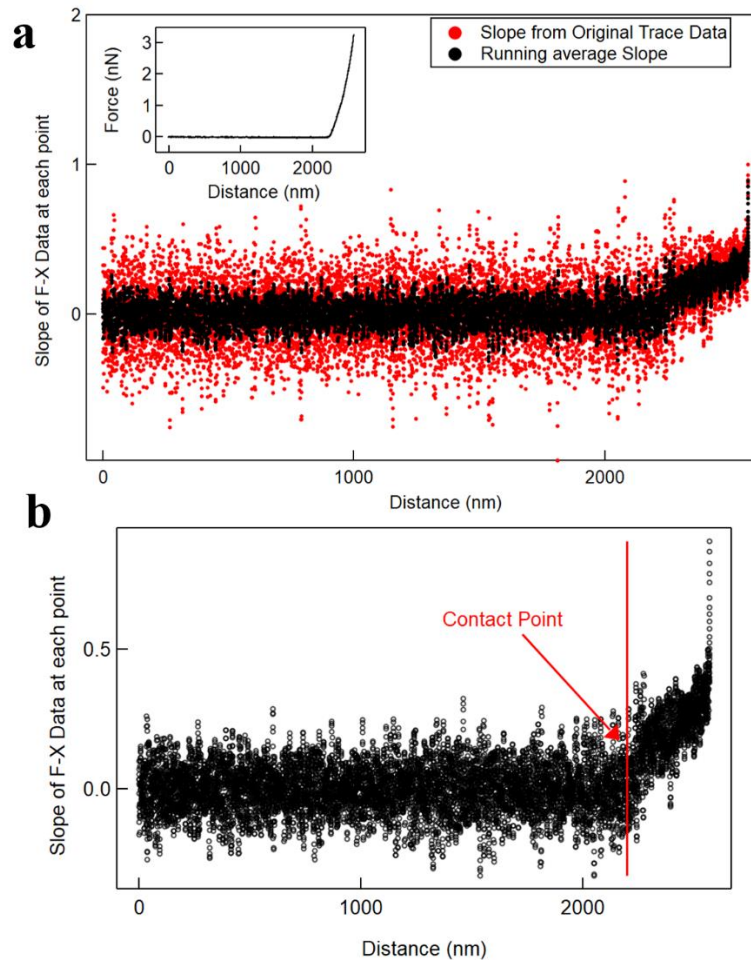


Figure A4.2 Estimating the contact point between the sample and cantilever: (a) The inset shows the transformed trace curve and the slope at each trace curve point is red. The running average of the slope vs distance is shown in black color. (b) The contact point between the sample and cantilever is shown here with the arrow and a vertical line.

Now, since we have found the contact point between the cantilever and the sample (see Figure A4.3a), the contact region can be isolated and is shown in the inset of Figure A4.3a. In order to use the Hertz model to estimate the sample's elasticity, we consider only small indentation, and the data (black circle) and the hertz model fit (red) are shown in Figure A4.3b. The entire Igor script and MATLAB code for extracting the raw data and data analysis are provided in Appendix 8.

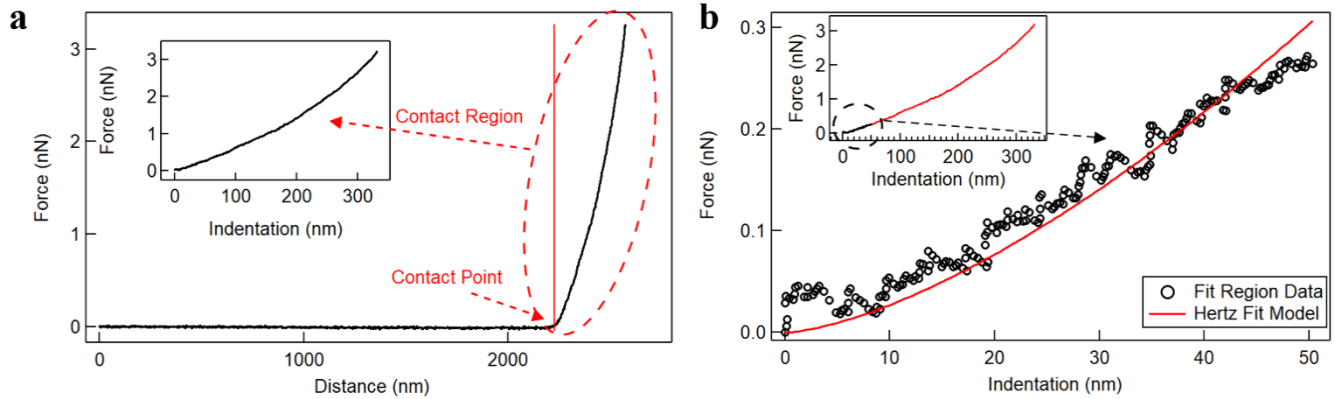


Figure A4.3 Fitting the force vs indentation data with the hertz model: (a) The contact point between the cantilever and sample in the F-X curve is highlighted with the red arrow. The dotted red region shows the entire contact region during the cantilever approach, and the force vs indentation for this contact region is shown in the inset. (b) A 50 nm indentation is considered for fitting (see inset), and the hertz fitting model (red) and the 50 nm indentation data (black circle) are shown here.

APPENDIX 5

Additional Experimental Data used in the chapter 3

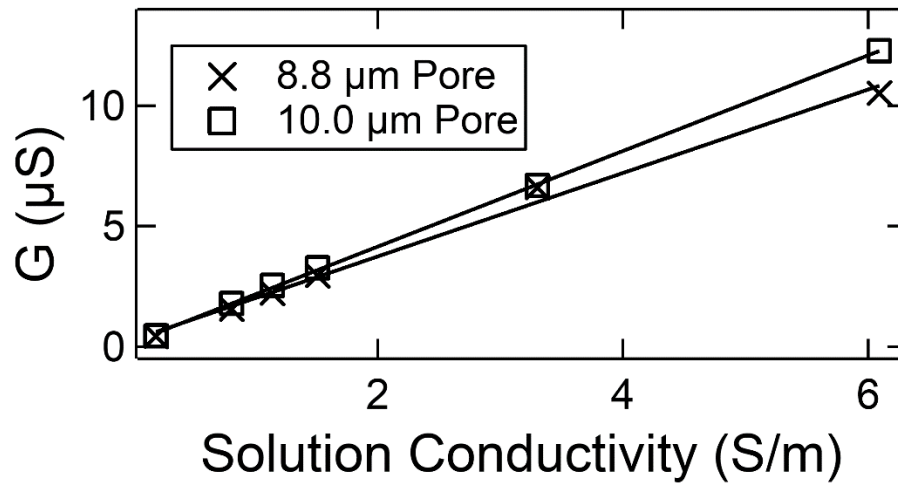


Figure A5.1: Conductance of micropore devices of diameter 8.8 μm and 10.0 μm is plotted with the solution conductivity. Solid lines are linear fit to data supporting equation (3.1).

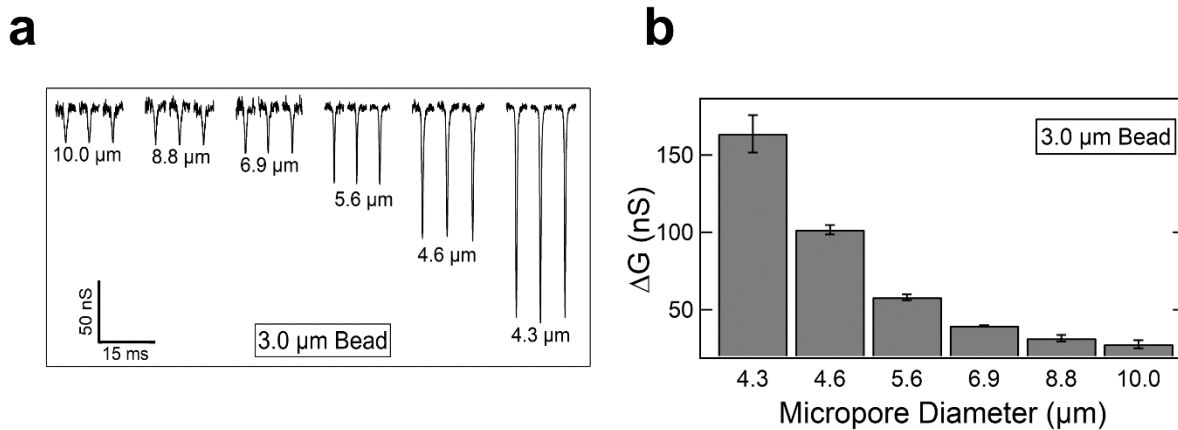


Figure A5.2: (a) Representative electrical events corresponding to beads of diameter 3.0 μm translocating through micropore diameters of 10.0 μm , 8.8 μm , 6.9 μm , 5.6 μm , 4.6 μm and 4.3 μm , respectively. (b) ΔG measured from collecting 1000s of events (as shown in a) is plotted against the micropore diameter ($N \geq 3$ datasets).

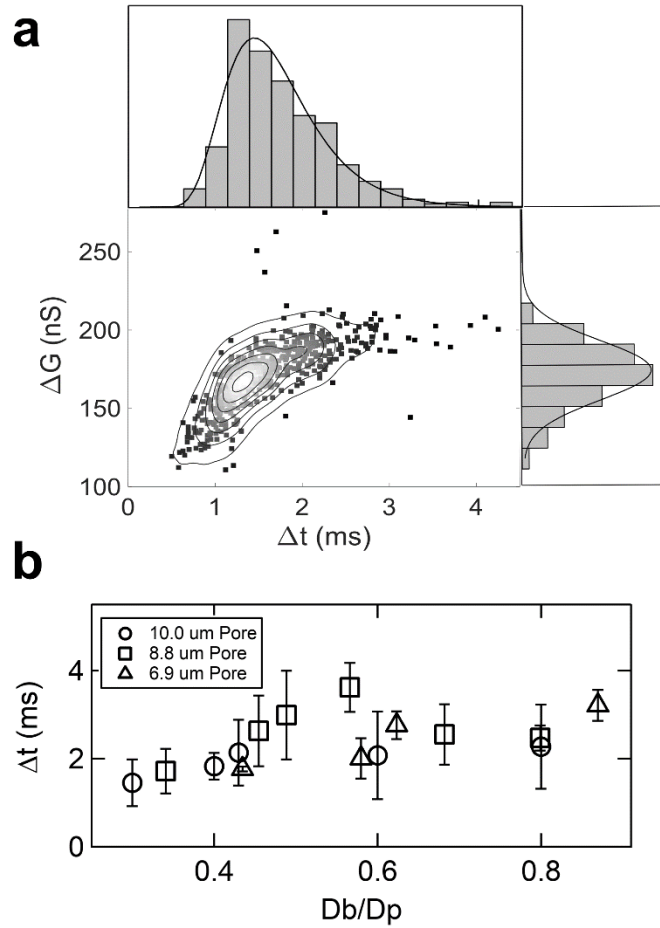


Figure A5.3: (a) Scatter plot (ΔG Vs Δt) for $N = 570$ events of $4.3 \mu\text{m}$ beads translocating through the $6.9 \mu\text{m}$ micropore. Histograms of ΔG and Δt along with Gaussian and Lognormal fitted functions are also shown along the right and top axes respectively. (b) Mean dwell times of events Δt measured for different bead diameters ($N > 3$ datasets for each bead diameter) translocating through a 10.0 , 8.8 , and $6.9 \mu\text{m}$ micropore devices is plotted against the ratio of bead to micropore diameter.

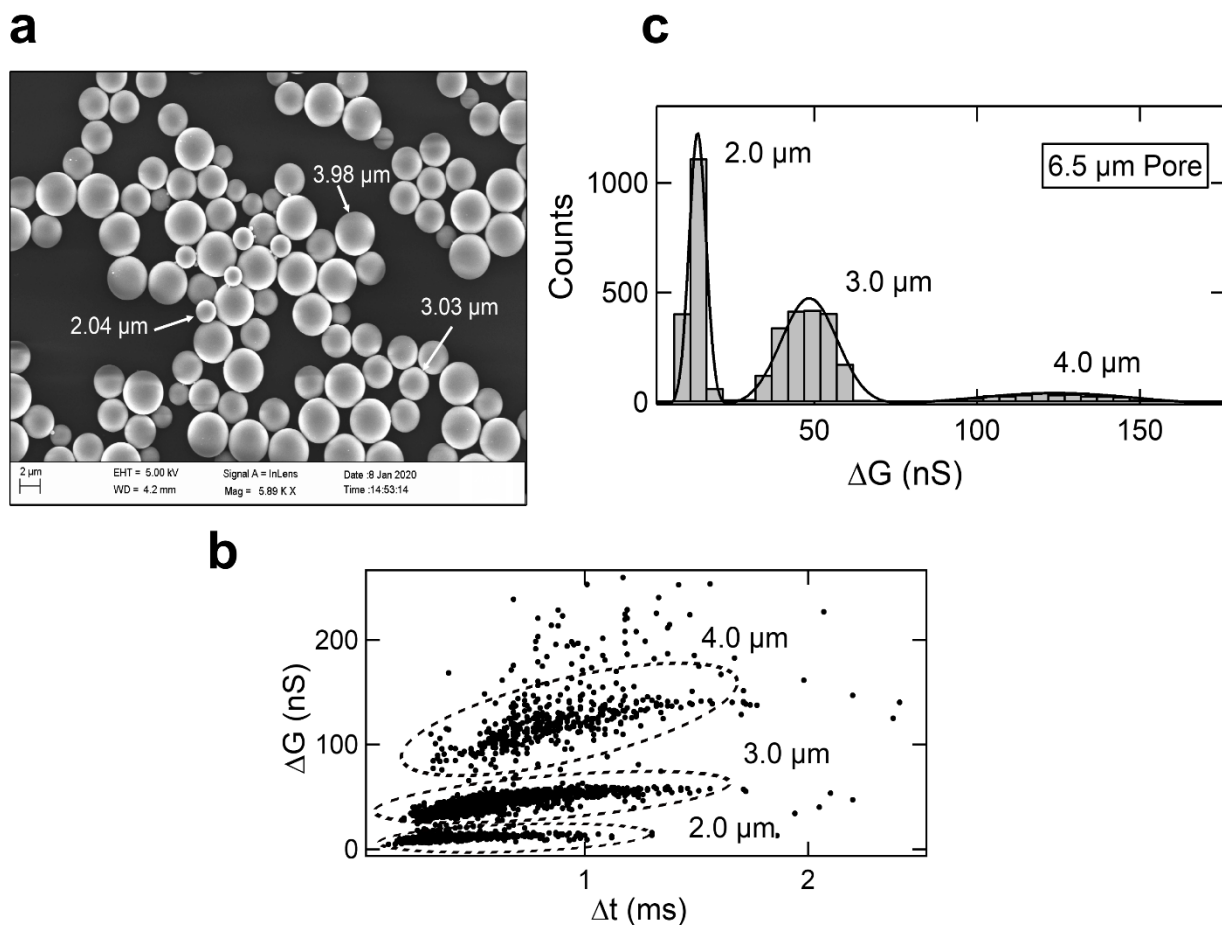


Figure A5.4 Quantitative detection of populations in a mixed sample. (a) SEM image of the three mixed beads. White arrows show an example of the three different bead diameters. (b) ΔG histogram with multi-Gaussian fit functions for a mixture of beads of $2.0 \pm 0.04 \mu\text{m}$, $3.0 \pm 0.1 \mu\text{m}$, and $4.0 \pm 0.1 \mu\text{m}$ diameter. Beads were mixed in a number ratio of 4:5:1 and measured through a $6.5 \mu\text{m}$ micropore. ΔG histograms showed three distinct peaks measured as 10.03 nS , 42.53 nS , and 115 nS respectively. A total of 1601, 1926, and 413 events were detected in these peaks and were attributed to $2.0 \mu\text{m}$, $3.0 \mu\text{m}$, and $4.0 \mu\text{m}$ beads respectively (total 3940 events). (c) ΔG and Δt scatter plot for the mixed beads data. Three different populations can be easily seen in this plot and are marked with dotted circles for clarity.

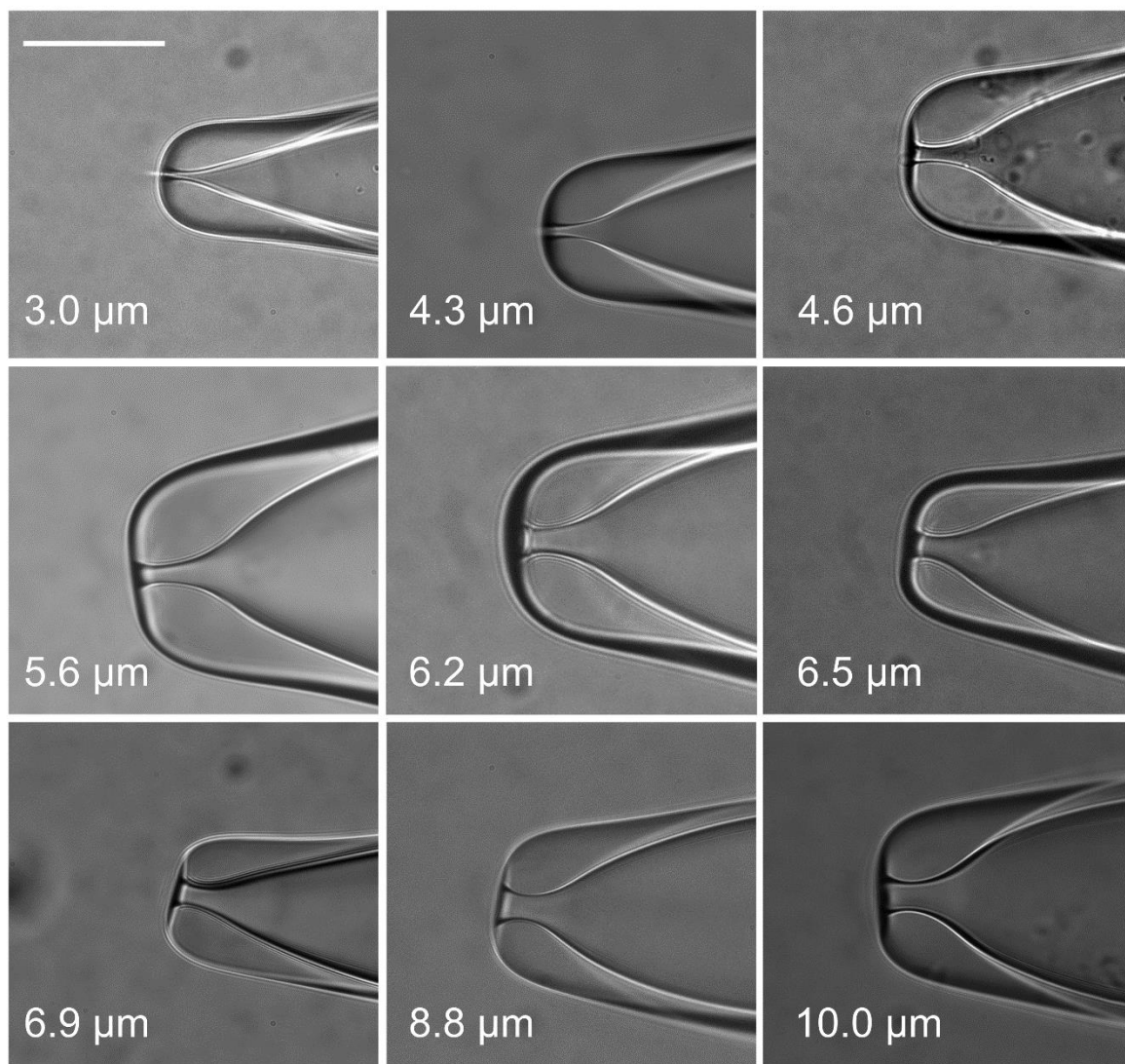


Figure A5.5: *Image library of micropores used for model cells (beads) measurements to understand the detection concept of our micropore device. The scale bar is common to all images and represents a length of 50 μm.*

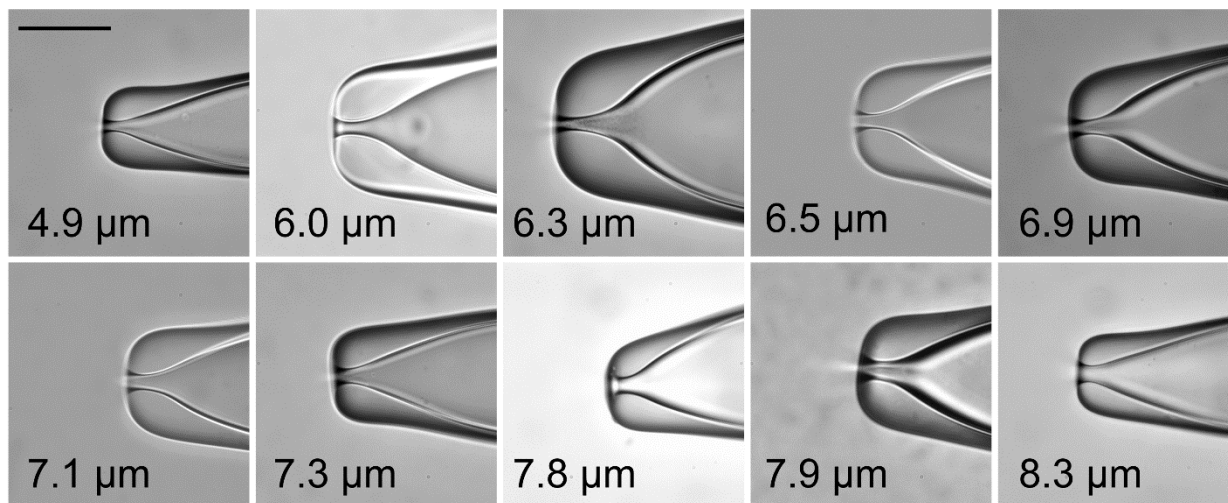


Figure A5.6: *Image library of micropores used in device characterization, quantitative population detection, and RBC volume measurements. The scale bar is common to all images and represents a length of 50 μm .*

Bead size (μm)	ΔG (nS)	# Events	Manufacturer's data (# $\times 10^3/\mu\text{l}$)
2.0	10.35	1601	1.08
3.0	44.7	1926	1.35
4.0	120.23	413	0.27
Ratio		3.9:4.7:1	4:5:1

Table A5.1 | Quantification of mixed bead data. *Quantitative measurement of a mixed sample containing beads of three different diameters, 2.0, 3.0, and 4.0 μm (in number ratio of 4:5:1) as shown in Figure A5.4. Of the total events recorded, the number of events assigned to each bead size is shown in column 3.*

Pore Diameter (μm)	$\Delta G_{4.0 \mu\text{m}}$ (nS)	$\Delta G_{4.3 \mu\text{m}}$ (nS)	Vol $_{4.0 \mu\text{m}}$ (fL)
6.5	115.03 ± 1.13	163.95 ± 3.35	29.22 ± 0.88
6.9	94.72 ± 2.73	128.14 ± 3.21	30.79 ± 1.66
8.8	83.98 ± 4.38	99.04 ± 5.40	35.32 ± 3.77
10.0	69.17 ± 2.34	81.98 ± 2.60	35.14 ± 3.19
Mean (fL)			32.62 ± 2.67

Table A5.2 | Quantifying model cell volumes for Fig. 3.2b. Bead with diameter $4.3 \pm 0.13 \mu\text{m}$ and volume $41.65 \pm 3.78 \text{ fL}$ is used as the calibration particle to estimate the volume of $4.0 \pm 0.1 \mu\text{m}$ bead in micropores of diameter 6.5, 6.9, 8.8 and $10.0 \mu\text{m}$ using equation (3.5). The mean volume measured is reasonably close to the volume estimated ($33.52 \pm 2.51 \text{ fL}$) from the manufacturer's data.

Pore Diameter (μm)	Pore Conductance (nS)	Beads Measured (μm)	L_{eff} (μm)
10	3434.6	3.0, 4.0, 4.3, 6.0, 8.8	24.12
8.8	2999.1	3.0, 4.0, 4.3, 4.98, 6.0, 7.06	24.93
6.9	2509.4	3.0, 4.0, 4.3, 6.0	20.75
6.5	2261.7	3.0, 4.0, 4.3, 6.0	20.43
6.2	2087.6	2.0, 2.8, 3.0, 4.0, 4.3	17.75
5.6	1397.8	2.0, 2.8, 3.0, 4.0	16.89
4.6	1327.8	2.0, 2.8, 3.0, 4.0	12.50
4.3	1124.1	2.0, 2.8, 3.0	12.26
3	904.8	1.0, 1.9, 2.0, 2.1	11.89

Table A5.3 | List of L_{eff} values for different pores used in Chapter 3. Columns 1 & 2 list all the different micropores along with their open pore conductance values used in this study. Column 3 lists different model cell diameters measured as plotted in Figure 4C. Column 4 shows the estimated L_{eff} using equation (3.3).

		ΔG (nS)											
D_{Bead}	D_{Pore}	1.0 μm	1.9 μm	2.0 μm	2.1 μm	2.8 μm	3.0 μm	4.0 μm	4.3 μm	4.98 μm	6.0 μm	7.03 μm	8.0 μm
3 μm		7.93 \pm 0.43	39.18 \pm 1.88	46.82 \pm 2.46	58.21 \pm 2.7	-	-	-	-	-	-	-	-
	4.3 μm	-	-	32.33 \pm 1.60	-	84.54 \pm 6.78	170.38 \pm 12.38	-	-	-	-	-	-
4.6 μm		-	-	23.90 \pm 0.52	-	68.54 \pm 2.60	106.97 \pm 3.07	353.12 \pm 4.81	-	-	-	-	-
	5.6 μm	-	-	15.64 \pm 0.56	-	46.57 \pm 4.07	61.95 \pm 2.04	188.53 \pm 26.87	-	-	-	-	-
6.2 μm		-	-	17.76 \pm 0.27	-	39.53 \pm 0.91	58.85 \pm 0.97	163.44 \pm 7.20	204.93 \pm 37.67	-	-	-	-
	6.5 μm	-	-	-	-	-	50.29 \pm 2.81	115.03 \pm 1.13	163.95 \pm 3.35	-	406.44 \pm 27.62	-	-
6.9 μm		-	-	-	-	-	42.99 \pm 0.36	94.72 \pm 2.73	128.14 \pm 3.21	-	410.83 \pm 12.0	-	-
	8.8 μm	-	-	-	-	-	34.49 \pm 2.21	83.98 \pm 4.38	99.04 \pm 5.40	129.37 \pm 6.05	273.74 \pm 29.57	457.14 \pm 14.9	-
10 μm		-	-	-	-	-	30.33 \pm 2.75	69.17 \pm 2.34	81.98 \pm 2.60	-	248.27 \pm 22.97	-	721.52 \pm 43.83
		-	-	-	-	-	-	-	-	-	-	-	-

Table A5.4: Summary of mean ΔG values ($N \geq 3$) for all the model cells (beads) measured using the 9 different micropore devices.

APPENDIX 6

Additional experimental data used in the chapter 4

S.no	Item Description	Quantity	Price/pc (INR)	Price (INR)
1	IC AD820	1	475	475
2	Electrical Resistors	1	11.12(1 M Ω) 2.80 (10 M Ω)	11.12(1 M Ω) 2.80 (10 M Ω)
3	Ceramic Capacitors	1	64	64
4	DB9 Connector Cable	1	362	362
5	DB9 Adaptor	1	144	144
6	LED	1	9	9
7	Aluminium Enclosure	1	899	899
8	Female BNCs	2	94	188
9	Crocodile Clips	2	55	110
10	Breadboard	1	275	275
11	DC Batteries	2	259	518
12	Connecting wires	5 meters	35	35
13	ON/OFF DPST toggle switch	1	304	304
TOTAL				3394

Table A6.1: Total Expenditure. The table shows the items used to make the amplifier, the quantity required, and the respective price to buy the items. Our total cost of INR 3394 (about USD 50) is about 100 times lower than the commercial amplifiers.

Amplifier Type (Commercial or Lab)	Legend	R_F (MΩ)	Range (nA)	Measured RMS Noise @ 1 kHz (pA)	Bandwidth (kHz)
Lab Amp	L1A	1	± 10000	193 ± 3	31.6
Lab Amp	L1B	1	± 10000	185 ± 4	30.1
Commercial Amp-1	D001-1	1	± 10000	159 ± 3	10
Lab Amp	L10A	10	± 1000	79 ± 5	9.5
Lab Amp	L10B	10	± 1000	82 ± 5	9.6
Commercial Amp-2	D01-10	10	± 1000	27.3 ± 0.5	10
Commercial Amp-3	AM10	10	± 1000	39 ± 3	10

Table A6.2: Summary of the comparison between all the amplifiers. Column 1 is the type of amplifier used (commercial or lab) with the respective legend code in column 2. The values in Column-3, 4, 5, and 6 are feedback resistor (R_F), the range of measurable current range (at ± 10 volts V_{CC}), RMS noise in the measured current for a 500 k Ω electrical resistor at 1 kHz software filter and the bandwidth of the amplifier respectively.

Filter Frequency	L1A	L1B	D001-1	L10A	L10B	D01-10	AM10
Unfiltered	1372 ± 7	1119 ± 8	1191 ± 6	177 ± 2	175 ± 2	121.2 ± 0.3	63 ± 2
50 kHz	1372 ± 7	1120 ± 8	1190 ± 6	177 ± 2	175 ± 2	121.3 ± 0.3	63 ± 2
30 kHz	1009 ± 5	858 ± 7	928 ± 5	155 ± 3	157 ± 2	96.4 ± 0.3	59 ± 2
20 kHz	837 ± 5	717 ± 6	779 ± 4	144 ± 3	146 ± 3	81.9 ± 0.2	55 ± 2
10 kHz	637 ± 5	531 ± 5	564 ± 4	126 ± 3	129 ± 3	61.8 ± 0.2	50 ± 2
5 kHz	461 ± 4	383 ± 4	385 ± 3	109 ± 4	112 ± 3	45.9 ± 0.3	47 ± 3
1 kHz	193 ± 3	185 ± 4	159 ± 3	79 ± 5	82 ± 5	27.4 ± 0.5	39 ± 3

Table A6.3: RMS Noise values of different amplifiers with a 500 kΩ load resistor: The table shows the RMS noise values (pA) in current measurements for L1, L10 series lab amplifiers and D001-1, D01-10, and AM10 commercial amplifiers at 1, 5, 10, 20, 30, 50 kHz filtered and unfiltered frequency. The current measurements were made at ±300 mV with a 500 kΩ load resistor (R_P).

Filter Frequency	L1A	L1B	D001-1	L10A	L10B	D01-10	AM10
unfiltered	1320 ± 10	1102 ± 9	1180 ± 7	141 ± 1	126 ± 2	122.2 ± 0.5	50.2 ± 0.8
50 kHz	1318 ± 9	1102 ± 9	1181 ± 7	141 ± 1	126 ± 2	122.2 ± 0.5	50.2 ± 0.8
30 kHz	969 ± 8	842 ± 7	919 ± 6	116 ± 1	106 ± 2	96.6 ± 0.4	44.7 ± 0.9
20 kHz	803 ± 7	702 ± 6	771 ± 5	102 ± 1	95 ± 2	82.1 ± 0.4	39 ± 1
10 kHz	608 ± 6	516 ± 5	559 ± 4	84 ± 1	80 ± 2	61.7 ± 0.3	32 ± 1
5 kHz	436 ± 4	370 ± 4	381 ± 3	68 ± 2	67 ± 2	45.5 ± 0.4	29 ± 1
1 kHz	181 ± 4	173 ± 4	159 ± 3	45 ± 2	46 ± 3	26.8 ± 0.6	22 ± 2

Table A6.4: RMS Noise values of different amplifiers with a 1 MΩ load resistor: The table shows the RMS noise values (pA) in current measurements for L1, L10 series lab amplifiers and D001-1, D01-10, and AM10 commercial amplifiers at 1, 5, 10, 20, 30, 50 kHz filtered and unfiltered frequency. The current measurements were made at ±300 mV with a 1 MΩ load resistor (R_P).

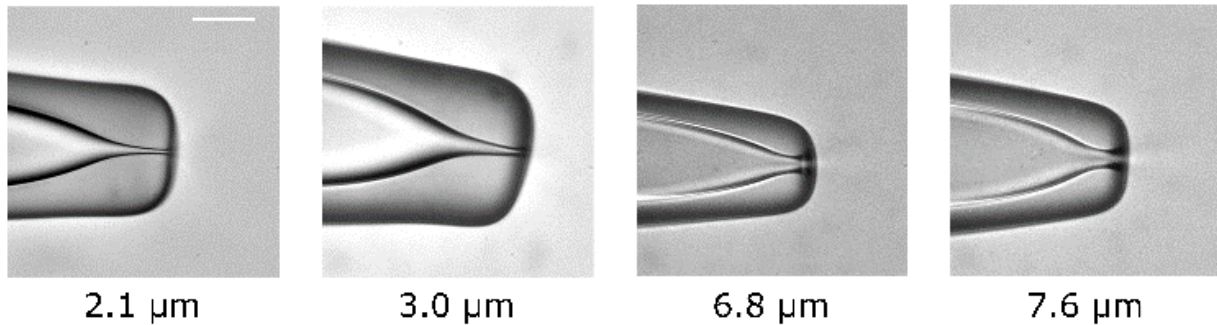


Figure A6.1: Optical Image library of micropores used in this paper. The scale bar (30 μm) is common to all images.

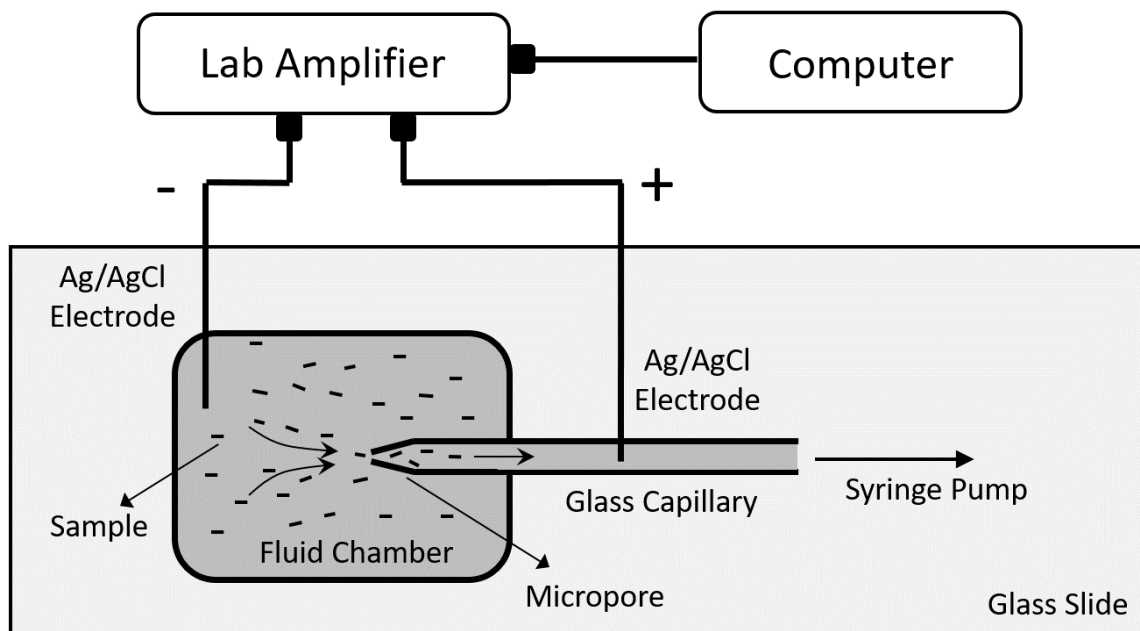


Figure A6.2: Schematic of the micropore setup. A glass micropore is mounted in the fluid chamber containing the suspension buffer and sample. The syringe pump is connected to the glass capillary to create a stable fluid flow to translocate the sample through the micropore. The translocation current signals are acquired using two Ag/AgCl electrodes, one immersed into the buffer in the fluid chamber and other inserted in the tubing. These electrodes are connected with the lab amplifier, which is controlled using a custom made LabVIEW code. The entire micropore device unit is mounted on a glass slide.

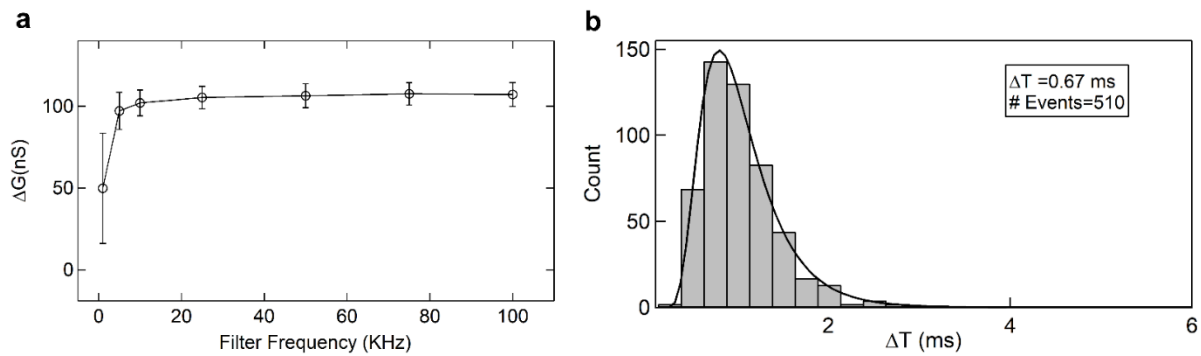


Figure A6.3: Effect of Filter frequency on ΔG values (a) Plot of ΔG values for $4.98 \mu\text{m}$ beads translocating through an $8.3 \mu\text{m}$ micropore data measured at 100 kHz (using commercial Axopatch 200B amplifier, flow velocity 500 nL/min) and digitally filtered at different filter frequencies. (b) ΔT histogram of $2.1 \mu\text{m}$ beads translocating through a $3.0 \mu\text{m}$ micropore data with mean translocation times of 0.67 milliseconds. A solid line is a log-normal fit to the distribution.

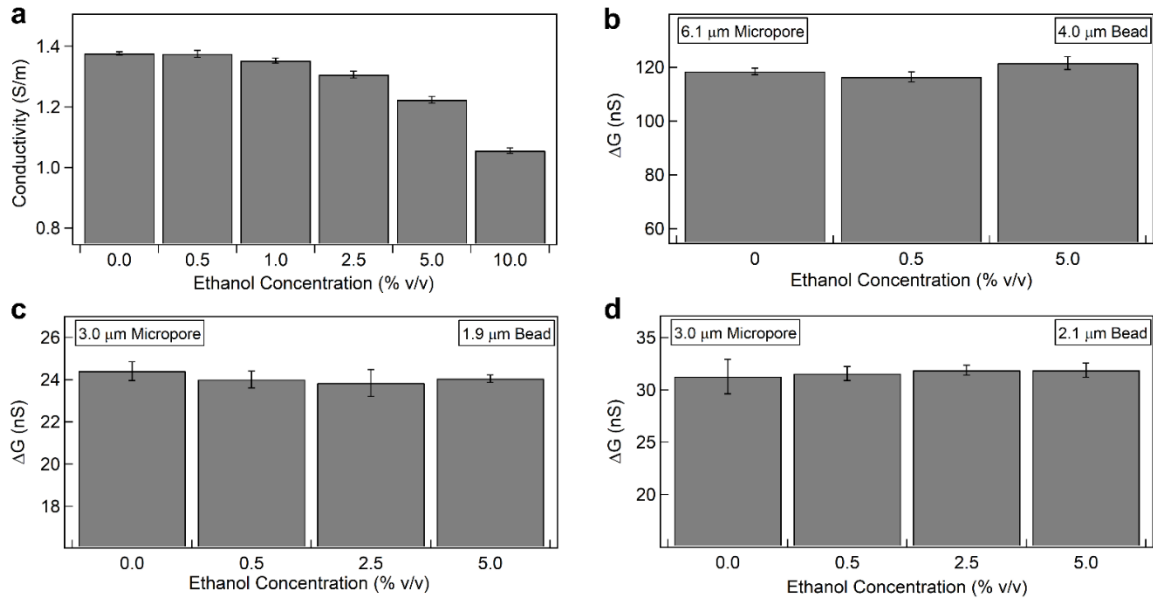


Figure A6.4: Demonstration of constant ΔG with changing ethanol concentration. (a) Absolute conductivity of phosphate saline buffer with different ethanol concentrations. (b) Bar plot of ΔG values for 4.0 μm beads translocating through a 6.1 μm micropore device with different ethanol concentrations in the suspension buffer. (c) and (d) Bar plot of ΔG values for 1.9 and 2.1 μm beads translocating through a 3.0 μm micropore device with different ethanol concentrations in the suspension buffer respectively.

APPENDIX 7

Additional experimental data used in the chapter 5

Pore Diameter	Pore Length ($D > 2 * D_p$)	Slope (1.15 ± 0.12)	Intercept(Free)	Ratio (L_p/D_p)
3.0 μm	136 μm	0.92 ± 0.08	0.97 ± 0.44	45.3
3.2 μm	117 μm	1.17 ± 0.12	0.1 ± 0.7	36.6
3.6 μm	156 μm	1.3 ± 0.13	0 ± 0.7	43.3
3.8 μm	184 μm	1.17 ± 0.10	1.9 ± 0.5	48.4
3.9 μm	193 μm	1.17 ± 0.06	1.95 ± 0.27	49.5

Table A7.1: Mapping RBCs elasticity with the micropore Δt measurements. This Table shows the linear dependence of the micropore Δt measurements with the elasticity of RBCs measured with the AFM. The average of the slope from multiples pore is 1.15 ± 0.12 .

Fit Distance (nm)	Fitting R2 Value				
	Native	0.25 μ M	0.50 μ M	0.75 μ M	1.00 μ M
25	0.97	0.91	0.95	0.92	0.96
50	0.99	0.98	0.98	0.98	0.97
75	0.99	0.98	0.99	0.99	0.99
100	0.99	0.99	0.94	0.97	0.99

Table A7.2: Fitting R2 Values for AFM force-distance curves. This Table shows the Fitting R2 values for the AFM force-distance curves fitted to 25, 50, 75, and 100 nm distance for RBCs treated with different Lat-A concentrations.

Flow Rate (nL/min)	Slope (b)	Intercept(a)
500	1.18 \pm 0.07	1.82 \pm 0.4
750	1.75 \pm 0.34	1.44 \pm 1.26
1000	2.11 \pm 0.41	1.70 \pm 1.20
1250	2.64 \pm 0.55	1.45 \pm 1.33
1500	3.25 \pm 0.65	1.34 \pm 1.31

Table A7.3: Mapping RBCs elasticity with the micropore Δt measurements at different flow rates. This Table shows the fit parameters for the linear relationship between the elasticity of RBCs treated with different Lat-A concentrations with the constricted Δt measurements at different flow-rates using a 3.8 μ m micropore device.

DOE	Constricted		FF	Sample	$\Delta G \pm \text{Err}$ (Constricted)	$\Delta G \pm \text{Err}$ (Free Flight)	MCV	$\Delta t \pm \text{Err}$ (Constricted)	Gel Electrophoresis Test (HPLC)			
	D_p (μm)	L_p (μm)	D_p (μm)						HbS	HbA	HbA2	HbF
31/08/23	4.6	165	7.2	Control-1	18.4 ± 0.8	51.6 ± 4.1	90.3	4.0 ± 0.1	0	95	2.9	0.3
				SCD Trait (P1)	22.5 ± 0.4	81.6 ± 3.4	102.2	15.1 ± 0.9	20.8	36	11.7	2.7
				SCD (P2)	12.4 ± 0.1	42.7 ± 0.5	59.9	9.6 ± 1.7	81	2	4.7	12
				Control-2	19.3 ± 0.9	49.0 ± 1.8	90.3	4.3 ± 0.3	0	95	2.9	0.3
07/09/23	4.3	182	8.7	Control-1	21.4 ± 0.2	67.2 ± 3.9	90.3	7.2 ± 2.4	0	95	2.9	0.3
				SCD (P3)	18.9 ± 0.5	64.5 ± 0.7	80.8	11.7 ± 0.9	76.3	1.9	2.7	18.3
				SCD (P4)	12.3 ± 0.3	48.2 ± 2.1	NA	13.5 ± 0.9	NA	NA	NA	NA
				Control-2	22.8 ± 0.3	61.4 ± 0.8	90.3	7.0 ± 0.7	0	95	2.9	0.3
11/9/2023	4.4	185	7.3	Control-1	15.1 ± 0.9	54.6 ± 4.2	90.3	5.9 ± 1.3	0	95	2.9	0.3
				SCD (P5)	16.5 ± 0.3	59.9 ± 1.4	90.6	16.1 ± 0.6	76	-	2	19.5
				SCD (P6)	17.2 ± 0.2	63.2 ± 4.3	NA	10.2 ± 1.1	73	3.3	3.1	21.5
				Control-2	14.5 ± 0.1	51.7 ± 1.4	90.3	5.5 ± 0.5	0	95	2.9	0.3
14/09/23	4.3	187	7.3	Control-1	16.1 ± 0.4	NA	90.3	7.4 ± 1.6	0	95	2.9	0.3
				SCD (P7)	11.9 ± 0.3	47.1 ± 2.2	80.3	11.8 ± 1.5	76	3.7	5.3	13.1
				SCD Trait (P8)	11.1 ± 0.1	43.2 ± 0.7	68.6	8.8 ± 0.5	26	69	3.2	1.5
				Control-2	15.8 ± 0.6	54.6 ± 4.2	90.3	7.8 ± 0.5	0	95	2.9	0.3
05/10/23	4.4	143	8.6	Control-1	17.6 ± 2.1	55.9 ± 2.1	89.9	5.4 ± 0.6	0	95	2.9	0.3
				SCD (P9)	15.9 ± 0.5	56.8 ± 2.4	88.2	8.0 ± 0.5	78.6	2.3	3.7	14.7
				Control-2	16.8 ± 0.3	NA	89.9	5.5 ± 0.5	0	95	2.9	0.3
12/10/23	3.8	144	8.1	SCD (P10)	18.9 ± 0.6	56.4 ± 1.5	96.6	13.0 ± 2.4	79.3	2.7	2.4	15.6
				Control	16.7 ± 0.3	77.1 ± 3.4	90.2	8.0 ± 0.7	0	95	2.9	0.3

Table A7.4: Summary of SCD patient data. In this table, we show the summary of electrofluidic (both free flight and constricted) and pathology (HPLC) data collected for healthy donor and SCD patients used in this study.

S.No	Sample	E_{relative}	Err	HbS
1	Patient-1	1.05	0.17	20.8
2	Patient-2	3.09	0.63	81
3	Donor-1	1.00	0.16	0
4	Patient-3	1.84	0.19	76.3
5	Patient-4	4.24	0.72	-
6	Donor-1	1.00	0.24	0
7	Patient-5	2.35	0.22	76
8	Patient-6	1.31	0.35	73
9	Donor-1	1.00	0.27	0
10	Patient-7	2.15	0.51	76
11	Patient-8	1.97	0.19	26
12	Donor-1	1.00	0.25	0
13	Patient-9	1.41	0.24	78.6
14	Donor-1	1.00	0.17	0
15	Patient-10	3.41	0.85	79.3
16	Donor-1	1.00	0.19	0

Table A7.5: Relative elasticity of SCD patients estimated using the empirical equation 6. This Table shows the relative elasticity of a sickle cell anemia patient's RBCs compared with a healthy donor's RBC and the HbS% values from both the donor and patient's HPLC reports.

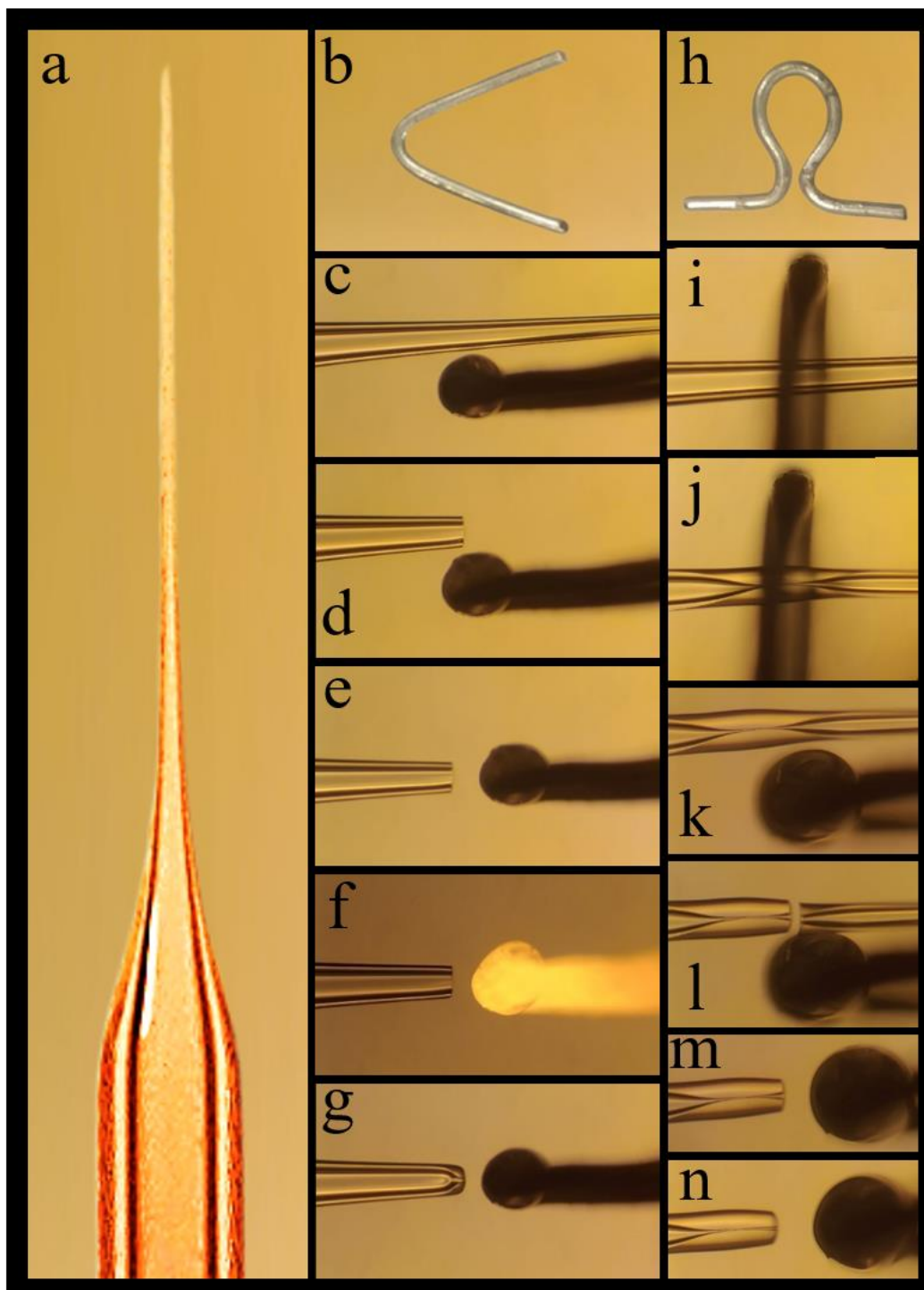


Figure A7.1: Steps involved in forging a micropore from a glass capillary: (a) The image of the glass capillary pulled using the Shutter Puller instrument is shown here. (b-g) Images of a 'V' shaped filament and the steps involved in forging a free-flight micropore are shown. (h-n) Images of an omega-shaped (Ω) filament and the steps involved in forging a constricted micropore are shown. Note that these images are not to be scaled.

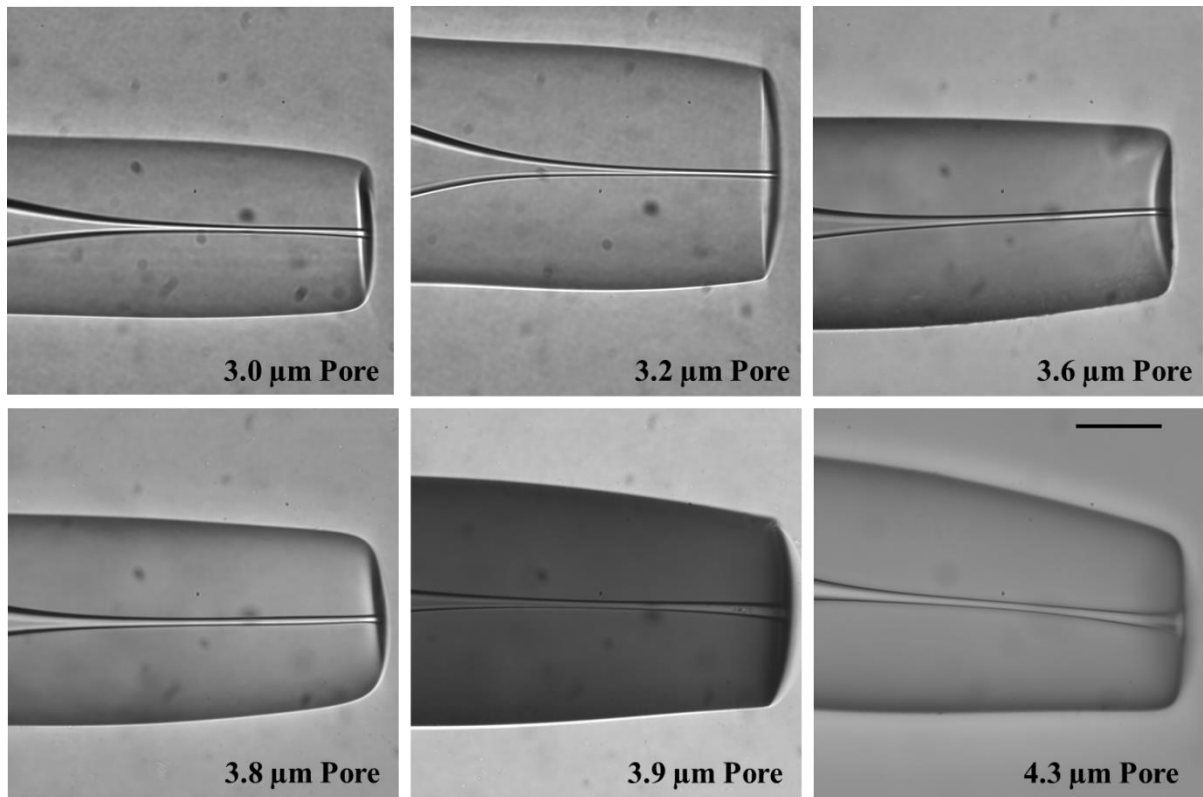


Figure A7.2 Image library of constricted micropores: We show the microscopic images of the constricted micropores used for the Lat-A study of the RBCs. The scale bar is 50 μm .

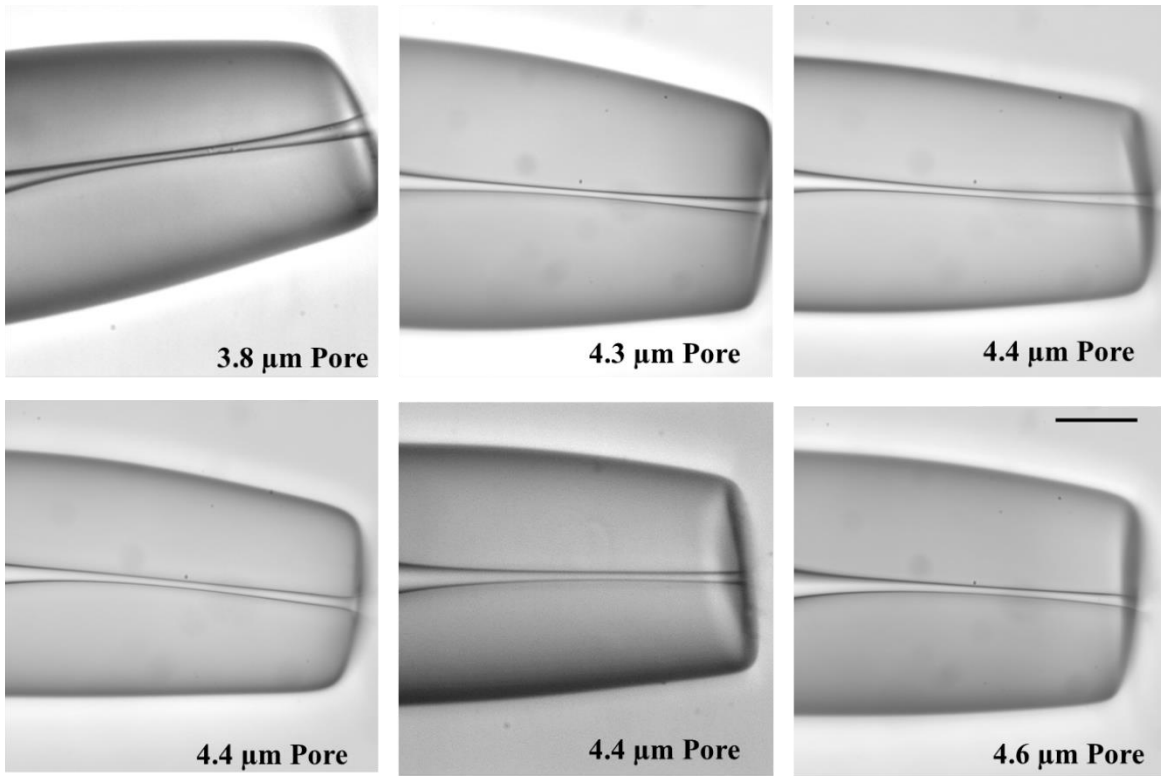


Figure A7.3 Image library of constricted micropores: We show the microscopic images of the constricted micropores used for the SCD Patient study. The scale bar is 50 μm.

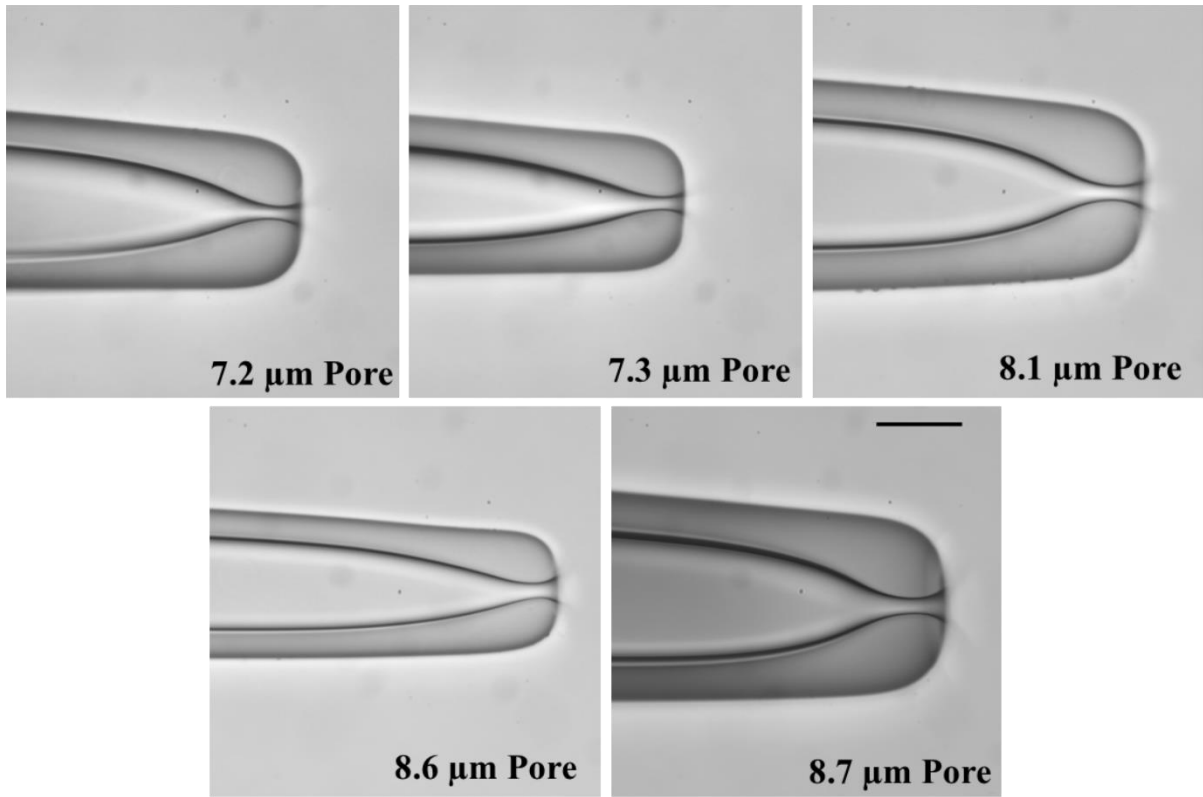


Figure A7.4 Image library of free-flight micropores: We show the microscopic images of the free-flight micropores used for the SCD Patient study. The scale bar is 50 μm.



Figure A7.5 AFM Sample Fluid Cell: A 100 μ L circular fluid cell made of silicone glue on a glass slide for AFM sample preparation.

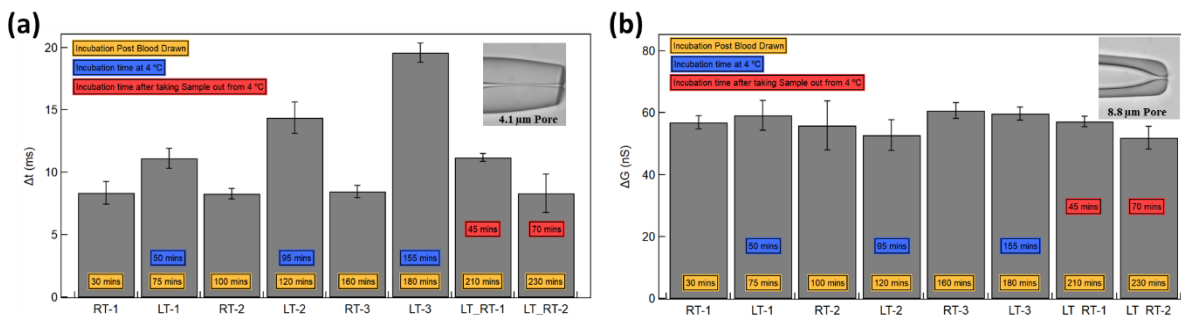


Figure A7.6 Effect of incubation temperature on translocation experiment: (a) The constricted Δt measured using a 4.1 μm micropore device for RBCs incubated at 4 °C and room temperature for different amount of time is shown. **(b)** The free flight ΔG were measured for the same aliquots, with same incubation conditions using an 8.8 μm micropore device. RT, LT and LT_RT in x axis represents the samples taken from aliquot incubated at room temperature, low temperature (4 °C) and low temperature aliquot sample taken out of the fridge and incubated at room temperature respectively

The incubation temperature affects the stiffness of RBCs [REF], hence to establish a relevant temperature condition for our stiffness estimation experiments we draw blood from a healthy donor and make two aliquots of it, kept one of them at room temperature, and store the other one at 4 °C. We then simultaneously perform the free flight and constricted translocation experiments on samples from both these aliquots using 8.8 and 4.1 μm micropores respectively. In Figure A7.6a and A7.6b, we show the Δt and ΔG bar plots respectively. In Figure A7.6, the RT, LT, and LT_RT in the x-axis represent the samples taken from the aliquot incubated at room temperature, low temperature (4 °C), and low-temperature aliquot samples taken out of the fridge and incubated at room temperature respectively. The numbers written in orange, blue, and red are the time duration of the sample incubated after blood was drawn from the healthy donor, incubated at 4 °C, and the sample was taken out of the fridge after incubating it for almost 150 minutes respectively. The ΔG bar plots in Figure A7.6b show that temperature has very little effect on the physiology of RBCs. Whereas the Δt bar plots in Figure A7.6a emphasize that the stiffness of RBCs when incubated at room temperature does not change, but when incubated at 4 °C it increases. We can also see that the LT_RT-1 and LT_RT-2 bars start to decrease, showcasing that when RBCs are brought back to room temperature, they start to get back to their original stiffness. Based on the understanding from this temperature experiment, we have performed all the experiments by incubating RBCs at room temperature.

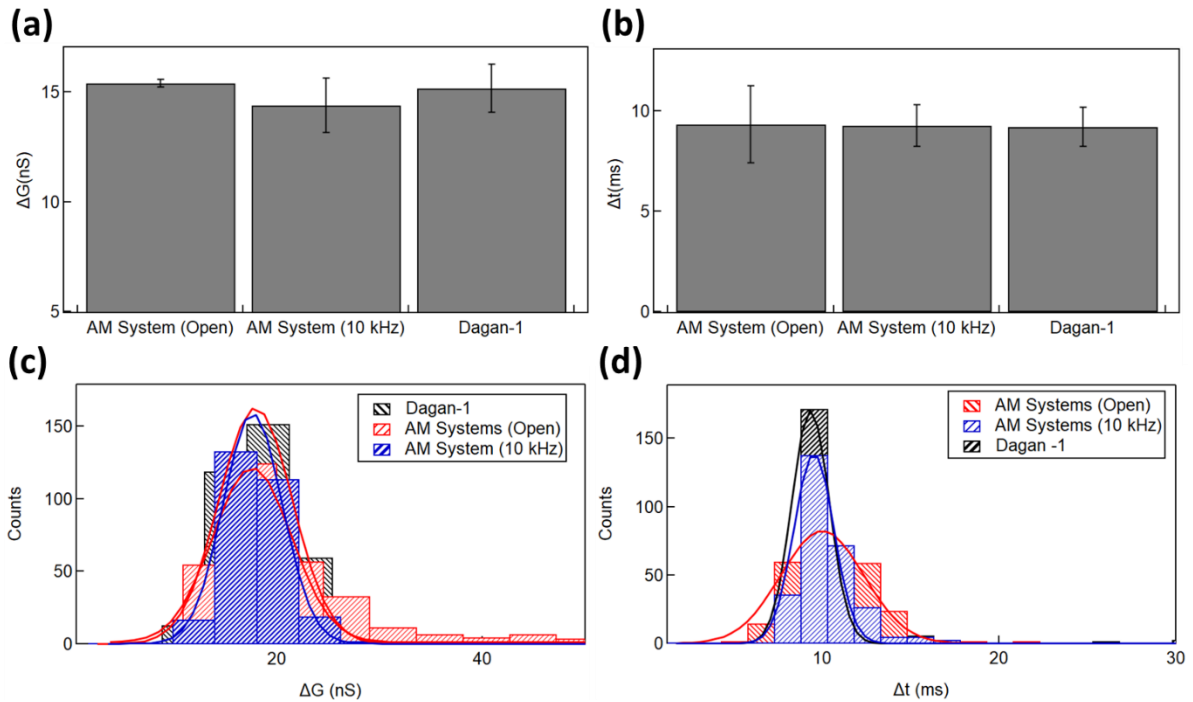


Figure A7.7 Effect of Amplifier Bandwidth on TL Data: (a) and (b) shows the bar plot of constricted ΔG and Δt through a $4.2 \mu\text{m}$ micropore device respectively done on AM System (40 kHz), AM System (10 kHz) and Dagan (10 kHz) amplifiers. (c) and (d) shows the ΔG and Δt histograms with Gaussian fittings respectively, for different amplifiers.

Note that, we are using two amplifiers in this study; AM system 2400 and Dagan Chem-Clamp. This was necessary as the in-hospital free flight and constricted experiments on SCD patient samples were performed side-by-side simultaneously (See Figure A7.15 for in-hospital setup). To make sure the choice of amplifier and its bandwidth will not affect the translocation data we, used a long constricted micropore of $4.2 \mu\text{m}$ diameter for translocating RBCs from a healthy donor using the AM system with 40 and 10 kHz bandwidth and Dagan Chem-Clamp with 10 kHz Bandwidth. The ΔG and Δt bar plots and histograms shown in Figure A7.7 establish that the choice of amplifier and its bandwidth does not affect the translocation data.

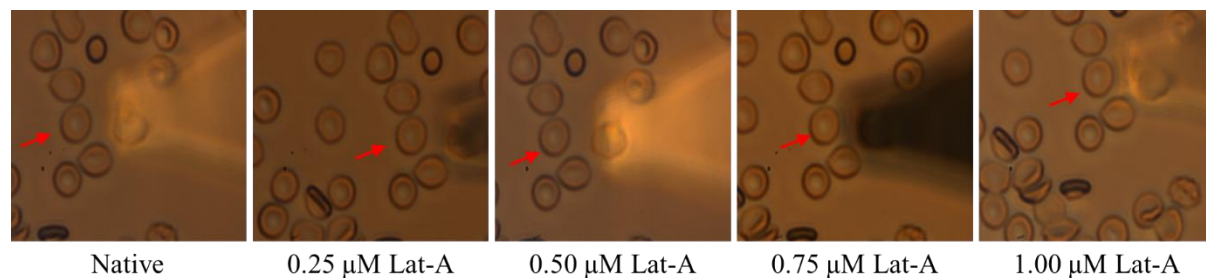


Figure A7.8 Image library of bright field image of RBCs used for AFM force spectroscopy measurements. A microscopic image of the same cell (marked with red arrow) treated with different concentration of Lat-A and probed with the spherical cantilever (pointed with red arrow) is shown here. A 60X objective was used for the images.

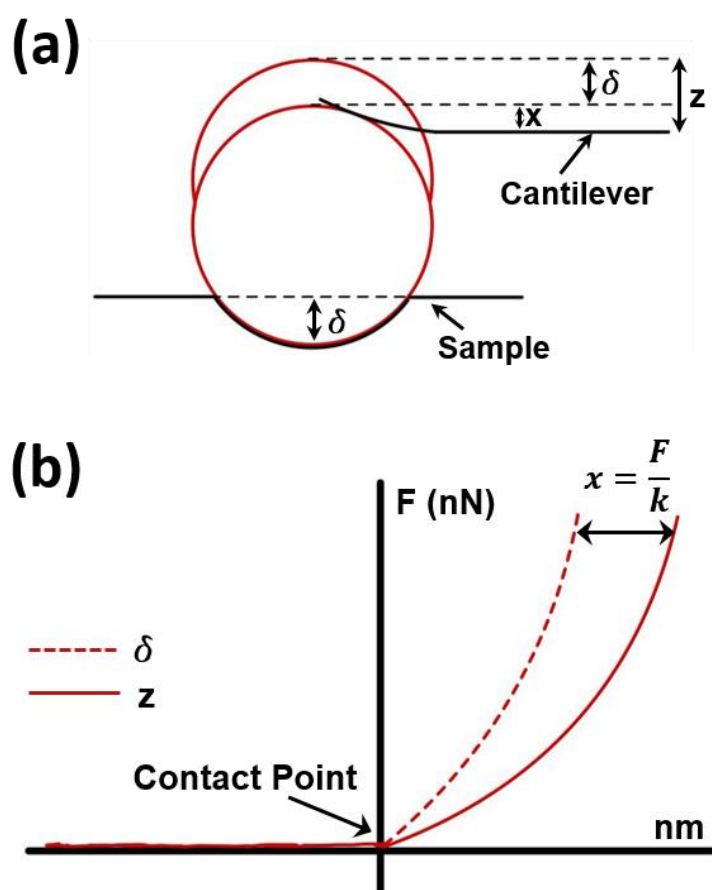


Figure A7.9 Schematic of AFM force-indentation experiment. **a** A spherical cantilever indenting a soft sample. Here the cantilever's piezo position (z), deflection of the cantilever (d), and the indentation into the sample (x) are also shown. **b** Schematic of the force-indentation curve is shown.

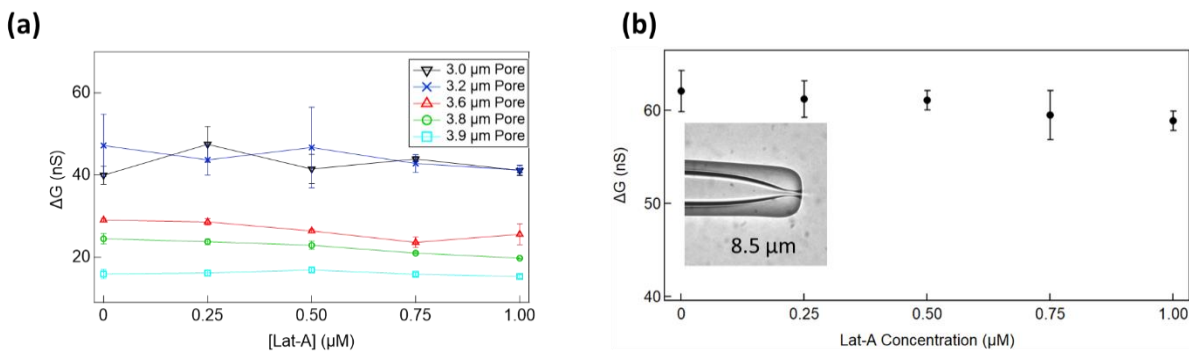


Figure A7.10 Effect of Lat-A on the constricted and free-flight ΔG of RBCs: (a) ΔG for RBCs treated with different concentrations of Lat-A measured using 3.0, 3.2, 3.6, 3.8, and 3.9 μm constricted micropores is shown here. (b) An 8.5 μm free-flight micropore is used to see any change in the size of RBCs when treated with different concentrations of Lat-A. The inset shows the microscopic image of the micropore used for this experiment.

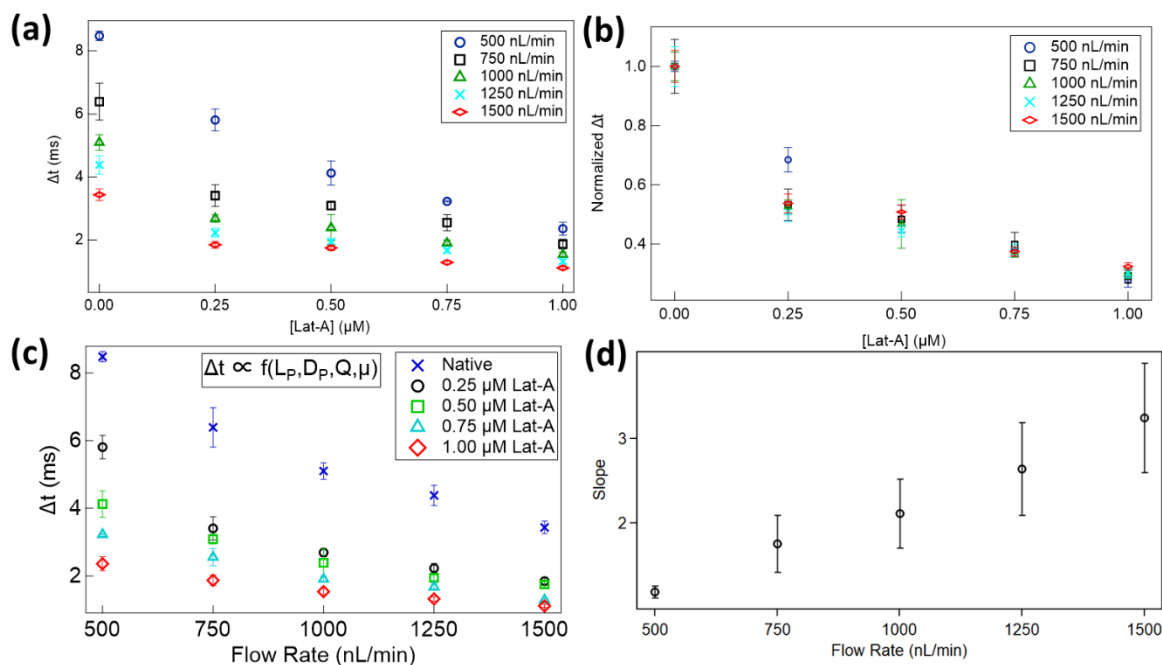


Figure A7. 11 Effect of flow rate on the Δt values of RBCs treated with different concentrations of Lat-A. (a) Constricted Δt for RBCs treated with different concentrations of RBCs translocating through a 3.8 μm micropore device at 500 (blue), 750 (black), 1000 (green), 1250 (cyan), and 1500 (red) nL/min constant fluid flow is shown here. (b) The normalized Δt values for different flow rates are plotted here. Note that the overlapping values of the normalized data imply that although the Δt values are decreasing with an increase in the fluid flow rates, but the effective stiffness changes inherited due the different concentrations of Lat-A remains same at all flow rates.(c) The linear relationship between the elasticity of RBCs treated with different Lat-A concentrations with the constricted Δt measurements is shown. (d) The slope of the linear relationship between elasticity and Δt for different constant fluid flow values is shown here.

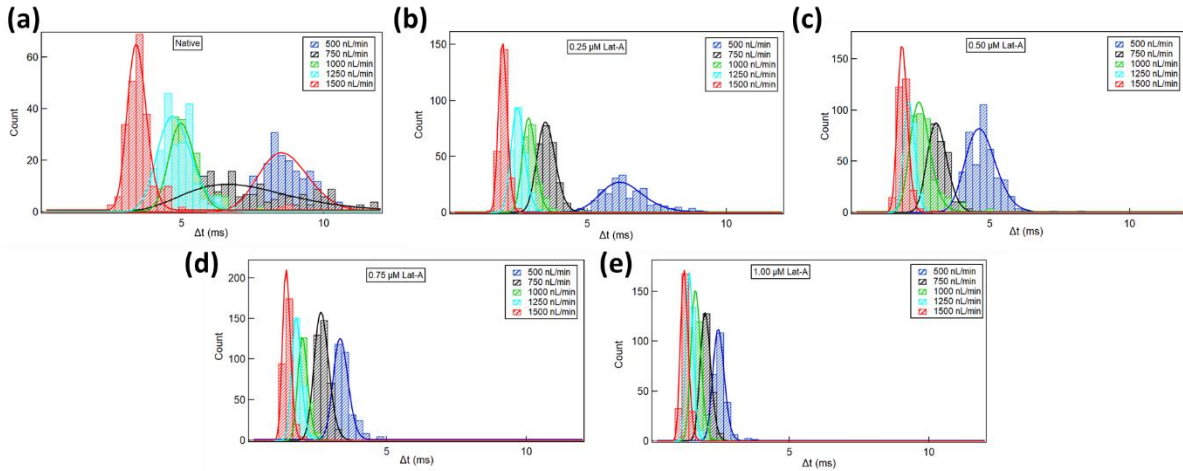


Figure A7.12 Δt histogram with the Gaussian fit for RBCs treated with different concentrations of Lat-A at different fluid flow. In (a), (b), (c), (d) and (e) we show the histogram of constricted Δt measured for RBCs treated with different concentration of Lat-A translocating through a $3.8 \mu\text{m}$ micropore device with 500 (blue), 750 (black), 1000 (green), 1250 (cyan) and 1500 (red) nL/min constant fluid flows. Note that all the histograms are Gaussian fitted.

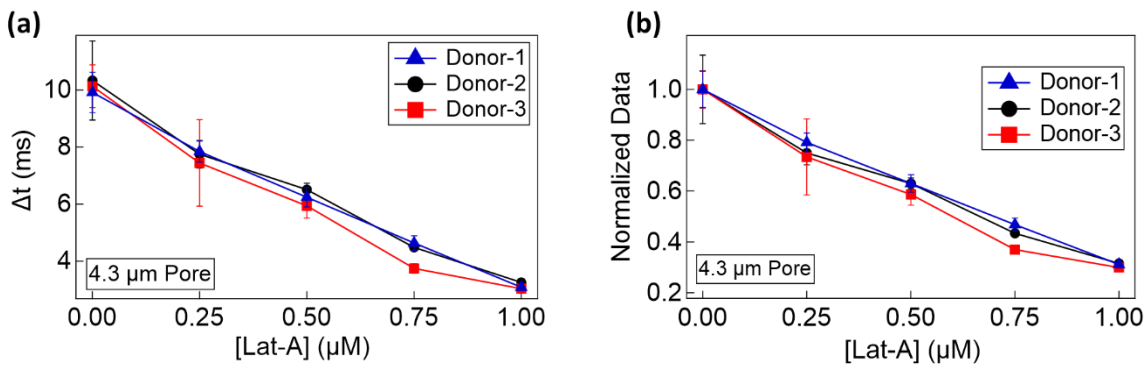


Figure A7.13 Effect of Lat-A on RBCs from different donors. (a) Dwell time (Δt) measurements taken on a $4.3 \mu\text{m}$ micropore device for RBCs different donors treated with different concentrations of Lat-A is shown here. (b) The normalised Δt measurements show that the Lat-A softens the RBCs similarly, irrespective of the donor.

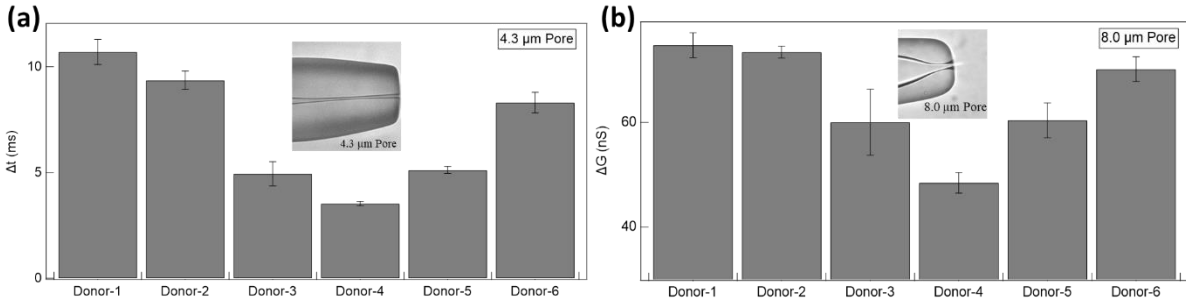


Figure A7.14 *Effect of sample size on the translocation experiment: (a) The constricted Δt is measured for different donors using a 4.3 μm micropore device (b) The free flight ΔG is measured for different donors using an 8.0 μm micropore device. Note that the ΔG of free flight corresponds to the size of the cell, and assuming that the RBCs from all the healthy donors have same elasticity the constricted Δt values follows the same trend as the free flight ΔG values, implying that the Δt measurements are dependent on the size of the cells.*

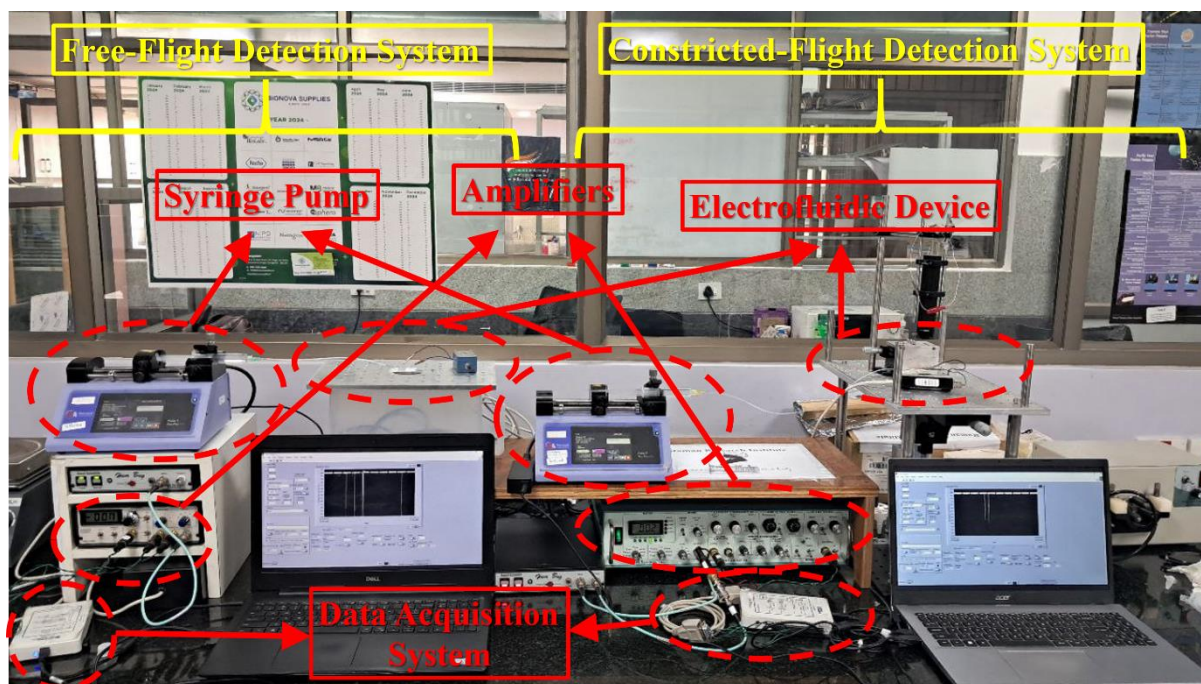


Figure A7.15 Hospital Setup: A mobile camera image of the Electrofluidic setup installed at St. Johns Medical Hospital is shown here. The free-flight and constricted-flight setups with their respective syringe pump, amplifiers, electrofluidic device mount and data acquisition system are highlighted in red dotted ovals.

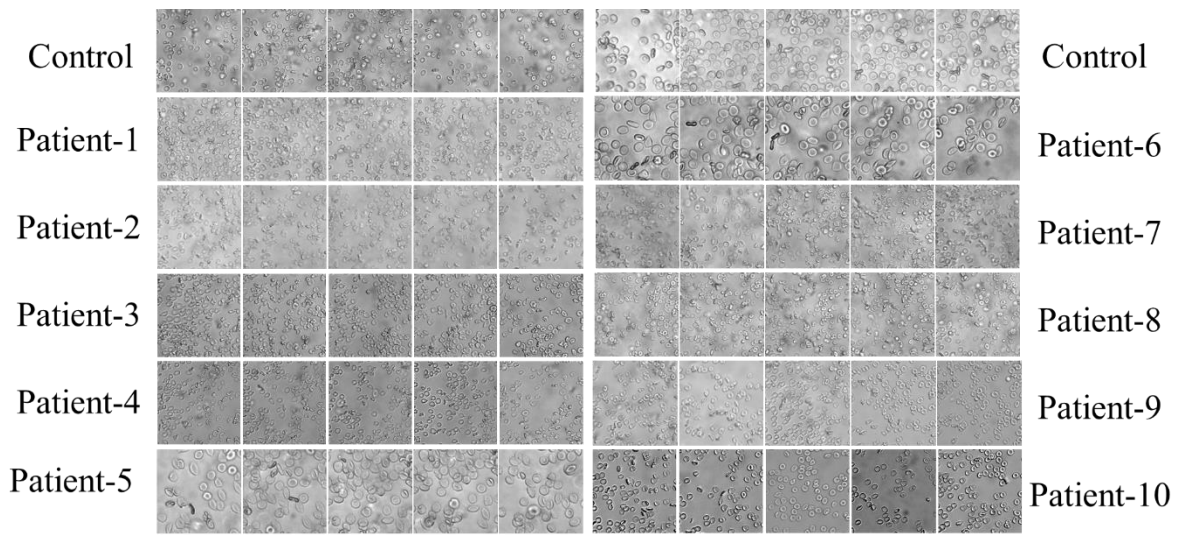


Figure A7.16 Image library of Red blood cells acquired from healthy donors and SCD patients. Microscopic images of red blood cells taken under a bright-field microscope with either 60X or 100X objective, for samples acquired from healthy and SCD patients.

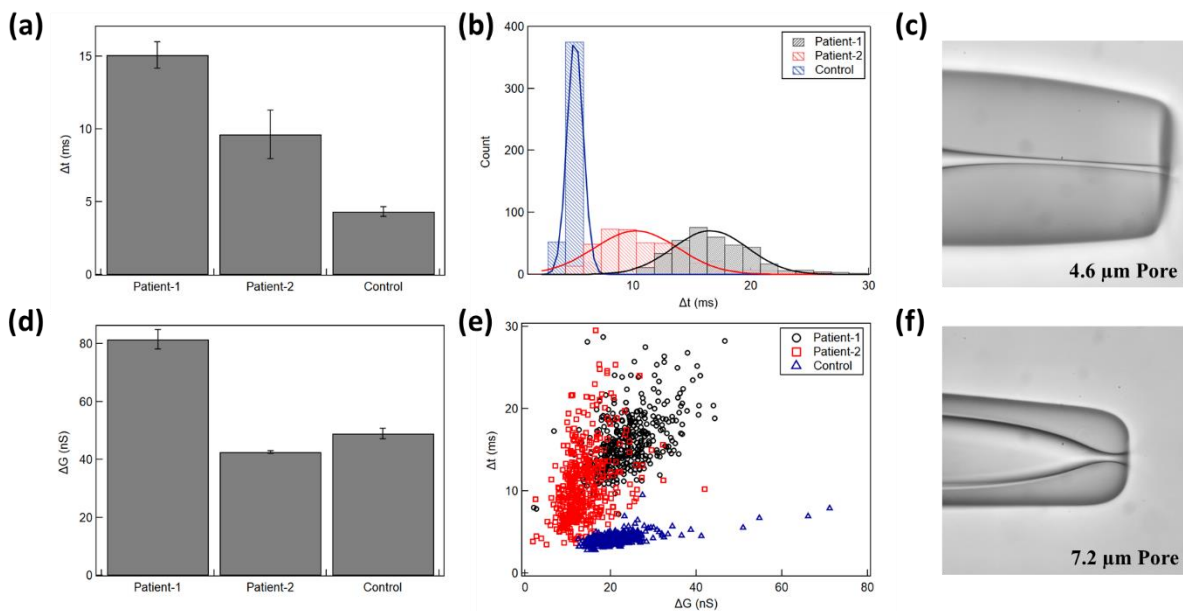


Figure A7.17 Translocation data for sickle cell anemia patient-1 and patient-2. (a), (b) and (e) show Δt bar-plot, Δt histogram, and Δt vs ΔG scatter plot of RBCs detected using a 4.6 μm constricted micropore for samples taken from a healthy donor and patients respectively. (c) and (f) are microscopic images of a constricted (4.6 μm) and a free flight (7.2 μm) micropore used here. (d) ΔG histogram of RBCs detected using a 7.2 μm free flight micropore for samples taken from a healthy donor and patients.

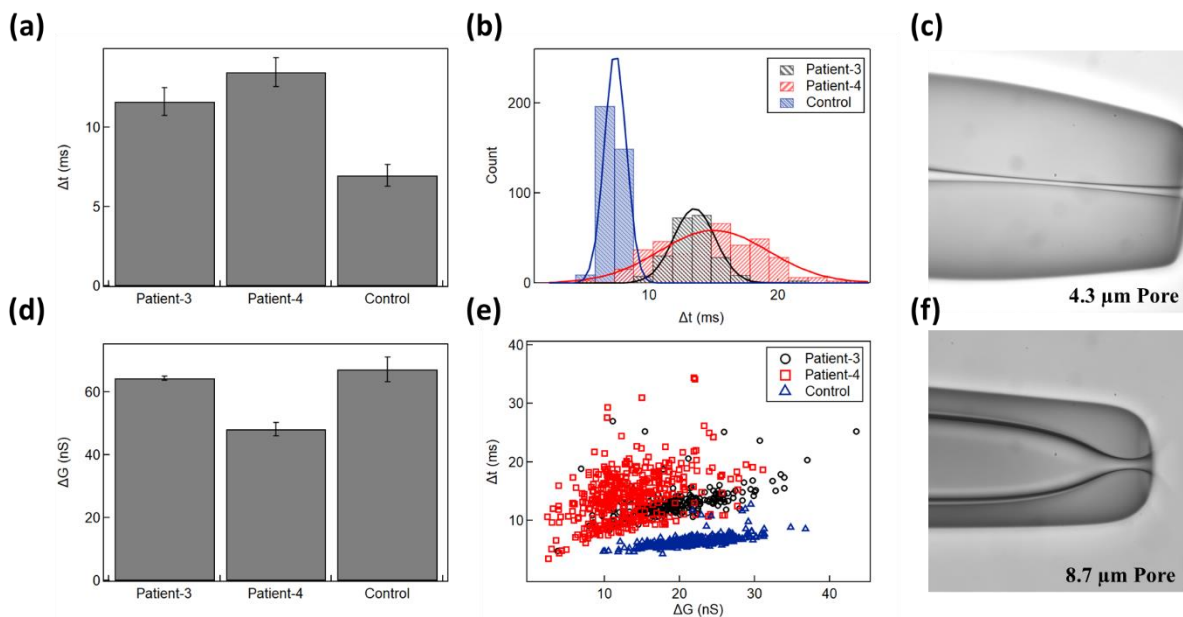


Figure A7.18 Translocation data for sickle cell anemia patient-3 and patient-4. (a), (b) and (e) show Δt bar-plot, Δt histogram, and Δt vs ΔG scatter plot of RBCs detected using a 4.3 μm constricted micropore for samples taken from a healthy donor and patients respectively. (c) and (f) are microscopic images of a constricted (4.3 μm) and a free flight (8.7 μm) micropore used here. (d) ΔG histogram of RBCs detected using a 8.7 μm free flight micropore for samples taken from a healthy donor and patients.

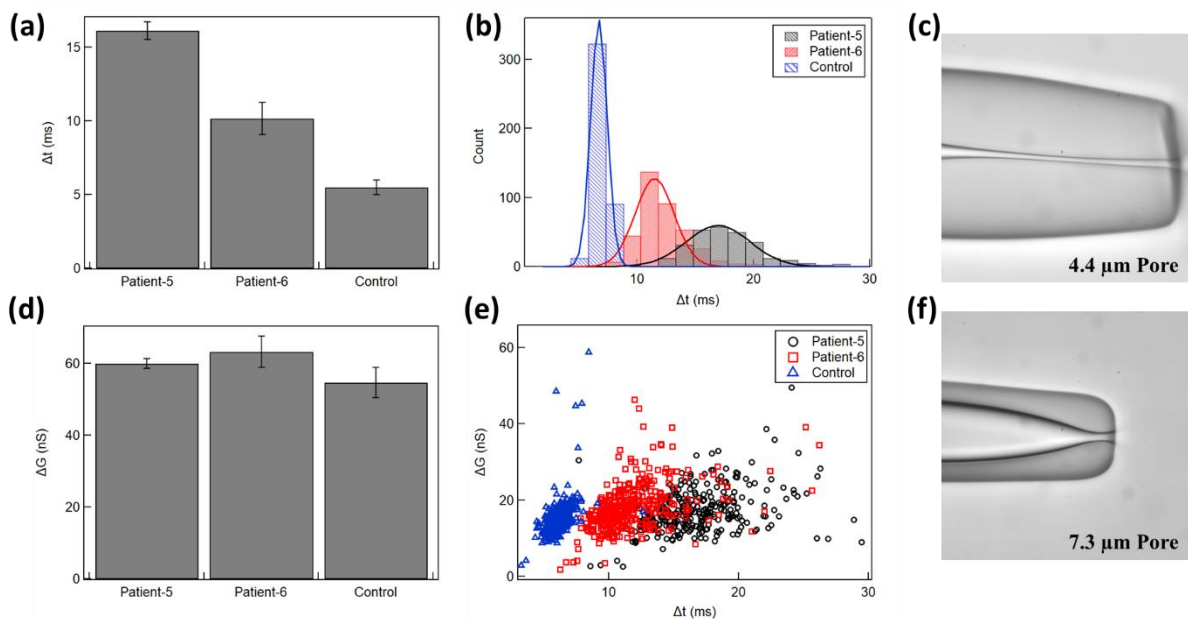


Figure A7.19 Translocation data for sickle cell anemia patient-5 and patient-6. (a), (b) and (e) show Δt bar-plot, Δt histogram, and ΔG vs Δt scatter plot of RBCs detected using a 4.4 μm constricted micropore for samples taken from a healthy donor and patients respectively. (c) and (f) are microscopic images of a constricted (4.4 μm) and a free flight (7.3 μm) micropore used here. (d) ΔG histogram of RBCs detected using a 7.3 μm free flight micropore for samples taken from a healthy donor and patients.

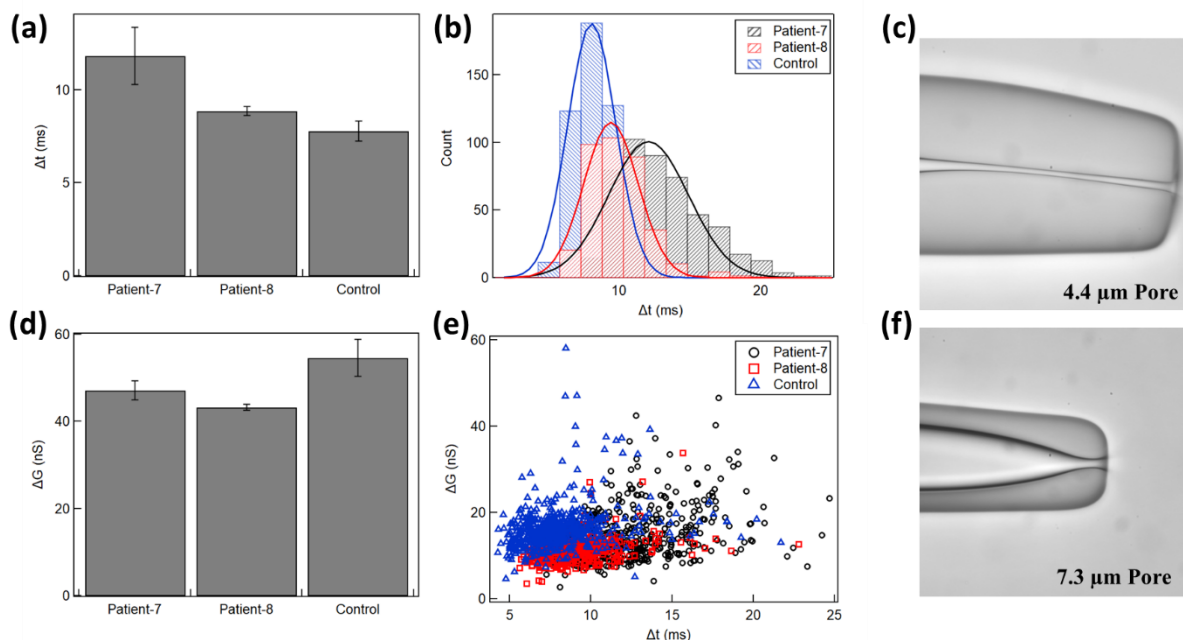


Figure A7.20 Translocation data for sickle cell anemia patient-7 and patient-8. (a), (b) and (e) show Δt bar-plot, Δt histogram, and ΔG vs Δt scatter plot of RBCs detected using a 4.4 μm constricted micropore for samples taken from a healthy donor and patients respectively. (c) and (f) are microscopic images of a constricted (4.4 μm) and a free flight (7.3 μm) micropore used here. (d) ΔG histogram of RBCs detected using a 7.3 μm free flight micropore for samples taken from a healthy donor and patients.

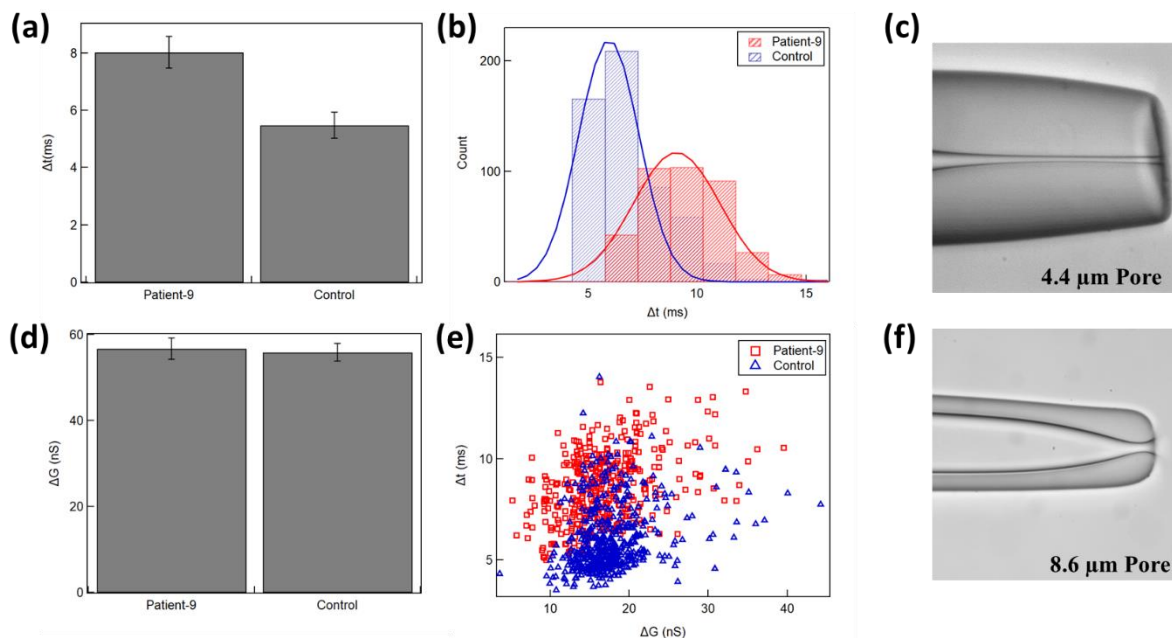


Figure A7.21 Translocation data for sickle cell anemia patient-9. (a), (b) and (e) show Δt bar-plot, Δt histogram, and ΔG vs Δt scatter plot of RBCs detected using a 4.4 μm constricted micropore for samples taken from a healthy donor and patients respectively. (c) and (f) are microscopic images of a constricted (4.4 μm) and a free flight (8.6 μm) micropore used here. (d) ΔG histogram of RBCs detected using a 8.6 μm free flight micropore for samples taken from a healthy donor and patients.

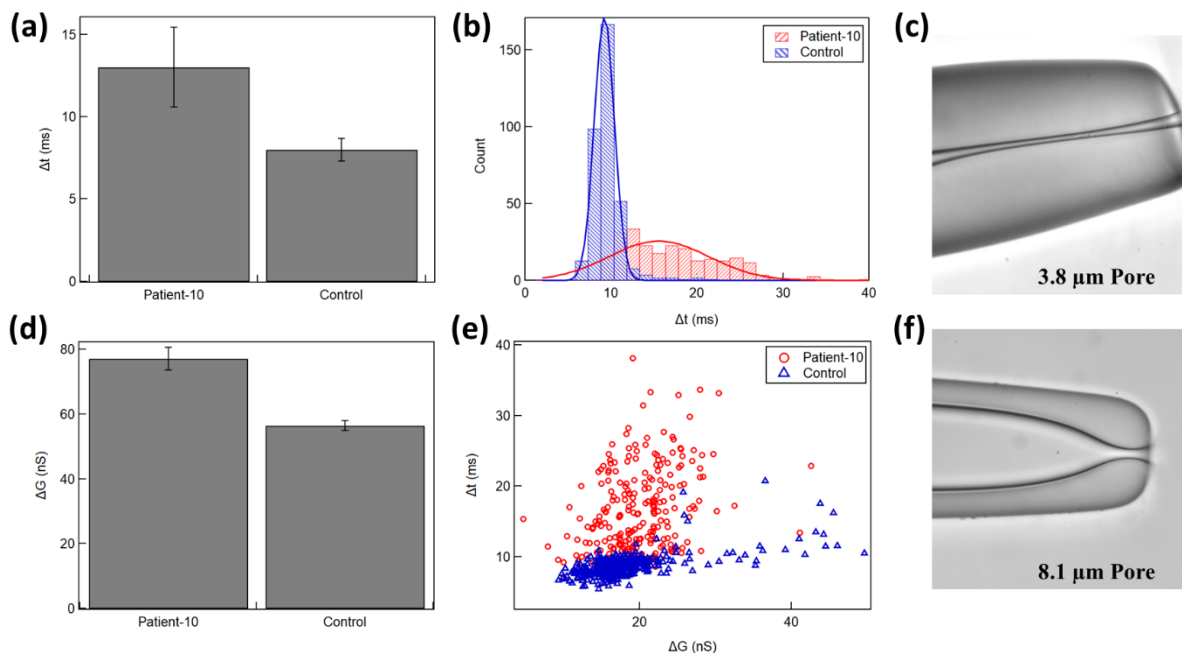


Figure A7.22 Translocation data for sickle cell anemia patient-10. (a), (b) and (e) show Δt bar-plot, Δt histogram, and ΔG vs Δt scatter plot of RBCs detected using a 3.8 μm constricted micropore for samples taken from a healthy donor and patients respectively. (c) and (f) are microscopic images of a constricted (3.8 μm) and a free flight (8.1 μm) micropore used here. (d) ΔG histogram of RBCs detected using a 8.1 μm free flight micropore for samples taken from a healthy donor and patients.

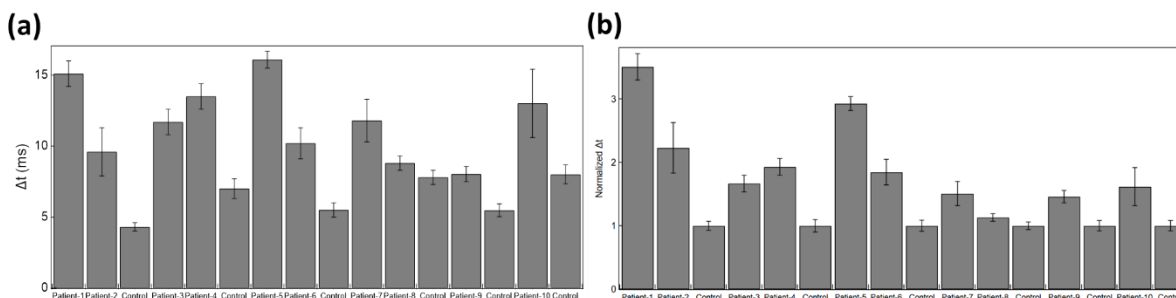


Figure A7.23 Summary of Δt values of the constricted micropore data acquired for healthy donors and SCD patients. (a) and (b) Shows The bar plot of the Δt values and normalized Δt values acquired in the constricted micropore translocation experiments performed on samples acquired from healthy donors and SCD patients normalized w.r.t. the healthy donor's data respectively.

APPENDIX 8

MATLAB Codes and Igor Scripts

A8.1 MATLAB code for analyzing the AFM force spectroscopy data

```
clear
clc
k=0.032793; %Spring Constant of the Cantilever (N/m)
R=4.5*10^3; %R converted to nm

Str_Raw='Cell*Raw.txt';
Str_ZSnsr='Cell*ZSnsr.txt';
Str_Defl='Cell*Defl.txt';

File_Raw=dir(Str_Raw);
File_ZSnsr=dir(Str_ZSnsr);
File_Defl=dir(Str_Defl);

%%
for g=1:1:length(File_Raw)
    try
        Raw=[]; Raw=importdata(File_Raw(g).name)*10^9; % Raw=data(:,1)*10^9;
        Def=[]; Def=importdata(File_Defl(g).name)*10^9; % Def=data(:,2)*10^9;
        Zsens=[]; Zsens=importdata(File_ZSnsr(g).name)*10^9; % Zsens=data(:,3)*10^9;
        Fit_D=File_Raw(g).name(6:8);
        Fit_D1=Fit_D;
        if(Fit_D(3)=='n')
            Fit_D(3)='';
            Fit_D1=['0',Fit_D];
        end
    end
end
```

```

R2(g,1)=0;
R2(g,2)=0;
R2(g,3)=0;
R2(g,4)= 0;
Fit_D1='50nm';
In_Check=str2num(Fit_D);
qRange=6;
Ind=Zsens-Def;
F=Def*k;
plot(Ind,F)
%=====
=====
%% Isolating just the Trace Part
DefT=Def(1:find(Def==max(Def)));
TraceZsens=Zsens(1:find(Def==max(Def)));
TraceInd=(TraceZsens-DefT);
TraceF=DefT*k;
%=====
=====
%% Offsetting to Zero Position
FT=(TraceF-mean(TraceF(1:floor(length(TraceF)/3))));
IndT=(TraceInd-mean(TraceInd(1:floor(length(TraceInd)/3))));
ZsensT=(TraceZsens-mean(TraceZsens(1:floor(length(TraceZsens)/3))));
%=====
=====
%% Finding the Contact point
XZ=ZsensT;
TD=Def(1:length(XZ));
%% Finding Slope of the F vs X (Def vs Zsens) at each Point
for j=1:1:length(DefT)-8
    x=XZ(j:j+7);

```

```

        y=TD(j:j+7);
%     plot(x,y);
        temp= polyfit (x, y, 1);
        slope(j)=temp(1);
end
slope_O=slope;
Xslope=IndT(1:length(IndT)-8);
plot(Xslope,slope)
%% Finding the Cutoff point between Contact and Non-Contact region
sig=3;
Sloperun=movmean(slope,10);    %Running Average of the slope
Slope3mean=mean(Sloperun(1:floor(length(Sloperun)/3)));
Slope3SD=std(FT(1:floor(length(Sloperun)/3)));
Slope_Threshold=Slope3mean+sig*Slope3SD;
CP=find(FT<Slope_Threshold);

C_Point=CP(length(CP));    %Contact Point

plot(Xslope,slope);hold on;plot(Xslope,Sloperun)
figure;
plot(Sloperun,'o');hold on;
plot([C_Point C_Point],[min(Sloperun) max(Sloperun)],'k','LineWidth',2);
E_Point=find(IndT==max(IndT));
% figure;
% plot(IndT,FTrun,'o');hold on;
% plot([IndT(C_Point) IndT(C_Point)],[min(FT) max(FT)],'k','LineWidth',2);
%
% plot(IndT,FT);
% hold on
% plot(IndT(C_Point),FT(C_Point),'ok');
% plot(IndT(E_Point),FT(E_Point),'sk');

```

```

F_Fit=FT(C_Point:E_Point)-FT(C_Point);
Ind_Fit=IndT(C_Point:E_Point)-IndT(C_Point);
Zsens_Fit=ZsensT(C_Point:E_Point)-ZsensT(C_Point);
plot(Ind_Fit,F_Fit);
qMax=Ind_Fit(length(Ind_Fit));
%% Fixing the Indentation Distance
% for q=1:1:4
q=2;
Fit_Distance=25*(q);
if qMax<Fit_Distance
    Fit_Distance=qMax;
end
%% Offsetting the Contact point to the Origin
C_Ind=(Ind_Fit-min(Ind_Fit));
C_Zsens=(Zsens_Fit-Zsens_Fit(1));
C_F=(F_Fit-F_Fit(1));
P_Fit=find(C_Ind>Fit_Distance);
if length(P_Fit)>0
    P_Dist=P_Fit(1);
    Fit_Ind=C_Ind(1:P_Dist);
    Fit_F=C_F(1:P_Dist);
else
    Fit_Ind=C_Ind;
    Fit_F=C_F;;
end
figure
plot(C_Ind,C_F);
hold on
plot(C_Zsens,C_F);
legend('IndTrace','ZsensTrace')
%% This part is if we want to use Spherical Ccantilever Fitting Function

```

```

xi=Fit_Ind(100);
fittest=fittype (@(E,x) 4/3*((4.5*1000)^0.5)*E/(1-0.495^2)*x.^(1.5));
[fitted_curve] = fit(Fit_Ind,Fit_F,fittest,'StartPoint',xi)

%% Parabolic Model
try
    EPa=Parabolic_Cantilever(Fit_Ind,Fit_F); %Calling the Fitting Fucntion
    Confid=confint(EPa);
    Elas_Parabola(g,q)=EPa.E*10^6;
    Elas_ParabolaBackup(g,q)=Elas_Parabola(g,q);
    EPaSD(g,q)=mean(abs(Confid-EPa.E))*10^6;
    Trigger_Pa(g,q)=str2num(Fit_D);
    FitDist_Pa(g,q)=Fit_Distance;
%%
close all;
catch
end
    EPa50=EPa;
    Fit_Ind50=Fit_Ind;
    Fit_F50=Fit_F;
    EP50=Elas_Parabola(g,q);
    EPERR50=EPaSD(g,q);
    F_O=Fit_F;
    F_E=4/3*((4.5*1000)^0.5)*EPa.E/(1-0.495^2)*Fit_Ind.^(1.5);
    Data1=[Fit_Ind,Fit_F];
    F1=sum(F_O);F2=sum(F_E);
    F1F2=sum(F_O.*F_E);
    F1Sq=sum(F_O.^2);F2Sq=sum(F_E.^2);
    n=length(F_O);
%% Calculating the R2 values for the fitting
    R1=((n*F1F2)-(F1*F2))/sqrt((n*F1Sq-(F1^2))*(n*F2Sq-(F2^2)))

```

```

R2(g,1)=R1^2;
R2(g,2)=Elas_Parabola(g,q);
R2(g,3)=Elas_Parabola(g,q);
R2(g,4)= EPaSD(g,q);

if (R2(g,1)<0.9)|| (Elas_Parabola(g,q)<0)
    R2(g,3)=0;
end
% end
%=====
=====
%% To Save the Graph at desired directory
h1=figure('units','normalized','outerposition',[0 0 0.5 0.75]);
hold on;
s=' ';
plot(Fit_Ind50,Fit_F50,'k','MarkerSize',12)
plot(EPa50,'k');
str2=["Trigger Distance:",s,Fit_D,s,' nm'];
str3=["Elasticity(50nm): ",s,num2str(EP50),s,char(177),s,num2str(EPErr50),s,' kPa'];
str4=["R^2 Value:",s,num2str(R2(g,1))];
xlabel('Indentation (nm)');ylabel('Force (nN)');
dim = [0.15 0.45 0.3 0.3];
str={num2str(g),'Parabolic Model Fit:',str3,str4};
annotation('textbox',dim,'String',str,'FitBoxToText','on');
Dir=[cd,'\New folder'];
FileName=[num2str(g),'_Trig_100',s,'nm.png'];
File=[Dir,FileName];
saveas(h1,File,'png');
end
end
saveas(R2,File,'.txt');

```

A8.2 MATLAB function ‘Parabolic_Cantilever’ used in the previous section

```
function [fitresult, gof] = createFit(Xin_T, Fin_T)
%CREATEFIT(XIN_T,FIN_T)
% Create a fit.
%
% Data for 'Parabolic_Cantilever' fit:
%   X Input : Xin_T
%   Y Output: Fin_T
% Output:
%   fitresult : a fit object representing the fit.
%   gof : structure with goodness-of fit info.
%
% See also FIT, CFIT, SFIT.

%% Fit: 'Parabolic_Cantilever'.
[xData, yData] = prepareCurveData( Xin_T, Fin_T );

% Set up fitype and options.
ft = fitype( '4/3*((4.5*1000)^0.5)*E/(1-0.495^2)*x^(1.5)', 'independent', 'x', 'dependent', 'y' );
opts = fitoptions( 'Method', 'NonlinearLeastSquares' );
opts.Display = 'Off';
opts.Robust = 'Bisquare';
opts.StartPoint = 0.421761282626275;

% Fit model to data.
[fitresult, gof] = fit( xData, yData, ft, opts );

% Plot fit with data.
```

```
% figure( 'Name', 'Parabolic_Cantilever' );  
figure  
h = plot( fitresult, xData, yData );  
legend( h, 'Force vs. Indentation', 'Parabolic_Cantilever', 'Location', 'NorthEast', 'Interpreter',  
'none' );  
% Label axes  
xlabel( 'X (nm)', 'Interpreter', 'none' );  
ylabel( 'Force (nN)', 'Interpreter', 'none' );  
grid on
```

A8.3 Igor scripts to extract the AFM force spectroscopy data to be used in MATLAB

```
#pragma rtGlobals=1           // Use modern global access method.
#include <Multi-peak fitting 2.0>
#include <InsertSubwindowInGraph>

//=====

macro Export_F_X_1Line()
Variable Lnum,Pnum
Lnum=10           //This has to be changed based on which Line is exported in the Data browser
                  folder by clicking on the F-map pixels.
Pnum=15           //This will be a fixed number for a particular F-map Matrix.
Export_1Line(Lnum,Pnum)
end

//=====

//=====

macro Export_Fmap_All()
Variable Lnum,Pnum
Lnum=31           //This has to be changed based on which Line is exported in the Data browser
                  folder by clicking on the F-map pixels.
Pnum=31           //This will be a fixed number for a particular F-map Matrix.
Export_All(Lnum,Pnum)
end

//=====

//=====

macro Export_FX_All()
Variable Tot
```

Tot= 51//This has to be changed based on which Line is exported in the Data browser folder
by clicking on the F-map pixels.

Export_All_FX(Tot)

end

//=====

//=====

Function Export_All_FX(Tot)

Variable Tot

String WaveRaw, WaveDefl, WaveZSnsr,UserPath

Variable i

for(i=Tot;i>=0;i-=1)

if (i<=9)

WaveRaw= "Image000"+num2str(i)+"Raw"

WaveDefl= "Image000"+num2str(i)+"Defl"

WaveZSnsr= "Image000"+num2str(i)+"ZSnsr"

elseif (i>=1000)

WaveRaw= "Image"+num2str(i)+"Raw"

WaveDefl= "Image"+num2str(i)+"Defl"

WaveZSnsr= "Image"+num2str(i)+"ZSnsr"

elseif (i>=100)

WaveRaw= "Image0"+num2str(i)+"Raw"

WaveDefl= "Image0"+num2str(i)+"Defl"

WaveZSnsr= "Image0"+num2str(i)+"ZSnsr"

elseif (i>=10)

WaveRaw= "Image00"+num2str(i)+"Raw"

WaveDefl= "Image00"+num2str(i)+"Defl"

WaveZSnsr= "Image00"+num2str(i)+"ZSnsr"

endif

print i

```
Save/G/M="\n"/P=Test $WaveRaw as WaveRaw+".txt"  
Save/G/M="\n"/P=Test $WaveDefl as WaveDefl+".txt"  
Save/G/M="\n"/P=Test $WaveZSnsr as WaveZSnsr+".txt"
```

```
endfor
```

```
end
```

```
//=====
```

```
//=====
```

```
Function Export_1Line(Lnum,Pnum)
```

```
Variable Lnum, Pnum
```

```
String WaveRaw, WaveDefl, WaveZSnsr,UserPath
```

```
Variable i
```

```
for(i=Pnum;i>=0;i-=1)
```

```
    if (Lnum<=9 && i<=9)
```

```
        WaveRaw=
```

```
"Line000"+num2str(Lnum)+"Point000"+num2str(i)+"Raw"
```

```
        WaveDefl=
```

```
"Line000"+num2str(Lnum)+"Point000"+num2str(i)+"Defl"
```

```
        WaveZSnsr=
```

```
"Line000"+num2str(Lnum)+"Point000"+num2str(i)+"ZSnsr"
```

```
    elseif (Lnum<=9 && i>=10)
```

```
        WaveRaw=
```

```
"Line000"+num2str(Lnum)+"Point00"+num2str(i)+"Raw"
```

```
        WaveDefl=
```

```
"Line000"+num2str(Lnum)+"Point00"+num2str(i)+"Defl"
```

```
        WaveZSnsr=
```

```
"Line000"+num2str(Lnum)+"Point00"+num2str(i)+"ZSnsr"
```

```
    elseif (Lnum>=10 && i<=9)
```

```
        WaveRaw=
```

```
"Line00"+num2str(Lnum)+"Point000"+num2str(i)+"Raw"
```

```

WaveDefl=
"Line00"+num2str(Lnum)+"Point000"+num2str(i)+"Defl"
WaveZSnsr=
"Line00"+num2str(Lnum)+"Point000"+num2str(i)+"ZSnsr"
elseif (Lnum>=10 && i>=10)
WaveRaw=
"Line00"+num2str(Lnum)+"Point00"+num2str(i)+"Raw"
WaveDefl= "Line00"+num2str(Lnum)+"Point00"+num2str(i)+"Defl"
WaveZSnsr=
"Line00"+num2str(Lnum)+"Point00"+num2str(i)+"ZSnsr"
endif
Save/G/M="\r\n" /W/P=X20220114_Native $WaveRaw as WaveRaw+".txt"
Save/G/M="\r\n" /W/P=X20220114_Native $WaveDefl as WaveDefl+".txt"
Save/G/M="\r\n" /W/P=X20220114_Native $WaveZSnsr as
WaveZSnsr+".txt"
endifor
end

//=====

```

A8.4 Igor scripts used for micropore data analysis

```
#pragma rtGlobals=1           // Use modern global access method.
#include <Multi-peak fitting 2.0>
#include <InsertSubwindowInGraph>

//=====

//CurveFit/ODR=2 Power, dTG_mean/X=dGFF/D/R=dTG_SD/XR=dGFFErr

//READ ME

//Step0() Creates the Waves to write the dG, dGSD, dT, dTSD and #Events in a set.
//Step1() Plots, fits and write the fitting values to the respective waves
//Step2() Creates the waves to write the mean and SD of dG and dT from different samples
//Step3() write the mean and Sd values of different samples
//=====

//Steps to Write Data to the File
//1) Run Step0() macro ONLY ONCE with the Red Cursor AT THE BEAD FOLDER (e.g
3.0umBead).
//2) Run Create_dG_Wave keeping the red cursor at the Set Folder
//3) Keep the Red Cursor to the Last Set(e.g Set4 and not Set Set1) and run Step1() macro, take to
the folder
//   above to the Last set(e.g Set3) and Run Step1() macro again.
//4) Run Step2() macro ONLY ONCE with the Red Cursor AT THE PORE FOLDER (e.g
10.0umPore).
//5) Run Step3() macro ONLY ONCE with the Red Cursor AT THE BEAD FOLDER (e.g
3.0umBead).

//Steps to Make the Layout
//1) Run ALL_PLOTS() marco
//2) Make Sure that the graph numbers are correct before running the Make_Layout() macro
```

```

//=====
macro StandardPlot()
ModifyGraph tick=2,mirror=2,nticks=3,fSize=16,font="Arial"
end
//=====

//=====
macro Create_dG_Wave()
Variable Voltage
Voltage=0.2
Duplicate maximum dG
dG=dG/Voltage
end
//=====
//=====
Macro Step0() //Creates a NULL Table. USE IT ONLY ONCE WHILE START
WRITING IN A FOLDER
Make/D
Set_Number,'dG_nS','dG_Sigma_nS','dT_ms','dT_Sigma_ms',Events,'dTG_ms','dTG_Sigma_ms'
Variable m
m=numpts(dG_Sigma_nS)
DeletePoints 0,m,dG_nS
DeletePoints 0,m,dG_Sigma_nS
DeletePoints 0,m,dT_ms
DeletePoints 0,m,dT_Sigma_ms
DeletePoints 0,m,dTG_ms
DeletePoints 0,m,dTG_Sigma_ms
DeletePoints 0,m,Set_Number
DeletePoints 0,m,Events
end
//=====

```

```

//=====
Macro Step1()
Variable/G n=1          //Set Number
n=n-1
Write_dG()
Write_dT()
dTCummulative()
end
//=====

//=====
macro Step2()          //USE IT ONLY ONCE WHEN THE DATA FOR BEADS
FOLDER IS WRITTEN IN THE WAVES
//Make/D 'dG_mean','dG_SD','dT_mean','dT_SD','Samp'
//Make/N=1/T Sample
Make/N=1/T Sample
Make/D 'dG_mean','dG_SD','dT_mean','dT_SD','dTG_mean','dTG_SD'
Variable m
m=numpts(dG_mean)
DeletePoints 0,m,dG_mean
DeletePoints 0,m,dG_SD
DeletePoints 0,m,dT_mean
DeletePoints 0,m,dT_SD
DeletePoints 0,m,dTG_mean
DeletePoints 0,m,dTG_SD
DeletePoints 0,m,Sample
end
//=====

macro Step3()
Variable n=0

```

```
InsertPoints 0,1, ::dG_mean
InsertPoints 0,1, ::dG_SD
InsertPoints 0,1, ::dT_mean
InsertPoints 0,1, ::dT_SD
InsertPoints 0,1, ::dTG_mean
InsertPoints 0,1, ::dTG_SD
//InsertPoints 0,1, ::Bead_dia
```

```
Variable dGmean,dGSD,dTmean,dTSD,dTGmean,dTGSD
```

```
string path
```

```
path=ParseFilePath(0, GetDataFolder(1), ":", 1, 0)
```

```
dGmean=mean(dG_nS)
```

```
dTmean=mean(dT_ms)
```

```
dTGmean=mean(dTG_ms)
```

```
dGSD=sqrt (variance (dG_nS))
```

```
dTSD=sqrt (variance (dT_ms))
```

```
dTGSD=sqrt (variance (dTG_ms))
```

```
::dG_mean(n)=dGmean
```

```
::dG_SD(n)=dGSD
```

```
::dT_mean(n)=dTmean
```

```
::dT_SD(n)=dTSD
```

```
::dTG_mean(n)=dTGmean
```

```
::dTG_SD(n)=dTGSD
```

```
end
```

```
//=====
```

```
//=====
```

```
macro Write_dG()
```

```
WaveStats dG
```

```

Variable b,bnum,start,last,dG_mean,dG_SD,Tevents,range
range=5
String dG_label, dGSD_label,counts
b=sqrt(V_avg) // Bin Width
bnum=sqrt(V_npnts)*3 // Total Bins
Tevents=V_npnts
counts="# Events="+num2str(V_npnts)
Make/N=100/O dG_Hist;DelayUpdate
Histogram/C/B={V_min-2*b,b,bnum} dG,dG_Hist;DelayUpdate
Display dG_Hist
ModifyGraph mode=5
CurveFit/M=0/W=0 gauss, dG_Hist/D
dG_mean=W_coef[2]
dG_SD=W_coef[3]
start=max(0,dG_mean -range*dG_SD) // X-axes Start
last=dG_mean + range*dG_SD // X-axes End
ModifyGraph offset(dG_Hist)={-b/2,0}
SetAxis bottom start,last
dG_label= "dG Mean="+num2str(dG_mean)+" nS"
dGSD_label= "dG SD="+num2str(dG_SD)+" nS"
TextBox/C/N=text0/A=MC "\\F'Times New Roman"+dG_label + "\\r"+dGSD_label+"\\r"+counts
ModifyGraph rgb(fit_dG_Hist)=(0,0,0)
Label left "\\F'Times New Roman'Counts";DelayUpdate
Label bottom "\\F'Times New Roman'dG (nS\\F'Times New Roman)"
ModifyGraph tick=2
ModifyGraph gFont="Times New Roman"
InsertPoints 0,1, ::dG_nS
InsertPoints 0,1, ::dG_Sigma_nS
InsertPoints 0,1, ::Set_Number
InsertPoints 0,1, ::Events
::dG_nS(n)=dG_mean

```

```

::dG_Sigma_nS(n)=dG_SD
::Events(n)=Tevents
::Set_Number(n)=SetNum
end

//=====

//=====

macro Write_dT()
WaveStats dwell_time
Variable bnum,start,last,Range,dT_mean,dT_SD,dTG_mean,dTG_SD
Variable/G b
Range=15 //To set the start and end of the plot. dT_mean (+-) dT_SD*Range is
the Plotting Range
String dT_label, dTSD_label,counts
counts="# Events="+num2str(V_npnts)
b=sqrt(V_avg)/2 // Bin Width
b=0.25
bnum=sqrt(V_npnts) // Total Bins
bnum=50
Make/N=100/O dwell_time_Hist;DelayUpdate
Histogram/C/B={0.0005,b,bnum} dwell_time,dwell_time_Hist
Display dwell_time_Hist
ModifyGraph mode=5
variable V_FitError
if (V_fitError)
Code to do whatever you want to do in this case.
endif
DeletePoints 0,1, dwell_time
K0 = 0;
CurveFit/M=2/W=0 LogNormal, dwell_time_Hist/D
dT_mean=W_coef[2]

```

```

dT_SD=W_coef[3]
start=max (0,dT_mean -Range*dT_SD)           // X-axes Start
last=min (20,dT_mean + Range*dT_SD)           // X-axes End
ModifyGraph rgb(fit_dwell_time_Hist)=(0,0,0),offset(fit_dwell_time_Hist)={0,0}
SetAxis bottom start,last
dT_label= "dT Mean="+num2str(dT_mean)+" ms"
dTSD_label= "dT SD="+num2str(dT_SD)+" ms"
TextBox/C/N=text0/A=MC "\\F"Times New Roman"+dT_label +"\r"+dTSD_label+"\r"+counts
ModifyGraph tick=2
ModifyGraph gFont="Times New Roman"
ModifyGraph offset(dwell_time_Hist)={0,0}
ModifyGraph offset(fit_dwell_time_Hist)={b/2,0}
duplicate dwell_time_Hist dwell_time_HistGauss
K0 = 0;
CurveFit/H="1000"/TBOX=768 gauss dwell_time_HistGauss /D
AppendToGraph fit_dwell_time_HistGauss
dTG_mean=W_coef[2]
dTG_SD=W_coef[3]
String countsG,dT_labelG,dTSD_labelG,FitTypeG
WaveStats dwell_time
FitTypeG="Gaussian Fit:"
countsG="# Events="+num2str(V_npnts)
dT_labelG= "dT Mean="+num2str(dTG_mean)+" ms"
dTSD_labelG= "dT SD="+num2str(dTG_SD)+" ms"
TextBox/C/N=text1/A=MC "\\F"Times New Roman"+FitTypeG+"\r"+dT_labelG
+"\r"+dTSD_labelG+"\r"+countsG
ModifyGraph tick=2
ModifyGraph gFont="Times New Roman"
ModifyGraph
lsize(fit_dwell_time_HistGauss)=1.5,rgb(fit_dwell_time_HistGauss)=(0,0,0);DelayUpdate
ModifyGraph offset(fit_dwell_time_HistGauss)={b/2,0}

```

```

ModifyGraph rgb(fit_dwell_time_HistGauss)=(1,4,52428)
Duplicate/O dwell_time_hist, dT_Cum
Wavestats dT_Cum
Integrate/meth=0 dT_Cum
dT_Cum=dT_Cum/dT_Cum(V_Sum)
InsertPoints 0,1, ::dT_ms
InsertPoints 0,1, ::dT_Sigma_ms
InsertPoints 0,1, ::dTG_ms
InsertPoints 0,1, ::dTG_Sigma_ms
::dT_ms(n)=dT_mean
::dT_Sigma_ms(n)=dT_SD
::dTG_ms(n)=dTG_mean
::dTG_Sigma_ms(n)=dTG_SD
StandardPlot()
end

//=====

//=====

macro Plot_dG()
WaveStats dG
Variable/G b,bnum,start,last,dG_mean,dG_SD,Tevents,range
range=5
String/G dG_label, dGSD_label,counts
b=sqrt(V_avg) // Bin Width
bnum=sqrt(V_npnts)*1.5 // Total Bins
Tevents=V_npnts
counts="# Events="+num2str(V_npnts)
Make/N=100/O dG_Hist;DelayUpdate
Histogram/C/B={V_min-2*b,b,bnum} dG,dG_Hist;DelayUpdate
Display dG_Hist
ModifyGraph mode=5

```

```

CurveFit/M=0/W=0 gauss, dG_Hist/D
dG_mean=W_coef[2]
print dG_mean
dG_SD=W_coef[3]
start=max (0,dG_mean -range*dG_SD)           // X-axes Start
last=dG_mean + range*dG_SD                   // X-axes End
ModifyGraph offset(dG_Hist)={-b/2,0}
SetAxis bottom start,last
dG_label= "dG Mean="+num2str(dG_mean)+" nS"
dGSD_label= "dG SD="+num2str(dG_SD)+" nS"
TextBox/C/N=text0/A=MC "\\F'Times New Roman"+dG_label +"\r"+dGSD_label+"\r"+counts
ModifyGraph rgb(fit_dG_Hist)=(0,0,0)
Label left "\\F'Times New Roman'Counts";DelayUpdate
Label bottom "\\F'Times New Roman'dG (nS\\F'Times New Roman)"
ModifyGraph tick=2
ModifyGraph gFont="Times New Roman"
print b
print bnum
print V_min
end

//=====

//=====

macro Plot_dT()
WaveStats dwell_time
Variable bnum,start,last,Range,dT_mean,dT_SD
Variable/G b
Range=15 //To set the start and end of the plot. dT_mean (+-) dT_SD*Range is
the Plotting Range
String dT_label, dTSD_label,counts
counts="# Events="+num2str(V_npnts)

```

```

b=sqrt(V_avg)/2 // Bin Width
b=0.25
bnum=sqrt(V_npnts) // Total Bins
bnum=50
Make/N=100/O dwell_time_Hist;DelayUpdate
Histogram/C/B={0.0005,b,bnum} dwell_time,dwell_time_Hist
Display dwell_time_Hist
ModifyGraph mode=5
//variable V_FitError
//if (V_fitError)
// Code to do whatever you want to do in this case.
//endif
K0 = 0;
CurveFit/M=2/W=0 LogNormal, dwell_time_Hist/D
dT_mean=W_coef[2]
dT_SD=W_coef[3]
start=max (0,dT_mean -Range*dT_SD) // X-axes Start
last=min (20,dT_mean + Range*dT_SD) // X-axes End
ModifyGraph rgb(fit_dwell_time_Hist)=(0,0,0),offset(fit_dwell_time_Hist)={0,0}
SetAxis bottom start,last
dT_label= "dT Mean="+num2str(dT_mean)+" ms"
dTSD_label= "dT SD="+num2str(dT_SD)+" ms"
TextBox/C/N=text0/A=MC "\\F"Times New Roman"+dT_label + "\\r"+dTSD_label+"\\r"+counts
ModifyGraph tick=2
ModifyGraph gFont="Times New Roman"
ModifyGraph offset(dwell_time_Hist)={0,0}
ModifyGraph offset(fit_dwell_time_Hist)={b/2,0}
end
//=====
//=====

```

```

macro Plot_Scatter()
Display dG vs dwell_time
ModifyGraph mode=2
ModifyGraph minor=1,standoff=0
Label left "dG(nS)";DelayUpdate
Label bottom "dT(ms)"
Variable dGmin,dGmax,dTmin,dTmax
Variable g1,t1
g1=2
t1=5
WaveStats dG
dGmin=max (0,V_avg - g1*V_sdev)
dGmax=V_avg + g1*V_sdev
WaveStats dwell_time
dTmin=max (0,V_avg - t1*V_sdev)
dTmax=V_avg + t1*V_sdev
SetAxis left dGmin,dGmax;DelayUpdate
SetAxis bottom dTmin,dTmax
ModifyGraph lsize=2
Label left "\\F'Times New Roman\\Z16dG(nS)";DelayUpdate
Label bottom "\\Z16\\F'Times New Roman'dT(ms)\\F'Tahoma\\F'Times New Roman"
ModifyGraph tick=2
end

```

=====

=====

```

macro Contour()
Display dG_G vs dwell_time
ModifyGraph mode=2,lsize=1.2
end

```

=====

```

//=====
macro FWHM()
WaveStats FWHM
Variable bnum,start,last,Range,dT_mean,dT_SD
Variable/G b
Range=15 //To set the start and end of the plot. dT_mean (+-) dT_SD*Range is
the Plotting Range
String dT_label, dTSD_label,counts
counts="# Events="+num2str(V_npnts)
b=sqrt(V_avg)/2 // Bin Width
b=0.25
bnum=sqrt(V_npnts) // Total Bins
bnum=50
Make/N=100/O FWHM_Hist;DelayUpdate
Histogram/C/B={0.0001,b,bnum} FWHM,FWHM_Hist
Display FWHM_Hist
ModifyGraph mode=5
//variable V_FitError
//if (V_fitError)
// Code to do whatever you want to do in this case.
//endif
CurveFit/M=2/W=0 LogNormal, FWHM_Hist/D
dT_mean=W_coef[2]
dT_SD=W_coef[3]
start=max (0,dT_mean -Range*dT_SD) // X-axes Start
last=min (20,dT_mean + Range*dT_SD) // X-axes End
ModifyGraph rgb(fit_FWHM_Hist)=(0,0,0),offset(fit_FWHM_Hist)={0,0}
SetAxis bottom start,last
dT_label= "dT Mean="+num2str(dT_mean)+" ms"
dTSD_label= "dT SD="+num2str(dT_SD)+" ms"

```

```

TextBox/C/N=text0/A=MC "\\F"Times New Roman"+dT_label +"\r"+dTSD_label+"\r"+counts
ModifyGraph tick=2
ModifyGraph gFont="Times New Roman"
ModifyGraph offset(FWHM_Hist)={0,0}
ModifyGraph offset(fit_FWHM_Hist)={b/2,0}
end

//=====

//=====

macro dTCumulative()
Duplicate/O dwell_time_hist, dT_Cum
Wavestats dT_Cum
Integrate/meth=0 dT_Cum
dT_Cum=dT_Cum/dT_Cum(V_Sum)
end

//=====

//=====

macro Create-Compatible_Waves()
duplicate wave1 filenum;
duplicate wave3 maximum;
duplicate wave5 dwell_time;
duplicate wave8 startt;
duplicate wave9 endd;
KillWaves
wave0,wave1,wave2,wave3,wave4,wave5,wave6,wave7,wave8,wave9,wave10,wave11,wave12,
wave13;
Variable Voltage
Voltage=0.2
Duplicate maximum dG

```

```
dG=dG/Voltage
```

```
end
```

```
//=====
```

```
//=====
```

```
macro Write_dT_dG_Square()
```

```
Variable/G n=1 //Set Number
```

```
n=n-1
```

```
dT_Square()
```

```
StandardPlot()
```

```
Write_dG()
```

```
StandardPlot()
```

```
end
```

```
//=====
```

```
//=====
```

```
macro dT_Square()
```

```
Variable bnum,start,last,Range,dT_mean,dT_SD,dTG_mean,dTG_SD
```

```
Make/N=75/O dwell_time_Hist;DelayUpdate
```

```
Histogram/C/B={0.5,1.5,60} dwell_time,dwell_time_Hist;DelayUpdate
```

```
Display dwell_time_Hist
```

```
ModifyGraph mode=5
```

```
K0 = 0;
```

```
CurveFit/H="1000"/NTHR=0 LogNormal dwell_time_Hist /D
```

```
dT_mean=W_coef[2]
```

```
dT_SD=W_coef[3]
```

```
String counts,dT_label,dTSD_label,FitType
```

```
FitType="Lognormal Fit:"
```

```
WaveStats dwell_time
```

```
counts="# Events="+num2str(V_npnts)
```

```

dT_label= "dT Mean="+num2str(dT_mean)+" ms"
dTSD_label= "dT SD="+num2str(dT_SD)+" ms"
TextBox/C/N=text0/A=MC "\\F"Times New Roman"+FitType+"\r"+dT_label
+"\r"+dTSD_label+"\r"+counts
ModifyGraph tick=2
ModifyGraph gFont="Times New Roman"
ModifyGraph lsize(fit_dwell_time_Hist)=1.5,rgb(fit_dwell_time_Hist)=(0,0,0);DelayUpdate
ModifyGraph offset(fit_dwell_time_Hist)={0.75,0}
Duplicate/O dwell_time_hist, dT_Cum
Wavestats dT_Cum
Integrate/meth=0 dT_Cum
//dT_Cum=dT_Cum/dT_Cum(V_Sum)
duplicate dwell_time_Hist dwell_time_HistGauss
Histogram/C/B={0.5,1.5,60} dwell_time,dwell_time_HistGauss;DelayUpdate
K0 = 0;
CurveFit/H="1000"/TBOX=768 gauss dwell_time_HistGauss /D
AppendToGraph fit_dwell_time_HistGauss
dTG_mean=W_coef[2]
dTG_SD=W_coef[3]
String countsG,dT_labelG,dTSD_labelG,FitTypeG
WaveStats dwell_time
FitTypeG="Gaussian Fit:"
countsG="# Events="+num2str(V_npnts)
dT_labelG= "dT Mean="+num2str(dTG_mean)+" ms"
dTSD_labelG= "dT SD="+num2str(dTG_SD)+" ms"
TextBox/C/N=text1/A=MC "\\F"Times New Roman"+FitTypeG+"\r"+dT_labelG
+"\r"+dTSD_labelG+"\r"+countsG
ModifyGraph tick=2
ModifyGraph gFont="Times New Roman"
ModifyGraph
lsize(fit_dwell_time_HistGauss)=1.5,rgb(fit_dwell_time_HistGauss)=(0,0,0);DelayUpdate

```

```

ModifyGraph offset(fit_dwell_time_HistGauss)={0.75,0}
ModifyGraph rgb(fit_dwell_time_HistGauss)=(1,4,52428)
Duplicate/O dwell_time_hist, dT_Cum
Wavestats dT_Cum
Integrate/meth=0 dT_Cum
dT_Cum=dT_Cum/dT_Cum(V_Sum)
InsertPoints 0,1, ::dT_ms
InsertPoints 0,1, ::dT_Sigma_ms
InsertPoints 0,1, ::dTG_ms
InsertPoints 0,1, ::dTG_Sigma_ms
::dT_ms(n)=dT_mean
::dT_Sigma_ms(n)=dT_SD
::dTG_ms(n)=dTG_mean
::dTG_Sigma_ms(n)=dTG_SD
StandardPlot()
end

//=====

//=====

macro dG_Square()
WaveStats dG
Variable/G b,bnum,start,last,dG_mean,dG_SD,Tevents,range
range=5
String/G dG_label, dGSD_label,counts
b=sqrt(V_avg) // Bin Width
bnum=sqrt(V_npnts)*1.5 // Total Bins
Tevents=V_npnts
counts="# Events="+num2str(V_npnts)
Make/N=100/O dG_Hist;DelayUpdate
Histogram/C/B={V_min-2*b,b,bnum} dG,dG_Hist;DelayUpdate
Display dG_Hist

```

```

ModifyGraph mode=5
CurveFit/M=0/W=0 gauss, dG_Hist/D
dG_mean=W_coef[2]
print dG_mean
dG_SD=W_coef[3]
start=max (0,dG_mean -range*dG_SD)           // X-axes Start
last=dG_mean + range*dG_SD                   // X-axes End
ModifyGraph offset(dG_Hist)={-b/2,0}
SetAxis bottom start,last
dG_label= "dG Mean="+num2str(dG_mean)+" nS"
dGSD_label= "dG SD="+num2str(dG_SD)+" nS"
TextBox/C/N=text0/A=MC "\\F"Times New Roman"+dG_label + "\\r"+dGSD_label+"\\r"+counts
ModifyGraph rgb(fit_dG_Hist)=(0,0,0)
Label left "\\F"Times New Roman'Counts";DelayUpdate
Label bottom "\\F"Times New Roman'dG (nS\\F"Times New Roman)"
ModifyGraph tick=2
ModifyGraph gFont="Times New Roman"
print b
print bnum
print V_min
InsertPoints 0,1, ::dG_nS
InsertPoints 0,1, ::dG_Sigma_nS
InsertPoints 0,1, ::Set_Number
InsertPoints 0,1, ::Events
::dG_nS(n)=dG_mean
::dG_Sigma_nS(n)=dG_SD
::Events(n)=Tevents
StandardPlot()
end
//=====

```

```

//=====
macro Plot_dT_Square()
Variable bnum,start,last,Range,dT_mean,dT_SD,dTG_mean,dTG_SD,
Make/N=75/O dwell_time_Hist;DelayUpdate
Histogram/C/B={0.5,1.5,60} dwell_time,dwell_time_Hist;DelayUpdate
Display dwell_time_Hist
ModifyGraph mode=5
K0 = 0;
CurveFit/H="1000"/NTHR=0 LogNormal dwell_time_Hist /D
dT_mean=W_coef[2]
dT_SD=W_coef[3]
String counts,dT_label,dTSD_label,FitType
FitType="Lognormal Fit:"
WaveStats dwell_time
counts="# Events="+num2str(V_npnts)
dT_label= "dT Mean="+num2str(dT_mean)+" ms"
dTSD_label= "dT SD="+num2str(dT_SD)+" ms"
TextBox/C/N=text0/A=MC "\\FTimes New Roman"+FitType+"\r"+dT_label
+"\r"+dTSD_label+"\r"+counts
ModifyGraph tick=2
ModifyGraph gFont="Times New Roman"
ModifyGraph lsize(fit_dwell_time_Hist)=1.5,rgb(fit_dwell_time_Hist)=(0,0,0);DelayUpdate
ModifyGraph offset(fit_dwell_time_Hist)={0.75,0}
Duplicate/O dwell_time_hist, dT_Cum
Wavestats dT_Cum
Integrate/meth=0 dT_Cum
//dT_Cum=dT_Cum/dT_Cum(V_Sum)
Histogram/C/B={0.5,1.5,60} dwell_time,dwell_time_HistGauss;DelayUpdate
K0 = 0;
CurveFit/H="1000"/TBOX=768 gauss dwell_time_HistGauss /D
AppendToGraph fit_dwell_time_HistGauss

```

```

dTG_mean=W_coef[2]
dTG_SD=W_coef[3]
String countsG,dT_labelG,dTSD_labelG,FitTypeG
WaveStats dwell_time
FitTypeG="Gaussian Fit:"
countsG="# Events="+num2str(V_npnts)
dT_labelG="dT Mean="+num2str(dTG_mean)+" ms"
dTSD_labelG="dT SD="+num2str(dTG_SD)+" ms"
TextBox/C/N=text1/A=MC "\\F"Times New Roman"+FitTypeG+"\r"+dT_labelG
+"\r"+dTSD_labelG+"\r"+countsG
ModifyGraph tick=2
ModifyGraph gFont="Times New Roman"
ModifyGraph
lsize(fit_dwell_time_HistGauss)=1.5,rgb(fit_dwell_time_HistGauss)=(0,0,0);DelayUpdate
ModifyGraph offset(fit_dwell_time_HistGauss)={0.75,0}
Label left "Count";DelayUpdate
Label bottom " $\Delta t$  (ms)"
ModifyGraph rgb(fit_dwell_time_HistGauss)=(1,4,52428)
SetAxis bottom *,30
StandardPlot()
end

//=====

//=====

macro Plot_dG_Square()
WaveStats dG
Variable/G b,bnum,start,last,dG_mean,dG_SD,Tevents,range
range=5
String/G dG_label, dGSD_label,counts
b=sqrt(V_avg) // Bin Width
bnum=sqrt(V_npnts)*1.5 // Total Bins

```

```

Tevents=V_npnts
counts="# Events="+num2str(V_npnts)
Make/N=100/O dG_Hist;DelayUpdate
Histogram/C/B={V_min-2*b,b,bnum} dG,dG_Hist;DelayUpdate
Display dG_Hist
ModifyGraph mode=5
CurveFit/M=0/W=0 gauss, dG_Hist/D
dG_mean=W_coef[2]
print dG_mean
dG_SD=W_coef[3]
start=max(0,dG_mean -range*dG_SD)           // X-axes Start
last=dG_mean + range*dG_SD                  // X-axes End
ModifyGraph offset(dG_Hist)={-b/2,0}
SetAxis bottom start,last
dG_label= "dG Mean="+num2str(dG_mean)+" nS"
dGSD_label= "dG SD="+num2str(dG_SD)+" nS"
TextBox/C/N=text0/A=MC "\\F'Times New Roman"+dG_label +"\r"+dGSD_label+"\r"+counts
ModifyGraph rgb(fit_dG_Hist)=(0,0,0)
Label left "\\F'Times New Roman'Counts";DelayUpdate
Label bottom "\\F'Times New Roman'dG (nS\\F'Times New Roman)"
ModifyGraph tick=2
ModifyGraph gFont="Times New Roman"
Label left "Count";DelayUpdate
Label bottom "ΔG (nS)"
SetAxis bottom 0,45
print b
print bnum
print V_min
StandardPlot()
end

//=====

```

```

//=====
macro Plot_dT_SquareGauss()
Variable bnum,start,last,Range,dTG_mean,dTG_SD
Make/N=75/O dwell_time_HistGauss;DelayUpdate
Histogram/C/B={0.5,1.5,60} dwell_time,dwell_time_HistGauss;DelayUpdate
Display dwell_time_Hist
ModifyGraph mode=5
K0 = 0;
CurveFit/H="1000"/TBOX=768 gauss dwell_time_HistGauss /D
AppendToGraph fit_dwell_time_HistGauss
dTG_mean=W_coef[2]
dTG_SD=W_coef[3]
String counts,dT_label,dTSD_label
WaveStats dwell_time
counts="# Events="+num2str(V_npnts)
dT_label= "dT Mean="+num2str(dTG_mean)+" ms"
dTSD_label= "dT SD="+num2str(dTG_SD)+" ms"
TextBox/C/N=text0/A=MC "\\F"Times New Roman"+dT_label +"\r"+dTSD_label+"\r"+counts
ModifyGraph tick=2
ModifyGraph gFont="Times New Roman"
ModifyGraph
lsize(fit_dwell_time_HistGauss)=1.5,rgb(fit_dwell_time_HistGauss)=(0,0,0);DelayUpdate
ModifyGraph offset(fit_dwell_time_HistGauss)={0.75,0}
Duplicate/O dwell_time_histGauss, dT_Cum
Wavestats dT_Cum
Integrate/meth=0 dT_Cum
dT_Cum=dT_Cum/dT_Cum(V_Sum)
StandardPlot()
end
//=====

```


APPENDIX 9

Additional experiments

A9.1 Effect of software filtering on the measured ΔG values.

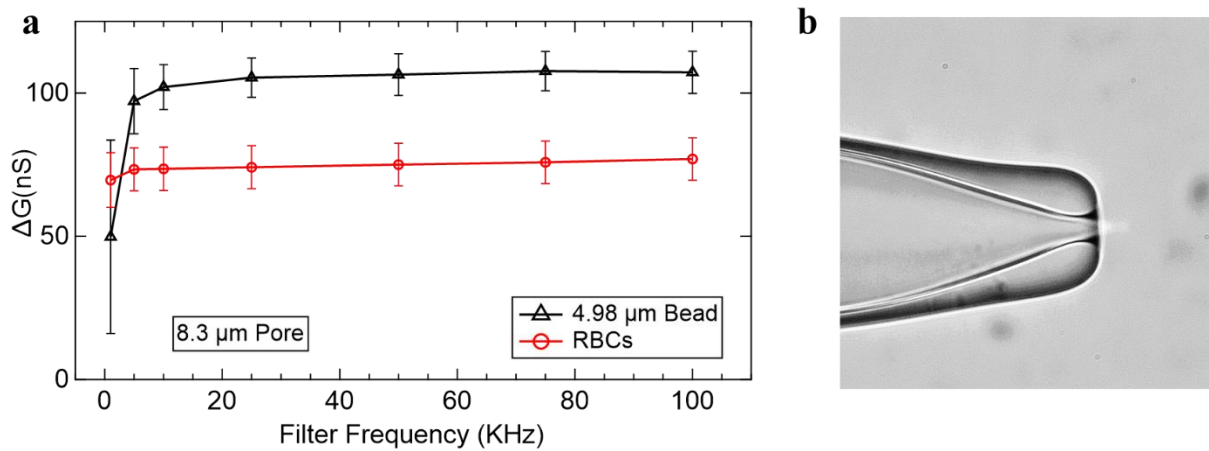


Figure A9.1 Effect of software filtering on the measured ΔG values: **a** Error plot of the ΔG values estimated at different software filter frequencies (4th order Butterworth) for translocation data of 4.98 μm beads (black) and RBCs (red) translocating through an 8.3 μm micropore device. **b** Microscopic image of the micropore used for the experiment. Note that the experiment was performed at constant fluid flow of 500 nL/min and the data was acquired at 200 kHz.

A9.2 Effect of Bovine Albumin Serum on EtOH-treated RBCs

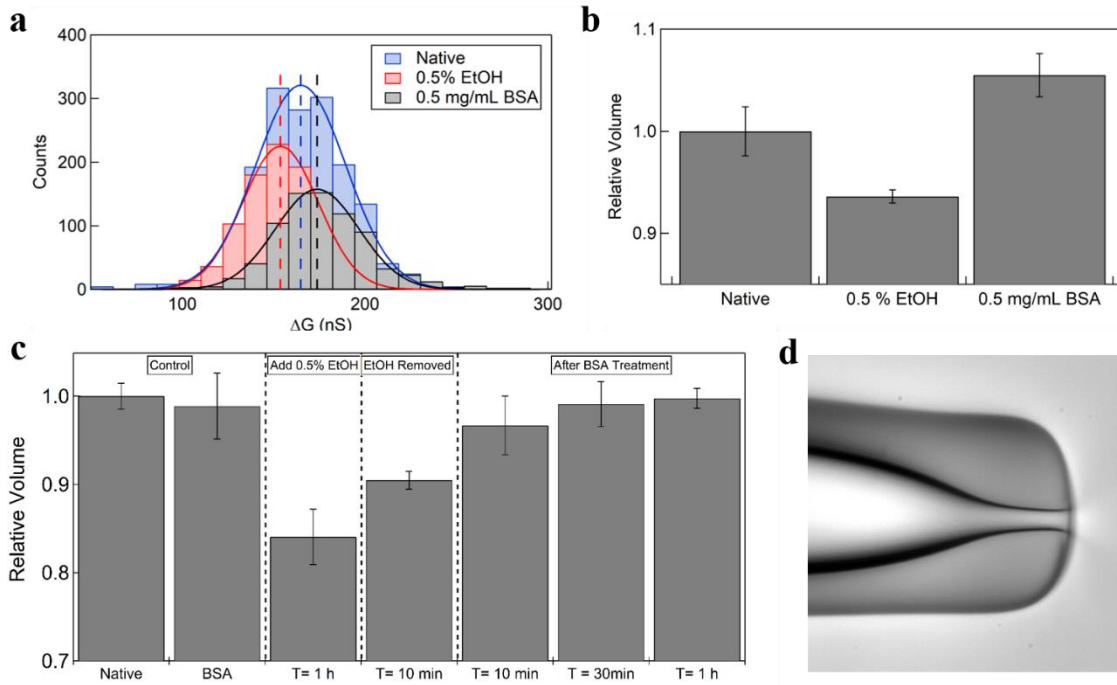


Figure A9.2: Effect of Bovine Albumin Serum on EtOH-treated RBCs: **a** The comparison of ΔG histograms of RBCs in their native state, 0.5 % EtOH, and treatment of the 0.5% EtOH RBCs with 0.5 mg/mL BSA are shown here. The histograms are Gaussian fitted and the dotted vertical lines show the peak of the Gaussian fit. **b** The bar plot shows the relative volume of RBCs detected by the experiment for the three states mentioned. **c** The bar plot shows the recovery effect of BSA on RBCs previously treated with 0.5 % EtOH for 1 hr. **d** Microscopic image of the 8.0 μm micropore used for the experiment.

A9.3 Electrofluidic detection of RBCs infected with malaria Parasite

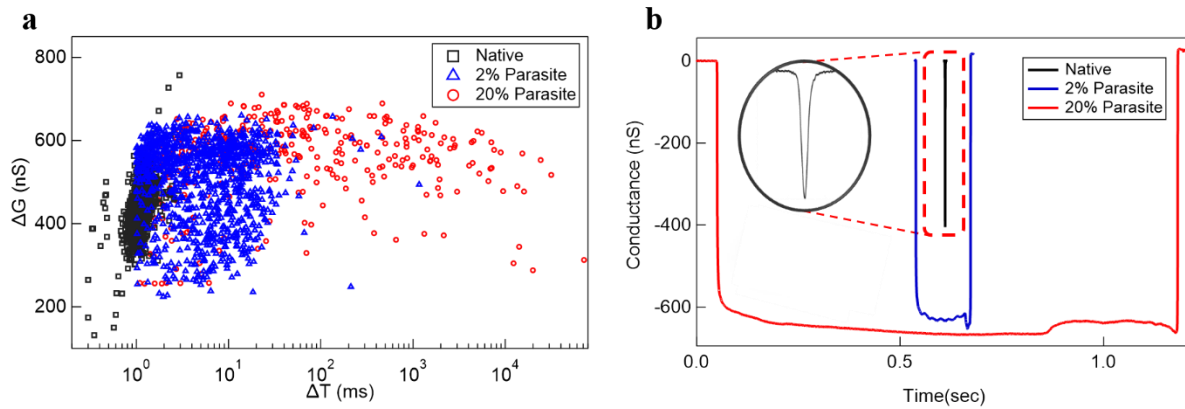


Figure A9.3 Electrofluidic detection of RBCs infected with malaria Parasite: **a** ΔG vs Δt scatterplot of the constricted translocation events for native RBCs (black), RBCs infected with 2% (blue) and 20% Malaria parasite (red) **b** The representative translocation events for a native RBCs (black), RBCs infected with 2% (blue) and 20% Malaria parasite (red) is shown here. The inset shows a zoom of the native RBCs translocation event.